406456   *228p*

The Telecommunications and Data Acquisition Progress Report 42-120

October–December 1994

Joseph H. Yuen
Editor

February 15, 1995

NASA

National Aeronautics and
Space Administration

Jet Propulsion Laboratory
California Institute of Technology
Pasadena, California

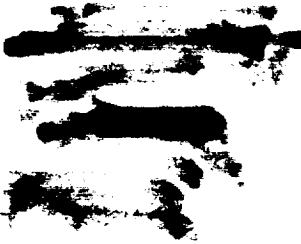# The Telecommunications and Data Acquisition Progress Report 42-120

October–December 1994

Joseph H. Yuen
Editor

February 15, 1995

NASA

National Aeronautics and
Space Administration

Jet Propulsion Laboratory
California Institute of Technology
Pasadena, California

Preface

This quarterly publication provides archival reports on developments in programs managed by JPL's Telecommunications and Mission Operations Directorate (TMOD), which now includes the former Telecommunications and Data Acquisition (TDA) Office. In space communications, radio navigation, radio science, and ground-based radio and radar astronomy, it reports on activities of the Deep Space Network (DSN) in planning, supporting research and technology, implementation, and operations. Also included are standards activity at JPL for space data and information systems and reimbursable DSN work performed for other space agencies through NASA. The preceding work is all performed for NASA's Office of Space Communications (OSC).

TMOD also performs work funded by other NASA program offices through and with the cooperation of OSC. The first of these is the Orbital Debris Radar Program funded by the Office of Space Systems Development. It exists at Goldstone only and makes use of the planetary radar capability when the antennas are configured as science instruments making direct observations of the planets, their satellites, and asteroids of our solar system. The Office of Space Sciences funds the data reduction and science analyses of data obtained by the Goldstone Solar System Radar. The antennas at all three complexes are also configured for radio astronomy research and, as such, conduct experiments funded by the National Science Foundation in the U.S. and other agencies at the overseas complexes. These experiments are either in microwave spectroscopy or very long baseline interferometry.

Finally, tasks funded under the JPL Director's Discretionary Fund and the Caltech President's Fund that involve TMOD are included.

This and each succeeding issue of *The Telecommunications and Data Acquisition Progress Report* will present material in some, but not necessarily all, of the aforementioned programs.

Contents

OSC TASKS
DSN Advanced Systems
TRACKING AND GROUND-BASED NAVIGATION

COMMUNICATIONS, SPACECRAFT–GROUND

DSN Systems Implementation
CAPABILITIES FOR NEW PROJECTS

NETWORK UPGRADE AND SUSTAINING

Orbit Determination of Highly Elliptical Earth Orbiters Using Improved Doppler Data-Processing Modes

J. A. Estefan
Navigation Systems Section

A navigation error covariance analysis of four highly elliptical Earth orbits is described, with apogee heights ranging from 20,000 to 76,800 km and perigee heights ranging from 1,000 to 5,000 km. This analysis differs from earlier studies in that improved navigation data-processing modes were used to reduce the radio metric data. For this study, X-band (8.4-GHz) Doppler data were assumed to be acquired from two Deep Space Network radio antennas and reconstructed orbit errors propagated over a single day. Doppler measurements were formulated as total-count phase measurements and compared to the traditional formulation of differenced-count frequency measurements. In addition, an enhanced data-filtering strategy was used, which treated the principal ground system calibration errors affecting the data as filter parameters. Results suggest that a 40- to 60-percent accuracy improvement may be achievable over traditional data-processing modes in reconstructed orbit errors, with a substantial reduction in reconstructed velocity errors at perigee. Historically, this has been a regime in which stringent navigation requirements have been difficult to meet by conventional methods.

I. Introduction

The principal focus of recent navigation-related research has been on the development of new or improved navigation techniques to simultaneously improve performance, while reducing navigation-related requirements levied upon spacecraft and associated mission operations. The motivation for such a focused effort is clear—tighter budgetary constraints imposed on current and future NASA space science missions. Advanced studies of interplanetary mission scenarios have shown that medium-to-high navigation accuracies (40 to 15 nrad in an angular sense) can be achieved through the use of nontraditional data-processing modes for Doppler and ranging data types acquired from the Deep Space Network (DSN) [1,2]. These new techniques take advantage of improved calibrations of the limiting ground system error sources affecting the data and make use of high-speed workstation computers to reduce the data. Studies are also being conducted to demonstrate the utility of these alternative data-processing modes with actual flight data acquired from the Ulysses and Galileo spacecraft [3,4].

These promising research findings prompted this investigation into the use of improved radio metric data-processing modes in tracking and navigational support of high Earth orbiter (HEO) missions. In this

article, a navigation error covariance analysis is described, which studies the utility of advanced data-processing modes for X-band (8.4-GHz) Doppler data acquired from DSN-based radio antennas. The analysis investigates two-way Doppler-only navigation performance; other radio metric data strategies, such as two-way radio ranging, are not addressed. A discussion of Doppler data-processing modes is presented along with assumptions for error covariance analysis derived from an improved set of data acquisition and orbit determination error-modeling strategies. Results from the covariance analysis are described for four sample highly elliptical orbits of the space very long baseline interferometry (SVLBI) mission set. A discussion section highlights some critical implications from the analysis and areas that will require further investigation.

II. Doppler Data-Processing Modes

A. Phase Versus Frequency

DSN Doppler data acquired in a two-way coherent mode are not direct frequency shift measurements, but integral counts of the number of cycles of the transmitted carrier signal relative to the received carrier signal that have accumulated over a tracking pass [1]. These cycle counts are differenced to form measurements of the average Doppler shift over short time intervals (typically 1 to 10 min); it is these *differenced-count Doppler* measurements that have traditionally been used for navigating spacecraft [5].[1] The purpose of differencing the Doppler counts was to overcome limitations in early tracking hardware that caused discontinuities in the data (known as *cycle slips*) that occurred when the ground receiver's phase-tracking loop would momentarily lose its lock on the spacecraft carrier signal. Cycle slips are most likely to occur when the spacecraft's Doppler frequency is large and varies rapidly or when the spacecraft carrier signal-to-noise ratio approaches the tracking threshold of the ground receiver.

The notion of using the original Doppler count as a navigation measurement was considered as early as 1966 by Curkendall [6], but the idea was not popularized because of the operational constraints cited above. Given the steady improvements in the DSN tracking system over the years, together with the development of robust methods for resolving occasional cycle slips, there is a renewed interest in using the original Doppler count (subsequently referred to as *total-count phase*) as a viable data type for spacecraft navigation [1].[2] The motivation for using total-count phase as a navigation measurement is that the precision of these data is very high (a few millimeters at X-band frequencies) whereas differencing cycle counts to construct a frequency-formulated observable effectively increases the data noise level. Furthermore, unlike Doppler that is differenced-count formulated, phase-formulated Doppler lends itself to a simpler data noise model since the errors are uncorrelated.

B. Filtering Strategies

The standard orbit determination filtering strategy used by flight project navigation teams treats various systematic error sources as unmodeled *consider* parameters, which are not estimated but whose effects are accounted for (i.e., "considered") in computing the error covariance of filter (estimated) parameters [7]. In a consider state analysis, the estimated parameter set's sensitivity to various unmodeled consider parameters can be computed via the partial derivatives of the state estimate with respect to the consider parameter set [8]. Depending on the magnitude of the resulting sensitivities, the filter-computed estimation error covariance is modified to account for unmodeled effects to generate a more realistic estimate of predicted navigation performance. The filter has no knowledge of the unmodeled parameters'

---

[1] Historically, the result of differencing cycle counts to form measurements of the average Doppler shift has been referred to as *differenced-range Doppler*, the convention originating from the mathematical formulation of the observable in which the station-to-spacecraft range is explicitly differenced over a specified integration, or "count," time.

[2] T. D. Moyer, "ODE and REGRES Modifications for Processing Block V Receiver Doppler Observables and Total Count Phase Observables," JPL Engineering Memorandum 314-568 (internal document), Jet Propulsion Laboratory, Pasadena, California, August 24, 1993.

contribution to uncertainty in the state estimate since the modified covariance (the consider covariance), including effects from both the estimated and consider parameters, is not fed back to the filter.

Some principal reasons for using a consider state filter are: (1) certain parameters, such as fiducial station locations, may be fixed in order to define a reference frame and/or length scale; (2) there may be a lack of adequate models for an actual physical effect; (3) computational limitations exist when attempting to adjust parameters of high order, such as the coefficients in a gravity field; or (4) if estimated, the computed uncertainty in model parameters would be reduced far below the level warranted by model accuracy [9,10]. Consider state filters have been known to experience failure modes, such as when additional data yield an increase in the consider covariance, or when the consider covariance propagates to an unreasonably large result over time [10]. In these instances, it is usually necessary to empirically "tune" the filter by adjusting data weights or model assumptions to obtain useful estimates.

A new sequential data-filtering strategy currently under study is the enhanced orbit determination filter, in which most or all of the major systematic ground-system calibration error sources affecting the data are treated as filter parameters, along with spacecraft trajectory parameters [1,11,12]. This strategy differs from current practice, in which the ground-system calibration error sources are represented as unestimated bias or consider parameters and accounted for only when computing the error covariance of the filter parameters. The motivation behind the enhanced filter is not so much to improve upon the a priori ground system calibrations, but to incorporate a more accurate model of the physical world into the filter [1].

III. Error Covariance Analysis Assumptions

Earlier orbit determination studies of DSN-based Doppler tracking for HEO missions focused on using the conventional frequency formulation of the Doppler observable along with a standard consider state filtering strategy [13]. For this new study, a revised error covariance analysis was performed to quantify the navigational utility of a phase formulation of the Doppler observable together with an enhanced data-filtering strategy, which treats the principal ground system calibration error sources as filter parameters. In this section, assumptions for the revised navigation error covariance analysis are provided, including orbit characteristics, data-acquisition and simulation strategies, and filter error modeling.

A. Sample Orbits

Four highly elliptical orbits, all derived from the international SVLBI mission set, were selected for analysis. The first orbit represents the current operational orbit design for the Japanese MUSES-B spacecraft of the VLBI Space Observatory Program (VSOP), targeted to launch in September 1996 [14]. Nominal orbit parameters are provided in Table 1. The MUSES-B orbit is the lowest of the four sample orbits, with perigee and apogee heights of 1,000 and 20,000 km, respectively. The second orbit is representative of the latest orbit design for the Russian RadioAstron project [15]. It is the most eccentric of the sample orbits, with perigee and apogee heights of 5,000 and 76,800 km, respectively. Table 2 lists the nominal orbit parameters for RadioAstron, targeted to launch in 1997 or 1998.

The two remaining sample orbits are both based on preliminary orbit designs for the Advanced Radio Interferometry Between Space and Earth (ARISE) SVLBI mission. ARISE is intended to be a next-generation SVLBI mission with a more ambitious set of scientific goals than VSOP and RadioAstron [16]. Current ARISE orbit design calls for perigee and apogee heights of about 5,000 and 12,000 to 50,000 km, respectively; final orbit selection will ultimately depend on the principal scientific objectives of the mission. For this analysis, two candidate orbits were assumed with apogee heights of 12,000 and 50,000 km. Nominal orbit parameters for a mission launch in 2005 are provided in Table 3. Note that ARISE will have very stringent orbit determination requirements that exceed the capability of current and anticipated ground-based radio tracking strategies, such as two-way Doppler, and will require a much more ambitious tracking and navigation strategy. Current design calls for two onboard Global

Table 1. Sample orbit parameters for the Japanese VSOP mission (MUSES-B).

Parameter	Value
Nominal launch date	September 1996
Initial spacecraft ephemeris	
Semimajor axis	16,878 km
Eccentricity	0.5629
Inclination	31.0 deg
Argument of perigee	134.24 deg
Longitude of ascending node	116.14 deg
Mean anomaly	0.0 deg
Additional parameters	
Perigee height	1,000 km
Apogee height	20,000 km
Orbit period	6.06 h

Table 2. Sample orbit parameters for the Russian RadioAstron project.

Parameter	Value
Nominal launch date	1997/98
Initial spacecraft ephemeris	
Semimajor axis	46,778 km
Eccentricity	0.7781435
Inclination	51.5 deg
Argument of perigee	190.0 deg
Longitude of ascending node	300.0 deg
Mean anomaly	0.0 deg
Additional parameters	
Perigee height	4,000 km
Apogee height	76,800 km
Orbit period	28 h

Positioning System (GPS) receivers [16].[3] However, for this analysis, it is the orbit characteristics that are of principal interest, not the actual mission requirements.

B. Tracking Data Simulation

Only two passes of two-way Doppler data were simulated from two different DSN sites. The lengths of the data arcs depend on the sample orbit being studied. For shorter orbit periods, such as the MUSES-B 6.06-h orbit, a 2.25-h pass from the Madrid site and a 2.43-h pass from the Canberra site were assumed.

---

[3] S. C. Wu and R. P. Malla, "GPS-Based Precision Determination of Highly Elliptical Orbits for Orbiting VLBI Applications," JPL Interoffice Memorandum 335.8-94-004 (internal document), Jet Propulsion Laboratory, Pasadena, California, March 29, 1994.

Table 3. Sample orbit parameters for the ARISE mission.

Parameter	Value
Nominal launch date	2005
Initial spacecraft ephemeris	
Semimajor axis	18,878.15 km/33,878.15 km
Eccentricity	0.40/0.66
Inclination	60.0 deg
Argument of perigee	0.0 deg
Longitude of ascending node	0.0 deg
Mean anomaly	0.0 deg
Additional parameters	
Perigee height	5,000 km
Apogee height	12,000 km/50,000 km
Orbit period	7.17 h/17.24 h

In the case of the ARISE 7.17-h orbit, a 4.07-h pass from Madrid and a 4.20-h pass from Goldstone were assumed. The two passes for the 28-h RadioAstron orbit consisted of a 3.03-h Goldstone pass and a longer 15.82-h Madrid pass. For the longer 17.24-h ARISE orbit, a 9.52-h Madrid pass and a 4.23-h Goldstone pass were assumed.

To account for random data noise, the measurement error models of [1] were assumed. These models are representative of the DSN's current X-band Doppler system for the 34-m high efficiency (HEF) stations with nominal values for spacecraft turnaround ratio, transmit frequency of the carrier signal, and sample time. For a differenced-count Doppler measurement at time t_k, denoted as f_k, the following model is assumed:

$$f_k \equiv \dot{\rho}_k + \nu_k \tag{1}$$

where

$$\dot{\rho}_k = \text{station-to-spacecraft range rate at time } t_k$$

ν_k = samples of a zero-mean white Gaussian sequence, in which each sample has constant variance and is uncorrelated with all other samples[4]

The random process ν incorporates both additive phase-measurement errors and errors due to ground system frequency instability that are integrated over the count time of each observation. For this analysis, differenced-count Doppler measurements were weighted with a 1-σ measurement uncertainty of 0.1 mm/s (metric value) for a 60-s count time. In addition, additive noise variances were adjusted by an elevation-dependent function to reduce the weight of the low-elevation data. No data were acquired at elevation angles below 10 deg from any DSN site.

For a total-count phase measurement at time t_k, denoted as ϕ_k to represent the Doppler count at time t_k, the following model is assumed:

---

[4] This approximation is not rigorously correct since successive differenced-count Doppler data points share common values of the Doppler count and, therefore, each data point is correlated with the two points adjacent to it. In practice, it is believed that the uncorrelated measurement error assumption does not yield significantly incorrect statistical calculations for the large Doppler data sets typically used in mission operations [1].

$$\phi_k \equiv (\rho_k - \rho_0) + \phi_0 + \eta_k + \xi_k \tag{2}$$

where

ρ_k = station-to-spacecraft range at time t_k

ρ_0 = station-to-spacecraft range at time t_0

ϕ_0 = unknown phase offset of Doppler counter at time t_0

and

η_k = additive phase-measurement error

ξ_k = cumulative phase-measurement error

The phase offset, ϕ_0, represents the Doppler counter initialization error and is assumed to be a random bias. The η_k samples are assumed to be a white, zero-mean Gaussian sequence with constant variance, and the ξ_k values represent the cumulative phase error induced by the integration of frequency variations by the Doppler counter. The total-count phase measurements were weighted for this analysis with a 1-σ measurement uncertainty of 2.5 mm (metric value).[5] As with differenced-count Doppler, the additive noise variances were adjusted by an elevation-dependent function to reduce the weight of low-elevation data, and a 10-deg lower elevation cut-off angle assumed for the DSN stations.

C. Orbit Determination Error Model

Table 4 provides the dynamic and observational error model assumptions that make up the enhanced orbit determination filter, along with a priori statistics, steady-state uncertainties for the Gauss–Markov parameters, and noise densities, N, for the random walk parameters. With the exception of the gravitational force model, all parameters were treated as filter parameters and grouped into three categories: spacecraft epoch state, spacecraft nongravitational force model, and ground system error model. The Earth's gravitational parameter (GM) and geopotential field harmonic coefficients were treated as unmodeled consider parameters and grouped in the gravitational force model category. By comparison, Table 5 gives the error modeling assumptions that comprise the standard consider state filter model.

A batch-sequential factorized Kalman filter was used in the estimation process, with a batch size of 840 min (14 h) for the standard-filtering strategy, reduced to 10-min batch intervals for the enhanced-filtering strategy so that short-term fluctuations could be tracked in the transmission media. For process noise, first-order Gauss–Markov (exponentially correlated) random processes were assumed. The process noise covariance is given by $q = (1 - m^2) \sigma_{ss}^2$ where $m = \exp[-(t_{j+1} - t_j)/\tau]$. Here, t_j is the start time for the jth batch and τ is the associated time constant. The term σ_{ss} is the steady-state uncertainty, i.e., the noise level that would be reached if the dynamical system were left undisturbed for a time much greater than τ. For the random walk, both σ_{ss} and τ are unbounded ($\tau = \infty$) and a steady state is never reached. The noise density for the random walk is characterized by the rate of change of the process noise covariance, $q = \Delta q / \Delta t$, where Δ is the batch size and Δq is the amount of noise added per batch [9].

---

[5] The data noise values for both differenced-count Doppler and total count phase can be readily modified for future navigation analyses as the performance specifications of the supporting ground system begin to mature.

Table 4. Enhanced orbit determination filter with ground-system error model representative of current DSN calibration accuracy.

Estimated parameter set	Uncertainty (1σ)	Remarks
Spacecraft epoch state	A priori	Constant parameters
Position	10^3 km	
Velocity	1 km/s	
Nongravitational force model		
Solar radiation pressure	Steady-state	Markov parameters
Specular/diffuse reflectivity	10 percent of nominal	0.25–3 day time constant
Anomalous accelerations	Steady-state	Markov parameters
Radial	10^{-12} km/s^2	1–3 day time constant
Transverse	10^{-12} km/s^2	1–3 day time constant
Ground system error model		
Doppler phase offset	A priori	Random walk
(each station)	100 km	1 cm^2/h
DSN station coordinates		
Crust fixed	A priori	Constant parameters
Spin radius (r_s)	0.18 m	
Z-height (z_h)	0.23 m	
Longitude (λ)	3.6×10^{-8} rad	
Geocenter offset	A priori	Constant parameters
Z-component	1 m	
Earth orientation	Steady-state	Markov parameters
Pole orientation	1.5×10^{-8} rad	1-day time constant
Rotation period	0.2 ms	12-h time constant
Transmission media	A priori	Random walk
Zenith troposphere	5 cm	1 cm^2/ h
(each station)		

Consider parameter set	Uncertainty (1σ)	Remarks
Gravitational force model	A priori	Constant parameters
Earth's GM	GM $\times$ 10^{-8}	
Harmonics	8 $\times$ 8 field (GEM-L2)	

The principal difference between the enhanced and standard filter models used for this study was the modeling of observational errors, namely:

(1) A random walk model (simple Brownian motion process) was used to track short-term fluctuations in the troposphere and assumed zenith delay calibration uncertainties representative of the current DSN-based calibration accuracy.

(2) A phase offset parameter for each station was included in the ground system error model. As with the tropospheric path delays, these parameters were modeled as random walk processes. Table 4 shows the noise density given for these parameters, which is derived from the white frequency noise representing ground-system frequency instability (see Section III.B).

(3) Three stochastic parameters were included in the ground system error model to account for dynamical uncertainties in the Earth's pole location and rotation period and to represent the pole model solutions developed by Finger and Folkner [17].

Table 5. Standard consider-state orbit determination filter with ground-system error model representative of current DSN calibration accuracy.

Estimated parameter set	Uncertainty (1σ)	Remarks
Spacecraft epoch state	A priori	Constant parameters
Position	10^3 km	
Velocity	1 km/s	
Nongravitational force model		
Solar radiation pressure	Steady-state	Markov parameters
Specular/diffuse reflectivity	10 percent of nominal	0.25–3 day time constant
Anomalous accelerations	Steady-state	Markov parameters
Radial	10^{-12} km/s^2	1–3 day time constant
Transverse	10^{-12} km/s^2	1–3 day time constant

Consider parameter set	Uncertainty (1σ)	Remarks
Ground system error model		
Station coordinates	A priori	Constant parameters
Spin radius (r_s)	0.18 m	
Z-height (z_h)	0.23 m	
Longitude (λ)	3.6×10^{-8} rad	
Geocenter offset	A priori	Constant parameter
Z-component	1 m	
Transmission media		
Zenith troposphere	A priori	Constant parameters
Wet	4 cm	
Dry	1 cm	
Gravitational force model	A priori	Constant parameters
Earth's GM	GM $\times 10^{-8}$	
Harmonics	8 $\times$ 8 field (GEM-L2)	

(4) The gravitational force model was the same model used in previous studies, with the Earth's GM and truncated (8 × 8) GEM-L2 geopotential field harmonic coefficients treated as consider parameters. This is the only element of the overall enhanced filter model that used a standard consider state filtering approach.[6]

IV. Results

Results of the numerical error covariance analysis, based on data-acquisition and error-modeling assumptions described in Section III, are summarized in Table 6. The 1-σ position and velocity uncertainties for reconstructed orbit estimates are tabulated in a root-sum-square (RSS) sense for two different Doppler data-processing modes: (1) differenced-count Doppler data reduced with the standard consider state filter and (2) total-count phase data reduced with the enhanced filter.

The radio navigation performance results in Table 6 assume that science data were collected over the radio metric tracking data arcs. Accordingly, it appears that navigation performance is significantly improved with the more modern Doppler data-processing mode of total-count phase data reduced with

---

[6] The argument for not treating the gravitational force model parameters as actual filter parameters is due principally to computational limitations when attempting to estimate the harmonic coefficients of the geopotential field (see discussion in Section II.B).

Table 6. Orbit accuracies of 1-σ for reconstruction over data arc.

Data-processing mode	VSOP	RadioAstron	ARISE (low)	ARISE (high)
	RSS position uncertainty, m			
Differenced-count Doppler with standard filter	12.6	10.9	11.5	83.5
Total-count phase with enhanced filter	5.5	6.5	6.5	30.0
	RSS velocity uncertainty, cm/s			
Differenced-count Doppler with standard filter	0.17	0.03	0.26	0.41
Total-count phase with enhanced filter	0.06	0.02	0.13	0.15

the enhanced filter. However, these results reflect the accuracies that are achievable only over the specific data arcs and not over the entire orbit arcs. More precise representations of the reconstructed orbit accuracies over the entire orbit arcs (and in some cases over multiple orbit arcs) are shown in Figs. 1 through 4. These figures were constructed from filter-generated error covariances, which were smoothed and combined with consider parameter sensitivities to produce full consider covariances, then mapped forward to give a time history of the reconstructed position and velocity uncertainties over a 24- or 28-h period, depending on the sample orbit being evaluated.

From the time history plots (Figs. 1 through 4), a significant improvement in reconstructed orbit accuracies is seen when Doppler data are processed as phase-formulated measurements and reduced with the enhanced filter. This is true for both position and velocity uncertainties for all four sample orbits, with the most significant improvement evident in the perigee regions for velocity reconstruction, a regime that has historically met with limited success when using traditional radio metric data-processing methods.

Table 7 attempts to better quantify the performance improvement by giving both the range in uncertainties and the average (percentage) improvement over the 24- and 28-h time histories. Actual values used to generate the percentages of improvement were computed by integrating each error curve over the mapped interval to compare total areas of improved versus reference (conventional) data-processing modes. From this summary table, relative percentage improvements ranging from about 40 to 60 percent are seen, depending on the sample orbit. A slightly more dramatic improvement is seen for reconstructed velocity uncertainties over reconstructed positional uncertainties. Again, these results reflect the orbit accuracies over the entire propagation or mapping period, i.e., 24 h for the VSOP and both ARISE sample orbits and 28 h for the RadioAstron sample orbit.

Recall that the gravitational force model parameters assumed for both the standard and enhanced orbit determination filter models were treated as unmodeled consider parameters (see Tables 4 and 5). This was true for both GM and geopotential harmonic coefficients. To gain insight into the effect of these consider parameters on the filtering strategy being used, the approximate percentage contribution of these error sources on the total reconstructed position and velocity uncertainties over the propagation periods was computed, as illustrated in Fig. 5. The altitude dependence of the gravitational force modeling errors to the total reconstructed orbit accuracies is clearly evident. Not surprisingly, these errors contribute far more to the nontraditional data-processing mode; but this is an artifact of the filtering strategy being used and not the formulation of the Doppler observable. These results suggest that if improved navigation accuracies are to be achieved when using the enhanced orbit determination filter, it may
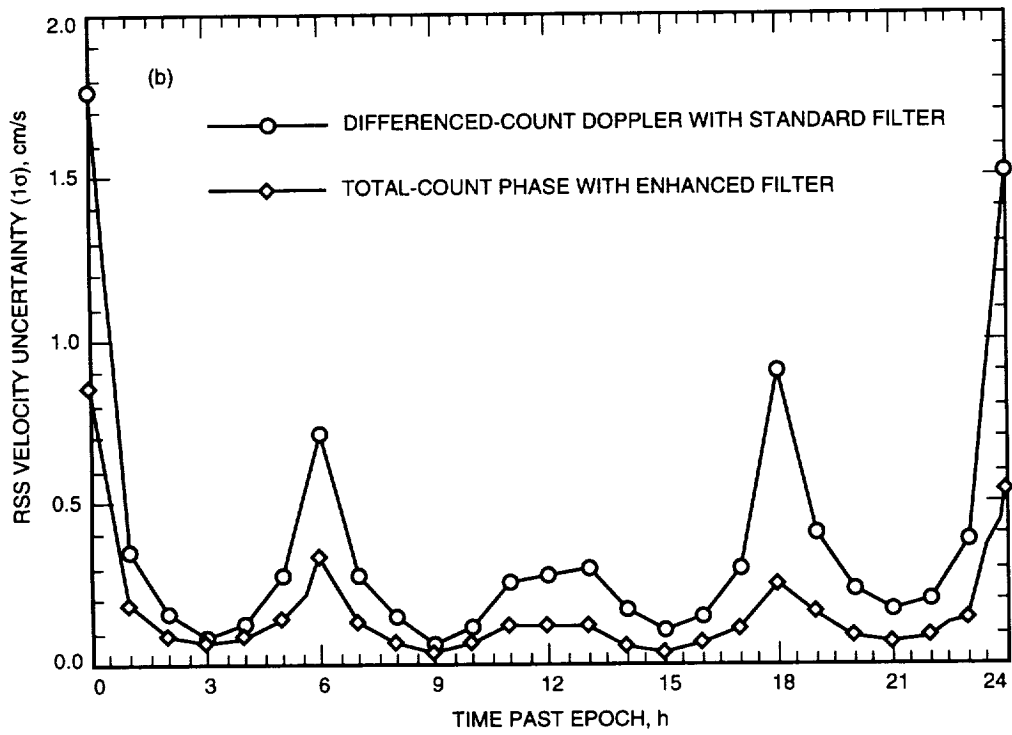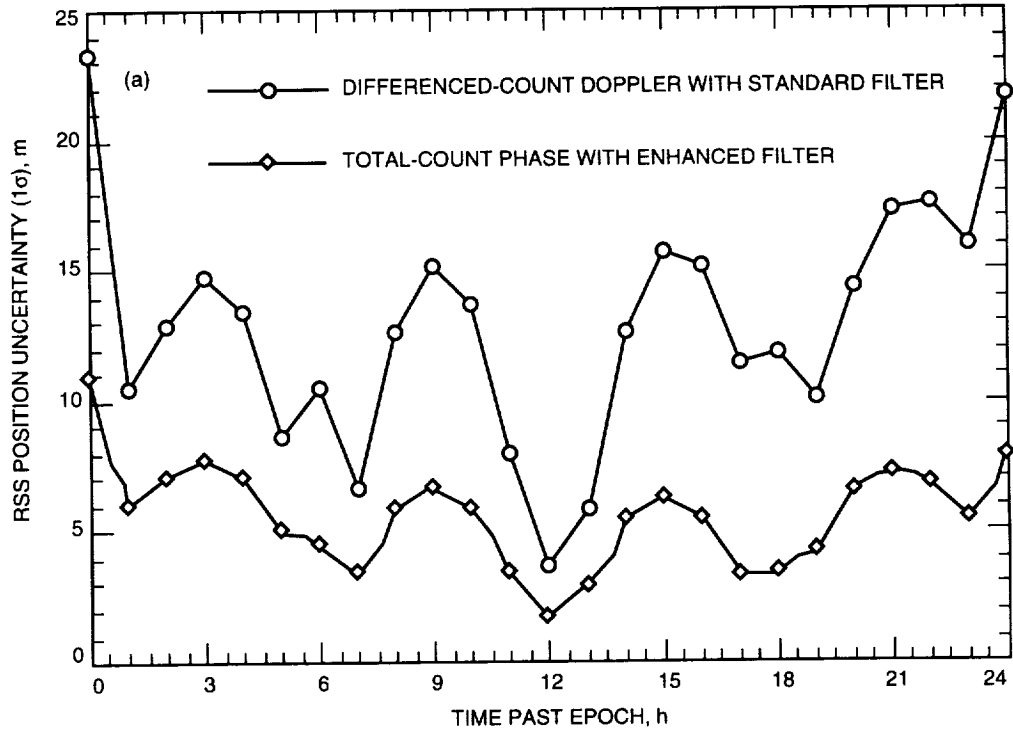
Fig. 1. VSOP 1-σ orbit determination accuracy statistics for expected RSS (a) total position
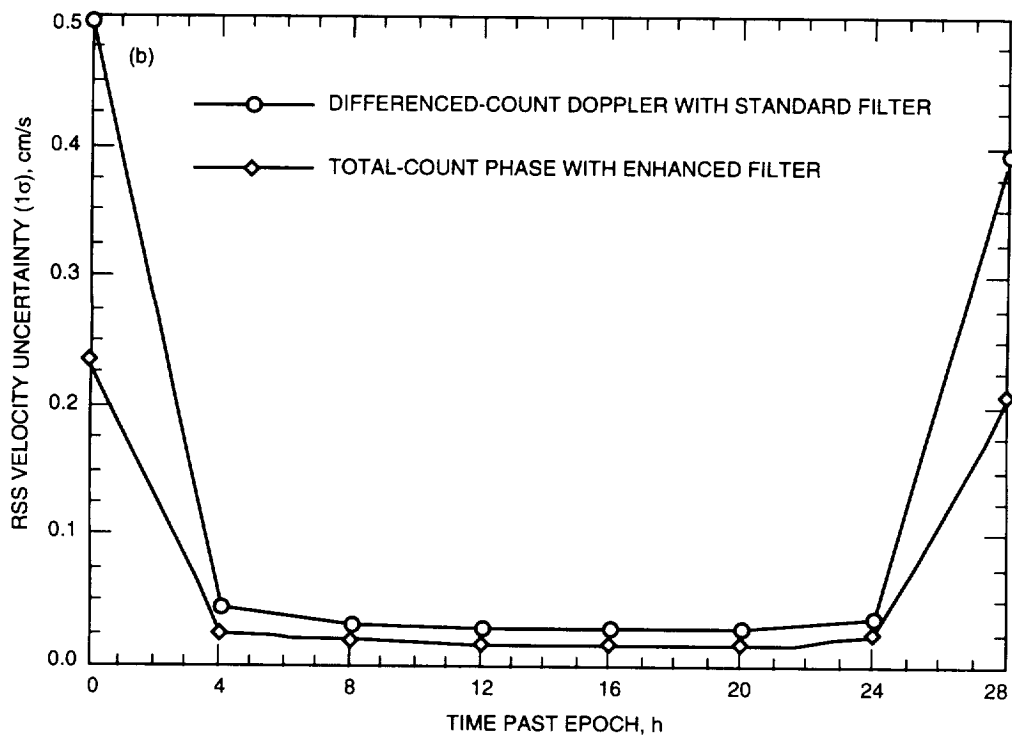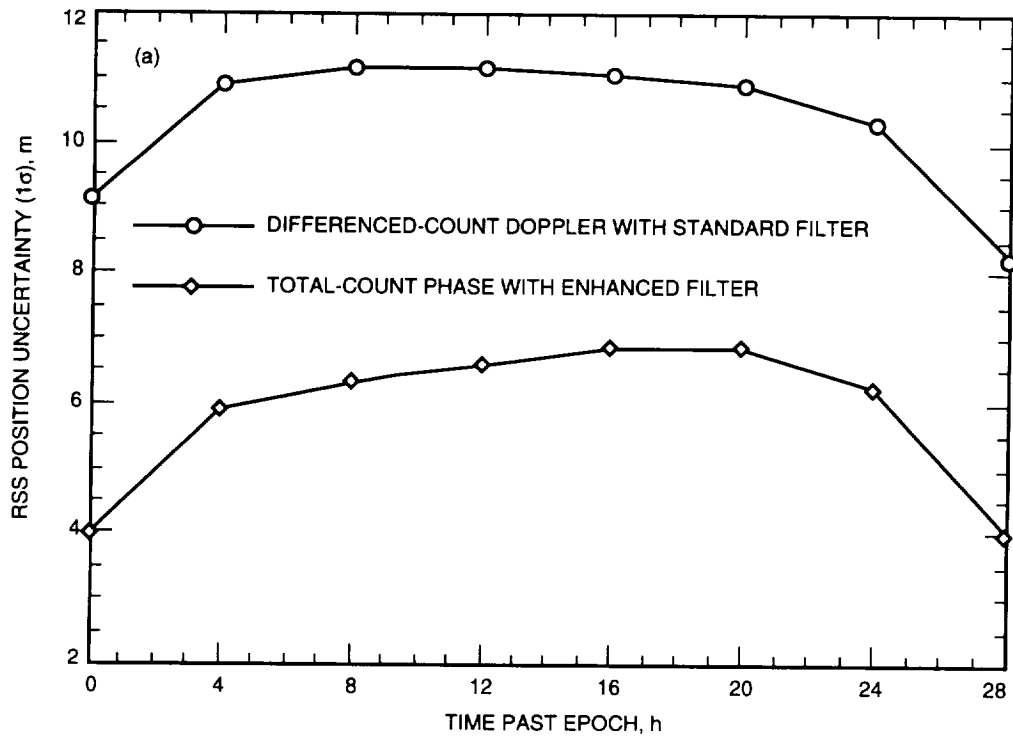uncertainty and (b) total velocity uncertainty.

Fig. 2. RadioAstron 1-σ orbit determination accuracy statistics for expected RSS (a) total position uncertainty and (b) total velocity uncertainty.
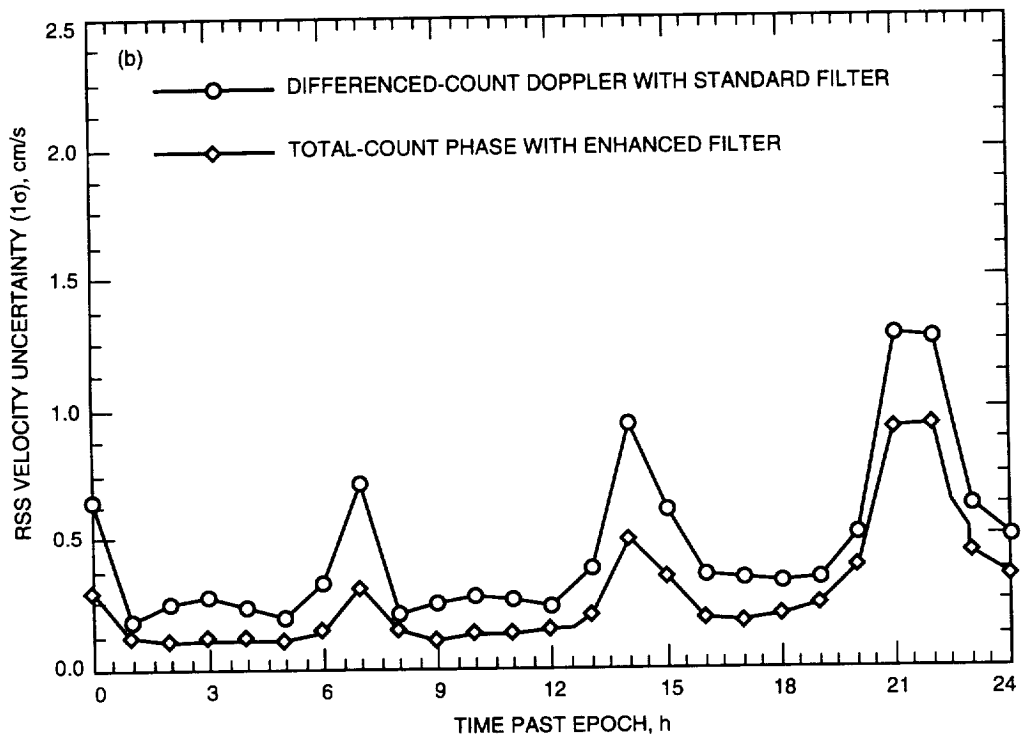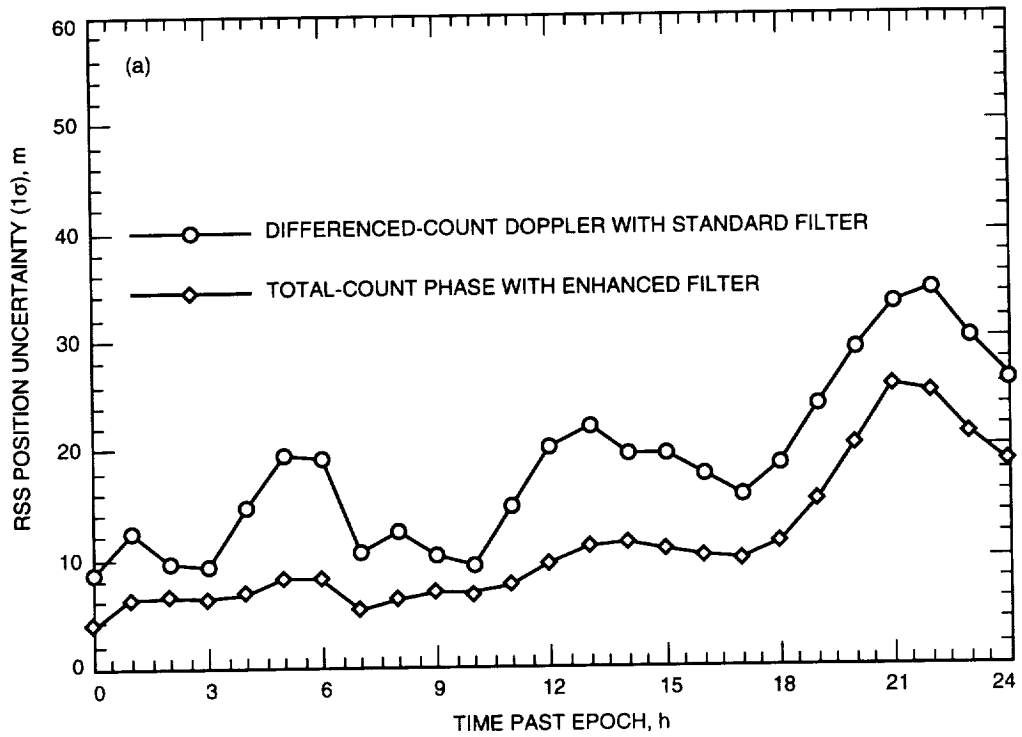
Fig. 3. ARISE (lower candidate orbit) 1-σ orbit determination accuracy statistics for expected RSS (a) total position uncertainty and (b) total velocity uncertainty.
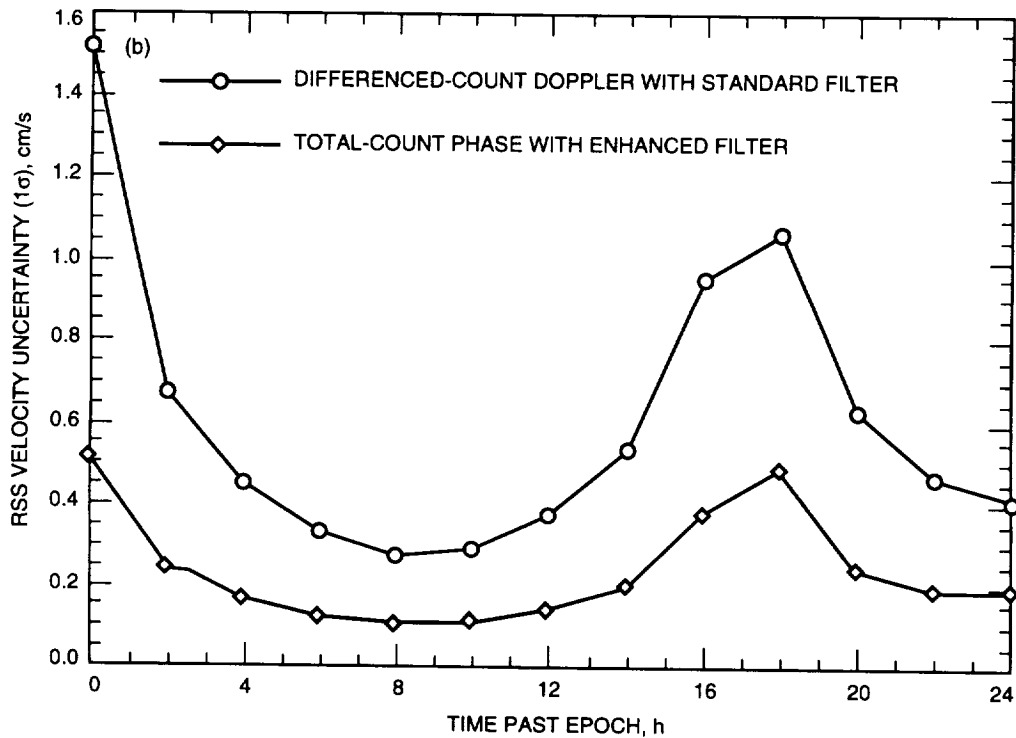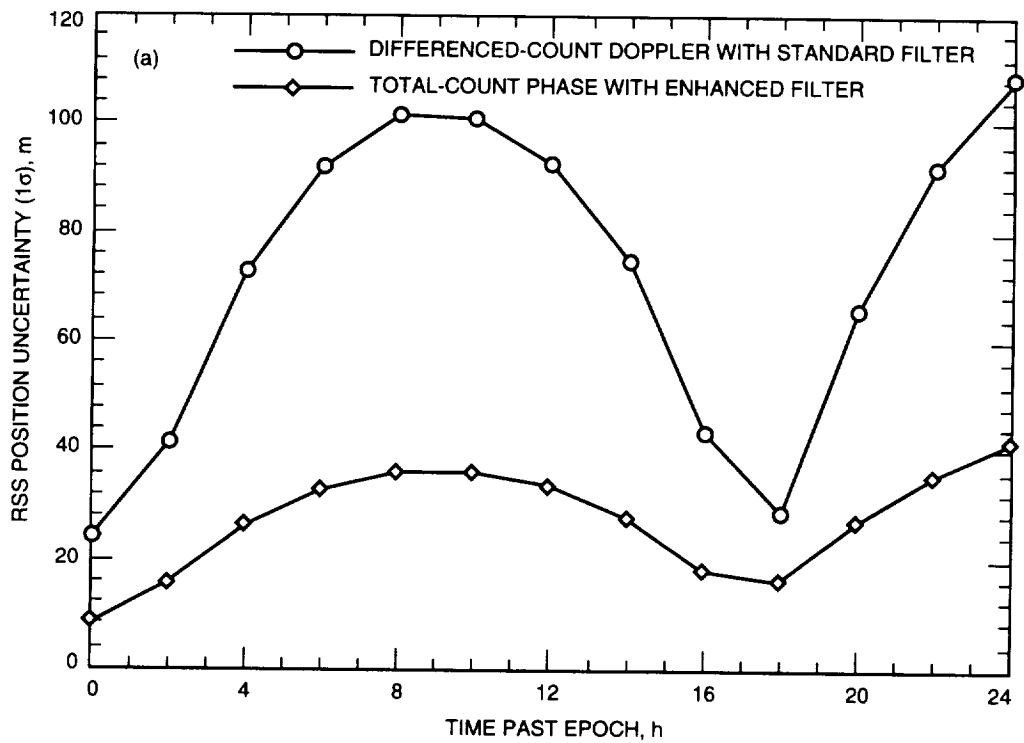
Fig. 4. ARISE (higher candidate orbit) 1-σ orbit determination accuracy statistics for expected RSS (a) total position uncertainty and (b) total velocity uncertainty.
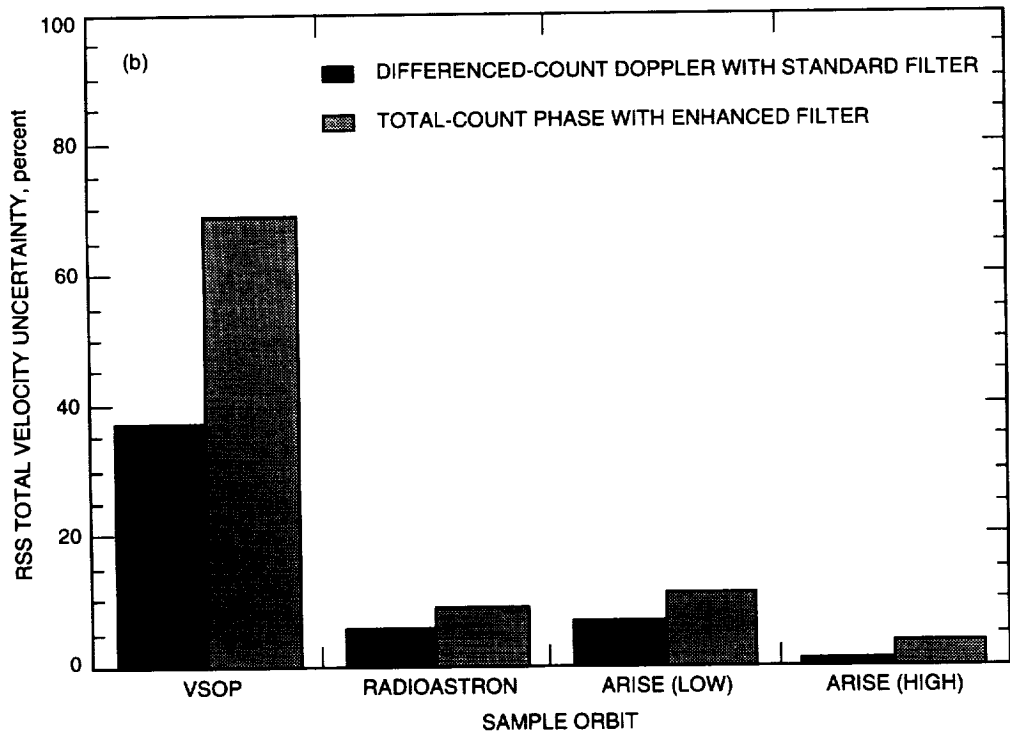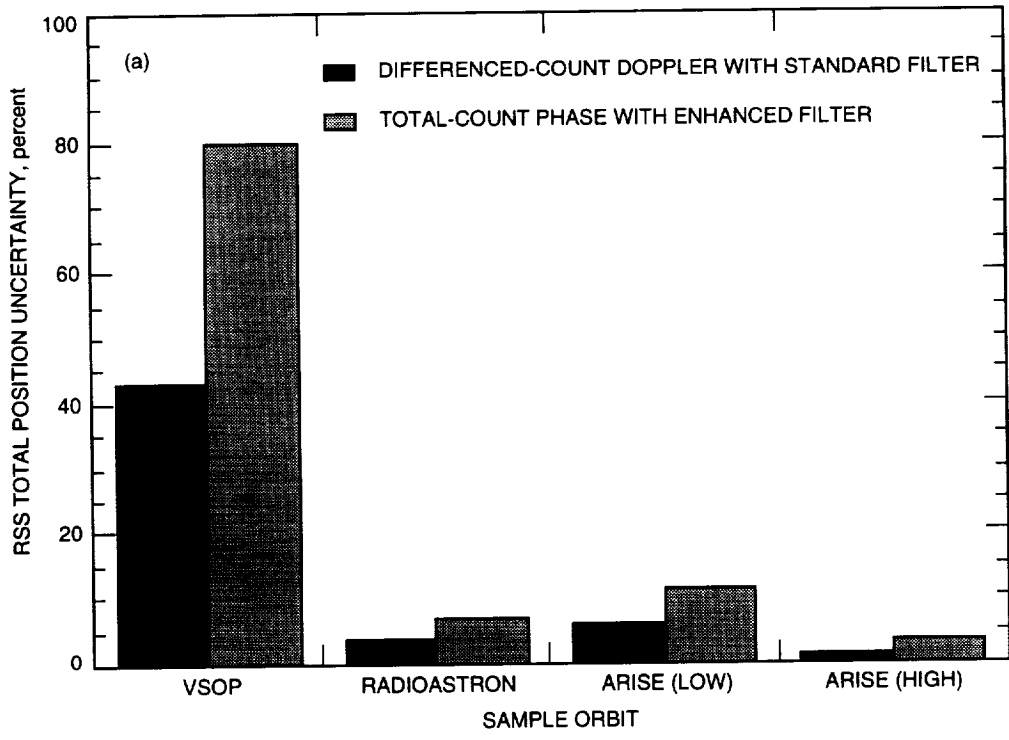
Fig. 5. Approximate percentage contribution of 1-σ gravitational force modeling errors (Earth GM and harmonics) to expected RSS (a) total position uncertainty and (b) total velocity uncertainty.

Table 7. Orbit accuracies of 1-σ for reconstruction over entire propagation period.

Data-processing mode	VSOP	RadioAstron	ARISE (low)	ARISE (high)
	RSS position uncertainty, m, and relative percentage improvement			
Differenced-count Doppler with standard filter	4–23	8–11	9–60	24–119
Total-count phaser with enhanced filter	2–11, 56 percent	4–7, 43 percent	4–49, 41 percent	8–48, 63 percent
	RSS velocity uncertainty, cm/s, and relative percentage improvement			
Differenced-count Doppler with standard filter	0.06–1.8	0.03–0.5	0.2–2.4	0.3–1.5
Total-count phase with enhanced filter	0.03–0.9, 58 percent	0.02–0.2, 48 percent	0.1–2.0, 41 percent	0.1–0.5, 62 percent

be necessary to more accurately model the gravitational error sources and possibly treat the relevant parameters as actual filter parameters to be estimated along with the spacecraft trajectory parameters. The principal motivating factor for using a more sophisticated filtering strategy ultimately depends on mission requirements, bearing in mind the altitude dependence of gravitational force modeling errors.

V. Discussion

Although the results from two other possible permutations of candidate Doppler data-processing modes were not presented—e.g., differenced-count Doppler with enhanced filter and total-count phase with standard filter—error covariance calculations performed for these special cases reflect mixed performance results. Phase data reduced with the standard filter actually exhibited about a 40-percent worse orbit accuracy than traditional frequency-formulated Doppler with the standard filter because the precision of these data is very high and, thus, extremely sensitive to unmodeled ground-system calibration errors. As studies of interplanetary trajectories have shown, it is necessary to incorporate major ground-system calibration errors affecting the data as filter parameters to take full advantage of Doppler phase (without artificially deweighting the data).

When differenced-count Doppler data were used exclusively and reduced with the enhanced filter, there was a modest improvement in reconstructed orbit accuracies (~20 percent). However, it is imprudent to use this more complicated filtering strategy for very little gain, unless actual orbit determination requirements can be easily met.

Because of the long data arc lengths assumed for the higher orbits considered in this study, concern arose as to whether the presence of broken tracking passes might significantly degrade total-count phase navigation performance. Therefore, additional error covariance calculations were made for the RadioAstron orbit case. The phase passes were broken into three shorter intervals of equal length with a 5-min break between passes. This resulted in a net loss of about 15 min of data from the original case. An independent phase offset parameter was assumed for each pass and the covariance matrix reset at the beginning of each track to represent a Doppler count initialization procedure at each station, effectively yielding a new phase offset for each pass [1]. Results from this modified tracking scenario exhibited no marked degradation in reconstructed orbit accuracies from the original case, despite a 15-min reduction

in overall data arc length. This result clearly illustrates the robustness of the enhanced filter to solve for additional offset parameters incurred from a data-acquisition scenario involving broken tracking passes.

VI. Conclusions

A revised navigation error covariance analysis was performed for four highly elliptical Earth orbiters derived from the SVLBI mission set. This new study focused on utilizing recently developed or enhanced Doppler data-processing modes to reduce X-band Doppler data acquired from DSN-based radio tracking stations. Preliminary error analysis suggests a factor of 2 to 4 improvement in orbit accuracies is achievable over traditional data-processing modes when Doppler data are formulated as total-count phase measurements rather than differenced-count frequency measurements and processed with an enhanced data-filtering strategy that incorporates the major ground-system calibration error sources affecting the data as filter parameters.

Future work in this area will focus on a thorough sensitivity analysis to determine which dynamic and observational sources of error will require further modeling improvement or additional calibration accuracy. Plans for concept demonstrations are also being drafted that will use actual DSN-based radio-metric tracking data acquired during past mission operations in support of highly elliptical Earth-orbiting spacecraft. The JPL operational orbit determination software set is currently undergoing verification and validation tests for new upgrades that will facilitate the use of phase-formulated Doppler observables for use in both interplanetary and Earth-orbiter mission navigation support.

Acknowledgment

References

[1] S. W. Thurman and J. A. Estefan, "Radio Doppler Navigation of Interplanetary Spacecraft Using Different Data Processing Modes," *Advances in the Astronautical Sciences*, vol. 82, part II, pp. 985–1004, 1993.

[2] J. A. Estefan, V. M. Pollmeier, and S. W. Thurman, "Precision X-Band Doppler and Ranging Navigation for Current and Future Mars Exploration Missions," *Advances in the Astronautical Sciences*, vol. 84, part I, pp. 3–16, 1993.

[3] T. P. McElrath, S. W. Thurman, and K. E. Criddle, "Navigation Demonstrations of Precision Ranging with the Ulysses Spacecraft," *Advances in the Astronautical Sciences*, vol. 85, part II, pp. 1635–1650, 1993.

[4] S. Bhaskaran, S. W. Thurman, and V. M. Pollmeier, "Demonstration of a Precision Data Reduction Technique for Navigation of the Galileo Spacecraft," Paper AAS 94-164, AAS/AIAA Spaceflight Mechanics Meeting, Cocoa Beach, Florida, February 14–16, 1994.

[5] T. D. Moyer, *Mathematical Formulation of the Double-Precision Orbit Determination Program*, Technical Report 32-1527, Jet Propulsion Laboratory, Pasadena, California, pp. 72–80, May 15, 1971.

Seamless Data-Rate Change Using Punctured Convolutional Codes for Time-Varying Signal-to-Noise Ratios

Y. Feria and K.-M. Cheung
Communications Systems Research Section

In a time-varying signal-to-noise ratio (SNR) environment, symbol rate is often changed to maximize data return. However, the symbol-rate change has some undesirable effects, such as changing the transmission bandwidth and perhaps causing the receiver symbol loop to lose lock temporarily, thus losing some data. In this article, we are proposing an alternate way of varying the data rate without changing the symbol rate and, therefore, the transmission bandwidth. The data rate change is achieved in a seamless fashion by puncturing the convolutionally encoded symbol stream to adapt to the changing SNR environment. We have also derived an exact expression to enumerate the number of distinct puncturing patterns. To demonstrate this seamless rate-change capability, we searched for good puncturing patterns for the Galileo (14,1/4) convolutional code and changed the data rates by using the punctured codes to match the Galileo SNR profile of November 9, 1997. We show that this scheme reduces the symbol-rate changes from nine to two and provides a comparable data return in a day and a higher symbol SNR during most of the day.

I. Introduction

In deep-space communications and other space communications, the signal-to-noise ratio (SNR) varies during a day. The degree of variation is determined by weather conditions, antenna elevation angle, antenna-pointing accuracy (both the transmitter and receiver antennas), changes in satellite latitude, and many other factors. For example, the total signal power-to-noise density ratio, P_t/N_o, during a typical 24-hour pass for the Galileo Mission can fluctuate in a range between 16 and 22 dB-Hz. In order to maximize the data return in this time-varying SNR environment, the transmitted symbol rate is varied as a function of the estimated P_t/N_o at the antenna. The symbol rate is set as high as possible under the constraint that the symbol SNR is high enough for the tracking loops to remain in lock and that the bit-error-rate (BER) requirement is met. In the Galileo Mission, there are six different symbol rates, and there can be as many as eight symbol-rate changes (from 10 to 640 symbols/s) during a day. One problem associated with the symbol-rate change at a low operating symbol SNR is that the symbol synchronization loop may have to reacquire the symbol phase, which may cause real-time data loss. A technique that involves opening the symbol loop at the moment of the symbol-rate change has been proposed,[1] but this

---

[1] J. Berner, "GLL Data Rate Changes," Project Notes (internal document), Jet Propulsion Laboratory, Pasadena, California, June 11, 1993.

[6] D. W. Curkendall, "Orbit Accuracy as a Function of Doppler Sample Rate for Several Data Taking and Processing Modes," *JPL Space Programs Summary 37-38*, vol. III, Jet Propulsion Laboratory, Pasadena, California, pp. 20–24, January–February 1966.

[7] G. J. Bierman, *Factorization Methods for Discrete Sequential Estimation*, San Diego, California: Academic Press, Inc., pp. 162–171, 1977.

[8] S. R. McReynolds, "The Sensitivity Matrix Method for Orbit Determination Error Analysis, With Applications to a Mars Orbiter," *JPL Space Programs Summary 37-56*, vol. 3, January–February 1969, Jet Propulsion Laboratory, Pasadena, California, pp. 85–87, March 31, 1969.

[9] S. M. Lichten, "Estimation and Filtering Techniques for High-Accuracy GPS Applications," *The Telecommunications and Data Acquisition Progress Report 42-97, January–March 1989*, Jet Propulsion Laboratory, Pasadena, California, pp. 1–20, May 15, 1989.

[10] D. J. Scheeres, "Failure Modes of Reduced-Order Orbit Determination Filters and Their Remedies," *The Telecommunications and Data Acquisition Progress Report 42-114, April–June 1993*, Jet Propulsion Laboratory, Pasadena, California, pp. 34–42, August 15, 1993.

[11] J. A. Estefan and P. D. Burkhart, "Enhanced Orbit Determination Filter Sensitivity Analysis: Error Budget Development," *The Telecommunications and Data Acquisition Progress Report 42-116, October–December 1993*, Jet Propulsion Laboratory, Pasadena, California, pp. 24–36, February 15, 1994.

[12] W. C. Masters, "Enhanced Orbit Determination Filter: Inclusion of Ground System Errors as Filter Parameters," *The Telecommunications and Data Acquisition Progress Report 42-116, October–December 1993*, Jet Propulsion Laboratory, Pasadena, California, pp. 37–41, February 15, 1994.

[13] J. A. Estefan, "Precise Orbit Determination of High-Earth Elliptical Orbiters Using Differenced Doppler and Range Measurements," *The Telecommunications and Data Acquisition Progress Report 42-106, April–June 1991*, Jet Propulsion Laboratory, Pasadena, California, pp. 1–22, August 15, 1991.

[14] T. Ichikawa and T. Kato, "Orbit Determination for MUSES-B Mission," Paper ISTS 94-c-21, 19th International Symposium on Space Technology and Science, Yokohama, Japan, May 15–24, 1994.

[15] J. Ellis, "Navigation of Space VLBI Missions: Radioastron and VSOP," *Proceedings of the Second International Symposium on Ground Data Systems for Space Mission Operations*, JPL Publication 93-5, Jet Propulsion Laboratory, Pasadena, California, pp. 625–628, March 1, 1993.

[16] J. S. Ulvestad, R. P. Linfield, and J. G. Smith, "ARISE: The Next Generation Space VLBI Mission," Paper AIAA 95-0824, 33rd Aerospace Sciences Meeting and Exhibit, Reno, Nevada, January 9–12, 1995.

[17] M. H. Finger and W. M. Folkner, "A Determination of the Radio–Planetary Frame Tie From Comparison of Earth Orientation Parameters," *The Telecommunications and Data Acquisition Progress Report 42-109, January–March 1992*, Jet Propulsion Laboratory, Pasadena, California, pp. 1–21, May 15, 1992.

technique requires very accurate time predicts on the moment of change. It is not clear if the predict information can be obtained within the required accuracy.

In this article, we are proposing a simple and low-cost alternative solution to the data rate–change problem by changing the data rate at the error-correcting coding stage rather than at the transmission stage. The data rate is changed by puncturing the low-rate convolutional code while the symbol rate is kept constant. In this way, the basic structures of the encoder and decoder remain unchanged, making the scheme simple and less costly. The idea is to minimize the number of symbol-rate changes and still maintain a high enough symbol SNR for the loops to remain in lock and the BER to stay low. Symbol rate is changed only if the symbol SNR goes too high (wasting bit SNR) or too low (making the receiver unable to track the symbols).

By allowing the code-rate change, we are essentially adding a degree of freedom in the data return–maximization problem. The code rate will share a part of the necessary data-rate changes with the symbol rate, therefore reducing the number of symbol-rate changes. This feature becomes even more important when the available bandwidth is fixed.

In Section II, we will present the definition and an overview of puncturing patterns. In Section III, we will discuss our procedure for selecting good puncturing patterns, and Section IV will provide an example of using the punctured convolutional code for the SNR profile of the Galileo Mission on November 9, 1997, which is an arbitrarily chosen day. In Section V, we will give some concluding remarks.

II. Definition and Enumeration of Puncturing Patterns

A. Definition of Puncturing Patterns

A regular-rate $1/N$ convolutional code generates N code symbols per bit. By periodically and systematically refraining from transmission of some of the code symbols, a higher rate code can be constructed from an original lower rate $1/N$ code. Let the period be L bits or NL code symbols. We define a puncturing pattern P of period NL symbols to be an NL binary-tuple, where a 1 denotes that the symbol in the corresponding location is to be sent and a 0 denotes that the symbol is to be deleted. If there are m zeros in P, the resulting punctured code is a higher rate $L/(NL - m)$ code, where $0 \leq m < (N - 1)L$. For example, let $N = 4$, $L = 4$, and one puncturing pattern be $P = \{0111\ 1110\ 1011\ 1101\}$. We define the rightmost digit to correspond to the first symbol and the rightmost group of four digits to correspond to the four symbols of the first bit. The puncturing pattern, P, indicates that the second symbol in the first bit, the third symbol in the second bit, the first symbol in the third bit, and the fourth symbol in the fourth bit in a period are not transmitted. The resulting punctured code is a rate $4/(4 \times 4 - 4) = 1/3$ code. With the leftmost digit being the most significant bit and the rightmost digit being the least significant bit, the puncturing pattern, P, can be represented as $7ebd$ in hexadecimal form.

B. Enumeration of Puncturing Patterns

In this section, we develop an exact expression to enumerate the number of unique puncturing patterns.

Clearly, there are $\binom{NL}{m}$ different possible patterns for P. Since P is repeated every L bits or NL symbols, any cyclic shift of N symbols in P gives the same code performance as P. However, this does not reduce the number of patterns that give a distinct code performance by a factor of N, as some of the $\binom{NL}{m}$ patterns may have a smaller period L_i. That is, L_i divides L, which is denoted by $L_i \mid L$. Let $f(L_i)$ denote the number of puncturing patterns with period L_i exactly (including 1). Notice that $f(L_i) = 0$ if the m zeros cannot be evenly divided among L/L_i partitions (i.e., $(L/L_i) \nmid m$). Also, among the $\binom{NL_i}{mL_i/L}$ patterns with period L_i, some may have smaller periods. Let p be a prime that divides L_i. If $p | (mL_i/L)$,

then there are $\binom{NL_i/p}{mL_i/(Lp)}$ patterns of P with period L_i/p. The total number of distinct puncturing patterns is, therefore,

$$\sum_{L_i|L} \frac{1}{L_i} f(L_i)$$

where $f(L_i)$ can be enumerated as follows:

$$f(L_i) = \binom{NL_i}{\frac{mL_i}{L}} - \sum_{p|L_i} \binom{\frac{NL_i}{p}}{\frac{mL_i}{Lp}}$$

Notice that we define the combinatoric function $\binom{m}{n} = 0$ if either m or n is not an integer. In the above example with $N = 4$, $L = 4$, and $m = 4$, an exhaustive search requires checking $\binom{16}{4} = 1820$ puncturing patterns. By taking into account the cyclic property of the puncturing patterns, the number of distinct puncturing patterns is now reduced to

$$\frac{1}{4}\left[\binom{16}{4} - \binom{8}{2}\right] + \frac{1}{2}\left[\binom{8}{2} - \binom{4}{1}\right] + \binom{4}{1} = 464$$

which is a reduction by almost a factor of 4.

III. Puncturing Pattern Search Procedure

In this section, we describe the search procedure that we used to find good puncturing patterns for a rate-$1/N$ convolutional code. Using this procedure, we searched for punctured patterns for the $(14,1/4)$ convolutional code used for Galileo. We punctured it from rate $1/4$ to rate $1/3$, then to rate $1/2$. A rate compatibility [1] restriction is added in the puncturing-pattern search. That is, a code symbol used in the high-rate code is also used in the low-rate code. For example, to search for a rate-$1/2$ punctured code, we puncture the rate-$1/3$ code found a step before, not the rate-$1/4$ code. This was necessary mainly because of limited computing resources.

For each punctured code rate, the goal is to find the puncturing pattern, P, that gives the lowest BER at that rate for a range of SNR values. Direct simulation of the punctured convolutional code is not viable since there are so many different puncturing patterns. As a first step in selecting the puncturing patterns, we computed the weight profile of each punctured code that includes the free distance, d_{free}, the number of paths of weight d, a_d, and the information bit error weight, c_d. To further simplify our search, we only searched for paths of weight d such that $d_{free} \le d \le d_{cut}$, where d_{cut} is some predetermined value that is large enough to infer the code's BER performance and small enough to complete the search in a reasonable time. Note that there are L different starting points for diverging paths, where L is the period of the puncturing patterns. The worst case is considered in comparing the puncturing patterns.

A systematic search is carried out to find the patterns with the maximum free distance and the minimum number of paths of weight d for Viterbi decoding. Three patterns with the largest free distance and smallest number of paths of weight d are then simulated to obtain three BER curves. The lowest BER curve is selected and used further to compute the BERs for the concatenated codes of convolutional code as the inner code and the Reed–Solomon (RS) (255,223) code as the outer code, assuming infinite interleaving.

20

Once we have the points of E_b/N_o versus BER of the concatenated code, we fit a curve through these points. These curves are used to determine the BER for a given SNR profile of the Galileo Mission. When the BER is less than 10^{-7}, we determine that the code rate can be used in that time period.

Note that the (14,1/4) Galileo code is used here only to demonstrate the alternative possibility of using punctured codes. In fact, the (14,1/4) code is composed of a (11,1/2) convolutional code and the NASA standard (7,1/2) code. The NASA standard (7,1/2) code was necessary because the hardware encoder on the spacecraft cannot be altered or bypassed.

A. Upper Bound on Free Distance

Before searching for the maximum free distances, we compute the upper bounds of the free distances to see the effect of the puncturing period on the free-distance bound of the punctured codes. The upper bounds on the free distances for convolutional codes can be computed using expressions given in [2]. Figure 1 shows some of the bounds on the free distances for codes punctured from code (14,1/4), with the minimum period from 1 to 4. By minimum period we mean that the period 4 does not include period 1 or 2. The results show that a shorter puncturing period gives a higher upper bound on the free distance, but the shorter puncturing period provides a smaller set of possible code rates.
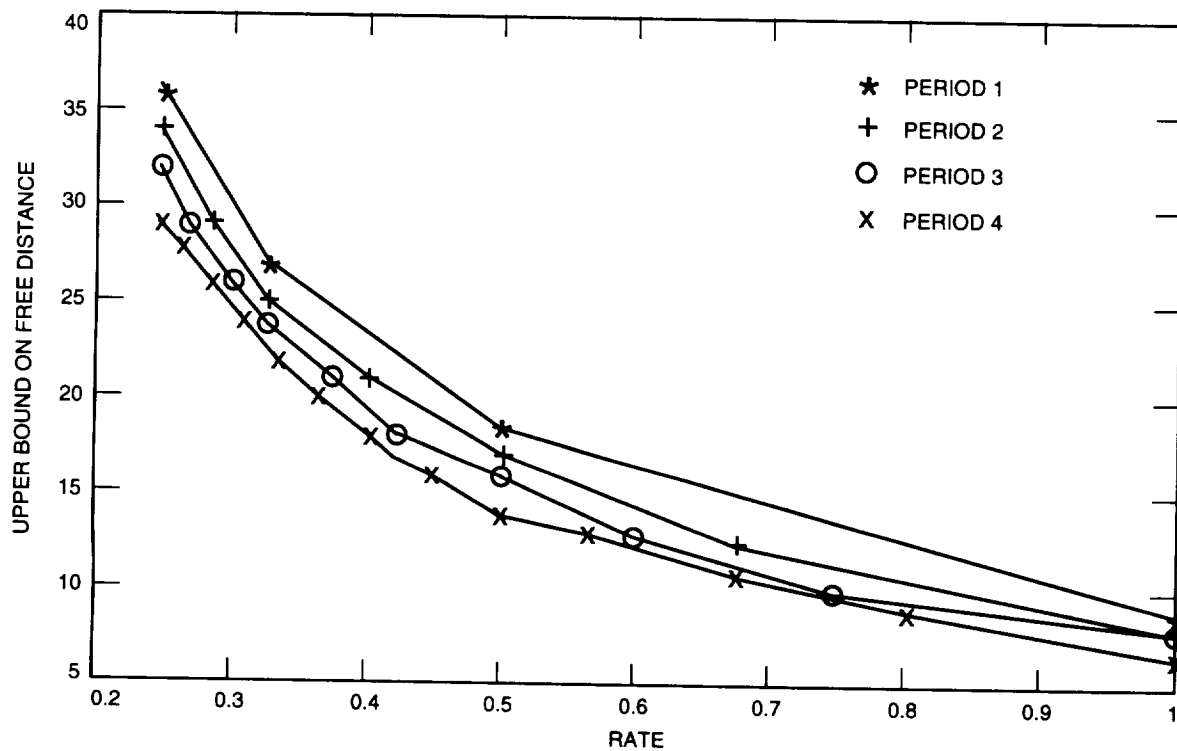

Fig. 1. Upper bounds on free distance for punctured codes from (14,1/4) code.

B. Weight Spectra of Punctured Codes

The parent code in this case has the following polynomials: $2c22$, $3d7d$, $2bcd$, and $1dd3$. First, we search for punctured codes from (14,1/4) to (14,1/3) and find the weight spectra corresponding to all different punctured patterns. The period in this case is 4, which corresponds to 464 different puncturing patterns. We then sort the weight spectra in ascending order according to the number of paths of weight d, a_d. Finally, we pick the best three patterns, and their weight spectra are shown in Table 1. According to the weight spectra, the best pattern is $bbbb$. This implies that the puncturing pattern has period 1, and the third symbol is punctured out every time. This corresponds to the (14,1/3) code with polynomials $2c22$, $3d7d$, and $1dd3$.

To further puncture the code to rate 1/2, we use the best 1/3 code found earlier as the parent code. The following patterns are found to be the best: 3636, 3535, and 3333 in octal numbers. The weight spectra of the three best puncturing patterns are shown in Table 2. Note that when searching for puncturing patterns with period 4, those patterns with period 1 and 2 are included.

Table 1. Weight spectra of punctured codes (14,1/3) from (14,1/4) parent code.

Pattern	d	23	24	25	26	27	28	29	30	31	32	33	34	35
bbbb	a_d	0	4	6	4	9	14	22	48	93	130	237	389	638
bdbd	a_d	1	1	3	8	13	21	27	54	68	137	225	400	652
bbbd	a_d	1	5	5	5	13	16	38	54	101	146	288	481	800
bbbb	c_d	0	14	18	18	55	72	122	322	641	920	1853	3134	5530
bdbd	c_d	1	3	9	35	60	121	139	320	486	938	1699	3150	5368
bbbd	c_d	5	14	19	24	77	91	240	347	724	1080	2313	4067	7068

Table 2. Weight spectra of punctured codes (14,1/2) from (14,1/3) parent code.

Pattern	d	13	14	15	16	17	18	19	20	21	22	23	24
3636	a_d	0	2	6	10	24	51	142	344	824	1956	4726	11363
3535	a_d	0	2	8	9	35	70	154	371	931	2286	5464	13234
3333	a_d	0	3	0	14	0	73	0	545	0	2884	0	16679
3636	c_d	0	5	20	70	146	354	1144	2914	7780	20229	52967	5525
3535	c_d	0	9	37	53	251	550	1298	3370	9353	25245	64261	35749
3333	c_d	0	9	0	71	0	520	0	4686	0	29943	0	4011

C. BER of Punctured Convolutional Code From Simulation

The weight-spectra search is only the first step in the code puncturing pattern search. To further compare their performance, the punctured codes are simulated with an encoder and the Viterbi decoder for several bit-SNR values. The traceback length used in the Viterbi decoder in this case is at least 160, and the input soft symbols are quantized with 8 bits. The simulated results are shown in Tables 3 and 4. Generally, the three puncturing patterns give similar BERs.

D. BER of Concatenated Code

Once we obtain the BER from the Viterbi decoder, we can compute the bit-error rate at the output of the RS decoder, assuming infinite interleaving using the expression given in [3, p. 256]. In the case of the Galileo Mission, there are 8 bits in a codeword, 255 codewords in a frame, and the number of correctable errors is 16. The computed BERs at the output of the RS decoder are shown in Tables 5 through 7.

IV. Example Using the Galileo Profile

We use the predicted SNR profile of the Galileo Mission on November 9, 1997, as an example to explain how the number of symbol-rate changes can be reduced with code-rate changes. For a given SNR

Table 3. BER of punctured convolutional codes (14,1/3).

E_b/N_o	Puncturing patterns		
	bbbb	*bdbd*	*bbbd*
−1.2494	0.3528	0.3532	0.3533
−0.7494	0.2320	0.2336	0.2330
−0.2494	0.1083	0.1100	0.1090
0.2506	0.0342	0.0345	0.0347
0.7506	0.0076	0.0077	0.0076
1.2506	0.0012	0.0012	0.0012

Table 4. BER of punctured convolutional codes (14,1/2).

E_b/N_o	Puncturing patterns		
	3636	3535	3333
−1.0103	0.4389	0.4339	0.4445
−0.5103	0.3573	0.3519	0.3625
−0.0103	0.2230	0.2206	0.2279
0.4897	0.0924	0.0934	0.0924
0.9897	0.0230	0.0243	0.0226
1.4897	0.0040	0.0043	0.0035
1.9897	0.0005	0.0005	0.0004
2.4897	4.7×10^{-5}	5.4×10^{-5}	3.5×10^{-5}

Table 5. BER output of RS decoder using punctured code (14,1/4).

E_b/N_o	BER input to RS decoder	BER output of RS decoder
−2.0	0.4218	0.4218
−1.5	0.3408	0.3408
−1.0	0.2139	0.2139
−0.5	0.1023	0.1023
0.0	0.0326	0.0194
0.5	0.0070	5.4×10^{-9}
1.0	0.0013	2.3×10^{-20}
1.5	0.0002	1.1×10^{-49}

Table 6. BER output of RS decoder using punctured codes (14,1/3).

E_b/N_o	BER input to RS decoder	BER output of RS decoder
−1.2494	0.3528	0.3528
−0.7494	0.2320	0.2320
−0.2494	0.1083	0.1083
0.2506	0.0342	0.0230
0.7506	0.0076	1.8×10^{-8}
1.2506	0.0012	1.0×10^{-20}

Table 7. BER output of RS decoder using punctured codes (14,1/2).

E_b/N_o	BER input to RS decoder	BER output of RS decoder
−1.0103	0.4389	0.4389
−0.5103	0.3573	0.3573
−0.0103	0.2230	0.2230
0.4897	0.0924	0.0924
0.9897	0.0230	0.0029
1.4897	0.0040	1.6×10^{-12}
1.9897	0.0005	3.7×10^{-27}
2.4897	4.7×10^{-5}	1.6×10^{-44}

profile—for example, the one shown in Fig. 2—the objective is to get the maximum data return under the conditions that the bit-error rate is below 10^{-7} and the symbol SNR is maintained above −6 dB for the carrier, subcarrier, and symbol loops to track. To achieve this goal, the current plan is to change the symbol rate using a fixed code rate, 1/4, and an alternate way is to allow the code rate to change as well, thus reducing the number of symbol-rate changes.

We arbitrarily select a set of three code rates, namely, 1/4, 1/3, and 1/2. The variable code rate can only take values from this set. Figure 3 shows the symbol rates using fixed and variable code rates. In the fixed–code rate case, there are nine symbol-rate changes, compared to two symbol-rate changes in the variable–code rate case. With these symbol rates, each of the two systems will have a symbol SNR above −6 dB, as required, where the variable–code rate case has a slightly higher symbol SNR for most of the day, as shown in Fig. 4. The code-rate changes are shown in Fig. 5.

Multiplying the code rates by the symbol rates, we obtain the bit rates as shown in Fig. 6 for the fixed– and variable–code rate cases. The areas under the two curves in Fig. 6 are the total data returns for the day. The data return using the variable code rate is found to be comparable with that using the fixed code rate.

V. Conclusions

In this article, we have described a simple and low-cost method to change the data rate to match the time-varying P_t/N_0 environment. This is done by puncturing the convolutional code at the error-correction coding stage rather than by changing the symbol rate at the transmission stage. The main advantages of this method are that it allows seamless transition from one data rate to another and that,
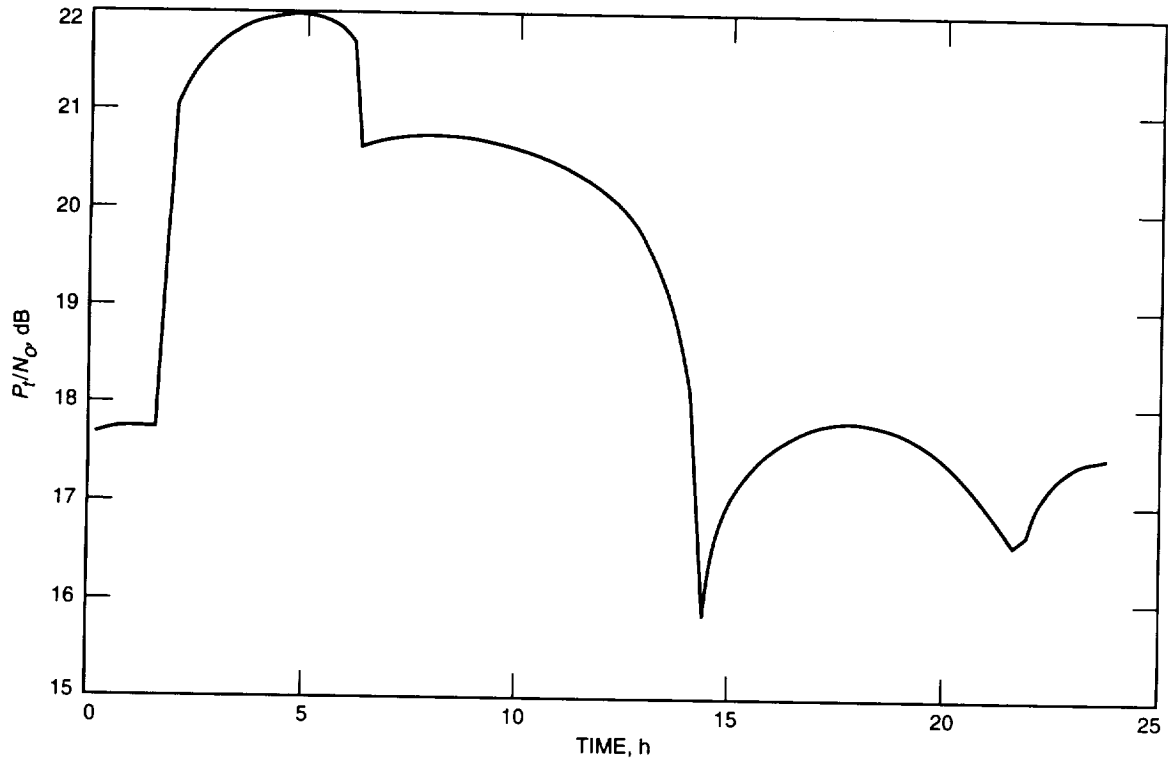
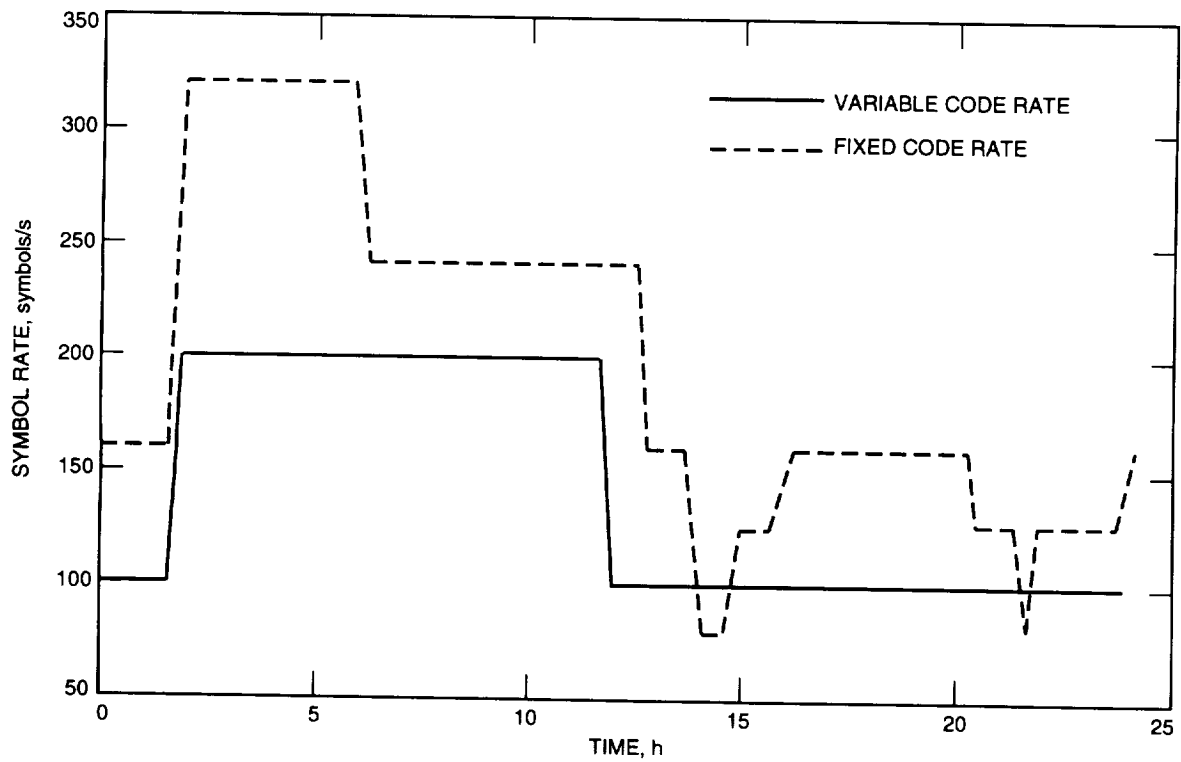Fig. 2. Arrayed P_t/N_o on November 9, 1997, from Galileo.

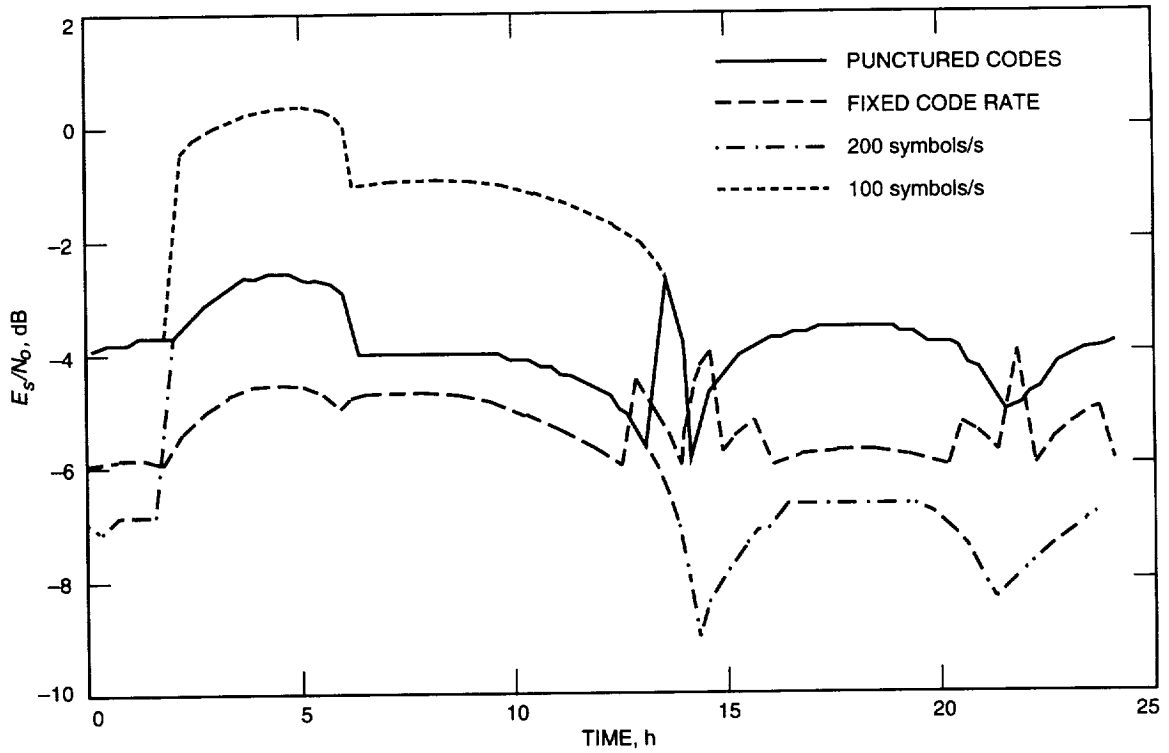Fig. 3. Symbol rates on November 9, 1997, for Galileo using fixed and variable code rates.

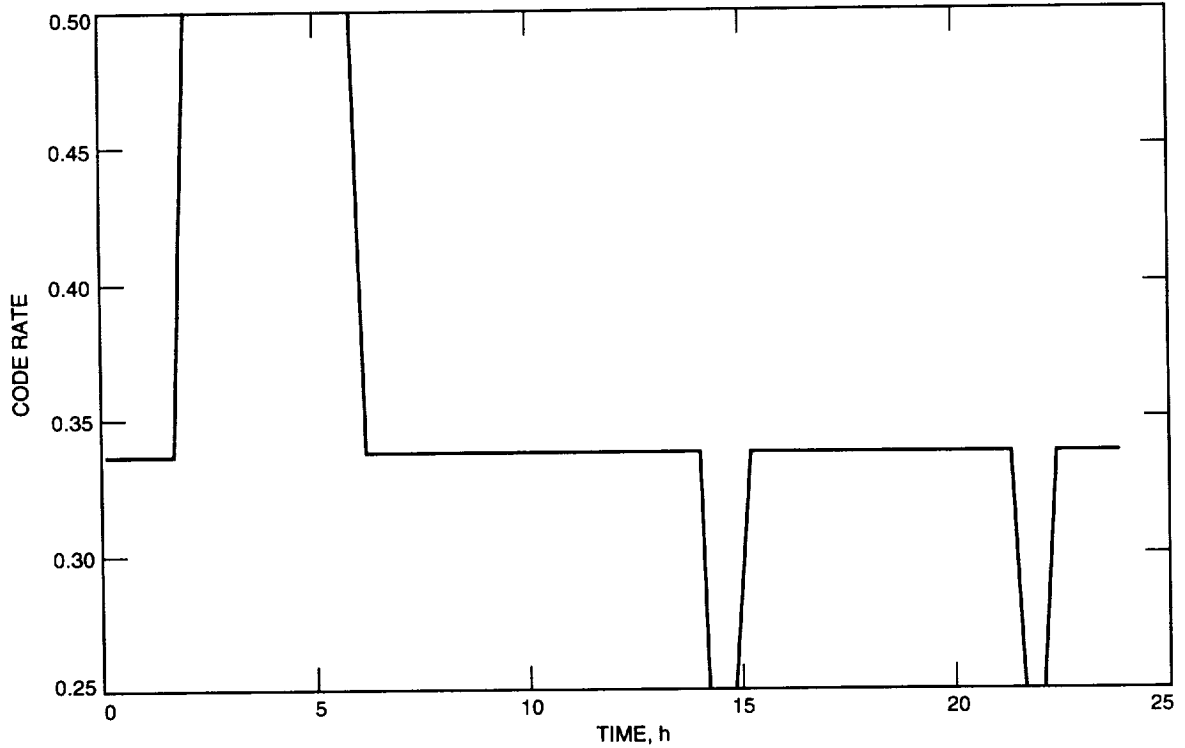**Fig. 4. Symbol SNR on November 9, 1997, for Galileo using fixed and variable code rates.**

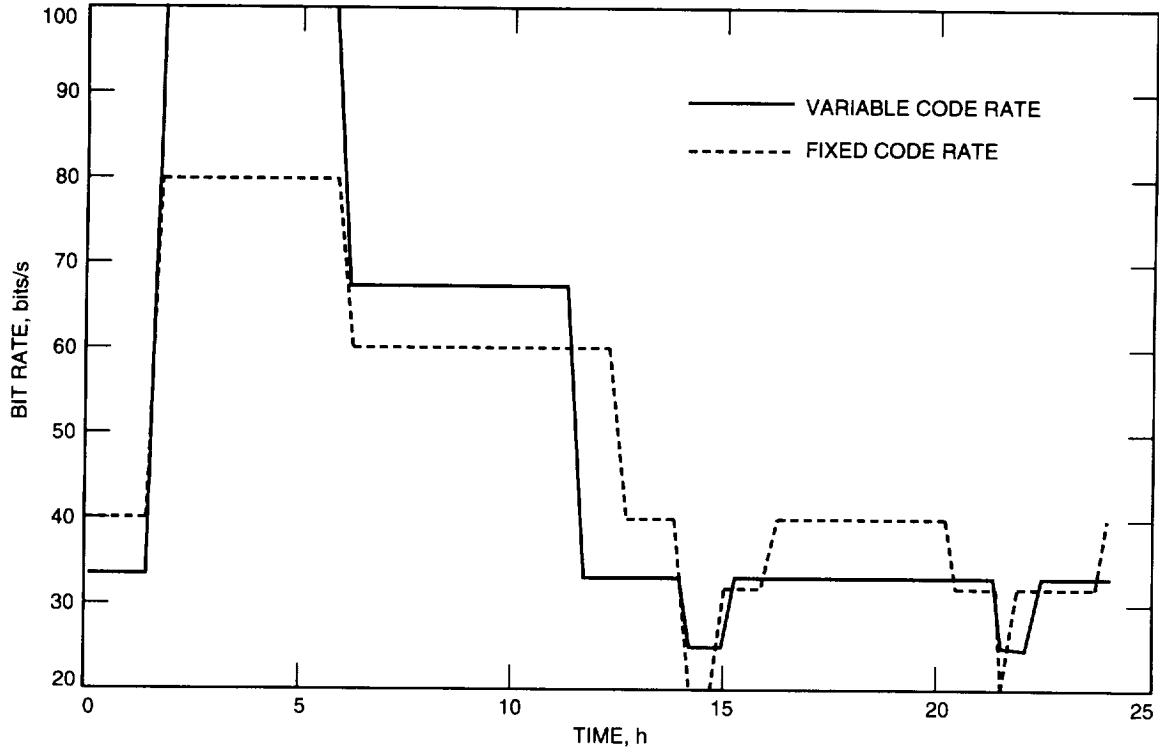**Fig. 5. Variable code rates on November 9, 1997, for Galileo.**

Fig. 6. Bit rates on November 9, 1997, for Galileo.

for a fixed available bandwidth, data rate is allowed to change for a larger data return. We applied this method to the Galileo SNR profile on November 9, 1997, as an example to demonstrate its effectiveness. We showed how this method reduces the number of symbol-rate changes from nine to two and gives a comparable data return in a day and a higher symbol SNR for most of the day.

Notice that, in this example, we arbitrarily picked 100 and 200 symbols/s as two symbol rates to be used. We are developing techniques to select the symbol rates that will maximize the data return. The problem is formulated below.

For a given SNR profile, $(P_t/N_o)(t)$, we wish to find the symbol rate $R_{sym}(t)$ and the code rate $R_c(t)$ such that the data return given by $\int_{t_1}^{t_2} R_{sym}(t)R_c(t)dt$ is maximal, subject to the following constraints:

(1) The number of changes of symbol rate R_{sym} is less than a desired number.

(2) The BER is below a designed value, $BER < BER_{design}$.

(3) The symbol SNR is above the minimum value for the tracking loops to maintain lock, $E_s/N_o > (E_s/N_o)_{min}$.

Acknowledgments

References

[1] J. Hagenauer, "Rate-Compatible Punctured Convolutional Codes (RCPC Codes) and Their Applications," *IEEE Transactions on Communications*, vol. 36, no. 4, pp. 389–400, April 1988.

[2] D. G. Daut, J. W. Modestino, and L. D. Wismer, "New Short Constraint Length Convolutional Code Constructions for Selected Rational Rates," *IEEE Transactions on Information Theory*, vol. IT-28, no. 5, pp. 794–800, September 1982.

[3] J. H. Yuen, *Deep Space Telecommunications Systems Engineering*, New York: Plenum Press, 1983.

1995115118

405742

10P9

N95- 21535

TDA Progress Report 42-120

February 15, 1995

Turbo Codes for Deep-Space Communications

D. Divsalar and F. Pollara
Communications Systems Research Section

Turbo codes were recently proposed by Berrou, Glavieux, and Thitimajshima [2], and it has been claimed these codes achieve near-Shannon-limit error correction performance with relatively simple component codes and large interleavers. A required E_b/N_o of 0.7 dB was reported for a bit error rate of 10^{-5}, using a rate 1/2 turbo code [2]. However, some important details that are necessary to reproduce these results were omitted. This article confirms the accuracy of these claims, and presents a complete description of an encoder/decoder pair that could be suitable for deep-space applications, where lower rate codes can be used. We describe a new simple method for trellis termination, analyze the effect of interleaver choice on the weight distribution of the code, and introduce the use of unequal rate component codes, which yields better performance.

I. Introduction

Turbo codes were recently proposed by Berrou, Glavieux, and Thitimajshima [2] as a remarkable step forward in high-gain, low-complexity coding. It has been claimed these codes achieve near-Shannon-limit error correction performance with relatively simple component codes and large interleavers. A required E_b/N_0 of 0.7 dB was reported for a bit error rate (BER) of 10^{-5}, using a rate 1/2 turbo code [2]. However, some important details that are necessary to reproduce these results were omitted. The purpose of this article is to shed some light on the accuracy of these claims and to present a complete description of an encoder/decoder pair that could be suitable for deep-space applications, where lower rate codes can be used. Two new contributions are reported in this article: a new, simple method for trellis termination and the use of unequal component codes, which results in better performance.

II. Parallel Concatenation of Convolutional Codes

The codes considered in this article consist of the parallel concatenation of two convolutional codes with a random interleaver between the encoders. Figure 1 illustrates a particular example that will be used in this article to verify the performance of these codes. The encoder contains two recursive binary convolutional encoders, with M_1 and M_2 memory cells, respectively. In general, the two component encoders may not be identical. The first component encoder operates directly on the information bit sequence $\mathbf{u} = (u_1, \cdots, u_N)$ of length N, producing the two output sequences $\mathbf{x}_{1i}$ and $\mathbf{x}_{1p}$. The second component encoder operates on a reordered sequence of information bits, $\mathbf{u}'$, produced by an interleaver of length N, and outputs the two sequences $\mathbf{x}_{2i}$ and $\mathbf{x}_{2p}$. The interleaver is a pseudorandom block scrambler defined by a permutation of N elements with no repetitions: a complete block is read into the interleaver and read out in a specified permuted order. Figure 1 shows an example where a rate $r = 1/n = 1/4$ code is generated by two component codes with $M_1 = M_2 = M = 4$, producing the
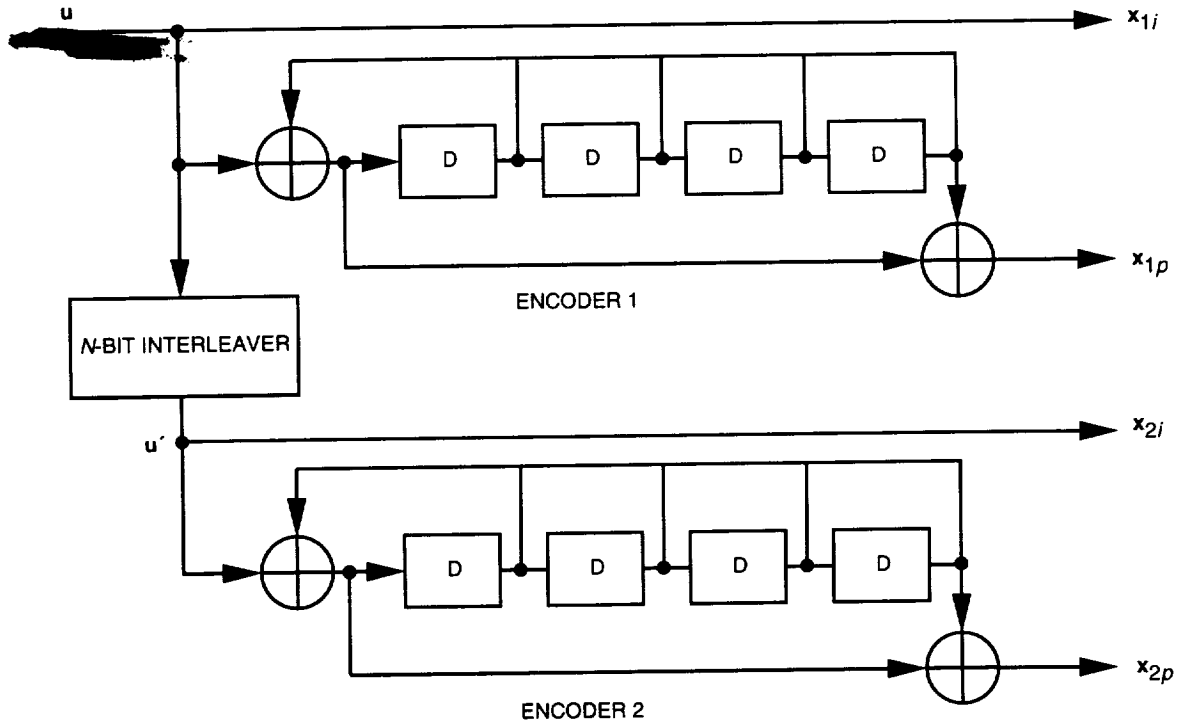
Fig. 1. Example of an encoder.

outputs $x_{1i} = u$, $x_{1p} = u \cdot g_a/g_b$, $x_{2i} = u'$, and $x_{2p} = u' \cdot g_a/g_b$, where the generator polynomials g_a and g_b have an octal representation of 21 and 37, respectively. Note that various code rates can be obtained by puncturing the outputs.

A. Trellis Termination

We use the encoder in Fig. 1 to generate a $(n(N + M), N)$ block code. Since the component encoders are recursive, it is not sufficient to set the last M information bits to zero in order to drive the encoder to the all-zero state, i.e., to terminate the trellis. The termination (tail) sequence depends on the state of each component encoder after N bits, which makes it impossible to terminate both component encoders with the same M bits. Fortunately, the simple stratagem illustrated in Fig. 2 is sufficient to terminate the trellis. Here the switch is in position "A" for the first N clock cycles and is in position "B" for M additional cycles, which will flush the encoders with zeros. The decoder does not assume knowledge of the M tail bits. The same termination method can be used for unequal rate and memory encoders.
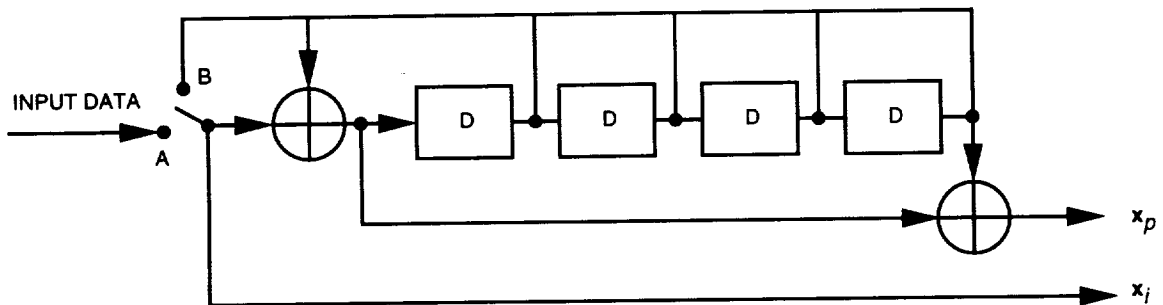
Fig. 2. Trellis termination.

B. Weight Distribution

In order to estimate the performance of a code, it is necessary to have information about its minimum distance, d, weight distribution, or actual code geometry, depending on the accuracy required for the bounds or approximations. The example of turbo code shown in Fig. 1 produces two sets of codewords, $\mathbf{x}_1 = (\mathbf{x}_{1i}, \mathbf{x}_{1p})$ and $\mathbf{x}_2 = (\mathbf{x}_{2i}, \mathbf{x}_{2p})$, whose weights can be easily computed. The challenge is in finding the pairing of codewords from each set, induced by a particular interleaver. Intuitively, we would like to avoid pairing low-weight codewords from one encoder with low-weight words from the other encoder. Many such pairings can be avoided by proper design of the interleaver. However, if the encoders are not recursive, the low-weight codeword generated by the input sequence $\mathbf{u} = (00 \cdots 0000100 \cdots 000)$ with a single "1" will always appear again in the second encoder, for any choice of interleaver. This motivates the use of recursive encoders, where the key ingredient is the recursiveness and not the fact that the encoders are systematic. For our example using a recursive encoder, the input sequence $\mathbf{u} = (00 \cdots 0010000100 \cdots 000)$ generates the minimum weight codeword (weight $= 6$). If the interleaver does not properly "break" this input pattern, the resulting minimum distance will be 12.

However, the minimum distance is not the most important quantity of the code, except for its asymptotic performance, at very high E_b/N_o. At moderate signal-to-noise ratios (SNRs), the weight distribution at the first several possible weights is necessary to compute the code performance. Estimating the complete weight distribution for a large N is still an open problem for these codes. We have investigated the effect of the interleaver on the weight distribution on a small-scale example where $N = 16$. This yields an (80,16) code whose weight distribution can be found by exhaustive enumeration. Some of our results are shown in Fig. 3(a), where it is apparent that a good choice of the interleaver can increase the minimum distance from 12 to 14, and, more importantly, can reduce the count of codewords at low weights. Figure 3(a) shows the weight distribution obtained by using no interleaver, a reverse permutation, and a 4×4 block interleaver, all with $d = 12$. Better weight distributions are obtained by the "random" permutation $\{2, 13, 0, 3, 11, 15, 6, 14, 8, 9, 10, 4, 12, 1, 7, 5\}$ with $d = 12$, and by the best-found permutation $\{12, 3, 14, 15, 13, 11, 1, 5, 6, 0, 9, 7, 4, 2, 10, 8\}$ with $d = 14$. For comparison, the binomial distribution is also shown. The best known (80,16) linear block code has a minimum distance of 28. For an interleaver length of $N = 1024$, we were only able to enumerate all codewords produced by input sequences with weights 1, 2, and 3. This again confirmed the importance of the interleaver choice for reducing the number of low-weight codewords. Better weight distributions were obtained by using "random" permutations than by using structured permutations as block or reverse permutations.
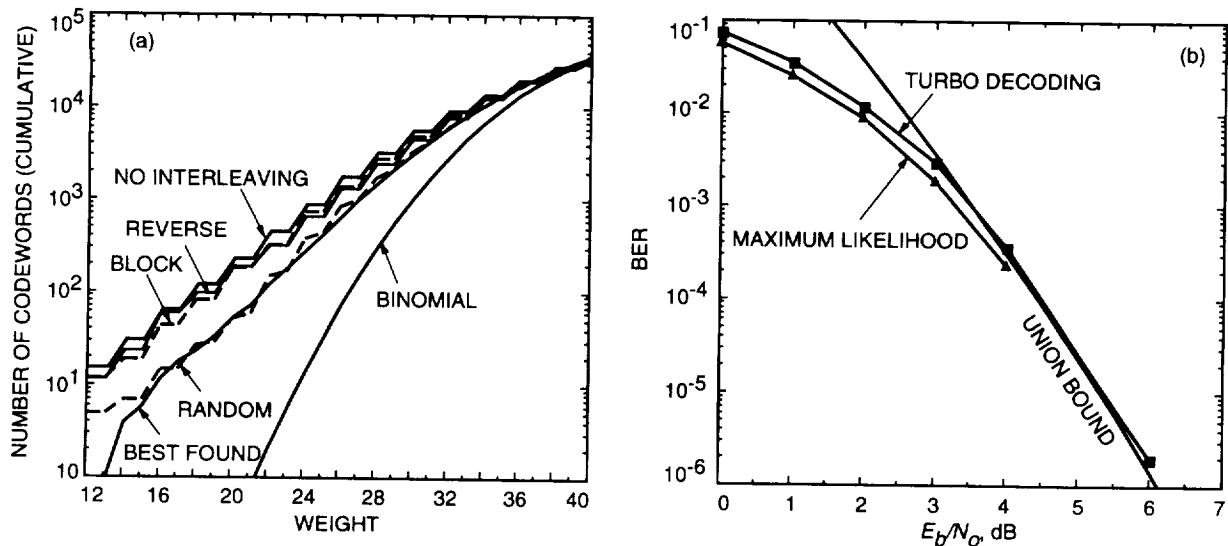

Fig. 3. The (80, 16) code (a) weight distribution and (b) performance.

For the (80,16) code using the best-found permutation, we have compared the performance of a maximum-likelihood decoder (obtained by simulation) to that of a turbo decoder with 10 iterations, as described in Section 3, and to the union bound computed from the weight distribution, as shown in Fig. 3(b). As expected, the performance of the turbo decoder is slightly suboptimum.

III. Turbo Decoding

Let u_k be a binary random variable taking values in $\{+1, -1\}$, representing the sequence of information bits. The maximum a posteriori (MAP) algorithm, summarized in the Appendix, provides the log likelihood ratio $L(k)$ given the received symbols $\mathbf{y}$:

$$L(k) = \log \frac{P(u_k = +1|\mathbf{y})}{P(u_k = -1|\mathbf{y})} \tag{1}$$

The sign of $L(k)$ is an estimate, $\hat{u}_k$, of u_k, and the magnitude $|L(k)|$ is the reliability of this estimate, as suggested in [3].

The channel model is shown in Fig. 4, where the n_{1ik}'s and the n_{1pk}'s are independent identically distributed (i.i.d.) zero-mean Gaussian random variables with unit variance, and $\rho = \sqrt{2E_s/N_o} = \sqrt{2rE_b/N_o}$ is the SNR. A similar model applies for encoder 2.
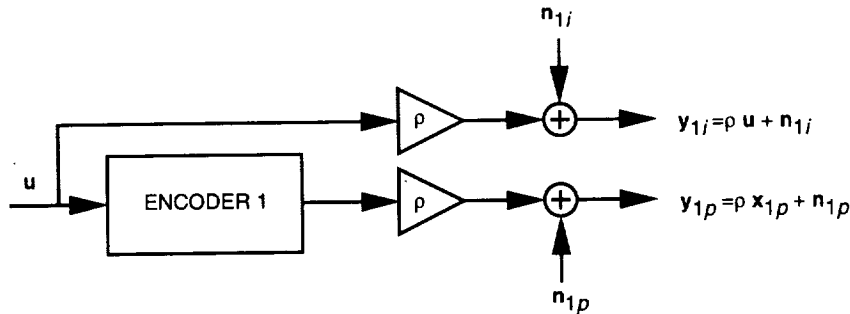
Fig. 4. The channel model.

Given the turbo code structure in Fig. 1, the optimum decoding rule maximizes either $P(u_k|\mathbf{y}_1, \mathbf{y}_2)$ (minimum bit-error probability rule) or $P(\mathbf{u}|\mathbf{y}_1, \mathbf{y}_2)$ (maximum-likelihood sequence rule). Since this rule is obviously too complex to compute, we resort to a suboptimum decoding rule [2,3] that separately uses the two observations $\mathbf{y}_1$ and $\mathbf{y}_2$, as shown in Fig. 5. Each decoder in Fig. 5 computes the a posteriori probabilities $P(u_k|\mathbf{y}_i, \tilde{u}_i), i = 1, 2$ see Fig. 6(a), or equivalently the log-likelihood ratio $L_i(k) = \log\left(P(u_k = +1|\mathbf{y}_i, \tilde{u}_i)\right) / \left(P(u_k = -1|\mathbf{y}_i, \tilde{u}_i)\right)$ where $\tilde{u}_1$ is provided by decoder 2 and $\tilde{u}_2$ is provided by decoder 1 (see Fig. 6(b)). The quantities $\tilde{u}_i$ correspond to "new data estimates," "innovations," or "extrinsic information" provided by decoders 1 and 2, which can be used to generate a priori probabilities on the information sequence $\mathbf{u}$ for branch metric computation in each decoder.

The question is how to generate the probabilities $P(\tilde{u}_{i,k}|u_k)$ that should be used for computation of the branch transition probabilities in MAP decoding. It can be shown that the probabilities $P(u_k|\tilde{u}_{i,k})$ or, equivalently, $\log\left(P(u_k = +1|\tilde{u}_{i,k})\right)/\left(P(u_k = -1|\tilde{u}_{i,k})\right)$, $i = 1, 2$ can be used instead of $P(\tilde{u}_{i,k}|u_k)$ for branch metric computations in the decoders. When decoder 1 generates $P(u_k|\tilde{u}_{2,k})$ or $\log\left(P(u_k = +1|\tilde{u}_{2,k})\right)/\left(P(u_k = -1|\tilde{u}_{2,k})\right)$ for decoder 2, this quantity should not include the contribution due to $\tilde{u}_{1,k}$, which has already been generated by decoder 2. Thus, we should have

$$\log \frac{P(u_k = +1|\tilde{u}_{2,k})}{P(u_k = -1|\tilde{u}_{2,k})} = \log \frac{P(u_k = +1|\mathbf{y}_1, \tilde{u}_{1,1}, \cdots, \tilde{u}_{1,k-1}, \tilde{u}_{1,k+1}, \cdots, \tilde{u}_{1,N})}{P(u_k = -1|\mathbf{y}_1, \tilde{u}_{1,1}, \cdots, \tilde{u}_{1,k-1}, \tilde{u}_{1,k+1}, \cdots, \tilde{u}_{1,N})} \tag{2}$$
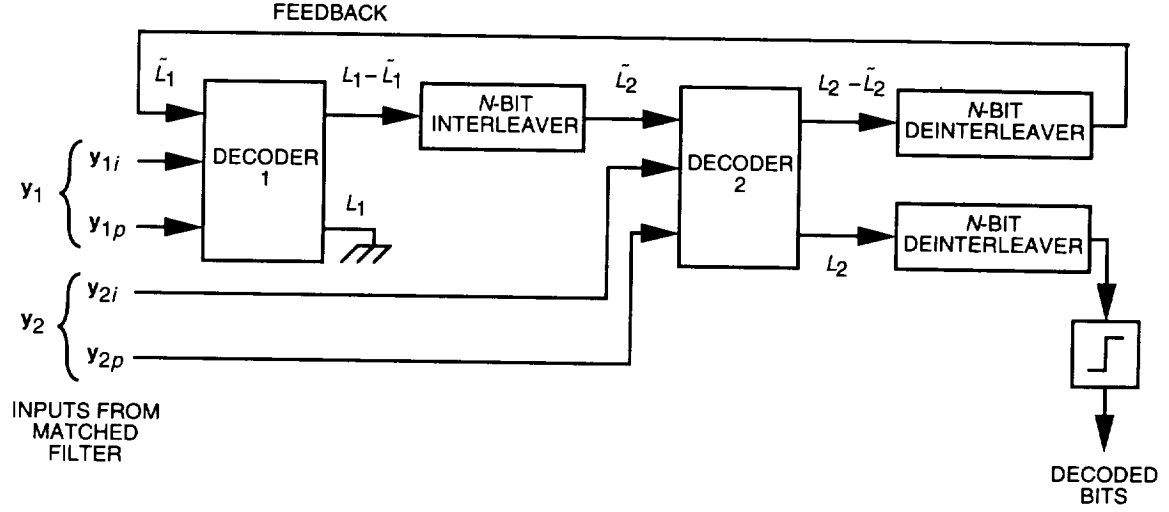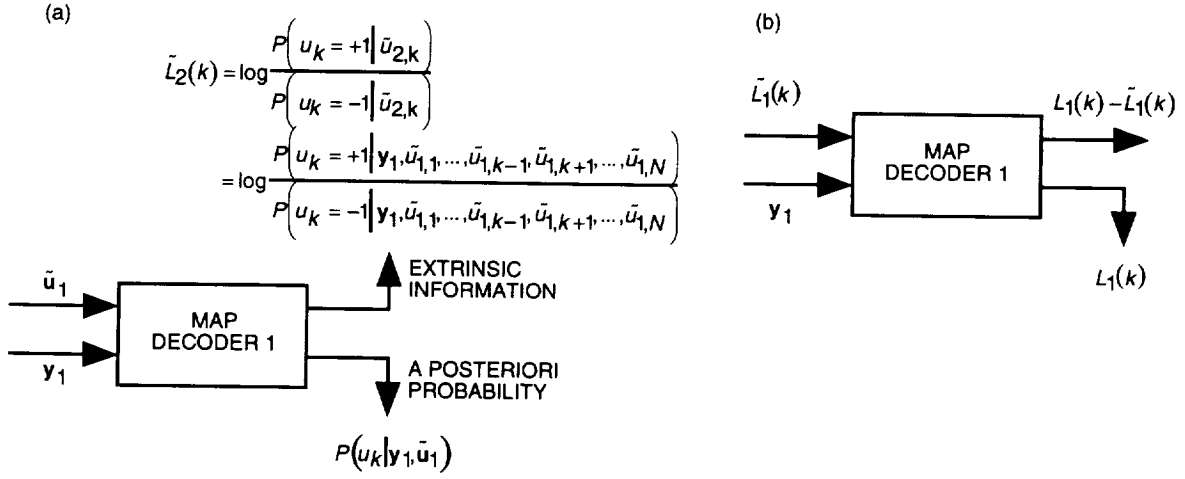
Fig. 5. The turbo decoder.

Fig. 6. Input/output of the MAP decoder: (a) a posteriori probability and (b) log-likelihood ratio.

To compute $\log\left(P(u_k = +1|\tilde{u}_{2,k})\right)/\left(P(u_k = -1|\tilde{u}_{2,k})\right)$, we note [see Fig. 6(a)] that

$$P(u_k|\mathbf{y}_1, \tilde{\mathbf{u}}_1) =$$

$$\frac{P(u_k|\mathbf{y}_1, \tilde{u}_{1,1}, \cdots, \tilde{u}_{1,k-1}, \tilde{u}_{1,k+1}, \cdots, \tilde{u}_{1,N}) P(\tilde{u}_{1,k}|u_k, \mathbf{y}_1, \tilde{u}_{1,1}, \cdots, \tilde{u}_{1,k-1}, \tilde{u}_{1,k+1}, \cdots, \tilde{u}_{1,N})}{P(\tilde{u}_{1,k}|\mathbf{y}_1, \tilde{u}_{1,1}, \cdots, \tilde{u}_{1,k-1}, \tilde{u}_{1,k+1}, \cdots, \tilde{u}_{1,N})} \quad (3)$$

Since $\tilde{u}_{1,k}$ was generated by decoder 2 and deinterleaving is used, this quantity depends only weakly on $\mathbf{y}_1$ and $\tilde{u}_{1,j}$, $j \neq k$. Thus, we can have the following approximation:

$$P(\tilde{u}_{1,k}|u_k, \mathbf{y}_1, \tilde{u}_{1,1}, \cdots, \tilde{u}_{1,k-1}, \tilde{u}_{1,k+1}, \cdots, \tilde{u}_{1,N}) \approx P(\tilde{u}_{1,k}|u_k) = 2P(u_k|\tilde{u}_{1,k})P(\tilde{u}_{1,k}) \quad (4)$$

Using Eq. (4) in Eq. (3), we obtain

$$P(u_k|\mathbf{y}_1, \tilde{u}_{1,1}, \cdots, \tilde{u}_{1,k-1}, \tilde{u}_{1,k+1}, \cdots, \tilde{u}_{1,N}) = \frac{P(u_k|\mathbf{y}_1, \tilde{\mathbf{u}}_1)P(\tilde{u}_{1,k}|\mathbf{y}_1, \tilde{u}_{1,1}, \cdots, \tilde{u}_{1,k-1}, \tilde{u}_{1,k+1}, \cdots, \tilde{u}_{1,N})}{2P(u_k|\tilde{u}_{1,k})P(\tilde{u}_{1,k})}$$

$$(5)$$

It is preferable to work with likelihood ratios to avoid computing probabilities not involving u_k (see Fig. 6(b)). Define

$$\tilde{L}_i(k) = \log \frac{P(u_k = +1|\tilde{u}_{i,k})}{P(u_k = -1|\tilde{u}_{i,k})}, \quad i = 1, 2 \qquad (6)$$

From Eqs. (2) and (5), we obtain $\tilde{L}_2^{(m)}(k) = L_1^{(m)}(k) - \tilde{L}_1^{(m-1)}(k)$ at the output of decoder 1, before interleaving, for the mth iteration. Similarly, we can obtain $\tilde{L}_1^{(m)}(k) = L_2^{(m)}(k) - \tilde{L}_2^{(m)}(k)$ at the output of decoder 2, after deinterleaving. Using the above definitions, the a priori probabilities can be computed as

$$P(u_k = +1|\tilde{u}_{i,k}) = \frac{e^{\tilde{L}_i(k)}}{1 + e^{\tilde{L}_i(k)}} = 1 - P(u_k = -1|\tilde{u}_{i,k}), \quad i = 1, 2 \qquad (7)$$

Then the update equation for the mth iteration of the decoder in Fig. 5 becomes

$$\tilde{L}_1^{(m)}(k) = \tilde{L}_1^{(m-1)}(k) + \alpha_m \left[L_2^{(m)}(k) - L_1^{(m)}(k) \right], \quad \alpha_m = 1 \qquad (8)$$

This looks like the update equation of a steepest descent method, where $\left[L_2^{(m)}(k) - L_1^{(m)}(k) \right]$ represents the rate of change of $L(k)$ for a given u_k, and α_m is the step size.

Figure 7 shows the probability density function of $\tilde{L}_1(k)$ at the output of the second decoder in Fig. 1, after deinterleaving and given $u_k = +1$. As shown in Fig. 7, this density function shifts to the right as the number of iterations, m, increases. The area under each density function to the left of the origin represents the BER if decoding stops after m iterations.

At this point, certain observations can be made. Note that $\tilde{L}_2(k')$ at the input of decoder 2 includes an additive component $2\rho y_{1ik}$, which contributes to the branch metric computations in decoder 2 at observation y_{2ik}. This improves by 3 dB the SNR of the noisy information symbols at the input of decoder 2. Similar arguments hold for $\tilde{L}_1(k)$. An apparently more powerful decoding structure can be considered, as shown in Fig. 8. However, the performances of the decoding structures in Figs. 8 and 5 are equivalent for a large number of iterations (the actual difference is one-half iteration). If the structure in Fig. 8 is used, then the log-likelihood ratio $\tilde{L}_2(k)$ fed to decoder 2 should not depend on $\tilde{u}_{1k}$ and y'_{1ik}, and, similarly, $\tilde{L}_1(k)$ should not depend on $\tilde{u}_{2k}$ and y'_{2ik}. Using analogous derivations based on Eqs. (2) through (5), we obtain

$$\tilde{L}_2(k) = L_1(k) - \tilde{L}_1(k) - 2\rho y'_{1ik}$$

$$\tilde{L}_1(k) = L_2(k) - \tilde{L}_2(k) - 2\rho y'_{2ik}$$

where $\mathbf{y}'_{1i}$ is the sum of $\mathbf{y}_{1i}$ with the deinterleaved version of $\mathbf{y}_{2i}$ and $\mathbf{y}'_{2i}$ is the sum of $\mathbf{y}_{2i}$ with the interleaved version of $\mathbf{y}_{1i}$. Thus, the net effect of the decoding structure in Fig. 8 is to explicitly pass to decoder 2 the information contained in $\mathbf{y}_{1i}$ (and vice versa), but to remove the identical term from the input log-likelihood ratio.
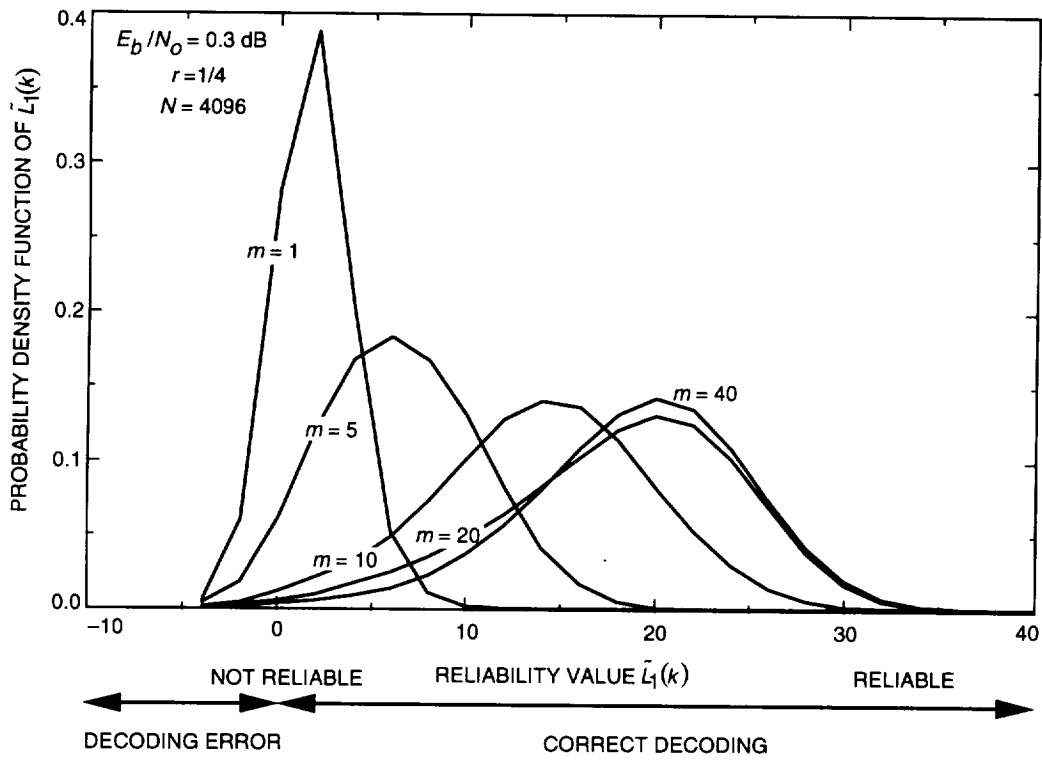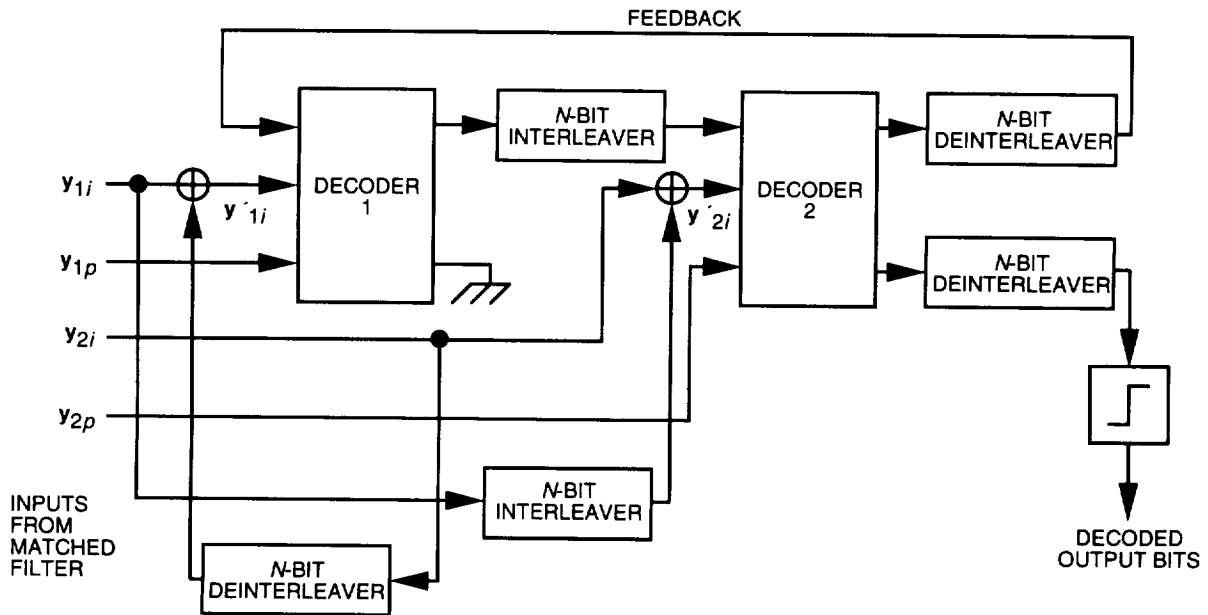
Fig. 7. The reliability function.

Fig. 8. An equivalent turbo decoder.

IV. Performance

The performance obtained by turbo decoding the code in Fig. 1 with random permutations of lengths $N = 4096$ and $N = 16384$ is compared in Fig. 9 to the capacity of a binary-input Gaussian channel for rate $r = 1/4$ and to the performance of a (15,1/4) convolutional code originally developed at JPL for the Galileo mission. At BER $= 5 \times 10^{-3}$, the turbo code is better than the (15,1/4) code by 0.25 dB for $N = 4096$ and by 0.4 dB for $N = 16384$.
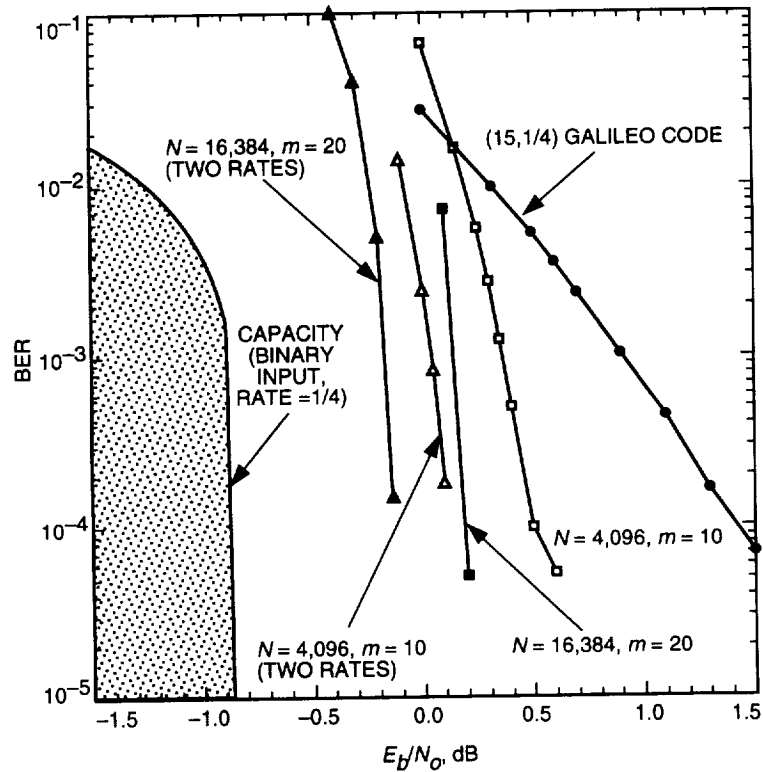
Fig. 9. Turbo codes performance, $r = 1/4$.

So far we have considered only component codes with identical rates, as shown in Fig. 1. Now we propose to extend the results to encoders with unequal rates, as shown in Fig. 10. This structure improves the performance of the overall rate 1/4 code, as shown in Fig. 9. The gains at BER $= 5 \times 10^{-3}$ relative to the (15,1/4) code are 0.55 dB for $N = 4096$ and 0.7 dB for $N = 16384$. For both cases, the performance is within 1 dB of the Shannon limit at BER $= 5 \times 10^{-3}$, and the gap narrows to 0.7 dB for $N = 16384$ at a low BER.

V. Conclusions

We have shown how turbo codes and decoders can be used to improve the coding gain for deep-space communications while decreasing the decoding complexity with respect to the large constraint-length convolutional codes currently in use. These are just preliminary results that require extensive further analysis. In particular, we need to improve our understanding of the influence of the interleaver choice on the code performance, to explore the sensitivity of the decoder performance to the precision with which we can estimate E_b/N_o, and to establish whether there might be a flattening of the performance curves at higher E_b/N_o, as it appears in one of the curves in Fig. 9. An interesting theoretical question is to determine how random these codes can be so as to draw conclusions on their performance based on comparison with random coding bounds.

In this article, we have explored turbo codes using only two encoders, but similar constructions can be used to build multiple-encoder turbo codes and generalize the turbo decoding concept to a truly distributed decoding system where each subdecoder works on a piece of the total observation and tentative estimates are shared among decoders until an acceptable degree of consensus is reached.
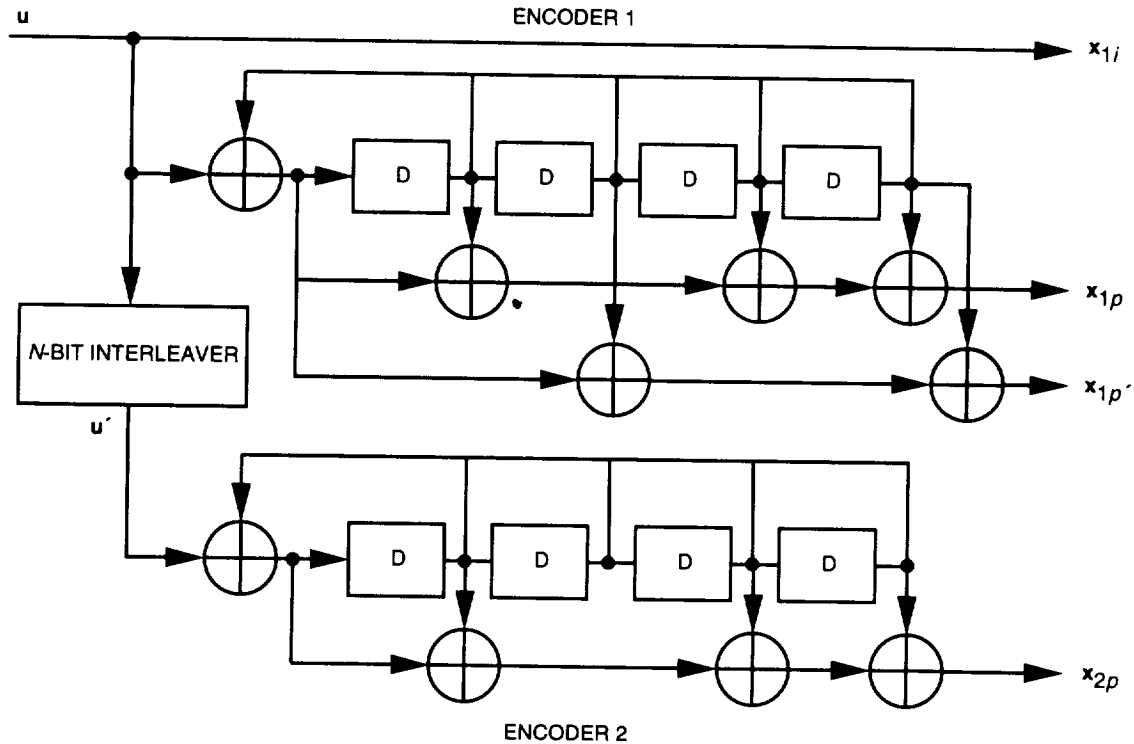

Fig. 10. The two-rate encoder.

Acknowledgments

References

[1] L. Bahl, J. Cocke, F. Jelinek, and J. Raviv, "Optimal Decoding of Linear Codes for Minimizing Symbol Error Rate," *IEEE Transactions on Information Theory*, vol. 20, pp. 284–287, March 1974.

[2] C. Berrou, A. Glavieux, and P. Thitimajshima, "Near Shannon Limit Error-Correcting Coding and Decoding: Turbo-Codes," *Proceedings of ICC '93*, Geneva, Switzerland, pp. 1064–1070, May 1993.

[3] J. Hagenauer and P. Robertson, "Iterative (Turbo) Decoding of Systematic Convolutional Codes With the MAP and SOVA Algorithms," *Proceedings of the ITG Conference on "Source and Channel Coding,"* Frankfurt, Germany, pp. 1-9, October 1994.

[4] P. L. McAdam, L. R. Welch, and C. L. Weber, "M.A.P. Bit Decoding of Convolutional Codes" (Abstract), *1972 International Symposium on Information Theory*, Asilomar, California, p. 91, May 1972.

Appendix

The MAP Algorithm

Let u_k be the information bit associated with the transition from time $k - 1$ to time k, and use s as an index for the states. The MAP algorithm [1,4] provides the log likelihood given the received symbols y_k, as shown in Fig. A-1.
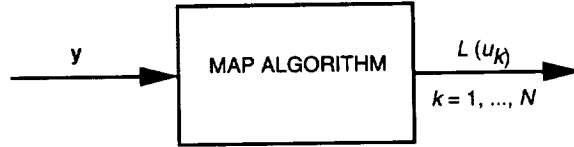
Fig. A-1. The MAP algorithm.

$$L(k) = \log \frac{P(u_k = +1|\mathbf{y})}{P(u_k = -1|\mathbf{y})} = \log \frac{\sum_s \sum_{s'} \gamma_{+1}(y_k, s', s)\alpha_{k-1}(s')\beta_k(s)}{\sum_s \sum_{s'} \gamma_{-1}(y_k, s', s)\alpha_{k-1}(s')\beta_k(s)} \tag{A-1}$$

The estimate of the transmitted bits is then given by $sign[L(k)]$ and their reliability by $|L(k)|$. In order to compute Eq. (A-1), we need the *forward* and *backward* recursions,

$$\alpha_k(s) = \frac{\sum_{s'} \sum_{i=\pm1} \gamma_i(y_k, s', s)\alpha_{k-1}(s')}{\sum_s \sum_{s'} \sum_{j=\pm1} \gamma_j(y_k, s', s)\alpha_{k-1}(s')} \tag{A-2}$$

$$\beta_k(s) = \frac{\sum_{s'} \sum_{i=\pm1} \gamma_i(y_{k+1}, s, s')\beta_{k+1}(s')}{\sum_s \sum_{s'} \sum_{j=\pm1} \gamma_j(y_{k+1}, s', s)\alpha_k(s')}$$

where

$$\gamma_i(y_k, s', s) = \begin{cases} \eta_k e^{\rho \sum_{\nu=1}^{n} y_{k,\nu} x_{k,\nu}(s',i)} & \text{if transition } s' \to s \text{ is allowable for } u_k = i \\ 0 & \text{otherwise} \end{cases} \qquad \text{(A-3)}$$

$\rho = \sqrt{2(E_s/N_0)}$, $\eta_k = P(u_k = \pm 1 | \tilde{u}_k)$, except for the first iteration in the first decoder, where $\eta_k = 1/2$, and $x_{k,\nu}$ are code symbols. The operation of these recursions is shown in Fig. A-2. The evaluation of Eq. (A-1) can be organized as follows:

Step 0: $\alpha_0(0) = 1 \quad \alpha_0(s) = 0, \forall s \neq 0$

$\qquad \qquad \beta_N(0) = 1 \quad \beta_N(s) = 0, \forall s \neq 0$

Step 1: Compute the γ_k's using Eq. (A-3) for each received set of symbols y_k.

Step 2: Compute the α_k's using Eq. (A-2) for $k = 1, \cdots, N$.

Step 3: Use Eq. (A-2) and the results of Steps 1 and 2 to compute the β_k's for $k = N, \cdots, 1$.

Step 4: Compute $L(k)$ using Eq. (A-1) for $k = 1, \cdots, N$.
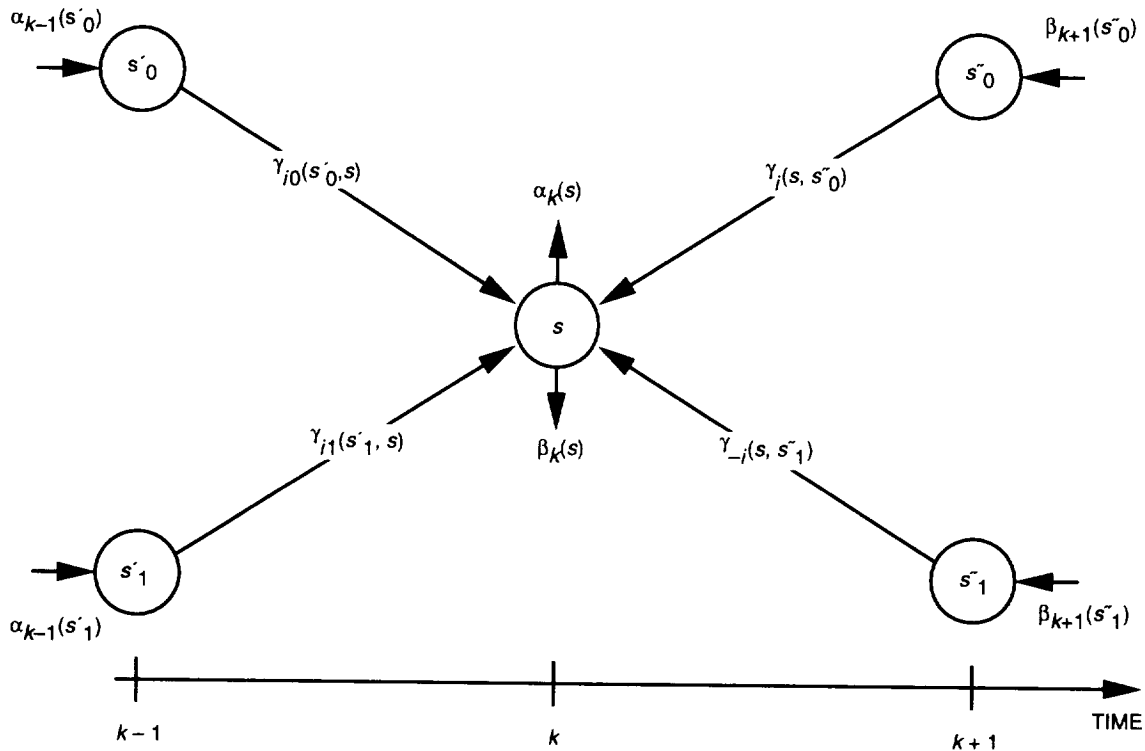
Fig. A-2. Forward and backward recursions.

39

CDMA With Interference Cancellation for Multiprobe Missions

D. Divsalar
Communications Systems Research Section

M. K. Simon
Telecommunications Systems Section

Code division multiple-access spread spectrum has been proposed for use in future multiprobe/multispacecraft missions. This article considers a general parallel interference-cancellation scheme that significantly reduces the degradation effect of probe (user) interference but with a lesser implementation complexity than the maximum-likelihood technique. The scheme operates on the fact that parallel processing simultaneously removes from each probe (user) the total interference produced by the remaining most reliably received probes (users) accessing the channel. The parallel processing can be done in multiple stages. The proposed scheme uses tentative decision devices with different optimum thresholds at the multiple stages to produce the most reliably received data for generation and cancellation of probe/spacecraft interference. The one-stage interference cancellation was analyzed for two types of tentative decision devices, namely, hard and null zone decisions. Simulation results are given for one- and two-stage interference cancellation for equal as well as unequal received power probes.

I. Introduction

Historically, the Pioneer Venus Mission employed frequency division multiple-access (FDMA) multiplexing to prevent any possible interference between the four probe signals and the two redundant flyby spacecraft bus signals. A 2-MHz open-loop recording bandwidth was sufficient to capture all six S-band (2.3-GHz) signals. Future missions have been proposed with significantly more probes and use of X-band for improved radio metric tracking. The addition of the higher X-band (8.4-GHz) frequency with higher Doppler shifts, and the much larger number of probes,[1] implies that a much larger bandwidth would be required if an FDMA scheme were used. As a result, Charles D. Edwards proposed that code division multiple-access (CDMA) multiplexing be used for future multiprobe missions.[2] This approach has the advantage of greatly reducing the required open-loop recording bandwidth, reducing the cost of the

---

[1] For example, the Venus Multiprobe Mission (VMPM) is a proposed Discovery Mission concept that delivers 18 small probes into the Venus atmosphere and two redundant flyby spacecraft bus signals. The science goal of the mission is to understand the superrotation of the Venusian atmosphere, which causes the clouds of Venus to rotate 60 times faster than the surface.

[2] C. Edwards, "VMPM Wind Experiment," viewgraph presentation (internal document), Jet Propulsion Laboratory, Pasadena, California, February 24, 1994.

recording systems and the complexity of the postencounter data reduction, and simplifying the probe design by allowing all probes to use the same ultrastable oscillator frequency and identical transmitter structure, with the exception that different seeds should be used for the pseudorandom noise (PN) codes.

In the following, the term "user" will be used for "probe," "spacecraft," or any direct sequence spread-spectrum transmitter that communicates with a central receiving Earth station, usually called a "base-station receiver."

Multiuser communications systems that employ CDMA exhibit a user capacity limit in the sense that there exists a maximum number of users that can simultaneously communicate over the channel for a specified level of performance per user. This limitation is brought about by the ultimate domination of the other user interference over the additive thermal noise. Over the years, researchers have sought ways to extend the user capacity of CDMA systems either by employing optimum (maximum-likelihood) detection [1] or interference-cancellation methods [2–4]. In this article, we discuss a general parallel interference-cancellation scheme that significantly reduces the degradation effect of user interference but with a lesser implementation complexity than the maximum-likelihood technique. The proposed scheme operates on the fact that parallel processing simultaneously removes from each user the total interference produced by the remaining reliably received users accessing the channel. In this way, each user in the system receives equal treatment in so far as the attempt is made to completely cancel his or her multiple user interference.

When compared with classical CDMA, which has no interference cancellation, and also with the successive (serial) interference-cancellation technique previously proposed by Viterbi [3], in which user interference is sequentially removed one user at a time (the first user sees all of the interference and the last user sees none), the parallel cancellation scheme discussed here achieves a significant improvement in performance. Aside from increasing the user capacity, the parallel cancellation scheme has a further advantage over the serial cancellation scheme with regard to the delay necessary to fully accomplish the interference cancellation for all users in the system. Since in the latter the interference cancellation proceeds serially, a delay on the order of M bit times (M denotes the number of simultaneous users in the CDMA system) is required, whereas in the former, since the interference cancellation is performed in parallel for all users, the delay required is only 1 bit time (for a single-stage scheme).

II. Single-Stage Interference Cancellation

A. Tentative Hard Decisions—Equal Power, Synchronous Users

We consider first the performance of the single-stage parallel interference-cancellation scheme illustrated in Fig. 1, where the tentative decision devices associated with each user are 1-bit quantizers (hard decisions). This particular case corresponds to the scheme proposed in [2] and [4]. We assume that all users have the same power; thus, it is sufficient to characterize only the performance of any one user, say the first, which will be typical of all the others. Furthermore, we assume that all users have synchronous data streams and purely random PN codes.[3] While the assumption of synchronous users is perhaps unrealistic from a practical standpoint, it can be shown that the synchronous user case results in worst-case performance and thus serves as a lower bound on the user capacity achievable with this scheme. Alternately stated, any degree of data asynchronism among the users will yield a better performance, e.g., more users capable of being supported for a given amount of signal-to-noise ratio (SNR) degradation, than that arrived at in this section.

In general, the received signal in Fig. 1 is the sum of M direct-sequence binary phase shift key (BPSK) signals, each with power S_i, bit time T_b, PN chip time T_c, and additive white Gaussian noise with

---

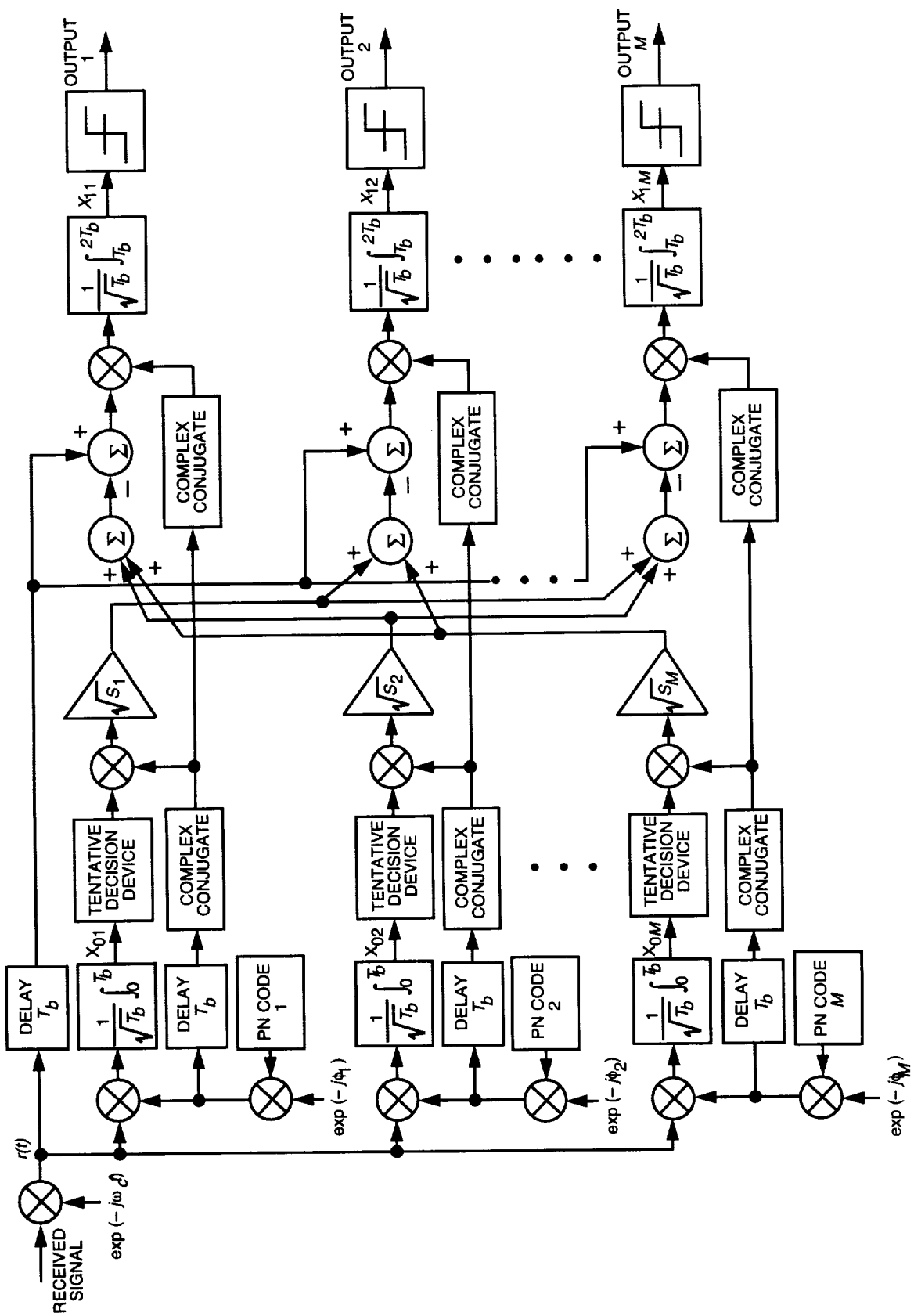[3] For very long linear feedback shift registers, PN codes can be assumed to be purely random.

Fig. 1. A single-stage interference cancellation scheme with parallel processing for CDMA (complex baseband model).

42

single-sided power spectral density (PSD) N_0 W/Hz, which at baseband can be written in the complex form[4]

$$r(t) = \sum_{i=1}^{M} \sqrt{S_i} m_i(t) PN_i(t) e^{j\phi_i} + n(t) \tag{1}$$

where, for the ith user, $PN_i(t)$ is the PN code; $m_i(t) = \sum_{k=-\infty}^{\infty} a_{ki} p(t - kT_b)$ is the modulation with the kth bit a_{ki} taking on equiprobable values ± 1 and unit power rectangular pulse shape $p(t)$ of duration T_b; and ϕ_i is the carrier phase. For our case of interest here, $S_i = S; i = 1, 2, \cdots, M$. After despreading and demodulating[5] r(t) with user 1's PN code and carrier reference signal (both of these operations are assumed to be ideal), the normalized output of the integrate-and-dump (I&D) circuit is given by

$$x_{01} = a_{01}\sqrt{E_b} + n_1 e^{-j\phi_1} + \sum_{i=2}^{M} a_{01} n_{1i} e^{j(\phi_i - \phi_1)} \triangleq a_{01}\sqrt{E_b} + n_1 e^{-j\phi_1} + \sqrt{E_b} \sum_{i=2}^{M} a_{0i}\gamma_{1i} e^{j(\phi_i - \phi_1)} \tag{2}$$

where $E_b = ST_b$ denotes the bit energy; a_{0i} is the polarity of user i's bit in the interval $0 \le t \le T_b$; $n_1 = 1/(\sqrt{T_b}) \int_0^{T_b} n(t) PN_1(t) dt$ is a zero-mean complex Gaussian random variable with variance $E\{|n_1|^2\} = N_0$ representing the thermal noise; and $n_{1i} = \sqrt{S/T_b} \int_0^{T_b} PN_1(t) PN_i(t) dt \triangleq \sqrt{E_b}\gamma_{1i}; i = 2, 3, \cdots, M$ are the interference noises contributed by the other $M - 1$ users, which are modeled as independent zero-mean Gaussian random variables, each with variance ST_c.[6] Also, the first subscript on x denotes the stage at which we are observing the I&D output, while the second subscript denotes the particular user. This notation will be useful later on in our discussion of multiple-stage cancellation schemes. The foregoing modeling of user interference as additive Gaussian noise follows from the assumptions made in a similar analysis of a CDMA system [5], namely, a large spreading ratio, $\eta = T_b/T_c$, and purely random PN codes.

Tentative hard decisions are made on the signals, $x_{0i}; i - 1, 2, \cdots, M$, and are used in an attempt to cancel the other user interference. If a correct tentative decision is made on a particular other user's bit, then the interference from that user can be completely cancelled. On the other hand, if an incorrect tentative decision is made, then the interference from that user will be enhanced rather than cancelled. A quantitative description of this will be given when we model the signal upon which final decisions are made. As we shall see, the performance analysis associated with this model is complicated by the fact that *the tentative decisions are not independent of one another*. More about this shortly.

After respreading/remodulation, interference cancellation, and despreading/demodulation, the normalized output of the I&D corresponding to the *final* decisions is given by

$$x_{11} = a_{01}\sqrt{E_b} + n_1 e^{-j\phi_1} + \overbrace{\sqrt{E_b} \sum_{i=2}^{M} \beta_i \gamma_{1i} e^{j(\phi_i - \phi_1)}}^{I_1} \tag{3}$$

where

---

[4] For convenience, we shall use complex notation to represent the various signals in the receiver.

[5] Since we are working with a baseband model, the term "remodulation" or "demodulation" refers to complex multiplication by the particular user's carrier phase or its complex conjugate, respectively.

[6] The normalized interference noises $\gamma_{1i}; i = 2, 3, \cdots, M$ have variance equal to the reciprocal of the spreading ratio, i.e., $\eta^{-1} = T_c/T_b$.

$$\beta_i = a_{0i} - \text{sgn}\left[Re\left\{\sqrt{E_b}\left(a_{0i} + \sum_{\substack{m=1\\m\neq i}}^{M} a_{0m}\gamma_{im}e^{j(\phi_m - \phi_i)}\right) + n_i e^{-j\phi_i}\right\}\right] \tag{4}$$

is a three-valued $(0, \pm 2)$ indicator random variable whose magnitude represents whether or not a correct tentative decision is made on the ith user's bit. It is tempting to model the β_i's as independent random variables. Unfortunately, this leads to optimistic results (when compared with the true performance results obtained from simulation). In addition to the fact that the β_i's are not themselves independent, they are also dependent on the PN cross-correlations, i.e., the γ_{1i}'s. Fortunately, however, the β_i's are not strongly dependent, i.e., the only terms that preclude *complete* independence of, say, β_i and β_j, are $a_{0j}\gamma_{ij}$ in β_i and $a_{0i}\gamma_{ji} = a_{0i}\gamma_{ij}$ in β_j. Hence, for sufficiently large M, it is reasonable to assume a Gaussian model for the total residual (after cancellation) interference term in Eq. (3). The accuracy of this model will improve as M increases (actually, as the number of nonzero terms in I_1 increases, which implies a high tentative-decision error rate). We shall be more detailed about this issue later on when comparing the performance results derived from this analytical model with those obtained from a true computer simulation of the receiver.

Assuming then a Gaussian model for I_1 (note that I_1 is not zero mean), then the average probability of error associated with the final decisions is given by

$$P_b(E) = \frac{1}{2}Pr\left\{Re\{x_{11} > 0|_{a_{01}=-1}\}\right\} + \frac{1}{2}Pr\left\{Re\{x_{11} < 0|_{a_{01}=1}\}\right\}$$

$$= Pr\left\{Re\{x_{11} > 0|_{a_{01}=-1}\}\right\} = Pr\left\{N_t > \sqrt{E_b} - \sqrt{E_b}\sum_{i=2}^{M}\overline{\beta_i\gamma_{1i}\cos(\phi_i - \phi_1)}\right\} \tag{5}$$

where[7]

$$N_t = Re\{n_1 e^{-j\phi_1} + I_1 - \overline{I_1}\} = N_1 + \sqrt{E_b}\sum_{i=2}^{M}\beta_i\gamma_{1i}\cos(\phi_i - \phi_1) - \sqrt{E_b}\sum_{i=2}^{M}\overline{\beta_i\gamma_{1i}\cos(\phi_i - \phi_1)} \tag{6}$$

is the effective noise seen by user 1 after cancellation, which in view of the above, is modeled as a real zero-mean Gaussian noise random variable whose thermal noise component N_1 has variance $\sigma_{N_1}^2 = N_0/2$. It is straightforward to compute the variance of N_t as

$$\sigma_{N_1}^2 = E_b(M-1)\overline{\beta_i^2\gamma_{1i}^2\cos^2(\phi_i - \phi_1)} - E_b(M-1)^2\left(\overline{\beta_i\gamma_{1i}\cos(\phi_i - \phi_1)}\right)^2$$

$$+ E_b(M-1)(M-2)\overline{\beta_i\gamma_{1i}\beta_j\gamma_{1j}\cos(\phi_i - \phi_1)\cos(\phi_j - \phi_1)} \tag{7}$$

where i can take on any value from the set $2, 3, \cdots, M$. Hence, from Eq. (5), the average probability can be obtained as

---

[7] To simplify the notation here and in what follows, it is understood that the statistical mean $\overline{\beta_i\gamma_{1i}\cos(\phi_i - \phi_1)}$ is computed under the hypothesis $a_{01} = -1$.

$$P_b(E) = Q\left(\sqrt{\frac{2E_b}{N_0}}\Lambda\right) \tag{8}$$

where

$$\Lambda \triangleq \frac{\left(1 - (M-1)\overline{\xi_{1i}}\right)^2}{1 + 2(E_b)/(N_0)(M-1)\left[\overline{\xi_{1i}^2} - (M-1)\left(\overline{\xi_{1i}}\right)^2 + (M-2)\overline{\xi_{1i}\xi_{1j}}\right]}; \xi_{1i} \triangleq \beta_i\gamma_{1i}\cos(\phi_i - \phi_1) \tag{9}$$

is an SNR degradation factor (relative to the performance of a single BPSK user transmitting alone) and $Q(x)$ is the Gaussian probability integral defined by

$$Q(x) \triangleq \frac{1}{\sqrt{2\pi}}\int_x^\infty \exp\left(-\frac{y^2}{2}\right)dy \tag{10}$$

Thus, the evaluation of $P_b(E)$ reduces to the evaluation of the various statistical averages (moments) of ξ_{1i} required in Eq. (9). These statistical averages, which must be performed over the Gaussian noise and interference random variables as well as the uniformly distributed carrier phases, are not trivial to compute. Nevertheless, they can be obtained in the form of definite integrals of tabulated functions with the following results:

$$\overline{\xi_{1i}} = \frac{1}{2\pi}\int_0^{2\pi}\sqrt{\frac{2\sigma^2\cos^2\phi}{\pi}\left(\frac{\alpha^2\sigma^2\cos^2\phi}{1+\alpha^2\sigma^2\cos^2\phi}\right)}\exp\left\{-\frac{\alpha^2}{2(1+\alpha^2\sigma^2\cos^2\phi)}\right\}d\phi \tag{11a}$$

$$\overline{\xi_{1i}^2} = \frac{1}{2\pi}\int_0^{2\pi}\sqrt{\frac{8}{\pi}}\sigma^4\cos^4\phi\left(\frac{\alpha^2}{1+\alpha^2\sigma^2\cos^2\phi}\right)^{3/2}\exp\left\{-\frac{\alpha^2}{2(1+\alpha^2\sigma^2\cos^2\phi)}\right\}d\phi$$

$$+ \frac{1}{2\pi}\int_0^{2\pi}(4\sigma^2\cos^2\phi)Q\left(\frac{\alpha}{\sqrt{1+\alpha^2\sigma^2\cos^2\phi}}\right)d\phi \tag{11b}$$

$$\overline{\xi_{1i}\xi_{1j}} = \left(\frac{1}{2\pi}\right)^2\int_0^{2\pi}\int_0^{2\pi}\frac{2}{\pi}\frac{\sigma^4\cos^2\phi_1\cos^2\phi_2\sqrt{B_1B_2}}{\sqrt{1+\sigma^2\cos^2(\phi_1-\phi_2)(B_1+B_2)}}$$

$$\times \exp\left\{-\frac{1}{2}\left[\frac{B_1+B_2}{1+\sigma^2\cos^2(\phi_1-\phi_2)(B_1+B_2)}\right]\right\}d\phi_1 d\phi_2 \tag{11c}$$

where

$$B_i = \frac{\alpha'^2}{1+\alpha'^2\sigma^2\cos^2\phi_i}; \quad i = 1,2$$

with

$$\alpha \triangleq \sqrt{\frac{2(E_b/N_0)_R}{1 + ((M-2)/\eta)\,(E_b/N_0)_R}}$$

$$\alpha' \triangleq \sqrt{\frac{2(E_b/N_0)_R}{1 + ((M-3)/\eta)\,(E_b/N_0)_R}} \tag{12}$$

$$\sigma^2 = \frac{1}{\eta} = \frac{T_c}{T_b}$$

where $(E_b/N_0)_R$ denotes the *required* bit energy-to-noise spectral density ratio for M users communicating simultaneously, each of which operates at an average bit error rate $P_b(E)$.

It is common in analyses of CDMA systems [5] to define a degradation factor (loss), D, as the ratio (in dB) of the E_b/N_0 required to achieve a given bit error rate in the presence of M users, namely, $(E_b/N_0)_R$, to that which would be required to achieve the same level of performance if only a single user were communicating, namely, $(E_b/N_0)_1$. By the definition of $(E_b/N_0)_1$, we have

$$P_b(E) = Q\left(\sqrt{2(E_B/N_0)_1}\right) \tag{13}$$

To obtain the degradation factor for a given value of $P_b(E)$, we substitute $D(E_b/N_0)_1 = D \times \left[(1/2)[Q^{-1}(P_b(E))]^2\right]$ for $(E_b/N_0)_R$ in Eq. (12), which in turn is substituted in Eq. (11). Then, using the given value of $P_b(E)$, one can solve for D. Unfortunately, a closed-form expression for D cannot be obtained, so the results will be obtained numerically. Before presenting these numerical results, however, we briefly review the analogous results for conventional CDMA and the successive (serial) interference-cancellation scheme proposed by Viterbi [3] (later patented by Dent [6]), since we shall use these as a basis of comparison to demonstrate the increased effectiveness of parallel cancellation.

1. Comparison With Conventional CDMA and Successive Interference Cancellation. In a conventional CDMA system, there is no attempt made to cancel the other user interference. Hence, $(E_b/N_0)_1$ is given by

$$\left(\frac{E_b}{N_0'}\right)_1 = \frac{(E_b)_R}{N_0 + (M-1)ST_c} = \frac{(E_b/N_0)_R}{1 + (M-1)\eta^{-1}(E_b/N_0)_R} \tag{14}$$

Thus, the degradation factor, D, is [5]

$$D = \frac{(E_b/N_0)_R}{(E_b/N_0)_1} = \frac{1}{1 - (M-1)\eta^{-1}(E_b/N_0)_1} \tag{15}$$

For the successive cancellation scheme [3], Viterbi showed that to guarantee that each user in the system sees the same amount of interference from the other users, the user powers should be assigned as

$$S_k = S_1\left(1 + \frac{S_1 T_b}{N_0}\eta^{-1}\right)^{k-1}, \quad k = M, M-1, \cdots, 2 \tag{16}$$

where S_1 is the power of the user to be processed last (the weakest one) and S_M is the power of the user to be processed first (the strongest one). Distributing the powers as in Eq. (16) ideally guarantees that all users see the same ratio of signal power to effective noise spectral density and, thus, the user to be processed first (the one that sees all the user interference) is not at any SNR disadvantage relative to the user to be processed last (the one for which all interference has been removed). In view of the above, the degradation factor for the kth user is given by

$$D_k = \frac{(E_b/N_0)_{R_k}}{(E_b/N_0)_1} = \frac{S_k}{S_1} = \left(1 + \eta^{-1}(E_b/N_0)_1\right)^{k-1} \tag{17}$$

where $(E_b/N_0)_{R_k}$ denotes the required bit energy-to-noise spectral density ratio for the kth user. The *average* degradation factor, D, for the M user system is obtained by averaging Eq. (17) over k, which yields

$$D = \frac{1}{M}\sum_{k=1}^{M} D_k = \frac{\left(1 + \eta^{-1}(E_b/N_0)_1\right)^M - 1}{M\eta^{-1}(E_b/N_0)_1} \tag{18}$$

It should be emphasized that the result in Eq. (18) ignores the effect of decision errors made at the various successive interference-cancellation stages; that is, the interference cancellation is assumed perfect. As a result, numerical results derived from Eq. (18) will be optimistic when compared to the actual performance of the scheme.

2. Numerical Results. To illustrate the significant performance advantage of the parallel interference-cancellation scheme in Fig. 1, we consider a plot of D versus M for an average bit error probability,[8] $P_b(E) = 10^{-2}$, and a spreading ratio, $\eta = 100$. Figure 2 shows the analytical performance of the three schemes (conventional, successive interference cancellation, and parallel interference cancellation) as well as computer simulation results for the latter. We see that for the conventional and parallel interference-cancellation schemes there exists a user capacity limit in that regardless of how much one is willing to increase $(E_b/N_0)_R$ (for a given $(E_b/N_0)_1$, or equivalently, a given $P_b(E)$), the required bit error rate cannot be achieved if more than M_{max} users simultaneously access the system. For conventional CDMA,

$$M_{max} = 1 + \frac{\eta}{(E_b/N_0)_1} = 1 + \frac{\eta}{(1/2)[Q^{-1}(P_b(E))]^2} \tag{19}$$

whereas for the parallel interference-cancellation scheme, the solution is determined from

$$10^{-2} = Q\left(\frac{1 - (M_{max} - 1)\overline{\xi_{1i}}}{\sqrt{(M_{max} - 1)\left[\overline{\xi_{1i}^2} - (M_{max} - 1)\left(\overline{\xi_{1i}}\right)^2 + (M_{max} - 2)\overline{\xi_{1i}\xi_{1j}}\right]}}\right) \tag{20}$$

together with the moments in Eq. (11), where now

$$\alpha \triangleq \sqrt{\frac{2}{\eta^{-1}(M_{max} - 2)}}, \quad \alpha' \triangleq \sqrt{\frac{2}{\eta^{-1}(M_{max} - 3)}} \tag{21}$$

---

[8] The value of $P_b(E) = 10^{-2}$ is chosen to allow for obtaining computer simulation results in a reasonable amount of time.
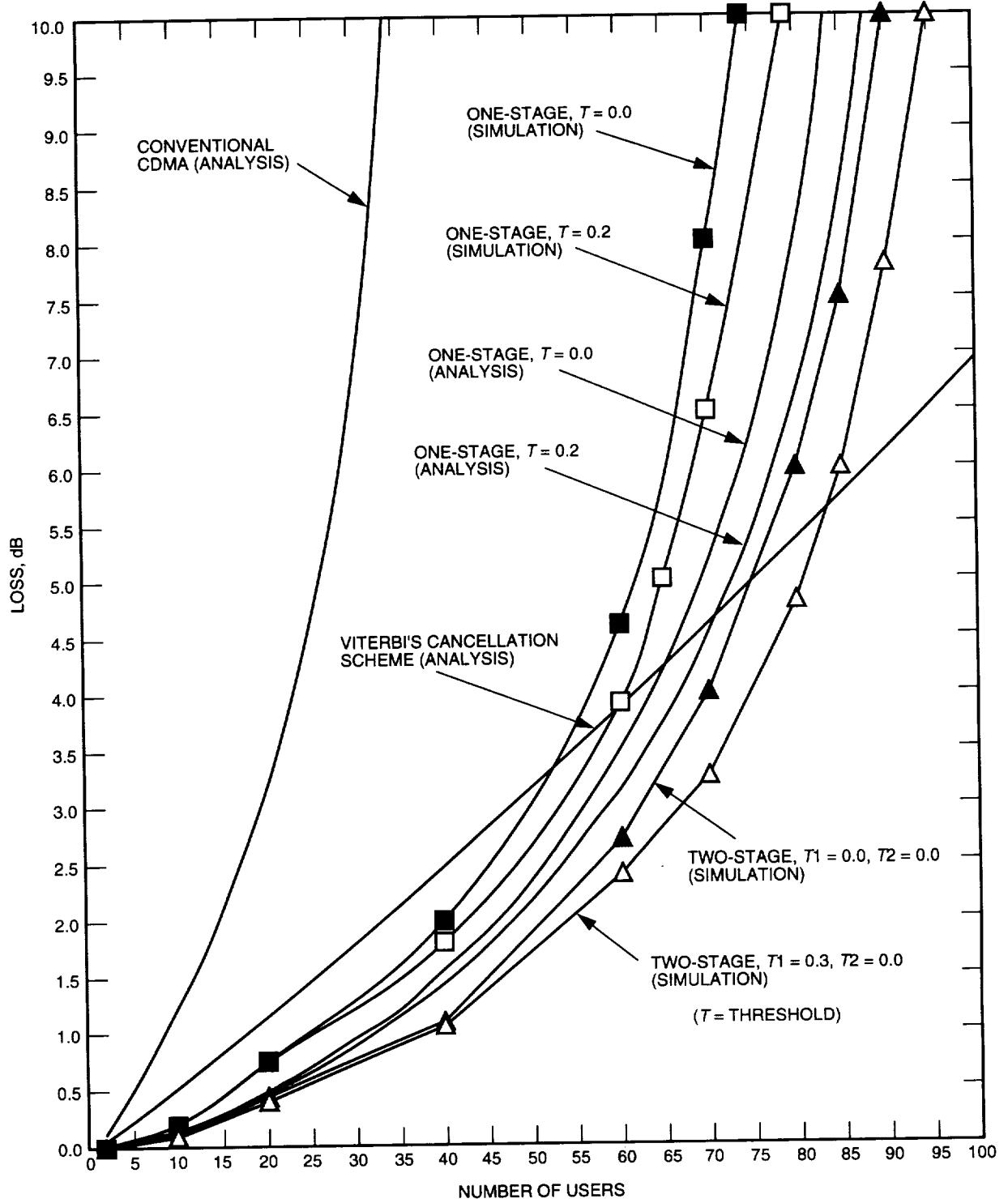
Fig. 2. Performance of interference cancellation schemes with equal power users (Viterbi's scheme with unequal power users is also shown).

It is emphasized that the user capacity limit for the parallel interference-cancellation scheme comes about entirely because of the finite probability of error associated with the tentative decisions. From Fig. 2, it appears that the successive interference cancellation does not have a user capacity limit. This is because in [3] it was assumed for this scheme that the interference cancellation is perfect, i.e., the effect of decision errors at the various interference-cancellation stages was not accounted for.

Comparing the analytical and simulation results for the parallel interference-cancellation scheme, we observe that the analytical results are somewhat optimistic. The discrepancy between the two stems from the assumption of an analytical Gaussian model for the total residual user interference in Eq. (3), whereas the computer simulation makes no such assumption and, thus, predicts the exact performance.

B. Tentative Hard Decisions—Unequal Power, Synchronous Users

The results of the previous section can be generalized to the case where the users have unequal powers, i.e., $S_i; i = 1, 2, \cdots, M$. Let $\alpha_{ij} = S_i/S_j$ denote the ratio of the power of the ith user to that of the jth user, who is arbitrarily considered to be the desired user. After interference cancellation, the normalized output of the I&D corresponding to the $final$ decisions of user j is, by analogy with Eq. (3),

$$
x_{1j} = a_{0j}\sqrt{E_{bj}} + n_j e^{-j\phi_j} + \overbrace{\sum_{\substack{i=1 \\ i \neq j}}^{M} \sqrt{E_{bi}}\beta_i \gamma_{ji} e^{j(\phi_i - \phi_j)}}^{I_j}
$$

$$
= a_{0j}\sqrt{E_{bj}} + n_j e^{-j\phi_j} + \sqrt{E_{bj}} \overbrace{\sum_{\substack{i=1 \\ i \neq j}}^{M} \sqrt{\alpha_{ij}}\beta_i \gamma_{ji} e^{j(\phi_i - \phi_j)}}^{I_j} \tag{22}
$$

where $n_j = (1/\sqrt{T_b}) \int_0^{T_b} n(t) PN_j(t) dt, j = 1, 2, \cdots, M$ is a zero-mean complex Gaussian random variable with variance N_0 representing the thermal noise of the jth user; $\gamma_{ji} \triangleq (1/T_b) \int_0^{T_b} PN_j(t) PN_i(t) dt, i \neq j$ are the normalized interference noises of the other $M - 1$ users as seen by user j (γ_{ji} has variance η^{-1}; see Footnote 6), and $E_{bi} \triangleq S_i T_b$ is the bit energy of the ith user. Also, analogous to Eq. (4), β_i is now defined by

$$
\beta_i = a_{0i} - \text{sgn}\left[Re\left\{ \sqrt{E_{bi}} \left(a_{0i} + \sum_{\substack{m=1 \\ m \neq i}}^{M} \sqrt{\alpha_{mi}} a_{0m} \gamma_{im} e^{j(\phi_m - \phi_i)} \right) + n_i e^{-j\phi_i} \right\} \right] \tag{23}
$$

Following steps analogous to Eqs. (5) through (7), we arrive at the desired result for the bit error probability of the desired (the jth) user, namely,

$$
P_{bj}(E) = Q\left(\sqrt{\frac{2E_{bj}}{N_0}} \Lambda_j \right) \tag{24}
$$

where (for $a_{0j} = -1$),

$$\Lambda_j \stackrel{\Delta}{=} \frac{\left(1 - \sum\limits_{\substack{i=1 \\ i \neq j}}^{M} \sqrt{\alpha_{ij}}\, \overline{\xi_{ji}}\right)^2}{1 + 2(E_{bj}/N_0)\left[\sum\limits_{\substack{i=1 \\ i \neq j}}^{M} \alpha_{ij}\, \overline{\xi_{ji}^2} - \left(\sum\limits_{\substack{i=1 \\ i \neq j}}^{M} \sqrt{\alpha_{ij}}\, \overline{\xi_{ji}}\right)^2 + \sum\limits_{\substack{i=1 \\ i \neq j}}^{M} \sum\limits_{\substack{m=1 \\ m \neq j,i}}^{M} \sqrt{\alpha_{ij}\alpha_{mj}}\, \overline{\xi_{ji}\xi_{jm}}\right]}; \quad \xi_{ji} \stackrel{\Delta}{=} \beta_i \gamma_{ji} \cos(\phi_i - \phi_j)$$

$$(25)$$

As an example, consider a group of M users with powers exponentially distributed (linearly distributed on a dB scale) over a range of 10 dB between the minimum and the maximum. This model might correspond to a distribution of users that are exponentially distant from the base station within a cell. Assume that we fix the error probability of the *lowest power user* (assumed to be user 1 for convenience of notation) equal to 10^{-2} (all others would then obviously have a lower error probability). Then, Fig. 3 illustrates the degradation factor, D_1, of user 1 versus M. For comparison, the results corresponding to conventional CDMA with the same user power distribution are also shown in this figure. By comparing Fig. 3 with Fig. 2, we observe that in the unequal power case, parallel interference cancellation offers more of an advantage over conventional CDMA. The reason behind this observation is that the larger power of the other users (which are producing the user interference to user 1) produces tentative decisions with a smaller error probability, which in turn results in a better degree of cancellation with regard to the final decisions.

III. Parallel Interference Cancellation Using Null Zone Tentative Decisions

Much like the idea of including erasures in conventional data detection to eliminate the need for making decisions when the SNR is low, one can employ a null zone hard-decision device [see Eq. (27)] for the tentative decisions to further improve the fidelity of the interference-cancellation process. The idea here is that when a given user's signal-to-interference ratio is low, it is better not to attempt to cancel the interference from that user than to erroneously detect his data bit and, thus, enhance his interference. Following the development in Section II.A for a single-stage scheme with equal-power synchronous users, then the normalized output of the I&D corresponding to the final decision on user 1's bit a_{01} is still given by Eq. (3), with β_i now defined by

$$\beta_i = a_{0i} - \text{nsgn}\left[Re\left\{\sqrt{E_b}\left(a_{0i} + \sum\limits_{\substack{m=1 \\ m \neq i}}^{M} a_{0m}\gamma_{im}e^{j(\phi_m - \phi_i)}\right) + n_i e^{-j\phi_i}\right\}\right] \qquad (26)$$

where "nsgn" denotes the null zone signum function defined by

$$\text{nsgn } x = \begin{cases} 1, & x > \zeta \\ 0, & -\zeta \leq x \leq \zeta \\ -1, & x < -\zeta \end{cases} \qquad (27)$$

Here β_i takes on possible values $(0, \pm 1, \pm 2)$, and its magnitude is an indicator of whether a correct decision is made (ith user's interference is perfectly cancelled), no decision is made (ith user's interference is unaltered), or an incorrect decision is made (ith user's interference is enhanced). Once again, a Gaussian assumption is made on the total residual interference; then, since the final decisions are still made as hard decisions, the average bit error probability is still given by Eq. (8) together with Eq. (9), with the statistical moments of ξ_{1i} now given by
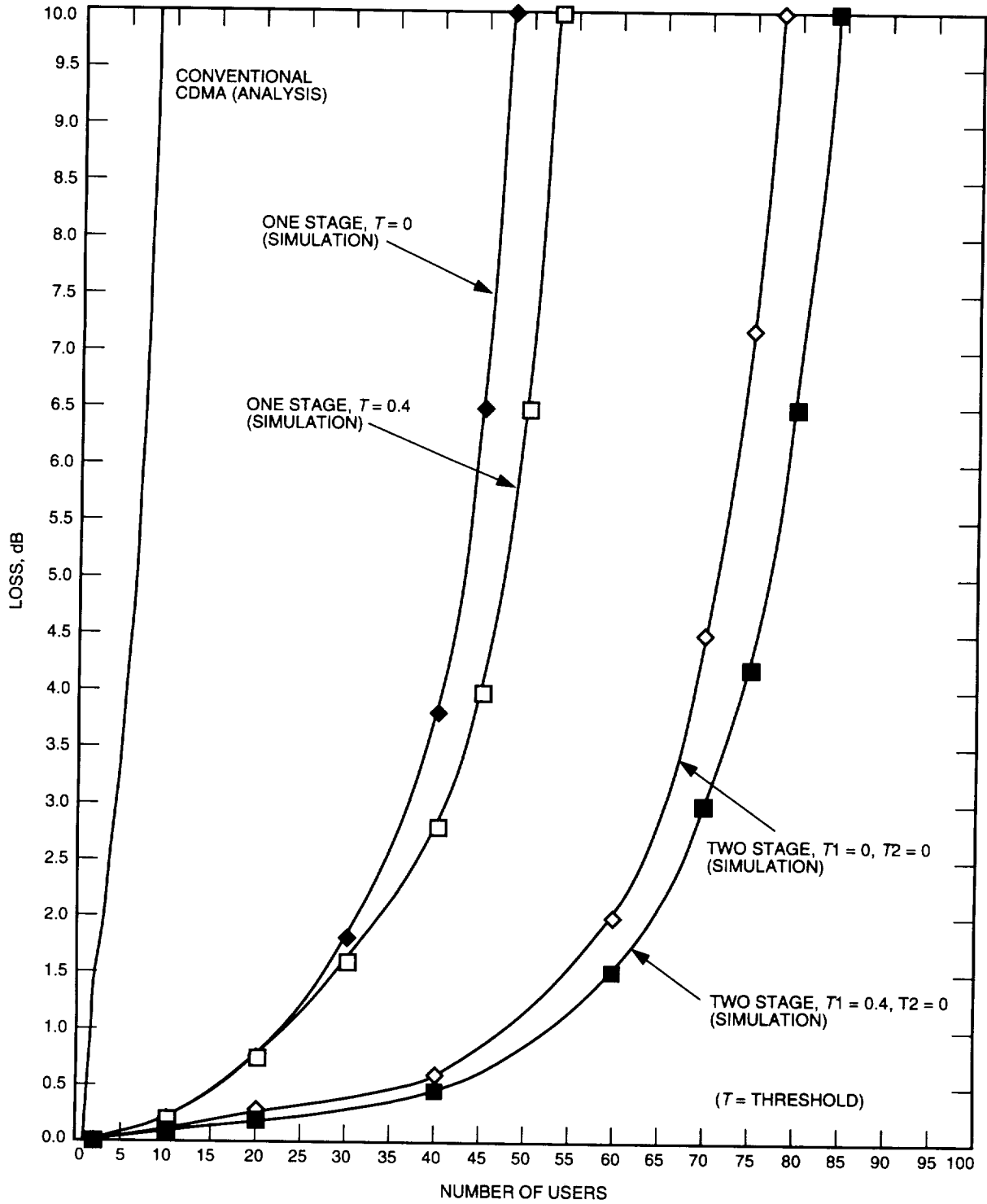
Fig. 3. Performance of interference cancellation schemes with unequal power users.

$$\overline{\xi_{1i}} = \frac{1}{2\pi} \int\limits_0^{2\pi} \sqrt{\frac{\sigma^2 \cos^2 \phi}{2\pi} \left(\frac{\alpha^2 \sigma^2 \cos^2 \phi}{1 + \alpha^2 \sigma^2 \cos^2 \phi} \right)}$$

$$\times \left[\exp\left\{ -\frac{\alpha^2(1 + \zeta')^2}{2(1 + \alpha^2 \sigma^2 \cos^2 \phi)} \right\} + \exp\left\{ -\frac{\alpha^2(1 - \zeta')^2}{2(1 + \alpha^2 \sigma^2 \cos^2 \phi)} \right\} \right] d\phi \qquad (28a)$$

$$\overline{\xi_{1i}^2} = \frac{1}{2\pi} \int\limits_0^{2\pi} \sqrt{\frac{1}{2\pi}} \sigma^4 \cos^4 \phi \left(\frac{\alpha^2}{1 + \alpha^2 \sigma^2 \cos^2 \phi} \right)^{3/2}$$

$$\times \left[3(1 + \zeta') \exp\left\{ -\frac{\alpha^2(1 + \zeta')^2}{2(1 + \alpha^2 \sigma^2 \cos^2 \phi)} \right\} + (1 - \zeta') \exp\left\{ -\frac{\alpha^2(1 - \zeta')^2}{2(1 + \alpha^2 \sigma^2 \cos^2 \phi)} \right\} \right] d\phi$$

$$+ \frac{1}{2\pi} \int\limits_0^{2\pi} (\sigma^2 \cos^2 \phi) \left[3Q\left(\frac{\alpha(1 + \zeta')}{\sqrt{1 + \alpha^2 \sigma^2 \cos^2 \phi}} \right) + Q\left(\frac{\alpha(1 - \zeta')}{\sqrt{1 + \alpha^2 \sigma^2 \cos^2 \phi}} \right) \right] d\phi \qquad (28b)$$

$$\overline{\xi_{1i}\xi_{1j}} = \left(\frac{1}{2\pi} \right)^2 \int\limits_0^{2\pi} \int\limits_0^{2\pi} \frac{1}{2\pi} \frac{\sigma^4 \cos^2 \phi_1 \cos^2 \phi_2 \sqrt{B_1 B_2}}{\sqrt{1 + \sigma^2 \cos^2(\phi_1 - \phi_2)(B_1 + B_2)}}$$

$$\times \left[\exp\left\{ -\frac{1}{2} \left[\frac{(B_1 + B_2)(1 + \zeta')^2}{1 + \sigma^2 \cos^2(\phi_1 - \phi_2)(B_1 + B_2)} \right] \right\} \right.$$

$$+ \exp\left\{ -\frac{1}{2} \left[\frac{4\zeta'^2 B_1 B_2 \cos^2(\phi_1 - \phi_2) + (1 + \zeta')^2 B_1 + (1 - \zeta')^2 B_2}{1 + \sigma^2 \cos^2(\phi_1 - \phi_2)(B_1 + B_2)} \right] \right\}$$

$$\left. + \exp\left\{ -\frac{1}{2} \left[\frac{4\zeta'^2 B_1 B_2 \cos^2(\phi_1 - \phi_2) + (1 - \zeta')^2 B_1 + (1 + \zeta')^2 B_2}{1 + \sigma^2 \cos^2(\phi_1 - \phi_2)(B_1 + B_2)} \right] \right\} \right] d\phi_1 d\phi_2 \qquad (28c)$$

where

$$B_i = \frac{\alpha'^2}{1 + \alpha'^2 \sigma^2 \cos^2 \phi_i}; \quad i = 1, 2$$

and $\zeta' = \zeta/\sqrt{E_b}$ is the normalized decision threshold that should be chosen to minimize D for a given $P_b(E)$ and $(E_b/N_0)_1$ determined from Eq. (13). Superimposed on the performance results for the hard limiter previously given in Fig. 2 are the results for the null zone limiter. For the specified processing gain and average bit error probability, we see that using a null zone limiter allows the maximum number of users that can be supported to be increased by about 10 percent. For convenience, the normalized threshold has been fixed at $\zeta' = 0.2$. For an unequal (exponentially distributed) power distribution among the users, the corresponding results using null zone tentative decisions are superimposed on those previously discussed in Fig. 3. For convenience, the normalized threshold has been fixed at $\zeta' = 0.4$. Here again we see a modest improvement in performance.

IV. Multiple-Stage Interference Cancellation

The single-stage scheme of Fig. 1 can be improved upon by cascading multiple stages of parallel interference cancellation. The idea here is to repeatedly improve the fidelity of the M tentative decisions since each successive stage sees less and less interference. Note that in principle this idea is similar to what Viterbi accomplishes in the serial interference-cancellation scheme except that here at each stage we simultaneously act on the interference from the most reliable users rather than one user at a time. An analysis of the performance of such a multistage scheme is difficult if not impossible to obtain due to the fact that the tentative decisions at the ith interference-cancellation stage depend on the tentative decisions at the $(i - 1)$st stage. Because of this difficulty, numerical results for the performance of the multistage parallel interference scheme will be obtained from computer simulation. Illustrated in Figs. 2 and 3 are performance results for a two-stage parallel interference canceller with hard and null zone[9] tentative decisions, respectively. We observe that there is significant gain to be achieved by going to more than one stage.

V. Conclusions

A parallel interference-cancellation scheme was proposed that uses tentative decision devices with different optimum thresholds at the multiple stages to produce the most reliably received data for generation and cancellation of user interference. The one-stage interference cancellation was analyzed for two types of tentative decision devices, namely, hard and null zone decision. Simulation results are given for one- and two-stage interference cancellation for equal as well as unequal power users. The results indicate that, by using multiple stages with optimum thresholds at each stage, performance can be significantly improved relative to conventional CDMA. Although linear tentative decisions can be used, the performance of such a scheme is inferior to one with nonlinear tentative decisions, as our simulations have shown. However, this scheme with noncoherent detection does not require amplitude and phase estimation.

References

[1] S. Verdu, "Minimum Probability of Error for Asynchronous Gaussian Multiple-Access Channels," *IEEE Transactions on Information Theory*, vol. IT-32, no. 1, pp. 85–96, January 1986.

[2] M. K. Varanasi and B. Aazhang, "Multistage Detection in Asynchronous Code-Division Multiple-Access Communications," *IEEE Transactions on Communications*, vol. 38, no. 4, pp. 509–519, April 1990.

[3] A. J. Viterbi, "Very Low Rate Convolutional Codes for Maximum Theoretical Performance of Spread-Spectrum Multiple-Access Channels," *IEEE Transactions on Selected Areas in Communications*, vol. 8, no. 4, pp. 641–649, May 1990.

[4] Y. C. Yoon, R. Kohno, and H. Imai, "A Spread-Spectrum Multiaccess System With Cochannel Interference Cancellation," *IEEE Journal on Selected Areas in Communications*, vol. 11, no. 7, pp. 1067–1075, September 1993.

[5] C. L. Weber, G. K. Huth, and B. H. Batson, "Performance Considerations of Code Division Multiple-Access Systems," *IEEE Transactions on Vehicular Technology*, vol. VT-30, no. 1, pp. 3–10, February 1981.

[6] P. W. Dent, *CDMA Subtractive Demodulation*, U.S. Patent 5,218,619, Washington, D.C., June 8, 1993.

---

[9] In the null zone results of Fig. 2, the normalized threshold in the first stage has been fixed at $\xi' = 0.3$ and, in the second stage, it has been set equal to 0, i.e., a hard-limited tentative decision.

Combining Image-Processing and Image Compression Schemes

H. Greenspan[1] and M.-C. Lee[2]
Communications Systems Research Section

An investigation into the combining of image-processing schemes, specifically an image enhancement scheme, with existing compression schemes is discussed. Results are presented on the pyramid coding scheme, the subband coding scheme, and progressive transmission. Encouraging results are demonstrated for the combination of image enhancement and pyramid image coding schemes, especially at low bit rates. Adding the enhancement scheme to progressive image transmission allows enhanced visual perception at low resolutions. In addition, further processing of the transmitted images, such as edge detection schemes, can gain from the added image resolution via the enhancement.

I. Introduction

There is a new trend developing in the image-processing and image compression fields that has to do with the convergence of the two fields. This convergence has now become known as "second generation" image coding. It is the result of a growing need to handle large amounts of image data either in transmission or in automated image handling—such as image database query and retrieval—while the classical compression schemes are reaching their limits. It is now accepted that, in order to achieve more advanced compression schemes, we need to use our knowledge about images and their characteristic behavior to advantage in compression.

In this article, we present an initial attempt to combine an image-processing scheme, specifically, an image enhancement scheme, with existing image compression schemes. At the image-processing end, we use our knowledge about the behavior of edges across scale (across different resolutions) in order to extrapolate in scale and increase the resolution of a blurred input image. The ability to extrapolate in scale is very useful for compression. We can envision data rate savings by not transmitting at certain frequencies and trying to reconstruct the information back at the receiver's end; we can think about combining image processing with existing image compression schemes, such as the subband coding (SBC) and pyramid schemes, to achieve additional savings; and, finally, we can use this ability in progressive transmission applications, whereby the lower resolution images get enhanced and, thus, information can be extracted at earlier stages of the transmission.

These are some of the issues that we investigate in this article. In Section II, we describe the pyramid compression schemes, specifically a variation on the Burt and Adelson scheme [1], and we investigate its

---

[1] Currently at the California Institute of Technology, Pasadena, California.

[2] Currently with Microsoft Corporation, Redmond, Washington.

combination with image enhancement. Section III follows similar steps in relation to the SBC compression scheme. Finally, in Section IV, the combination with progressive transmission for savings in analysis time is described.

II. Combining Image Processing With Pyramid Compression Schemes

A. The Pyramid Representation

The pyramid scheme codes an input image in a multiresolution representation via the generation of subimages of various scales, as shown in Fig. 1. Here, $\boxed{M_{x_k} \downarrow M_{y_l}}$ denotes subsampling by M_{x_k} and M_{y_l} in the x and y directions, respectively. Low-resolution subimages G_k are created by passing G_{k-1} through a low-pass filter, H, and the decimation box. In the encoder [Fig. 1(a)], we transmit subimages $\{L_0, L_1, \cdots, L_K, G_{K+1}\}$ obtained by

$$
\begin{aligned}
L_0 &= G_0 - G_{1i} \\
L_1 &= G_1 - G_{2i} \\
&\cdots \\
L_K &= G_K - G_{(K+1)i} \\
G_{K+1}
\end{aligned}
\tag{1}
$$

where L_k is the difference subimage at the kth level, G_k is the low-resolution subimage of the kth level, and G_{ki} is the interpolated version of G_k (using filter F). In the decoding part [Fig. 1(b)], we reverse Eq. (1) to get the original signal, G_0. The pyramid representation has been introduced in the literature for coding purposes, as it was shown to be a complete representation [1]. Perfect reconstruction is guaranteed if there is no quantization of the transmitted data, regardless of the choice of filters H and F.

B. Compression Via the Pyramid Representation

The pyramid structure can be used for compression purposes. Using the pyramid coding scheme, we decompose the original image into several subimages, with different sizes, and then apply different quantization and encoding strategies in the different subimages, depending on the signal characteristics. For example, in a linear (e.g., Laplacian) pyramid, the signal variance in different subimages tends to be different. Usually, lower-frequency subimages have higher variance. Therefore, we would allocate a different number of bits to the subimages (more bits per pixel for higher variance subimages).

There are several points to be made about compression via the pyramid scheme:

(1) As stated, this is an oversampled system. This means that the number of output pixels at the transmitter is greater than that of the original image. Specifically, if the original size is $N \times N$ and the decimation box is $\boxed{2 \downarrow 2}$ in every level (K levels overall), then the total number of output pixels is

$$
\mathcal{N} = \sum_{i=0}^{K} \frac{N}{2^i} \times \frac{N}{2^i}
\tag{2}
$$

Compared to subband and transform coding, which are critically sampled systems, it seems that the compression ratios we can obtain using this structure are lower because we have to transmit more data. However, due to the following two properties, this is not always the case.
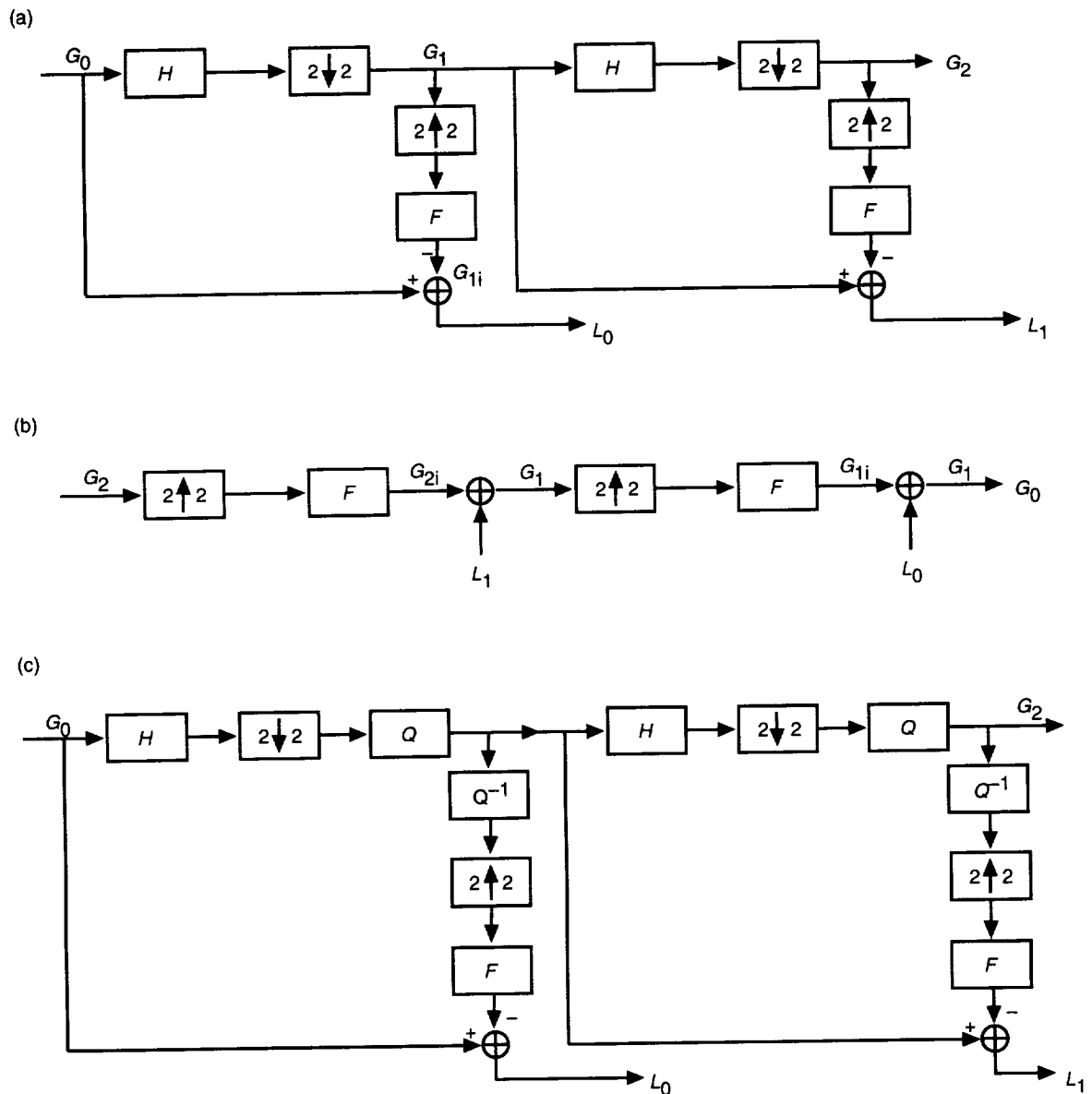
Fig. 1. Pyramid scheme: (a) encoding, (b) decoding, and (c) new concepts.

(2) No matter how we design the decimation filter H and the interpolation filter F (see Fig. 1), we can always obtain perfect reconstruction. Therefore, we can incorporate desired filters for H and F such that the signal characteristics in every level are better suited for compression. This provides great flexibility. For example, we can apply a very long filter or a nonlinear filter for image compression or include a motion-compensated filter for video compression. This implies that we can take advantage of some nonlinear characteristics of images to help the compression. Compared to subband and transform coding, which have a lot of constraints on designing perfect-reconstruction systems, we can get many advantages here.

(3) In tree-structured subband coding, the quantization noise of the higher level will propagate to the lower level. This is not desirable, because it is hard to describe the quantization noise behavior if we pass it through too many stages of filters. Especially when the quantization stepsize is large or the quantization noise is high, the noise behavior cannot be modeled using a simple expression. Therefore, some strange effects become apparent. However, in the Laplacian case, we can modify the structure to avoid this problem. As shown in Fig. 1(c), we can interpolate the quantized low-passed and decimated signals, and then take the difference. The advantage is that we now have exactly the same-difference subimages as in the receiving end. Therefore, if we quantize these subimages, the quantization noise will not propagate. Overall, it is much easier to control the noise behavior.

C. Gaussian and Laplacian Pyramids

In this article, we mainly concentrate on Gaussian and Laplacian pyramids, as described by Burt and Adelson, commonly referred to as the "Burt pyramid" [1], and Anderson, known as the "filter subtract decimate (FSD) pyramid" [2]. The Gaussian pyramid consists of low-pass filtered (LPF) versions of the input image, with each stage of the pyramid computed by low-pass filtering of the previous stage and corresponding subsampling of the filtered output. The Laplacian pyramid consists of bandpass filtered (BPF) versions of the input image, with each stage of the pyramid constructed by the subtraction of two corresponding adjacent levels of the Gaussian pyramid. The Burt and Anderson Laplacian pyramids differ in the details of when the subsampling step is applied and have slightly different bandpass characteristics. The Burt pyramid follows Fig. 1 exactly, whereas the Anderson pyramid, as defined in Eq. (3), is a variation leading to more computational efficiency. In the following, we refer to the input image as G_0; the LPF versions are labeled G_1 through G_{K+1} with decreasing resolutions, and the corresponding difference images are labeled L_0 through L_K, respectively. A recursive procedure allows for the creation of the Anderson pyramid, as follows:

$$G_{n+1}^0 = W * G_n$$
$$L_n = G_n - G_{n+1}^0$$
$$G_{n+1} = \text{Subsampled } G_{n+1}^0 \tag{3}$$

where G_n is termed the nth-level Gaussian image and L_n is termed the nth-level Laplacian image. Generally, the weighting function, W, is Gaussian in shape and normalized to have the sum of its coefficients equal to 1. The values used for the LPF, which is a 5-sample separable filter, are (1/16, 1/4, 3/8, 1/4, 1/16). Figure 2 presents an example of a Laplacian pyramid representation.

Fig. 2. Multiscale sequence of edge maps. Presented from left to right are the Laplacian pyramid components L_0, L_1, and L_2, respectively. The pyramid components have been appropriately expanded to match in size.

It has been shown [1] that the Laplacian pyramid forms an overcomplete representation of the image, thus enabling full reconstruction. The reconstruction process entails adding to a given LPF version of the image, G_N, the bandpass images, $L_n(n = N - 1, \cdots, 0)$, thus reconstructing the Gaussian pyramid, level by level, up to the original input image, G_0. This is a recursive process, as in Eq. (4):

$$G_n = L_n + G_{(n+1)i}, \qquad n = N - 1, \cdots, 0 \tag{4}$$

where $G_{(n+1)i}$ is the interpolated version of G_{n+1}.

D. How Does Image Enhancement Come In?

Several things can be noted from the above description of the pyramid representation. First, we note that the Laplacian pyramid consists of the edge maps of the input image at the different resolutions (see Fig. 2). We also note that when coding the image into its Laplacian components, most bits need to be allocated to the L_0 level. The first observation leads us to the idea of combining our knowledge about edge behavior across scale. The second observation allows the combination with compression. Our goal is to learn about the behavior of edges across scale so that we can "predict" the L_0 level of the pyramid using only the lower-resolution edge maps up to L_1.

1. **The Image Enhancement Scheme.** In our image enhancement work [3], we concentrate on the edge representation of an image across different image resolutions. Edges are an important characteristic of images, since they correspond to object boundaries or to changes in surface orientation or material properties. An edge can be characterized by a local peak in the first derivative of the image brightness function or by a zero in the second derivative, the so called zero crossings (ZCs). An ideal edge (a step function) is scale invariant in that no matter how much one increases the resolution, the edge appears the same (i.e., remains a step function). This property provides a means for identifying edges and a method for enhancing real edges.

We concentrate on the edge representation of an image across different image resolutions. For this we view the image in a multiresolution framework via the Gaussian and Laplacian pyramids. The Laplacian pyramid preserves the shape and phase of the edge maps across scale (see Fig. 2).

The application of the Laplacian transform to an ideal edge transition results in a series of self-similar transient structures, as illustrated in Fig. 3(a). An edge of finite resolution would produce a decrease in amplitude of these transients with increasing spatial frequency, with the magnitude of the edge going to zero at frequencies above the Nyquist limit [see Fig. 3(b)]. An edge of finite resolution can be created by starting with a low-resolution Gaussian image and then adding on all the bandpass transient structures. To create an edge with twice the resolution requires the creation of a self-similar transient at the next level, hereby referred to as L_{-1}. The most essential features of these transient structures are that they are of the same sign at the same position in space; hence, their ZCs line up, and they all have roughly the same amplitude. The precise shape of the structures need not necessarily be maintained so long as their scaled spatial frequency responses are similar. The simple procedure described next creates localized transients for L_{-1} that satisfy all these constraints except for the maintenance of constant amplitude. While more complicated procedures could handle the amplitude constraint, it was found that sharpening the stronger value edges produces in itself visually pleasing results.

The pyramid representation can be viewed as a discrete version of the scale-space description of ZC that has been introduced in the literature [4-6]. The scale-space formalism gives the position of the ZC across a continuum of scales. One of the main theorems states that ZCs of an image filtered through a Gaussian filter have nice scaling properties, one of which is that ZCs are not created as the scale increases. If an edge appears at lower resolutions of the image, it will consistently appear as we shift to higher resolutions (see Fig. 3). Although theoretically defined, not much work has yet taken advantage
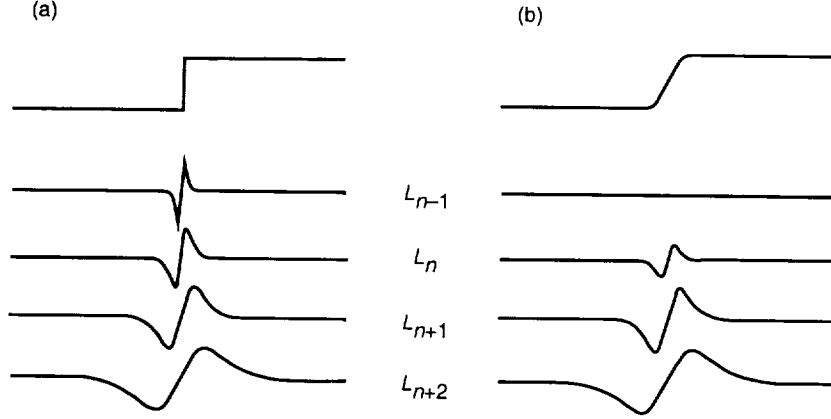
Fig. 3. Laplacian transform on (a) an ideal edge and (b) an edge of finite resolution.

of the image representation across scale. In our work, we utilize the shape invariant properties of edges across scale based on the pyramid representation and in agreement with the consistency characteristic of the scale-space formalism.

The objective is to form the next higher harmonic of the given signal while maintaining phase. Figure 4 illustrates a one-dimensional high-contrast edge scenario. The given input, G_0, is shown in (0) of the figure, together with its pyramid components, L_0 and G_1, shown in (1) and (2), respectively. From the pyramid reconstruction process, we know that adding the high-frequency component L_0 to the G_1 component can sharpen G_1 to produce the input G_0. Ideally, we would like to take this a step further. We would like to predict a higher-frequency component, L_{-1}, preserving the shape and phase of L_0, as shown in (3) of the figure, so that we can use the reconstruction process to produce an even sharper edge, which is closer to the ideal-edge objective, as shown in (4) of Fig. 4. The L_{-1} component cannot be created by a linear operation on the given L_0 component (i.e., the frequency spectrum cannot be augmented using a linear operator). We can, thus, never hope to create a higher-frequency output by a linear enhancement technique.

It remains to show how the L_{-1} component of the pyramid can be generated. We extrapolate to the new resolution by preserving the Laplacian-filtering waveform shape, together with sharpening via a nonlinear operator. The waveform as in (5) of Fig. 4 is the result of clipping the L_0 component, multiplying the resultant waveform by a constant, α, and then removing the low frequencies present (via bandpass filtering) in order to extract a high-frequency response.

Equation (5) formalizes the generation of L_{-1}:

$$L_{-1} = \alpha(C(L_0))$$ (5)

where $C(S)$ is defined as

$$C(S) = \begin{cases} T & \text{if } S > T \\ S & \text{if } -T \leq S \leq T \\ -T & \text{if } S < -T \end{cases}$$

Here, $T = 0.04(G_0)_{max}$.
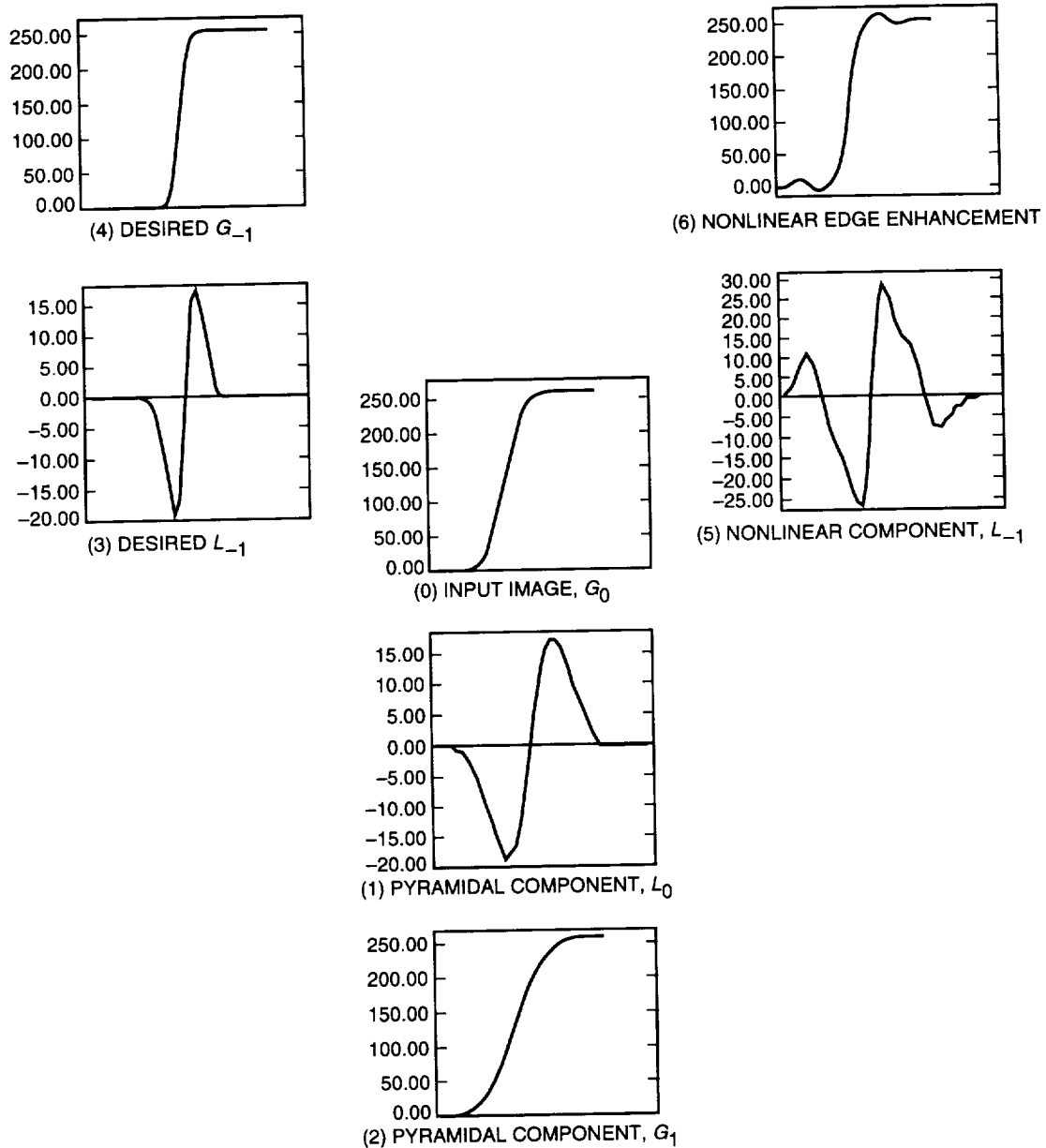
Fig. 4. The one-dimensional ideal-edge scenario.

Generating the new output image entails taking the L_{-1} image as the high-frequency component of the pyramid representation. Based on the reconstruction capability of the pyramid representation [Eq. (4)], the new output is generated next as the sum of the given input, G_0 and L_{-1}, as in Eq. (6):

$$Enhanced\ Image\ = G_{-1} = L_{-1} + G_0 \tag{6}$$

2. Enhancement Results. We next show experimental results that indicate that the enhancement scheme augments the frequency content of an input image, achieving a visually enhanced output.

A rock scene example is displayed in Fig. 5. Figure 5(a) presents the enhancement results; Fig. 5(b) displays the corresponding power spectral characteristics. The blurred input, which can be the result of

(a)

(b)
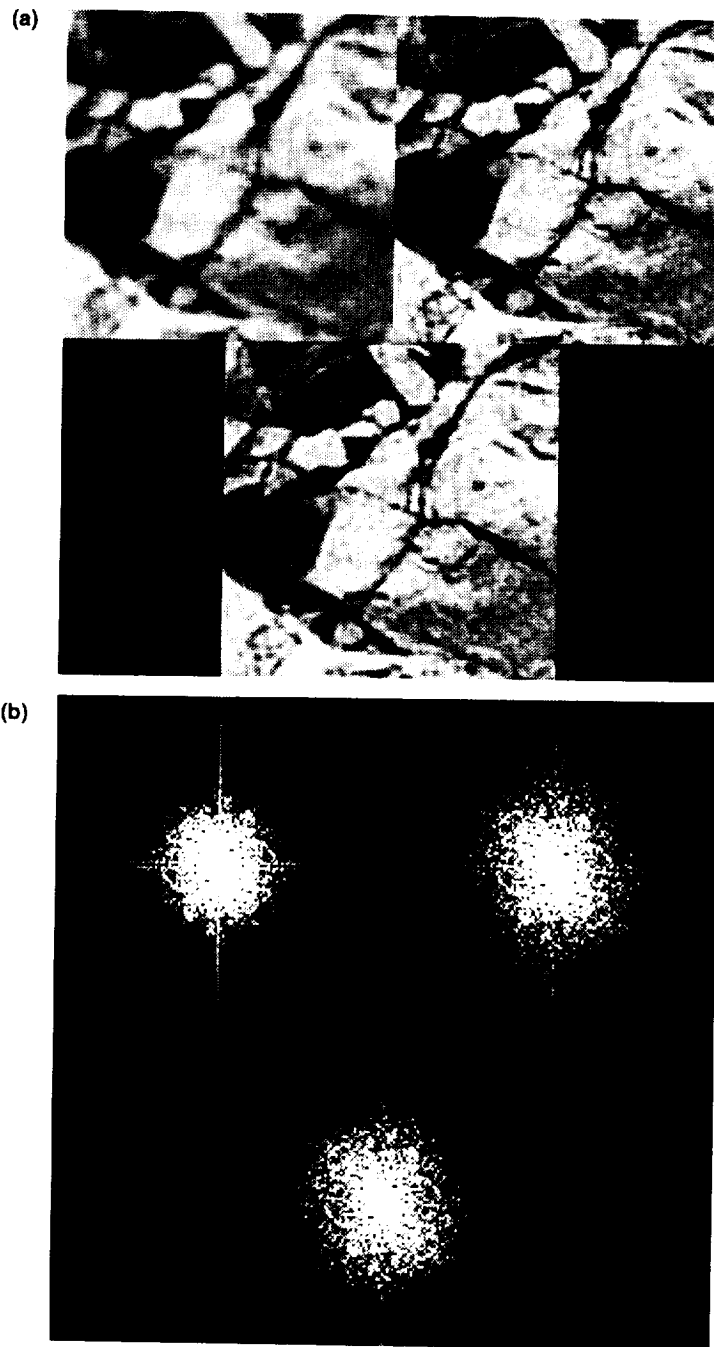
Fig. 5. A rock scene example: (a) enhancement results and (b) corresponding power-spectrum characteristics. In each of the above figures, the blurred input and original image are presented (top left and top right, respectively), followed by the enhanced output (bottom). Both visual perception enhancement and power-spectrum augmentation are evident.

cutting off high frequencies due to bandwidth considerations or a "zoom-in" application, is presented at the top-left corner. The original image, which we are assuming is not available to the system and which we wish to reproduce, is presented at the top right. The result of applying the previously presented algorithm to the blurred input is depicted in the bottom of each figure. We get an overall enhancement

perception. The enhanced image very closely matches the original one, and the power spectrum of the enhanced image is very close to the original power spectrum. For additional enhancement results, the reader is referred to [3,10].

In conclusion, the enhancement scheme addresses the most important features (edges) required in producing enhanced-resolution versions of existing images. The simplicity of the computations involved and ease of implementation enable it to be incorporated into real-time applications.

E. Combining Image Enhancement With Pyramid Coding

In this section, we combine the image enhancement scheme, described above, with the pyramid coding scheme. We have shown the possibility of predicting the L_0 level of the Laplacian pyramid using lower-resolution edge maps. The next step is to code an image with and without the L_0 component and evaluate the corresponding rate-distortion performance, i.e., investigate the compression savings versus the output image results that we can achieve.

We decompose the original image, G_0, into $\{L_0, L_1, L_2, G_3\}$. We scalar quantize L_2, L_1, and L_0 and then compute the entropy of the quantized signals. For G_3, we first apply differential pulse-code modulation (DPCM), then compute the entropy. The average entropy of these subimages represents the rate (bits per pixel). Here we use peak signal-to-noise ratio (PSNR) as the distortion criterion, defined as

$$PSNR = 10 \log_{10} \frac{255^2}{\frac{1}{XY} \sum_{i=1}^{X} \sum_{j=1}^{Y} (I_{ij} - \widehat{I}_{ij})^2} \tag{7}$$

where I_{ij} is the ijth pixel of image I, and X and Y represent the horizontal and vertical size of the input image, respectively.

The Lenna image is used for this coding task. Figure 6 presents the rate-distortion curves for Lenna. We concentrate first on the two pyramid-coding curves. We note that in using the L_0 component we have all pyramid levels and, thus, the reconstruction would be exact apart from the quantization errors induced. Using a *predicted* L_0 (i.e., the actual L_0 component is not being used), we introduce additional noise in the reconstruction process. In general, we note the slow degradation of the rate-distortion curve using the enhancement scheme, as opposed to the almost linear drop of the original (nonenhanced) curve. Of even more interest is that, at very low bit rates, the ability to estimate the L_0 component from the given L_1 component, or the ability to extrapolate in frequency space, allows for *better* PSNR.

An example of two images, with and without the L_0 component (top left and top right, respectively), is shown in Fig. 7, as compared with the original Lenna image (bottom). Both images are coded with approximately 1 bit/pixel. We have 0.99 bit/pixel with $PSNR = 34.77$ dB for the enhanced image and 1.053 bits/pixel with $PSNR = 33.54$ dB for the image decompressed with all its L_i components. In this case, we get a better PSNR and better perceived similarity to the original for the enhanced image with the predicted L_0 component than for the image with *all* components present. This is a very interesting and encouraging result.

Next, we compare the pyramid compression with the discrete cosine transform (DCT) (refer again to Fig. 6). The DCT clearly "wins" the PSNR comparison. We note that, at the very low bit rates, the differences are quite minimal. In addition, we need to compare the actual images, as opposed to the PSNR ratios, as is shown in Fig. 8. We note that the blockiness with the DCT is very evident and possibly more distracting to the eye than the artifacts introduced by the pyramid-plus-enhancement scheme. A zoom-in image taken from Fig. 8 is presented in Fig. 9. In the DCT coding scheme, we can see strong blocking
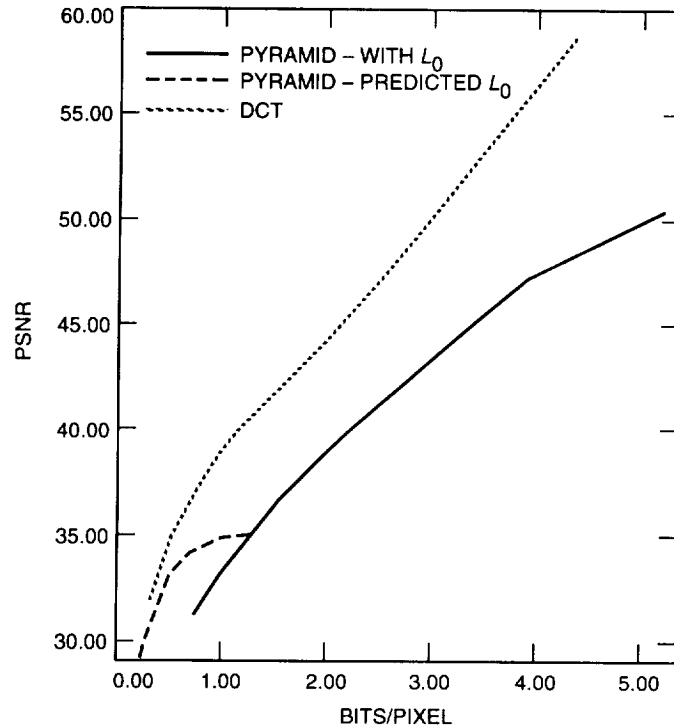
Fig. 6. Rate distortion curves for the Lenna image.

effects in the quantized image (this is the case especially when the bit rate is low or when we zoom the image up). This phenomenon results from the independent quantization of blocks. This reinforces the claim that the PSNR does not in all instances match our visual perception.

A similar investigation is done on a moon image, whose rate distortion curves are shown in Fig. 10. As before, we note the slow degradation of the rate-distortion curve with the enhancement. We see again that, at low bit rates, better PSNR is achieved by *predicting* the L_0 component via the enhancement processing stage. When comparing it with the DCT rate-distortion curve [Fig. 10(b)], we notice that at very low bit rates we actually achieve *better* performance than the DCT.

We conclude this section with a few of the moon images. Figure 11 displays the slow degradation phenomenon. Two images are displayed: The left one has 1.27 bits/pixel with $PSNR = 31.69$ dB, and the right image has almost *half* the bit rate, at 0.65 bit/pixel, with a very similar PSNR value of 31.1 dB. The two images look identical. In Fig. 12, we compare the pyramid scheme (left) to DCT (right) at the low bit rate of 0.47 bit/pixel. The PSNR ratio is larger for the pyramid coding in this case, $PSNR = 30.53$ dB, whereas the DCT case has $PSNR = 30.49$ dB. The blockiness of the DCT is certainly visible here. Note the blocks on the main rocks, which actually degrade the possibility of identifying rock boundaries, etc.

In this section, we have shown encouraging results in combining the image enhancement scheme with pyramid coding. The results are interesting especially at low bit rates. Possible modifications to the pyramid structure can help us in achieving higher compression ratios. Different filters can be applied in the pyramid structure to get better performance. We know that no matter what we put in the decimation and interpolation filters (see Fig. 1), perfect reconstruction is always guaranteed if there is no quantization and transmission loss. This provides great flexibility, since we can design a better filter to achieve better rate-distortion performance however the distortion is defined. For example, we can apply a nonlinear filter to take advantage of the nonlinear features of the human visual system. We can then obtain better

Fig. 7. Comparison of the Lenna image with and without L_0. The top left image includes L_0 in the compression, the top right uses a predicted L_0, and the bottom is the original Lenna image.

image quality with a greater perceptual effect. The use of a median filter has been shown to achieve such an improvement [7]. The combination of the enhancement scheme with modified pyramid coding schemes remains to be investigated.

III. SBC Schemes

A. Introduction

SBC schemes have recently aroused much attention in the areas of image and video compression. There are several advantages to these coding schemes that make the technique attractive. Recently, the Motion

64

Fig. 8. The Lenna image compressed with pyramid scheme plus enhancement (top left) and with DCT (top right). The original image is on the bottom.

Fig. 9. Pyramid (left) versus DCT (right).
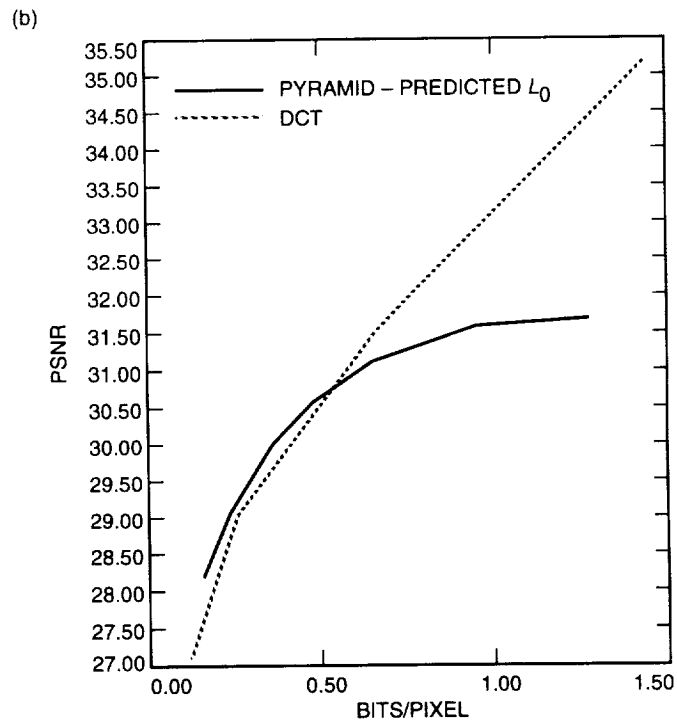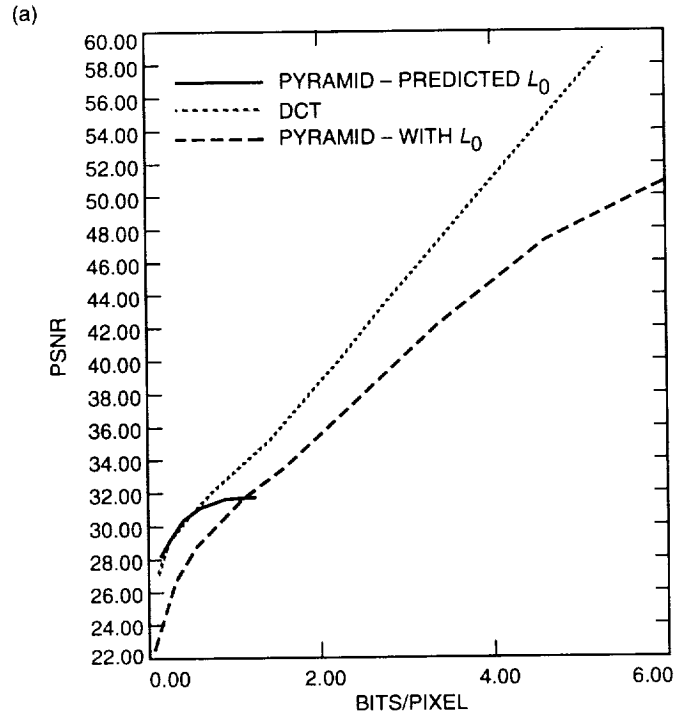
Fig. 10. The Moon image: (a) rate distortion curves
and (b) comparison with DCT—zoom in.

Fig. 11. Slow degradation phenomenon at low bit rates.

Fig. 12. Comparison of pyramid (left) versus DCT (right) at low bit rates.

Pictures Experts Group (MPEG) has proposed using this technique for its audio compression part. It is the belief of many people that SBC may take over DCT as a new image and video compression standard. Generally speaking, the compression capability of SBC is fairly good. Among all the linear multiscale techniques—such as DCT, the Laplacian pyramid, and SBC—it has been shown that SBC can provide the

best compression ratio in the rate-distortion mean-squared-error (MSE) sense, although the computational complexity is typically higher than that of DCT in achieving this. The picture quality generated by this technique is good compared to the annoying blocky effect generated by DCT. One whole frame is processed and quantized at a time as opposed to the block-by-block DCT process. However, there is another kind of distortion based on *aliasing effects* that degrades the picture quality substantially when the compression ratio is high or the bit rate is low. This is due to the signal loss in the subbands, which results in the aliasing cancellation effect provided by the filter bank being lost. This phenomenon gets more visible when the quantization noise is higher. It is generally agreed that the picture quality provided by SBC is better than that of block coding techniques. An additional advantage of SBC is that it is intrinsically progressive. This is achieved by dividing the original images into subimages in different frequency bands. One then sequentially transmits subimages with, usually, increasing frequencies. Progressive transmission is a desired property for many applications, such as data browsing and image frame conversion between different signal formats like high-definition television (HDTV) and standard TV. Although DCT can be implemented progressively, it is not as immediate a process.

The basic principle of SBC is, like other linear techniques, to take advantage of the nonuniform distribution of the signals' power spectrum. It is well known that the power spectrum of image signals tends to be nonuniform. We first use a filter bank (and decimators) to decompose the original image into several subimages in different frequency bands. One then allocates different numbers of bits in different bands depending on the signal variance in that band, thus achieving compression. It can be shown that in the uniform filter bank case, the quantization step size in every band has to be equal in order to obtain minimum MSE. However, taking account of the features of the human visual system (HVS), the quantization step sizes in different frequency bands should be different. It has been shown in testing that HVS is more sensitive to the lower frequency components. Therefore, we usually set the step sizes in lower bands to be smaller. Although not always true, typically, longer tapped filters can provide better rate-distortion performance due to better energy compaction.

There is much literature available on the principles, implementation techniques, and different types of multirate filter banks and SBC [8]. We use octave wavelet (tree-structured wavelet)-based decomposition. As shown in Fig. 13, we decompose the low-low subimage into four subimages of the next level, i.e.,

$$LL_i \longrightarrow LL_{i+1}, HL_{i+1}, LH_{i+1}, HH_{i+1}$$

by a specific filter (e.g., for the HL subimage, it is a high-pass filter in the x direction and a low-pass filter in the y direction) and a decimator that decimates the signals by 2 in both x and y directions. Therefore, if we decompose the image up to N levels (level $0, \cdots, N-1$), then there will be $3N+1$ subimages. At the receiving end, we recursively reconstruct the signals by

$$LL_i = \mathcal{E}(LL_{i+1}) + \mathcal{E}(LH_{i+1}) + \mathcal{E}(HL_{i+1}) + \mathcal{E}(HH_{i+1})$$

where $\mathcal{E}()$ represents expanding the signals first (inserting a zero between two pixels), then passing them through the corresponding filter that was originally used in the decomposition.

68
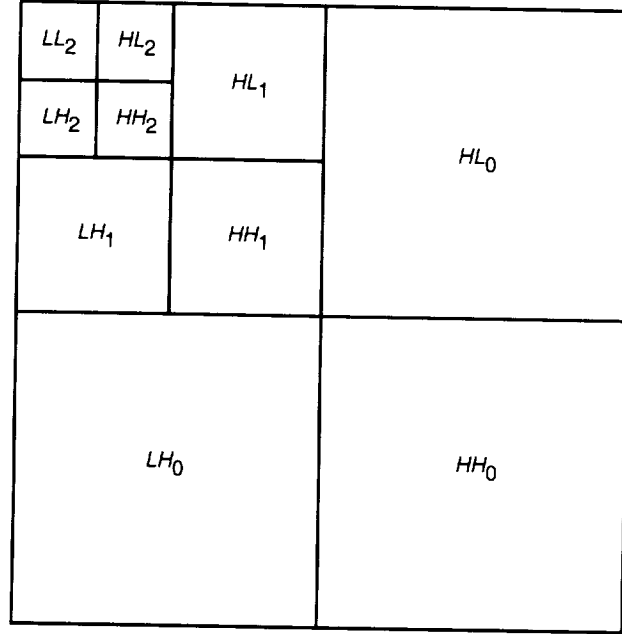
Fig. 13. SBC block diagram.

B. The Combination With Image Processing

As for the pyramid concepts of the previous section, we wish to explore the possibility of using signal correlations across frequency bands to be able to extrapolate from a lower frequency band to a higher frequency one, thus eliminating the need of transmitting all the bands.

The main difference between this case and the Laplacian pyramid case is that here we have the three difference subimages (LH_i, HL_i, HH_i) per scale instead of the single bandpass (BP) L_i component. We propose to estimate a higher-frequency level from a lower-frequency one by expanding the low-frequency level (using $\mathcal{E}$) and adding the different subimage components, as in the SBC reconstruction scheme, with an additional intermediate enhancement step.

Several possibilities come to mind in this new scenario:

(1) We can estimate each higher-level, i, subimage component from its corresponding component in the previous level, $i + 1$, as follows:

$$LH_{i+1} \longrightarrow LH_i, \qquad HL_{i+1} \longrightarrow HL_i, \qquad HH_{i+1} \longrightarrow HH_i$$

where LH_i represents the low-high (x-y directions) difference subimage in level i.

(2) We can combine all BP components in level $(i + 1)$ and then estimate the corresponding subimage summation in level (i):

$$LH_{i+1} + HL_{i+1} + HH_{i+1} \longrightarrow LH_i + HL_i + HH_i$$

(3) We can use only the low-low components and try to predict their behavior across the levels, i.e., $LL_{i+1} \longrightarrow LL_i$.

Continuing work on the Lenna image, Fig. 14 (top row) displays level 2 of Lenna in the SBC decomposition. Figure 14 (center row) shows the estimation of the level-1 subimages, following expansion and enhancement of the corresponding level-2 images, while the bottom row presents the original level-1 subimages. There is both a resemblance and a difference between the estimated bandpass images and the original ones. We wish to see how well we can estimate level-0 images based on the *estimated* level-1 components, i.e., using information from components in level 2 alone. Adding level-2 components together, we generate an *exact LL_1* image (see Section III.A). We next expand that image and each of the estimated level-1 BP subimages of Fig. 14 (center row) and sum these together to generate the estimated LL_0 image [option (1) above] as displayed in Fig. 15 (left). Aliasing effects are evident. Another experiment is to take the expanded LL_1 and enhance it [option (3)]. This produces the LL_0 image at the right of Fig. 15. Again, very strong aliasing effects are evident. In order to first add all the bandpass components together and then expand [as in option (2)], we need to first define an appropriate filter for the combined subbands. The $\mathcal{E}$ function of the original SBC decomposition uses specific filters for the specific subbands and, thus, is not suitable for the task.

In the remaining experiments, we examine the possibility of expanding a given LL_1 image via *Gaussian* interpolation followed by the enhancement procedure. Figure 16 presents the results of such a procedure on Lenna. The expanded image is presented in the top left, and the enhanced image is shown in the top right. This result very closely matches the original LL_0 image, which is displayed at the bottom of the figure. We have thus achieved a good reconstruction of the 0-level image based on the information in level 2 alone, eliminating the need to transmit the level-1 subimages. Quite surprisingly, the similarity we see between the generated and original images is not reflected in the PSNR ratios. Considering the Lenna image, the PSNR value for the blurred input (top left) as compared to the bottom image is 25.1 dB. The PSNR for the enhanced image (top right) is 24.58 dB. This is quite unexpected, especially as we look at the global statistics of the three images as presented in Table 1. We note that the enhanced image has statistical characteristics that closely match the original input image.

We can conclude the following:

(1) The PSNR estimate relates to local pixel-value discrepancies between two images. Since the enhancement scheme does not attempt to reconstruct back exact pixel values of the original image, we are well aware that it is not ideal for the PSNR measure. Still, it is very apparent that the PSNR also does not represent the human perception (as in the example of Fig. 16). It is quite clear with this example that the estimated (enhanced) image is very close to the original. Because of this mismatch, we choose not to produce rate-distortion curves with the PSNR measure.

(2) Overall, we can conclude that there is no immediate step to be taken from the pyramid representation case (Section II) to the SBC case. This is probably most evident due to the aliasing effects. Ignoring certain bandpass components seems to be more crucial since these components are needed for dealiasing. All SBC subimages are needed in order to eliminate the aliasing (a theoretical analysis of this characteristic can be found in [9]). We can compensate for the missing frequencies, but unless more work is done on how to resolve the aliasing problem, this issue remains the main obstacle.

The overall conclusion at this time is that the particular image-processing scheme suggested in this article is not applicable, without major modifications, to the SBC scheme.

IV. Image Enhancement and Progressive Transmission

We conclude this article with an additional aspect of possible interest, which is the combination of image-processing with progressive image transmission schemes. Here, instead of looking for additional
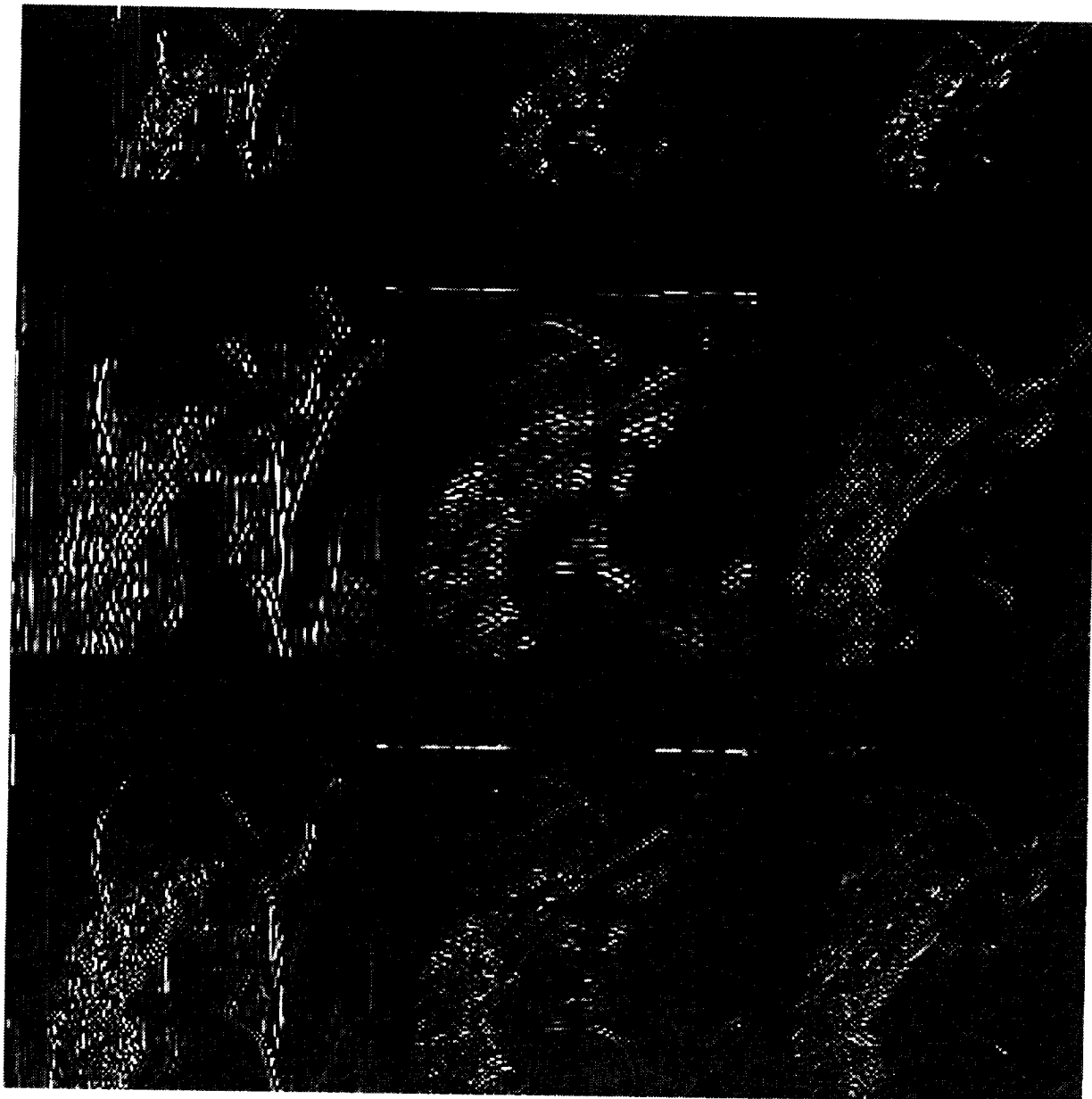
Fig. 14. SBC decomposition of Lenna. Difference subimages of levels 2, estimated level 1, and original level 1, top to bottom, respectively.

Table 1. Global statistics of the images in Fig. 16.

Characteristic	Original	Expanded image	Expanded plus enhanced image
Mean	1.344×10^2	1.344×10^2	1.344×10^2
Standard deviation	41.3	39	40
Power	140.6	140	140.3

Fig. 15. Prediction level 0 of Lenna—aliasing effects.

bit compression capabilities, we are interested in achieving successive approximations in *time*. By this we are referring to progressively transmitting information, from low resolution to high resolution, with the desire to extract information during the transmission without waiting to receive the high-resolution image. Moreover, we would like to determine at an early stage of the transmission process if the image is at all of interest, so as to determine if the high-resolution image is to be transmitted.

In Fig. 17, we demonstrate the combination of the integer subband coding (ISBC) scheme[3] of the Gaspra image with the enhancement scheme. We note the possibility of detecting the craters and other points of interest much more clearly in the enhanced images, even at extreme compression ratios. For the scientist, this can be a tool for determining interest in the region. If it does look interesting, the full-resolution image can be transmitted, without any loss.

Another domain of interest is detection of objects in a given scenery. For this task, an initial phase of edge detection is usually performed. We have looked into the combination of an edge detection scheme with the enhancement scheme to allow for better and quicker object detection.

A. Combining Edge Detection and Image Enhancement

The purpose of combining edge detection and image enhancement is two-fold: First, this scheme can be applied to progressive multiresolution image-compression systems (and progressive transmission), such as the (integer) subband coding schemes and the Laplacian-based pyramid coding scheme, to detect the edges of low-resolution images received at the early stages of transmission. We need an edge detector to catch the locations of the desired objects as soon as the low-resolution images are available. Scientists can then select and send back only the images (and acquired resolutions) of interest, thus saving in the required transmission power.

The second purpose is that, after combining the edge detection and image enhancement schemes, we get more enhanced and clear images as compared with the original images. By doing so, we can capture many more details in the received images and get a highly detailed edge map.

---

[3] K.-M. Cheung, "Low-Complexity Progressive Image Transmission Schemes for Space Applications," JPL Interoffice Memorandum 331-93.2-064 (internal document), Jet Propulsion Laboratory, Pasadena, California.

Fig. 16. Predicting level 0 of Lenna image from level 2 information: expanding LL_1 level (top left) with enhancement (top right) as compared to the original image (bottom).

An edge is usually defined as the point where a significant change (normally, intensity) occurs. In the results presented, we use a gradient-based method. Here, several difference (high-passed) filters are designed at 45-deg orientation interval preferences. After passing the original images through these filters, we add all the filtered (absolute) values in every direction and take a threshold. If the added sum is larger than the threshold, then the corresponding pixel is claimed as an edge point. This scheme achieves results comparable to common edge-detection schemes found in the literature. Additional details can be found in [7].

We apply the edge detection scheme on a low-resolution image: Figure 18(a) shows a low-resolution image of an oilfield image, and Fig. 18(b) shows the detected edge map. It is expected that fewer details (edges) can be captured, due to lost high-frequency components. However, we can improve this by first passing the low-resolution image through the image enhancer and then performing the edge detection. Figure 18(c) shows the enhanced image, and Fig. 18(d) shows the detected edge map. We see that more
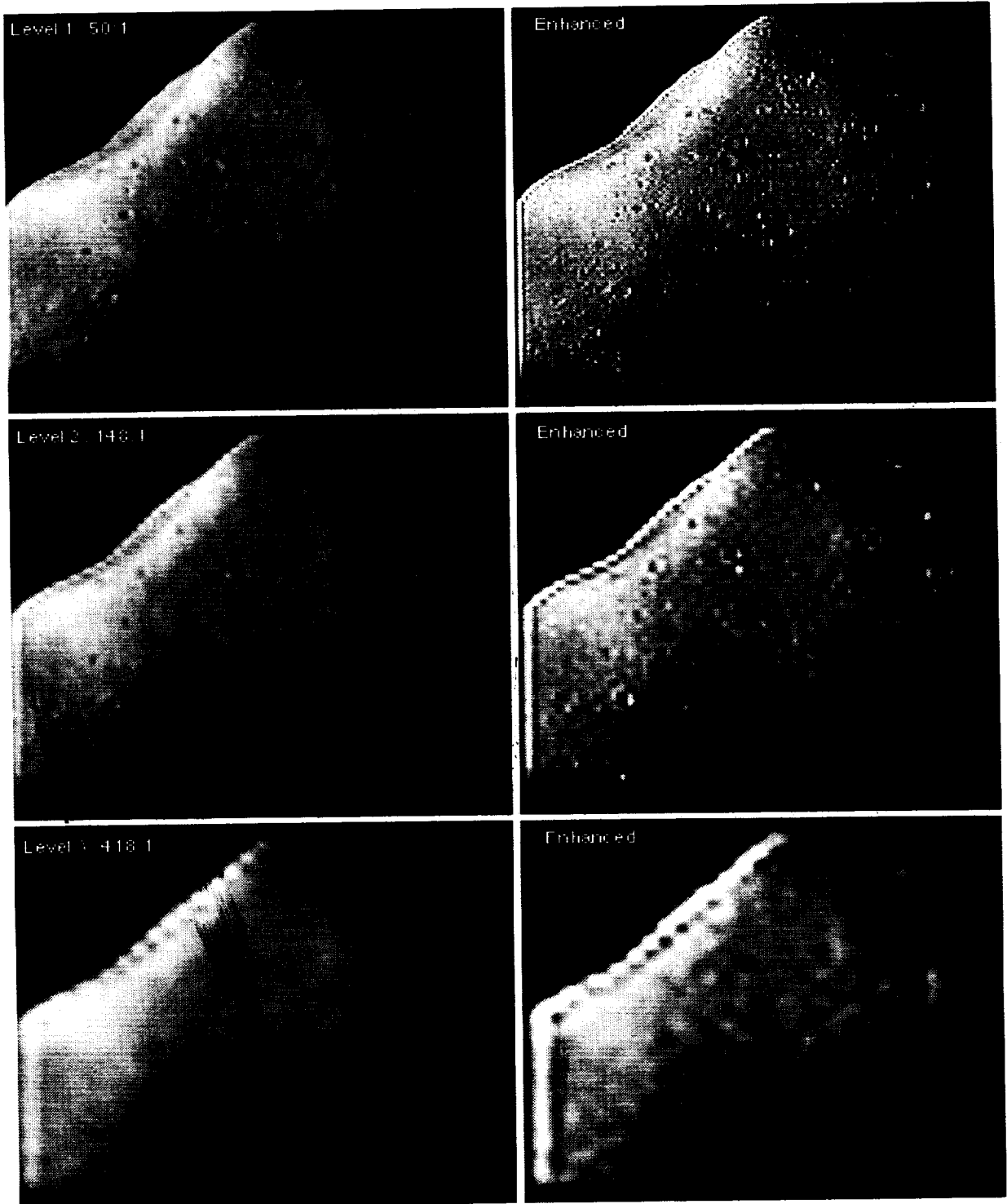
Fig. 17. Combining image enhancement with progressive transmission.
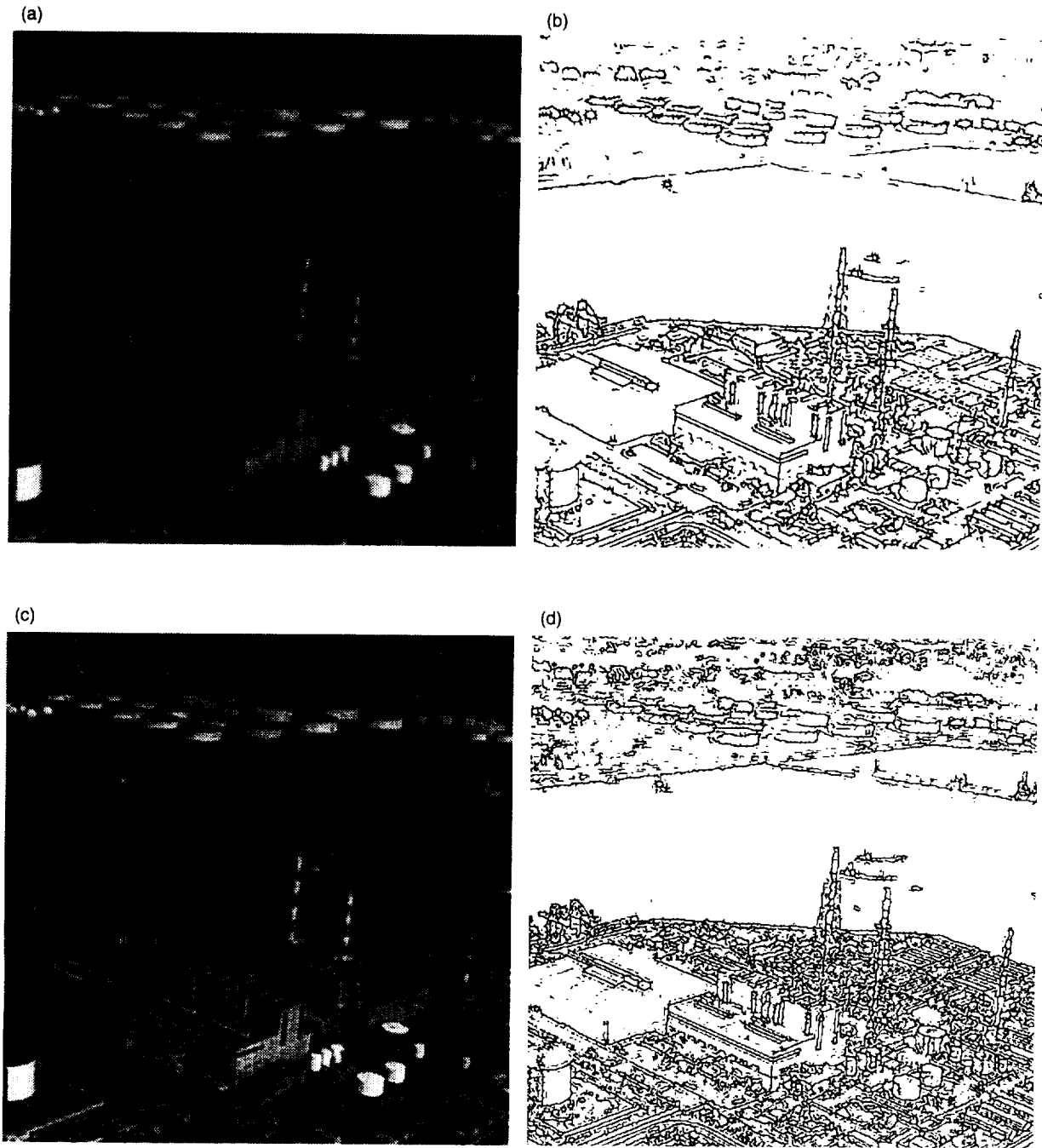
Fig. 18. Edge detection of the oilfield image: (a) a low-resolution image; (b) the detected edge map for (a); (c) an enhanced image; and (d) the detected edge map for (c).

details can indeed be captured. For example, we can count more oil tanks (top), detect the ships more clearly (center), and perceive more of the building structures (bottom).

V. Summary and Conclusions

In this article, we have done a preliminary analysis on the combination of image compression with image-processing schemes, specifically image enhancement. Encouraging results have been achieved with

the pyramid compression scheme, especially at low bit rates (which is the new frontier in the compression field). The combination of the image enhancement scheme and SBC was not as successful. Overall, we conclude that a scheme that needs all frequency bands for dealiasing cannot be easily altered and, specifically, cannot have bands removed and processed without introducing aliasing effects. Finally, the case for including enhancement in progressive image transmission was made, with results indicating the enhanced visual perception at low resolutions. In addition, further processing of the transmitted images, such as basic edge detection schemes, can gain from the added image resolution via the enhancement.

Several issues for further exploration stem from this work. In the pyramid scheme, we are interested in the possibility of pursuing steps similar to the ones described, at lower resolutions, i.e., predicting one level from a lower-resolution one, at the low resolutions of the pyramid, thus extending the compression from the L_0 level to L_1, etc. Initial investigation indicates that this is not a simple extension to the existing algorithm. As the resolution is decreased substantially, it is more difficult to locate the edges. In addition, the sharpening process will require more investigation as to how to "fill-in" the regions in the image that have been blurred and now have been sharpened. Overall, this idea requires further research.

From the SBC investigation, we learn that it could be the case that the compression and image-processing schemes cannot be combined as is. It is not always possible to take the existing algorithms and combine; rather, we might need to rethink the compression scheme together with the image-processing algorithms to generate new compression schemes.

The work presented is very preliminary work. Still, we believe that the results are interesting enough to support future work in this direction. We have only touched upon one category of image-processing schemes, image enhancement. Other processing, such as actual segmentation of images based on content, "model-based coding," and more, is attracting much interest in the research community as the new frontier for image compression.

References

[1] P. J. Burt and E. A. Adelson, "The Laplacian Pyramid as a Compact Image Code," *IEEE Transactions on Commununications*, vol. COM-31, pp. 532–540, 1983.

[2] C. H. Anderson, *A Filter-Subtract-Decimate Hierarchical Pyramid Signal Analyzing and Synthesizing Technique*, United States Patent 4,718,104, Washington, D.C., 1987.

[3] H. Greenspan and C. H. Anderson, "Image Enhancement by Non-Linear Extrapolation in Frequency Space," *Proceedings of SPIE on Image and Video Processing II*, vol. 2182, pp. 2–13, 1994.

[4] A. Witkin, "Scale-Space Filtering," *Proceedings of IJCAI*, Karlsruhe, West Germany, pp. 1019–1021, 1983.

[5] A. L. Yuille and T. Poggio, "Scaling Theorems for Zero-Crossings," A. I. Memorandum 722, Massachusetts Institute of Technology, Cambridge, Massachusetts, 1983.

[6] A. L. Yuille and T. Poggio, "Fingerprints Theorems for Zero Crossings," A. I. Memorandum 730, Massachusetts Institute of Technology, Cambridge, Massachusetts, 1983.

[7] M.-C. Lee, *Still and Moving Image Compression Systems Using Multiscale Techniques*, Ph.D. Dissertation, California Institute of Technology, Pasadena, California, 1994.

[8] P. P. Vaidyanathan, *Multirate Systems and Filter Banks*, Englewood Cliffs, New Jersey: Prentice-Hall, 1993.

[9] E. P. Simoncelli, W. T. Freeman, E. H. Adelson, and D. J. Heeger, "Shiftable Multi-Scale Transforms," *IEEE Transactions on Information Theory*, vol. 38, no. 2, pp. 587–607, 1992.

[10] H. Greenspan, *Multi-Resolution Image Processing and Learning for Texture Recognition and Image Enhancement*, Ph.D. Thesis, California Institute of Technology, Pasadena, California, 1994.

A Method Using Focal Plane Analysis to Determine the Performance of Reflector Antennas

P. W. Cramer and W. A. Imbriale
Ground Antennas and Facilities Engineering Section

S. R. Rengarajan
California State University, Northridge

Reflector antenna optimization schemes using array feeds have been used to recover antenna losses resulting from antenna distortions and aberrations and to generate contour coverage patterns. Historically, these optimizations have been carried out using the antenna far-field scattered patterns. The far-field patterns must be calculated separately for each of the array feed elements. For large or complex antennas (which include beam-waveguide antennas), the far-field calculation times can be prohibitive. This article presents a method with which the optimization can be carried out in the antenna focal region, where the scattering calculation needs only to be done once independently of the number of the elements in the array. This article also includes the results of a study, utilizing this unique technique, to determine the capabilities and limitations of using array feeds to compensate for gravitational induced losses in large reflector antennas.

I. Introduction

Array feeds for reflectors have a number of important uses, which include (1) generating contour coverage patterns, (2) correcting for reflector distortions, and (3) improving wide-angle scan. Typical methods for optimizing the array feed, for each of these applications, are very efficient when a fixed-array geometry is utilized and only the feed excitation coefficients are optimized. For this case, only one calculation of the radiating fields for each array element is required. For example, to maximize gain in a given direction, the optimization can be as simple as taking the complex conjugate of the secondary fields resulting from the illumination of the reflector in the given direction by each of the array feed elements. For most existing methods, an optimization that allowed the element spacing and size to vary would be extremely time consuming since a radiation integral evaluation would be required for each feed element at each step of the optimization process.

A new method of computing the performance of reflector antennas with array feeds is presented that obviates the need to recompute the reflector radiation fields when the feed element size or spacing is varied. This allows the optimization technique to efficiently include size and spacing as parameters.

The mathematical formulation is based upon the use of the Lorentz reciprocity theorem, which convolves the focal-plane field distribution of the reflector system with the feed-element aperture field distribution to obtain the element response. Thus, the time-consuming reflector-system radiation integral

evaluation is only done once for a given scan direction or reflector surface distortion for all array feed geometries and types considered. Table 1 tabulates the relative merits of focal region analysis (sometimes referred to as reverse or receive scattering) and far-field analysis (sometimes referred to as forward or transmit scattering). A rough rule of thumb is that any analysis that requires evaluating the radiated fields at a number of far-field observation points is best done with conventional far-field analysis. However, analysis that requires investigating many different feed or array feed designs is accomplished faster and more easily by using focal plane analysis.

Examples are given using the technique to design an array feed for the correction of gravity-induced distortions of a large dual-shaped ground antenna, both conventional and beam waveguide (BWG), and to design an array feed for improved wide-angle scan. The main emphasis of the examples, however, is on beam-waveguide designs as exemplified by the Deep Space Network (DSN) Deep Space Station (DSS)-13 34-m antenna at Ka-band (33.67 GHz).

Table 1. Comparison of antenna computational techniques for a single reflector design.

Characteristic	Forward method, far field	New reversed method, focal plane
Fields calculated	Far field	Focal plane
Number of far-field points	Any number	One
Number of focal-field points	Not applicable	Any number
Number of individual feeds	One	Any number
Number of array combinations	One	Any number
Typical computation time for 34-m BWG antenna at 33.67 GHz (Cray Y-MP2),[a] h	6–12	6–12
Time to calculate focal plane currents, h	Not applicable	3–4
Time for additional far-field points	Trivial	6–12
Time for additional feeds or array cases, h	6–12	0.1–0.5

[a] Due to priority restrictions for large jobs, turnaround times can be more significant than actual computational times.

II. Focal Plane Analysis

The calculation of the gain of an antenna system, using the antenna focal plane analysis technique, can be illustrated by a simple single-reflector antenna, as shown in Fig. 1. Referring to Fig. 1(a), the first phase of the analysis consists of several steps. First, the focal-plane fields produced by a plane wave impinging upon the reflector antenna aperture are computed. Second, the aperture fields of the feed horns located at the focal plane are determined, and these fields are then convolved with the focal plane fields to provide a set of complex feed weights. The process can be explained as follows: Consider a reflector antenna fed by a horn. We wish to determine the gain of this system in a given direction, (θ_0, ϕ_0), in the receive mode. First, consider the Lorentz reciprocity theorem:

$$-\iint_s \{\overline{E}_a \times \overline{H}_b - \overline{E}_b \times \overline{H}_a\} \cdot \overline{ds} = \iiint_v \{\overline{E}_a \cdot \overline{J}_b - \overline{H}_a \cdot \overline{M}_b - \overline{E}_b \cdot \overline{J}_a + \overline{H}_b \cdot \overline{M}_a\} dv \qquad (1)$$

In this expression, $\overline{E}_a$ and $\overline{H}_a$ are fields radiated by a set of sources $\overline{J}_a$ and $\overline{M}_a$, and also $\overline{E}_b$ and $\overline{H}_b$ are fields radiated by sources $\overline{J}_b$ and $\overline{M}_b$. The left integral is over a closed surface that encloses the volume defined by the integral on the right side. Over an infinite region, the surface integral becomes zero. The Lorentz reciprocity theorem can, therefore, be rewritten as

$$\iiint_v \{\overline{E}_a \cdot \overline{J}_b - \overline{H}_a \cdot \overline{M}_b\} dv = \iiint_v \{\overline{E}_b \cdot \overline{J}_a - \overline{H}_b \cdot \overline{M}_a\} dv \qquad (2)$$
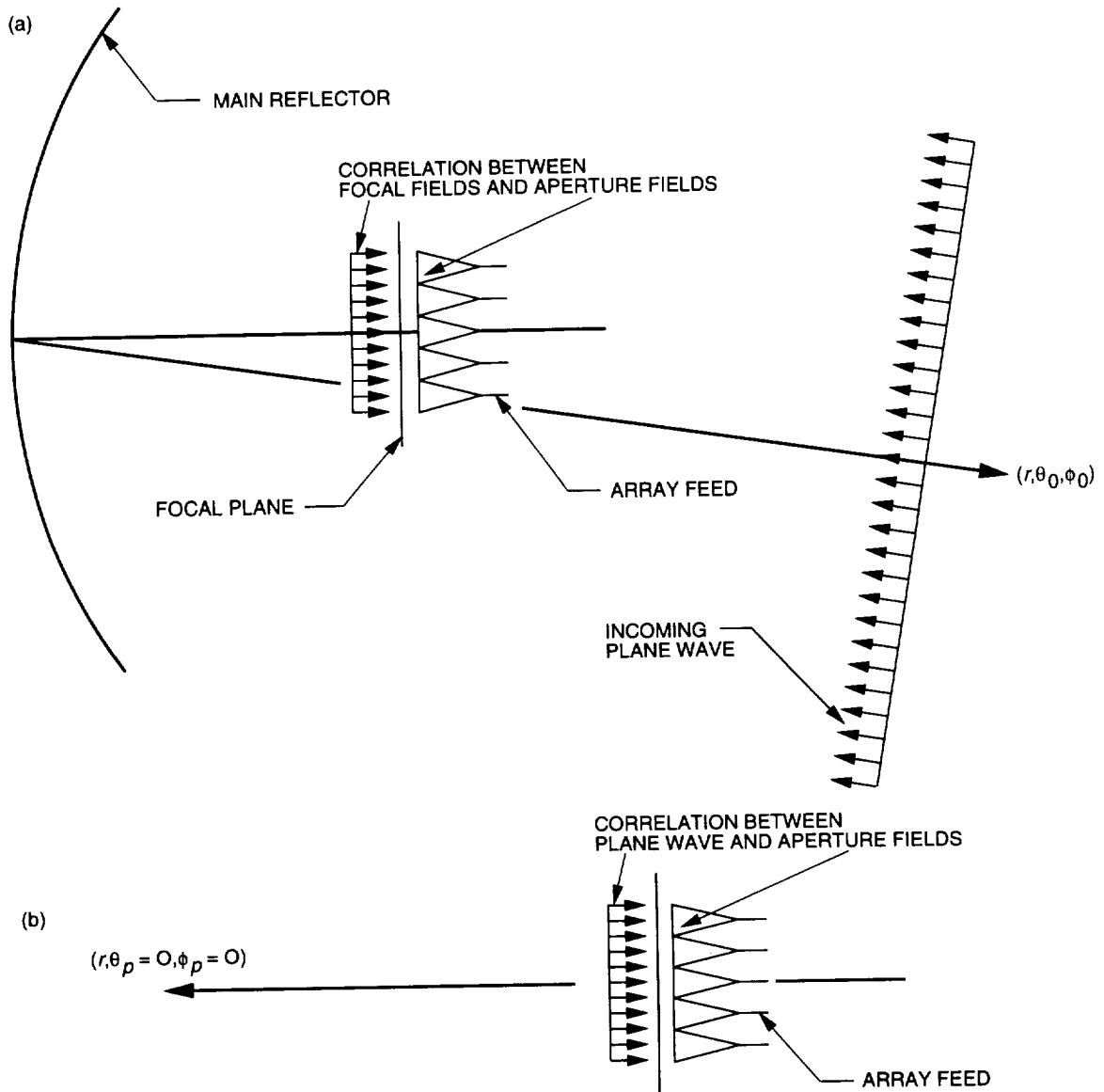
Fig. 1. Focal plane analysis geometry: correlation between (a) focal fields and aperture fields and (b) plane wave and aperture fields.

which says that, as long as the relationship between the fields and their source currents holds true, the results will be the same wherever the integrals are evaluated in the region. Let us redefine the a sources as sources $\overline{J}_{ha}$ and $\overline{M}_{ha}$, to be associated with the feed horn apertures and generating the fields $\overline{E}_{ha}$ and $\overline{H}_{ha}$ in the aperture plane of the feed. In turn, let us redefine the b sources as sources $\overline{J}_{fp}$ and $\overline{M}_{fp}$, to be associated with the antenna reflector system when illuminated by an incident plane wave source from a direction (θ_0, ϕ_0) and evaluated in the reflector system focal plane. The feed horn apertures are defined to be coplanar with the antenna focal plane.

Since the integration is limited to the aperture plane/focal plane, the integrals reduce to surface integrals. Each integral is proportional to the feed-horn output voltage [1]. The left-hand equation is used in this work since the program that generates the focal-plane equivalent currents outputs currents and the program that computes the feed-horn aperture distributions outputs fields. The expression relating the feed-horn outputs, v_{r_A}, to the currents from the antenna reflector system and the feed-horn aperture fields is then

$$v_{r_A} \propto \iint_s \{\overline{E}_{ha} \cdot \overline{J}_{fp} - \overline{H}_{ha} \cdot \overline{M}_{fp}\}ds \tag{3}$$

The $\overline{E}_{ha}$ and $\overline{H}_{ha}$ should be determined in the presence of the antenna reflector system, and the focal plane currents $\overline{J}_{fp}$ and $\overline{M}_{fp}$ should be obtained when the feed horn is present. Such computations would require that the interactions between the feed horns and the reflectors be taken into consideration. Taking into account these interactions seriously complicates the analysis and increases the computational time. Often $\overline{E}_{ha}$ and $\overline{H}_{ha}$ are approximated to the aperture fields of a horn radiating into an infinite homogeneous free space (no reflector), and the focal-plane currents $\overline{J}_{fp}$ and $\overline{M}_{fp}$ of the antenna reflector system are also obtained in the absence of a feed. This is a reasonable assumption when the feed and antenna reflector system are widely separated in terms of wavelengths.

As will be seen later, there is also a need to obtain the performance of a feed horn in the presence of a plane-wave incident field arriving from a direction (θ_p, ϕ_p) and in the absence of the antenna reflector system, Fig. 1(b). In the same manner as presented above, it can be shown that the output voltage for such a feed horn is

$$v_{r_P} \propto \iint_s \{\overline{E}_{ha} \cdot \overline{J}_{pw} - \overline{H}_{ha} \cdot \overline{M}_{pw}\}ds \tag{4}$$

where $\overline{J}_{pw}$ and $\overline{M}_{pw}$ are the currents in the feed aperture plane due to the incident plane wave field.

In Eqs. (3) and (4), the proportionality constants should be the same, being a function of the horn aperture characteristics. The proportionality constants can be eliminated by performing the ratio of Eqs. (3) and (4) as follows:

$$\frac{v_{r_A}}{v_{r_P}} = \frac{\iint_s \{\overline{E}_{ha} \cdot \overline{J}_{fp} - \overline{H}_{ha} \cdot \overline{M}_{fp}\}ds}{\iint_s \{\overline{E}_{ha} \cdot \overline{J}_{pw} - \overline{H}_{ha} \cdot \overline{M}_{pw}\}ds} \tag{5}$$

Let us now consider two transmit situations. First, let the feed horn radiate in the absence of the antenna reflectors and let the radiated field at (r, θ_p, ϕ_p) be E_h and the power be P_o. Then the gain of the feed horn in the direction (θ_p, ϕ_p) is

$$G_h = \frac{4\pi r^2}{\eta P_o}|E_h|^2 \tag{6}$$

Next, let the horn illuminate the reflector system. The scattered field at (r, θ_o, ϕ_o) is E_a. Assume that the power that is radiated by the feed horn is still P_o. Then the gain of the complete antenna system in the direction (θ_0, ϕ_0) is

$$G_a = \frac{4\pi r^2}{\eta P_o}|E_a|^2 \tag{7}$$

and, consequently,

$$G_a = G_h \frac{|E_a|^2}{|E_h|^2} \tag{8}$$

From reciprocity, we know that the radiated fields and horn output voltages are related by

$$\frac{|E_a|^2}{|E_h|^2} = \frac{|v_{r_A}|^2}{|v_{r_P}|^2} \tag{9}$$

Therefore, by combining Eqs. (5) and (9), the overall gain of the reflector antenna system can be found in the receive mode from

$$G_a = G_h \cdot \left[\frac{|\iint_s \{\overline{E}_{ha} \cdot \overline{J}_{fp} - \overline{H}_{ha} \cdot \overline{M}_{fp}\}ds|}{|\iint_s \{\overline{E}_{ha} \cdot \overline{J}_{pw} - \overline{H}_{ha} \cdot \overline{M}_{pw}\}ds|}\right]^2 \tag{10}$$

It should be noted that (θ_0, ϕ_0) and (θ_p, ϕ_p) need not be the same. Therefore, (θ_p, ϕ_p) has been set to (0.0, 0.0) for simplicity of analysis when evaluating the interactions of the array feed with an incident plane wave and computing the feed horn far-field gain, G_h.

III. Optimization Technique

The optimization technique used in obtaining the maximum gain for an antenna reflector system illuminated by a group or an array of feed elements is referred to as the conjugate weight or match method [2]. Consider a reflector antenna with an array feed operating in the transmit mode and with each feed element excited with equal signal levels. In some direction (θ_0, ϕ_0), in which the maximum output fields are desired, the output field for each feed element is determined. Let f_i represent the complex output field voltage of the antenna for feed element i in the direction (θ_0, ϕ_0). Then the maximum or optimum output field in that direction would be

$$v_t = \sum_{i=1}^{N} f_i^* f_i \tag{11}$$

If in the receive mode, c_i is the output voltage from the ith feed element of the reflector antenna system, when illuminated with a plane wave arriving from the direction (θ_0, ϕ_0); then the total received signal from the antenna where each feed element is weighted by its complex conjugate is

$$v_r = \sum_{i=1}^{N} c_i^* c_i \tag{12}$$

From reciprocity, $c_i/f_i = const$ for all i. Therefore, except for a constant, the expressions that are based on the complex weighting in the receive mode are identical to those in the transmit mode. Thus, v_r also represents an optimum gain solution. In this analysis, the effects of mutual coupling between array elements have been ignored. For the size and type of feed elements considered in this study, this is not a limitation.

If the integral portion of Eqs. (3) and (4) are rewritten as follows,

$$c_i = \iint_s \{\overline{E}_{ha_i} \cdot \overline{J}_{fp} - \overline{H}_{ha_i} \cdot \overline{M}_{fp}\} ds \tag{13}$$

$$d_i = \iint_s \{\overline{E}_{ha_i} \cdot \overline{J}_{pw} - \overline{H}_{ha_i} \cdot \overline{M}_{pw}\} ds \tag{14}$$

by the use of Eq. (12), Eq. (10) can be rewritten as

$$G_a = G_h \cdot \left[\frac{\sum_{i=1}^{N} c_i^* c_i}{|\sum_{i=1}^{N} c_i^* d_i|} \right]^2 \tag{15}$$

This expression is used to determine the optimum antenna gain simply by knowing the focal plane currents of the antenna, the array feed geometry, and the feed element aperture fields. The gain of the array feed in the absence of the antenna reflectors, G_h, is obtained by first performing a physical optics integration over the E_{ha} fields in each feed element aperture to obtain the far-field pattern for each element. Then the power and peak fields are computed from the total fields from all elements in the conventional manner and used to compute G_h.

The analysis method consisted of computing the focal plane currents of a reflector system using reverse (receive-mode) scattering programs. Physical optics is used for a single-reflector antenna design and a combination of geometrical optics off of the main reflector and physical optics off of a subreflector is used in a dual-reflector antenna system. Both electric and magnetic focal plane currents are computed on a fixed grid over which the array-feed element aperture distributions are superimposed. This grid becomes the integration grid over which the convolution of the focal plane currents and feed aperture field distributions are integrated. The feed aperture fields are in effect interpolated to fall on the points established by the reverse scattering program's focal plane grid. To generate the feed element aperture fields at the required grid locations, the far field element patterns are expanded into a set of circular waveguide modes. These modes can then be evaluated at the required grid locations to obtain the feed aperture fields.

IV. Accuracy Considerations

To determine the accuracy of the focal plane technique, the gain of a single reflector antenna was calculated using three different approaches: (1) the focal plane technique combined with a physical optics program that took a plane wave impinging on the reflector and computed the required focal plane currents,

(2) a forward scattering program, using a physical optics technique that made use of the Jacobi/Bessel series to describe the output fields [3], and (3) a forward scattering program, using a physical optics method that used a triangular integration grid [4]. The gain pattern was calculated for a number of far-field observation points. Obviously, for the forward approach, this simply meant specifying the locations of the observation points. For the focal plane approach, however, calculating the gain pattern required the incoming plane wave direction to be adjusted such that the direction of propagation was from the observation point. Table 2 summarizes the results. As can be seen, all three techniques agreed within a few hundredths of a dB for pattern gain variations of 7 dB. The only precautions needed to get this accuracy were to make sure sufficient integration points were used and that all series representations of fields had converged.

Table 2. Accuracy of the focal plane method, antenna gain.

Pattern angle, deg	Classical forward method		Reversed method focal plane, dB
	Jacobi/Bessel, dB	Standard PO, dB	
0.00	44.16	44.15	44.17
0.35	43.15	43.14	43.16
0.60	41.14	41.14	41.15
0.90	37.14	37.14	37.15

V. Use of Optimization to Minimize Beam Scan Loss

One application of the optimization approach described in this article is to minimize the scan losses of an antenna where the antenna beam has been scanned off the axis of symmetry by a lateral displacement of the feed system. Depending on the size of the displacement, the losses can be quite large, due to the optical aberrations produced. The test case used consisted of a 423.55 cm–diameter parabolic reflector with a focal length-to-diameter ratio (F/D) of 0.5. The compensating array feed consisted of up to 37 elements. The main beam was scanned 6.15 deg off the axis of symmetry to produce a scan loss on the order of 8 dB. The primary array element that produces the specified beam scan was located 24.36 cm off the antenna axis. The antenna parameters and the improvement in performance due to array feed optimization is shown in Table 3. The gain for several numbers of array elements is shown. The gain for an antenna with the single-feed element is 44.8 dB. With complex conjugated weights applied to 37 elements, the gain is increased to 51.9 dB for a net improvement of 7.1 dB.

VI. Compensating Reflector Distortions by Optimization

As was mentioned in the introduction, the main purpose of the focal plane optimization technique was to reduce the amount of computer time required to optimize the design of an antenna system to maximize the gain. This is particularly true for studying large, complex antennas such as the 34-m beam-waveguide dual-shaped reflector antennas, operating at 33.67 GHz, that are used at the Jet Propulsion Laboratory/NASA deep space tracking network. However, a second advantage of the focal analysis is that it allows the actual focal field distributions to be displayed. This can many times give some insight into why the antenna behaves the way it does. In the conventional far-field optimization approach [5], a full scattering calculation is required for each array feed element, for each antenna configuration, and for each array geometry. In the focal plane analysis, a scattering calculation is required only for each antenna configuration. Any number of array geometries and any number of feed elements can be studied without any further scattering calculations.

Although considerable effort was expended to develop the focal plane analysis technique, the main purpose of the study was to determine the properties of a shaped antenna illuminated by an array feed

Table 3. Compensating for beam scan loss using conjugate weights.

Number of elements in array	Pattern gain, dB	Gain improvement, dB
1	44.8	0.0
7	49.1	4.3
19	50.4	5.6
37	51.9	7.1

Geometry
Reflector diameter   423.55 cm
F/D   0.5
Array element diameter   1.59 cm
Frequency   11.8 GHz
Array center offset   24.36 cm
Beam peak direction   6.15 deg

where the array feed's purpose is to compensate for various antenna aberrations or distortions. The focal plane technique is simply the enabling technology. A conjugate weighting technique is used to determine the excitation weights for each array feed element so that the antenna losses might be recovered. The goal was to compensate the antenna for gain losses that resulted from gravity-induced distortions as a function of the antenna's elevation angle, where the surface is adjusted for minimum distortion at a 45-deg elevation angle. The main application is for a beam-waveguide (BWG) antenna where the array feed system is mounted in a room below the antenna. However, to expedite the validation of the focal plane analysis technique, the initial calculations were limited to the main focal plane of the antenna, i.e., no BWG. Figure 2 illustrates the geometry of the DSS-13 34-m BWG antenna, the properties of which were made the basis of this study. The frequency used was 33.67 GHz. Of particular interest is the focal region at F1, where the initial calculations were made. A second set of calculations was made at F3, the focal region created by the beam-waveguide system in the basement or pedestal room of the antenna. Although the beam-waveguide system consists of two parabolic mirrors, one elliptical mirror, and three plane mirrors, only the three curved mirrors are included in the analysis. The three plane mirrors, if properly sized, should not affect the performance of the antenna system. Figure 3 shows an array feed with the RF front-end setup at F3 that was used in another study for an experimental evaluation of using array feeds to compensate for antenna distortion losses. Figure 4 shows a seven-element array, with 4.45-cm diameter dual-mode horns, used in the experimental system. This illustrates a typical application for the results of the trade-off study discussed later in this article.

A summary of results at F1 and F3 for 7.5- and 45-deg elevation angles is shown in Table 4. The results are based on the use of optimum feed horn sizes and focus. Both the focal plane or reversed scattering method and the forward or conventional scattering method were used. The results for the forward method are from an optimization study done at the time DSS 13 was completed. As can be seen, the results for the forward and reversed approaches are very close.

A. Optimization at F1

The case used for the evaluation consisted of an array feed of seven equally sized elements in a circular cluster on a triangular grid. The first step was to select an element size that minimized the antenna loss at one of the distortion extremes, such as at an elevation angle of 7.5 deg. A set of 13 element diameters was selected, ranging from 2 to 13 cm. For each element diameter, the focal plane optimization technique was used to determine the feed element weights that gave the best performance improvement. Figure 5 contains two curves. The first curve shows the performance of the antenna that results from a single

C-2
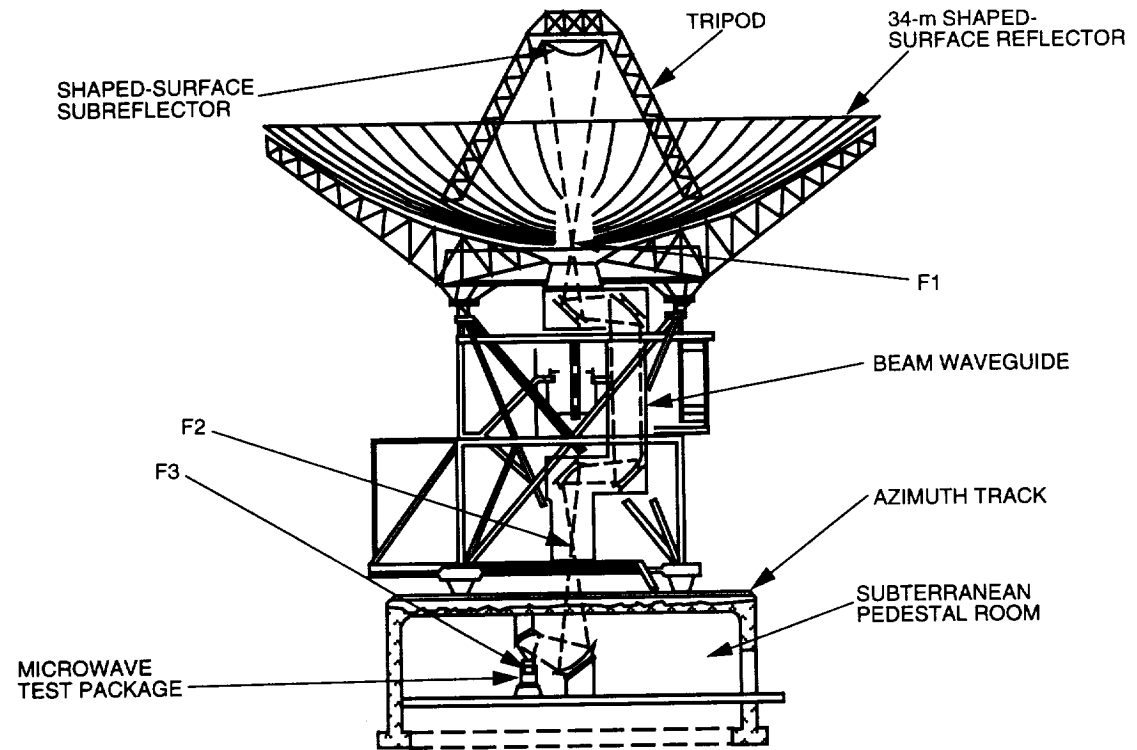
Fig. 2. DSS-13 34-m beam-waveguide antenna.

Fig. 3. An array feed with the RF front-end set up at F3.
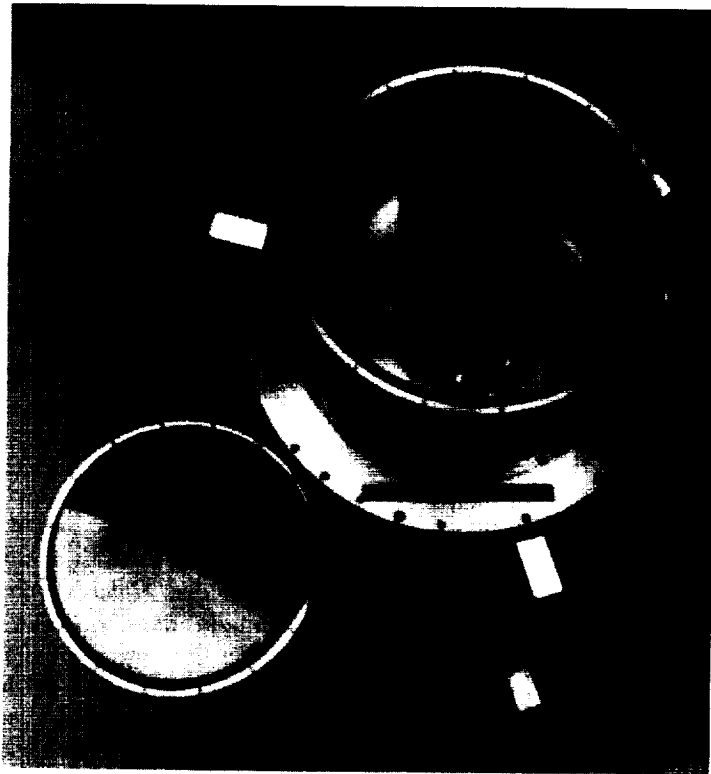
Fig. 4. A seven-element array with 4.45-cm diameter dual-mode horns.
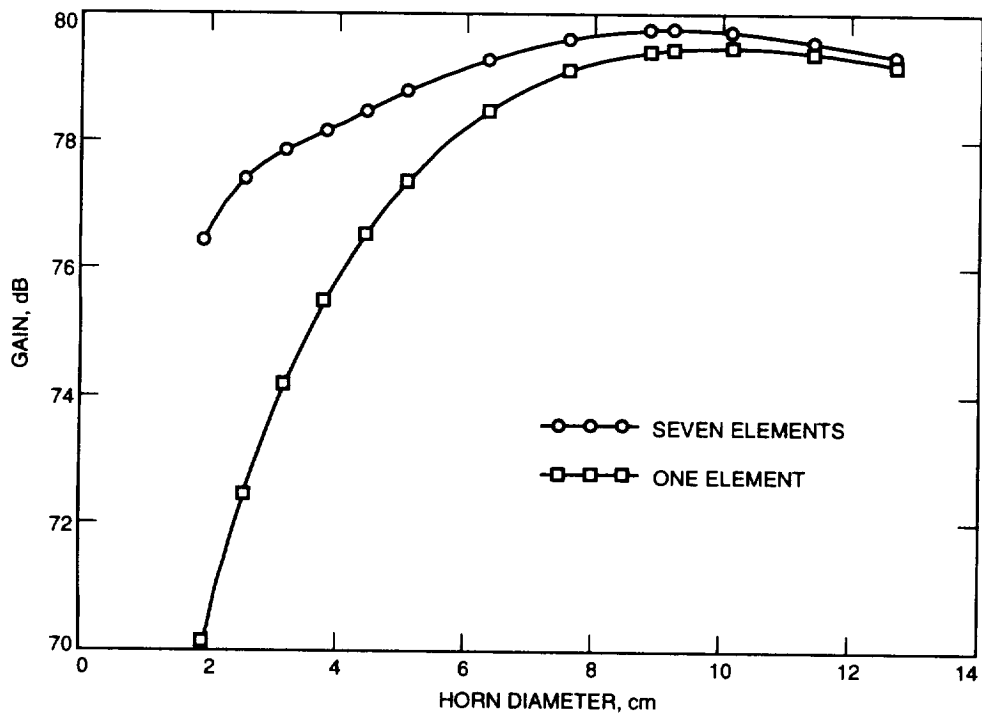
Fig. 5. Optimum antenna gain versus feed element diameter (7.5-deg elevation angle).

Location	Calculation method	Evaluation angle, deg	One element, dB	Seven elements, dB
Antenna focal point F1	Reverse	45.0	81.120	81.129
Antenna focal point F1	Forward	45.0	81.109	—
BWG focal point F3	Reverse	45.0	81.039	81.046
BWG focal point F3	Forward	45.0	81.044	—
Antenna focal point F1	Reverse	7.50	79.442	79.733
BWG focal point F3	Reverse	7.50	79.338	79.557

[a] Antenna surface shape is optimized at a 45.0-deg elevation angle.

on-axis element as a function of element size. The second curve shows the best performance for an array of equally sized elements. From the curve, it was found that an array of elements with diameters of 9.26 cm gave the best performance at an elevation angle of 7.5 deg. Calculations using the optimization technique were repeated for a series of antenna elevation angles, using the 9.26 cm–diameter elements, to determine the best performance that can be obtained with the optimum element size determined at 7.5 deg. Figure 6 summarizes the result. The first curve illustrates the performance that would be expected due to reflector distortions as a function of elevation angles if a single feed horn were used. The second curve shows the improvement in performance that can be obtained with the seven-element array using the optimum element weights computed by the optimization technique. The maximum improvement at an elevation angle of 7.5 deg is 0.29 dB out of a distortion loss of 1.68 dB. It was found that if the number of elements in the ring around the center element was increased from 6 to about 12 elements, an additional improvement of 0.18 dB could be obtained for an overall improvement of 0.47 dB (Fig. 7).

As indicated earlier, the availability of the focal plane fields from the focal plane analysis program can give an insight into why the antenna performs the way it does. Figure 8 shows the focal plane field distribution at F1 for an elevation angle of 45 deg. Overlaying the field distribution are the outlines of the optimum-size feed horns. As can be seen, the center horn covers the field distribution from in excess of 5.0 dB down to almost −15.0 dB. The outer ring of feed horns covers a region of ripples indicated by the multiple contour rings at −22.5 and −30.0 dB. These multiple rings also indicate that phase reversals are present in the region of the outer horns. Thus, the center horn captures the majority of the focal plane fields, whereas the outer horns couple very little of the fields because of the low field strengths and the fact that the phase reversals will cancel out a large part of what field levels are available. Hence, the outer elements will not improve the antenna performance, as can be seen in Fig. 6. Figure 9 is a similar plot for an elevation angle of 7.5 deg. In this case, the center horn captures less energy since the peak level has dropped and the contour associated with the edge of the horn aperture is now only −5.0 dB. Although the outer ring of horns covers a region of levels primarily between −5.0 and −25.0 dB, which appears to represent the majority of the energy missed by the center horn, as is seen in Fig. 6, only a small part of the lost energy was recovered at 7.5 deg. This is due to the fact that the typical feed-horn aperture distribution is Gaussian and couples the most energy when associated with a Gaussian focal plane distribution, such as is seen in Fig. 8 for the center horn for the 45-deg elevation case. In the case of the outer horns at 7.5 deg, the focal plane distribution they see is essentially wedge shaped in a radial direction and, therefore, these horns are very inefficient in coupling the energy within their apertures.

A question raised during the study was whether the array feed could recover losses due to diffraction from the subreflector support tripod. Calculations were made to address this question at an elevation angle of 45 deg. To simplify the calculation and to avoid developing a special program to compute
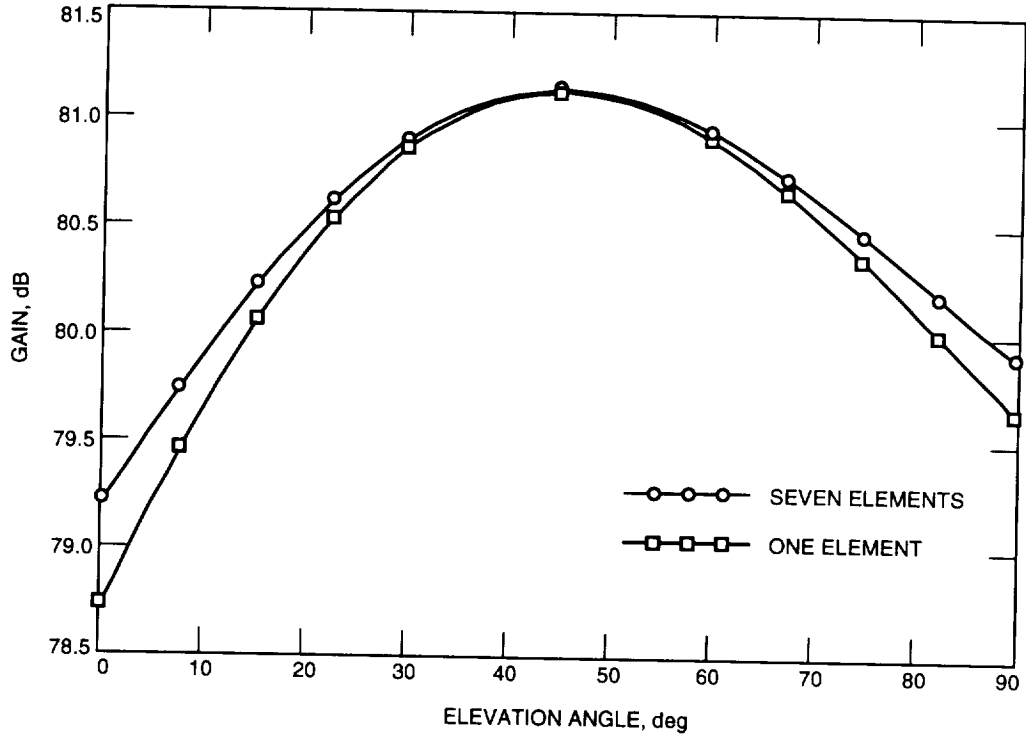
Fig. 6. Optimum antenna gain versus antenna elevation angle (9.26-cm horn diameter).
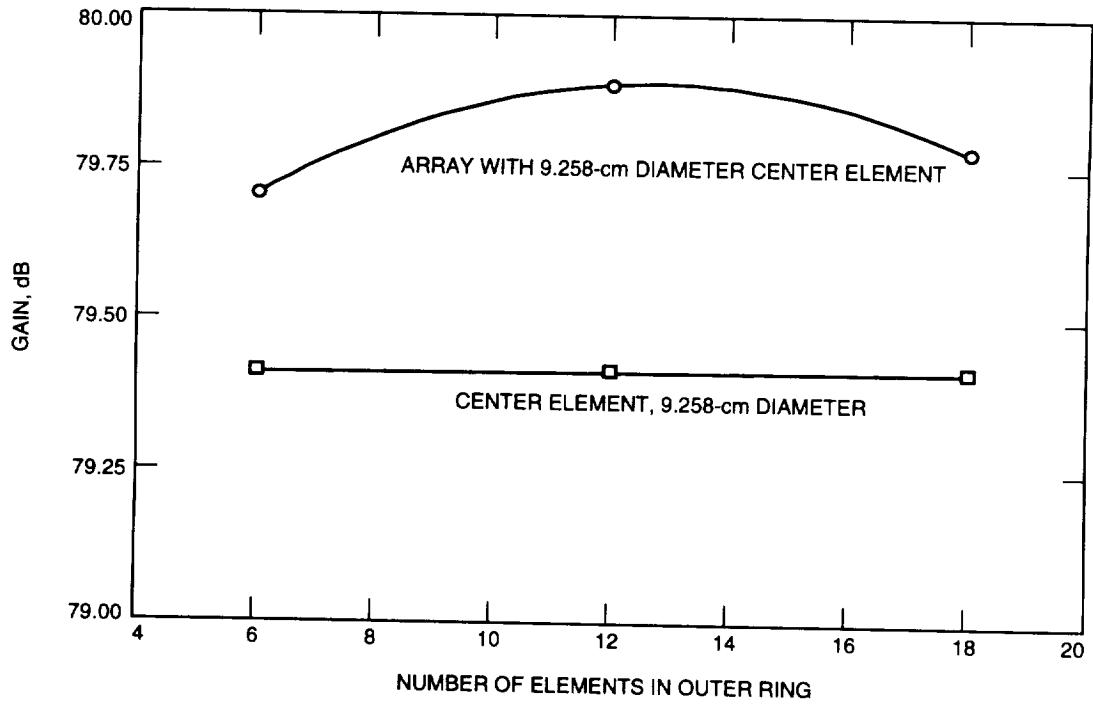
Fig. 7. Antenna gain versus number of elements in outer ring (7.5-deg elevation angle).
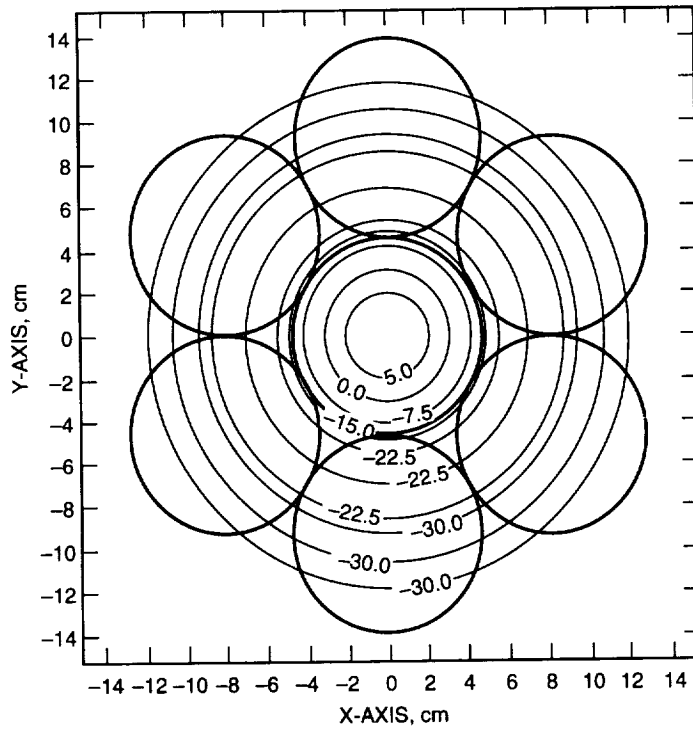
Fig. 8. Focal plane field distribution overlaid with the outline of the 9.258-cm diameter horns at F1 for a 45-deg elevation angle.
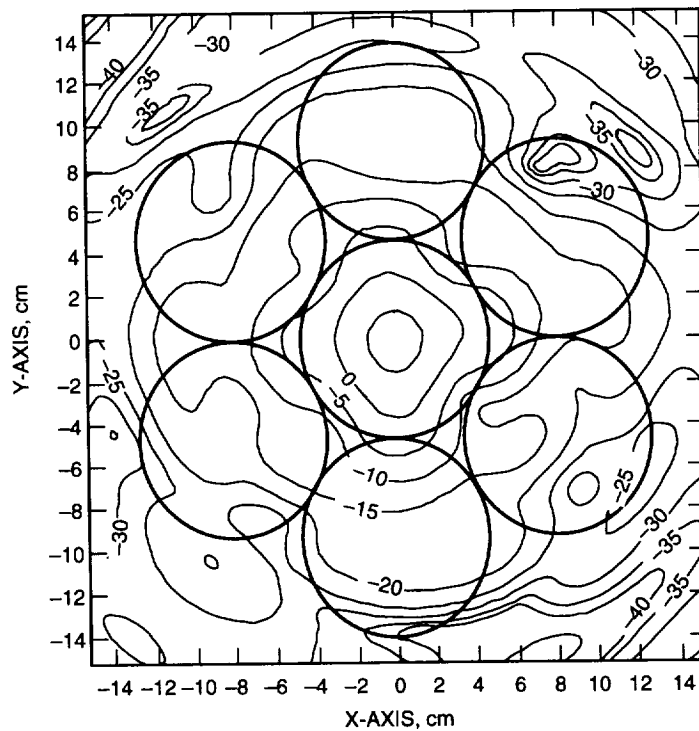
Fig. 9. Focal plane field distribution overlaid with the outline of the 9.258-cm diameter horns at F1 for a 7.5-deg elevation angle.

the diffraction from the support tripod, the decision was made to project the tripod blockage onto the main reflector similarly to that done with holography. In the area of the projected blockage, the main-reflector surface currents were set to zero. Using the physical optics scattering program, the fields on the subreflector were then computed. Using the reverse scattering program, the focal plane currents in turn were computed from the subreflector currents. Using the focal plane analysis, the gain of the antenna with support tripod blockage was determined. As a reference, the gain for no blockage was calculated using the same technique. For one horn, the loss (or difference in gain) due to blockage was 0.44 dB. For an array of seven horns, again the loss due to blockage was 0.44 dB. The array provided an improvement on the order of 0.01 dB for both with and without blockage. Therefore, the array was incapable of recovering blockage losses, and the calculated losses were due to the support tripod scattering fields outside of the region occupied by the array.

B. Optimization at F3

The major part of the study was done with the array feed located at F3 since this location would be used for a practical implementation. The design approach used followed that used at F1, where first the gain as a function of horn diameter was calculated. This was done at one extreme elevation angle, such as 7.5 deg, rather than at 45 deg, so as to optimize the array design at the point where the losses would be the greatest. This calculation was done at two axial focal positions of 0.0 and −8.89 cm from F3 so as to bracket the optimum focal position. Figures 10 and 11 illustrate the results for an array of seven horns, where the best horn diameter for a focal position of 0.0 cm was 5.88 cm, and, for a focal position of −8.89 cm, the best diameter was 5.08 cm. Next, the calculations were repeated as a function of the axial focal position, where the horn diameters were linearly interpolated at each focal position using the two best horn diameters previously calculated at the bracketing focal positions. The calculations were done at elevation angles of 7.5 and 45 deg. In Figs. 12 and 13, it is seen that the performance for an array of seven horns peaks at focal positions of −6.67 cm for an elevation angle of 7.5 deg and −6.1 cm for an elevation angle of 45 deg. Since the gain is quite flat in the vicinity of the best focus, a focal position between the best focal position for the two elevation angles was selected as the focal position for the remainder of the calculations. The selected axial focal position is −6.35 cm for a horn aperture diameter of 5.31 cm.

Having selected the nominal location for a seven-horn array and the best central horn diameter, the rest of the study consisted of varying the various parameters of the array design. Figure 14 shows the antenna performance as a function of elevation angle for the center horn only and for an array of seven horns. At an elevation angle of 45 deg, the center horn and the array have the same performance, as expected, since the antenna surface was adjusted at this angle. At an elevation angle of 7.5 deg, the single-horn performance shows a loss of 1.70 dB relative to the performance at the 45-deg elevation angle. Using the array to recover this loss of performance, only a 0.22-dB improvement was obtained. Earlier calculations using the forward or transmit mode to compute the possible performance improvement showed improvements of about 0.4 dB. The earlier calculations used the array geometry that was used in an experimental program, where the array horn diameters were not optimized and the horns were operated 1.67 GHz away from their design frequency, allowing more room for improvement. In this study, the horn size was optimized, as discussed in the previous paragraph.

The calculation in the first paragraph of this section was for a seven-horn array, where the center horn and the six horns in a ring around the center horn had the same diameters. The next calculation investigated the effect of using different numbers of horns in the ring around the center horn and adjusting the diameter of these horns to completely fill the ring. The larger the number of horns in the rings, the smaller the horn diameters. Figure 15 illustrates the performance for this case. In the figure, the performance of the center horn is included as a baseline and is a straight line since it is not affected by the number of outer-ring horns. Also, the figure shows calculations for one outer ring and two outer rings. Where two rings are used, both rings have the same number of horns, the second ring nesting in the first ring. This necessitates the horns in the second ring being larger than those in the first ring.
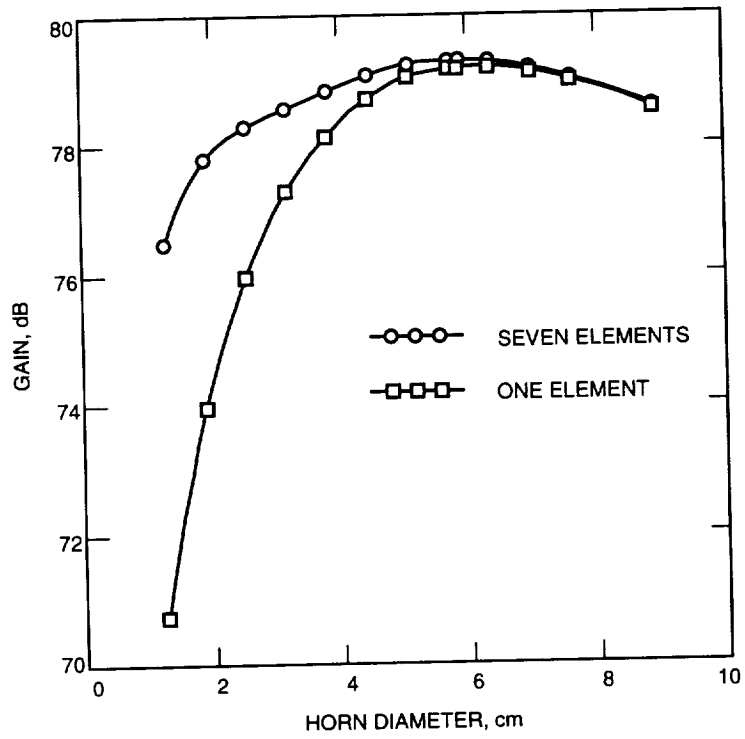
Fig. 10. Antenna gain versus horn diameter, z (focus) = 0.0 cm (7.5-deg elevation angle).
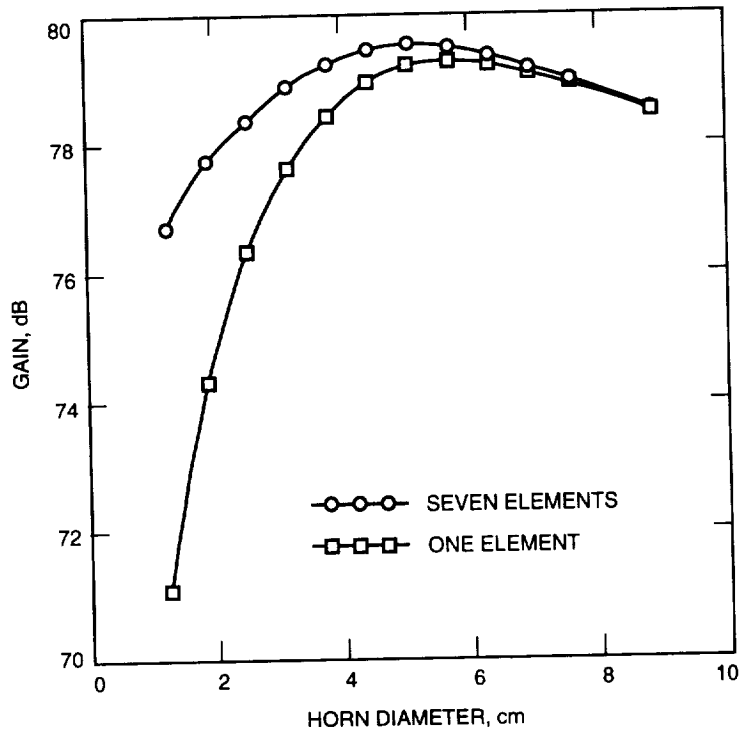
Fig. 11. Antenna gain versus horn diameter, z (focus) = –8.89 cm (7.5-deg elevation angle).
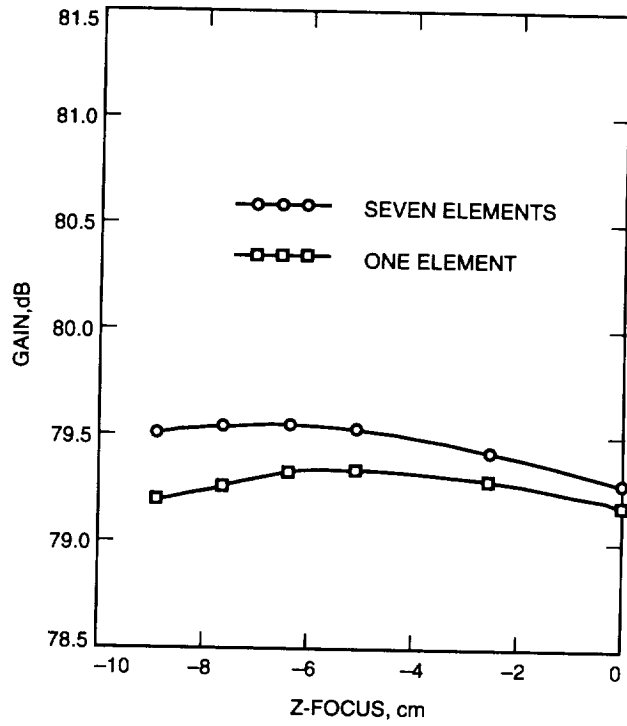
Fig. 12. Optimum antenna gain versus z (focus) at F3,
7.5-deg elevation angle (optimum horn diameter).
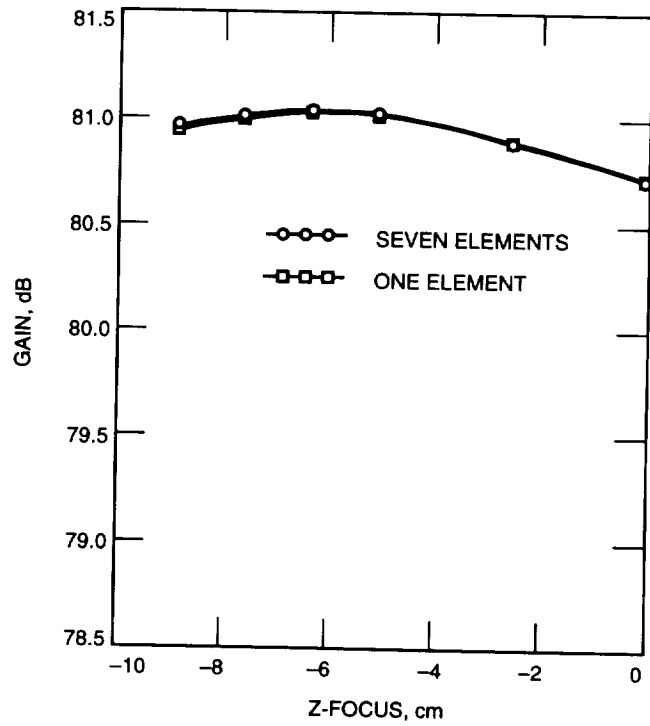
Fig. 13. Optimum antenna gain versus z (focus) at F3,
45-deg elevation angle (optimum horn diameter).
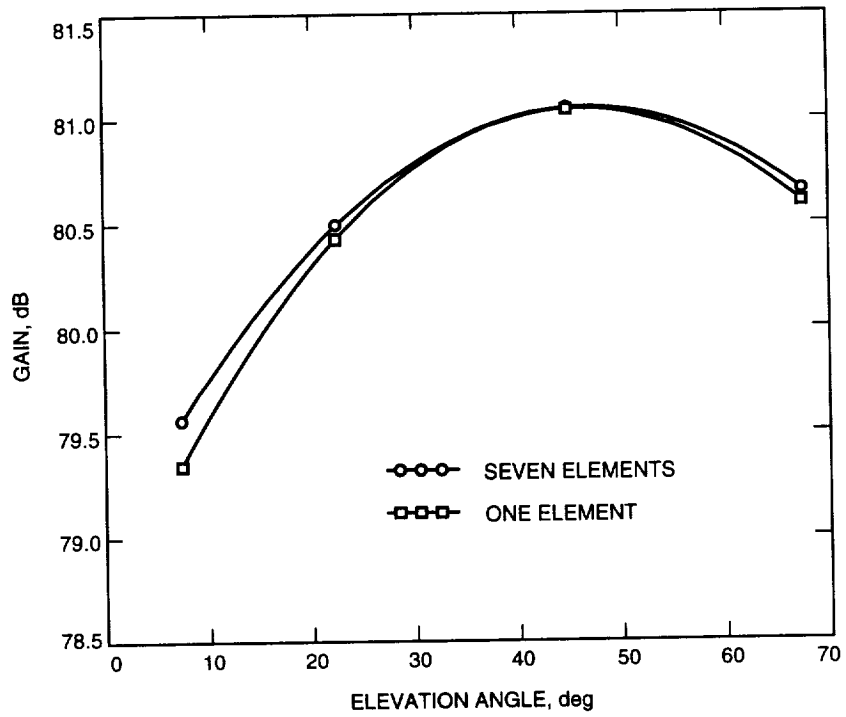
Fig. 14. Optimum antenna gain versus elevation angle (z (focus) = –6.35 cm, horn diameter = 5.309 cm).
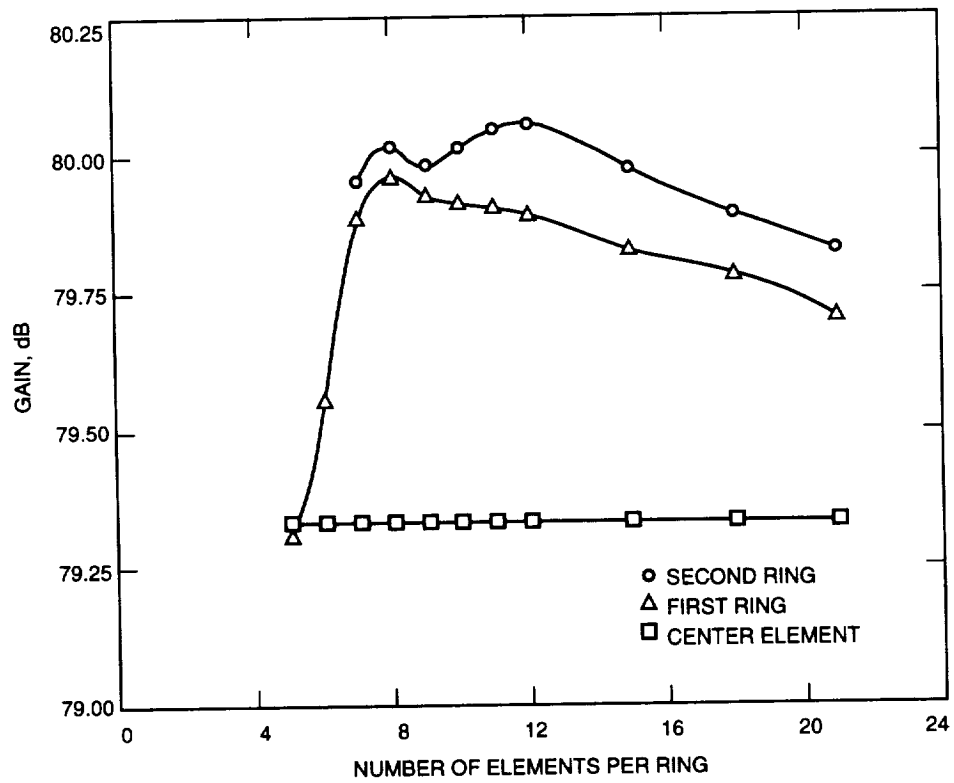
Fig. 15. Antenna gain versus number of array elements per ring (z (focus) = –6.35 cm, horn diameter = 5.309 cm, elevation angle = 7.5 deg).

For one ring of six horns, the improvement was 0.22 dB, as shown before. However, if the number is increased to eight horns, the improvement jumps to 0.63 dB and then drops off for a larger number of horns. Using 2 rings, an improvement of 0.72 dB can be gained for 12 horns in each ring. However, using the second ring, which implies a 25-horn array, only gives an improvement of 0.09 dB over the single-ring case, which is a 9-horn array. Therefore, the use of a second ring is not practical considering the increased complexity. The reason that increasing the number of horns makes an improvement can be seen by reviewing the focal plane distribution. Figure 16 shows the focal distribution overlaid with the outline of the 5.31-cm diameter horns in the seven-horn case. It can be seen that the center horn encompasses the region where the fields are best behaved. The horns in the outer ring, however, are so large that they cover an area where the fields slope across the aperture from −5 to −35 dB and, therefore, do a poor job of coupling the fields. The horns like to see a Gaussian distribution for best performance. Figure 17 shows the focal distribution overlaid with the outline of the horns for the eight horns-per-row case, where the center horn is 5.31 cm in diameter. Here the smaller horns in the first row do a better job of sampling the fields since the fields do not vary more than 10 to 15 dB across their apertures. The horns in the second row, however, cover regions where the fields are not well behaved and recover very little of the field energy. This case shows that increasing the number of horns by two can cause a significant improvement. However, it should be noted that the array geometry is driven by the focal distribution, which is unique for a given antenna system design and associated aberrations and, therefore, the results could be significantly different for other antenna designs. This case is interesting because it is an example of the type of cases that are amenable to the focal plane analysis technique.

In an earlier study, ray tracing techniques were applied to a seven-horn array, using the same geometry used in this article. It was found that with all the array horn axes parallel to each other at F3, at their image point at F1, the beams associated with the horns in the ring around the center horn pointed away from the antenna axis. This could be likened to an array located at F1 having all but its center horn rotated outward from the antenna axis. The effect is to improperly illuminate the antenna subreflector. At F3, it was found that by rotating all but the center horn inward by 2.62 deg in an aberration-free environment, all the beams at F1 could be made to be parallel. Another way of viewing this situation is that the phase patterns of the focal field distribution at F3 for a BWG antenna are not uniform, but tapered. The horns need to be rotated to better match the focal plane phase distribution. Since with optimum horn diameters the outer horns are only useful in the presence of antenna aberrations, it was of interest to see if rotating the horns could help in recovering more of the losses due to aberrations. At an elevation angle of 7.5 deg, a series of calculations was made, rotating all but the center horn inward. In Figure 18, it is shown that, for a seven-horn case, rotating the horns 5.2 deg inward improved the performance by 0.46 dB. A similar calculation was made for the case that had the optimum eight horns in the ring (nine-horn array). In this case, rotating the horns about 4.0 deg had little effect. Evidently, significant phase variations in the focal region were beyond the area covered by the smaller outer horns for the nine-horn array, but were within the region covered by the larger outer horns of the seven-horn array. Figure 19 shows the performance as a function of elevation angle for the seven-horn case, with the horn rotation angle set at 5.2 deg.

There are some asymmetries in the BWG geometry that are not significant to horns mounted on the antenna optical axis, but could be of concern for off-axis horns such as are used in an array feed system. Of concern was what effect these aberrations might have on the array performance as a result of a rotation of the antenna in azimuth. Azimuthal rotations cause a change in the relative rotational position of one section of BWG mirrors to another. Figure 20 shows the antenna performance at an elevation angle of 7.5 deg as the antenna rotates in azimuth. For the center horn only, the variation is only 0.04 dB, which is negligible. For the array, the variation is 0.13 dB, still not significant. The other issue is what happens when the array is rotated about its axis at F3. Does this affect the way the outer horns sample the focal fields? For example, is there an optimum angle? Calculations made on the 10-horn array showed variations on the order of 0.1 dB.
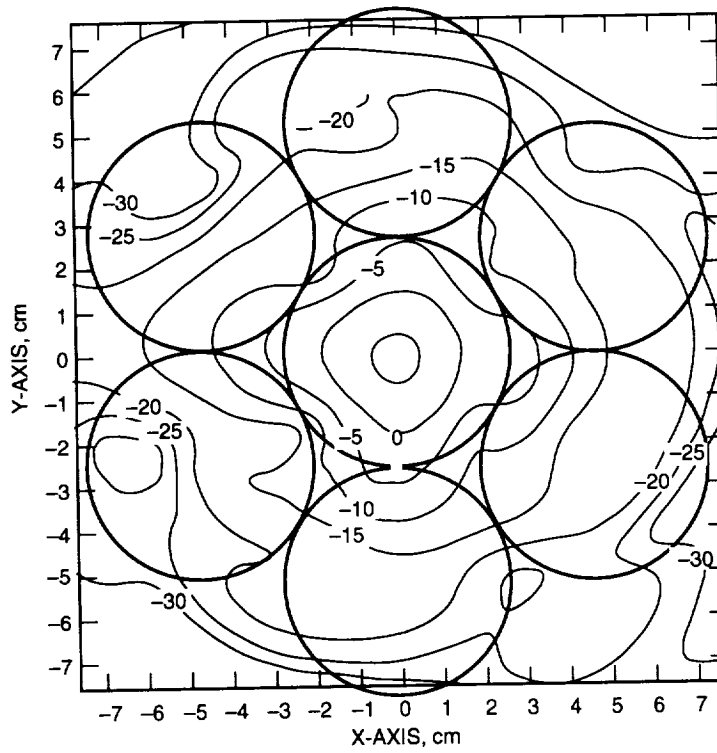
Fig. 16. The focal distribution overlaid with the outline of the horns for the seven-horn case (z (focus) = –6.35 cm, elevation angle = 7.5 deg, horn diameter = 5.309 cm).
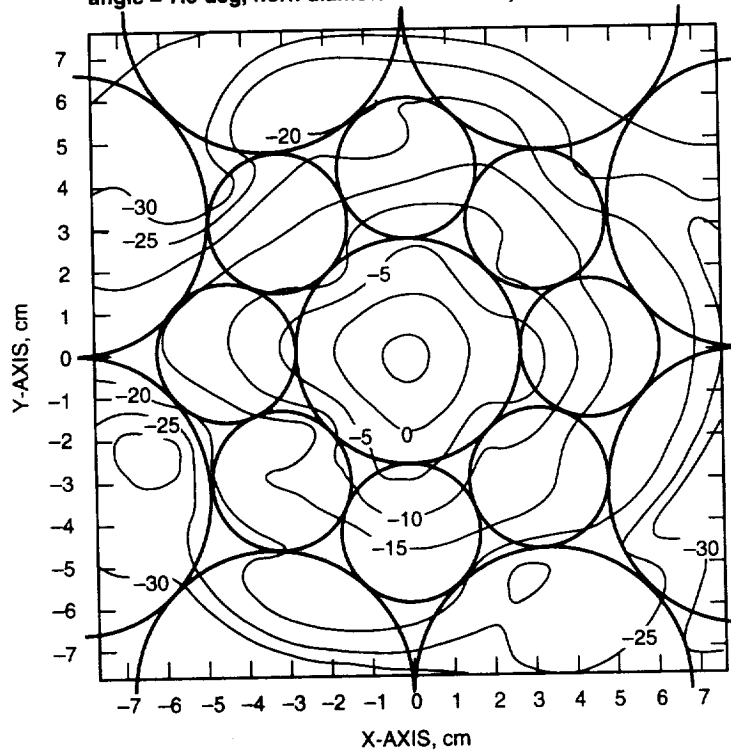
Fig. 17. The focal distribution overlaid with the outline of the horns for the eight horns-per-row case (z (focus) = –6.35 cm, elevation angle = 7.5 deg, horn diameter = 5.309 cm).

96
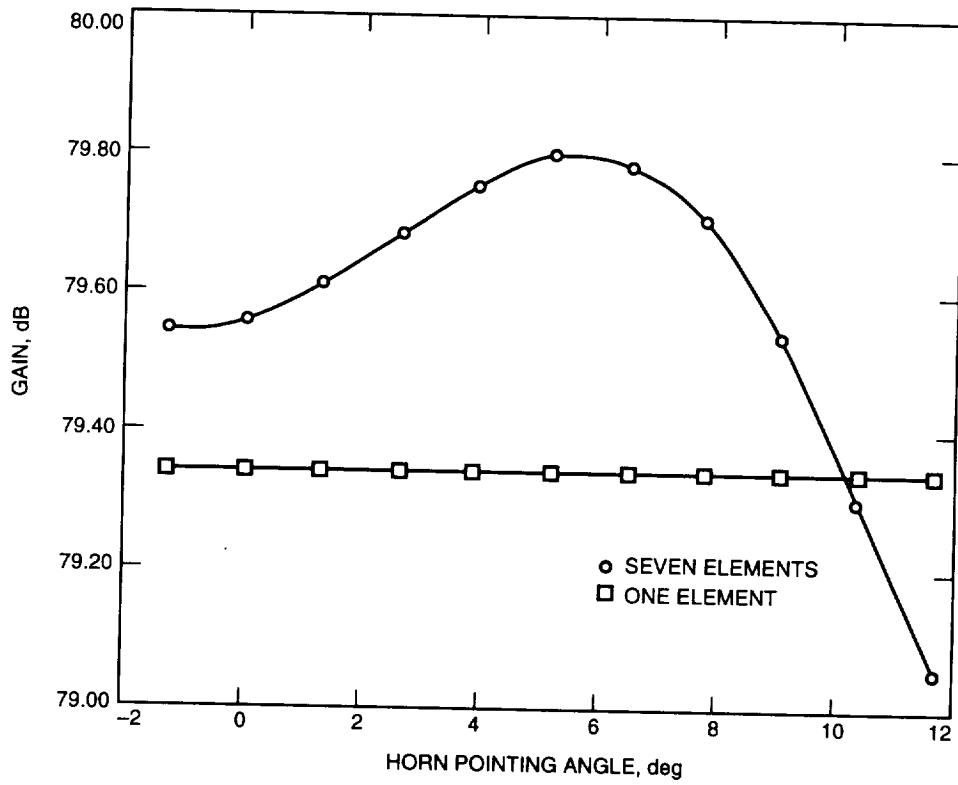
Fig. 18. Antenna gain versus horn pointing angle (z (focus) = –6.35 cm, elevation angle = 7.5 deg, horn diameter = 5.309 cm).
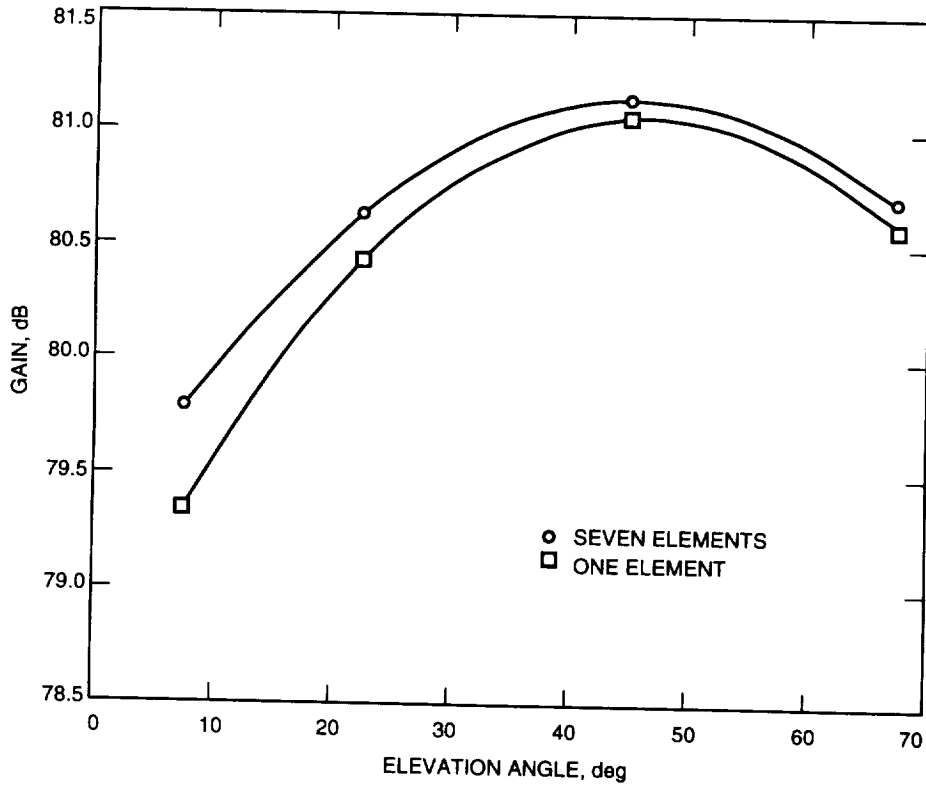
Fig. 19. Antenna gain versus elevation angle (horns pointed) (horn angle = 5.2 deg, z (focus) = –6.35 cm, horn diameter = 5.309 cm).
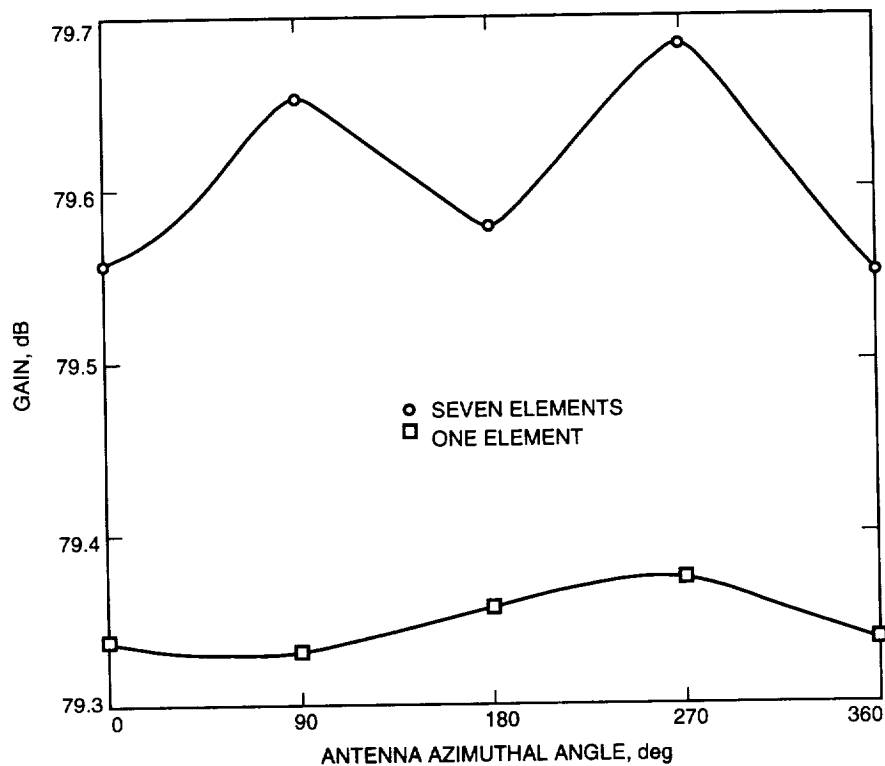
Fig. 20. Antenna gain versus antenna azimuthal angle (z (focus) = –6.35 cm, elevation angle = 7.5 deg, horn diameter = 5.309 cm).

Figures 21 and 22 display the focal plane fields for the antenna and are provided for general interest. Figure 21 shows the focal fields for antenna elevation angles of 7.5, 22.5, and 45 deg at the optimum axial focal position of −6.35 cm. The primary effect of elevation angle–induced distortions on the focal plane distribution is a lowering and spreading of the fields. At 45 deg, the field distribution is approximately rotationally symmetric. At F1, the distribution is perfectly circular, as is seen in Fig. 8. The lack of perfect circular symmetry shown in Fig. 21(c) is due to the effects of the BWG. Figure 22 shows the effect of axial focus changes on the focal fields at an elevation angle of 7.5 deg. There appears to be a rotation in the structure of the focal fields in the vicinity of the distribution main lobe as the focus is changed. Figure 22(b) shows the best focal position, where the array position is −6.35 cm.

VII. Analysis of Experimental Configuration

An experimental program, supported by another task, was performed at DSS 13 using a seven-horn array located at F3 that had the same geometry as used in this study, with one exception: The array horns were restricted to a nonoptimum diameter of 4.45 cm. Another difference is the dual-mode horns used in the experiment were designed for 32.0 GHz but operated at 33.67 GHz. This change in frequency degraded the pattern properties of the horns. Because of the degraded horn performance, the results presented in the previous section are not typical of what would be expected from the experimental program. To provide better predictions, different horn-mode models were developed to account for the change in performance. While the ratio of the TM_{11} mode to the TE_{11} mode was 0.405 for the dual-mode horns used in this study, to model the horns in the experimental program, a mode ratio of 0.206 with a phase of −71.73 deg was required.

Calculations were made to determine the best axial focal position for the array. Figure 23 shows the results for an elevation angle of 7.5 deg. For a single horn, the best position was −7.62 cm, and for
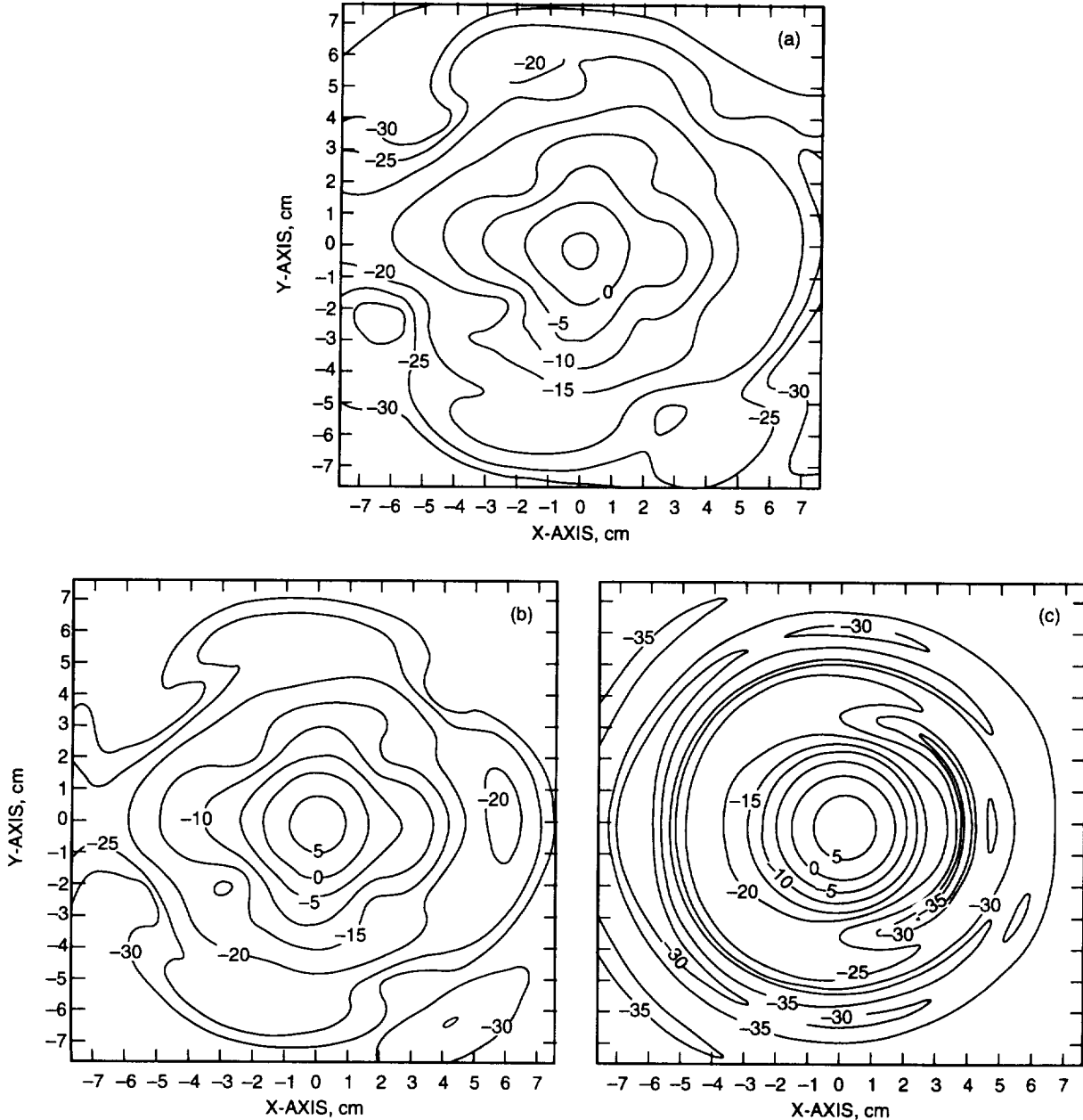
Fig. 21. The focal fields for antenna elevation angles of (a) 7.5, (b) 22.5, and (c) 45 deg (z (focus) = −6.35 cm).

a seven-horn array, the best position was −8.89 cm. Figure 24 shows results for an elevation angle of 45 deg, and, for both the single horn and for the array, the best focal position is −7.62 cm. Since the focus curve is essentially flat in the region of −8.0 cm and the experimental measurements were made at −8.89 cm, the predictions were calculated at −8.89 cm. Figure 25 shows the antenna gain as a function of elevation angle. At an elevation angle of 45 deg, the gain is 80.66 dB for a single horn and 80.70 dB for the array, for an improvement of 0.04 dB. At an elevation angle of 7.5 deg, the gain is 78.89 dB for a single horn and 79.39 dB for the array, for an improvement of 0.50 dB as compared with a loss due to surface distortions of 1.77 dB.

To determine if rotations of the antenna in azimuth would affect the performance of the array at F3, a series of calculations was made, where the azimuthal position of the antenna was changed in increments
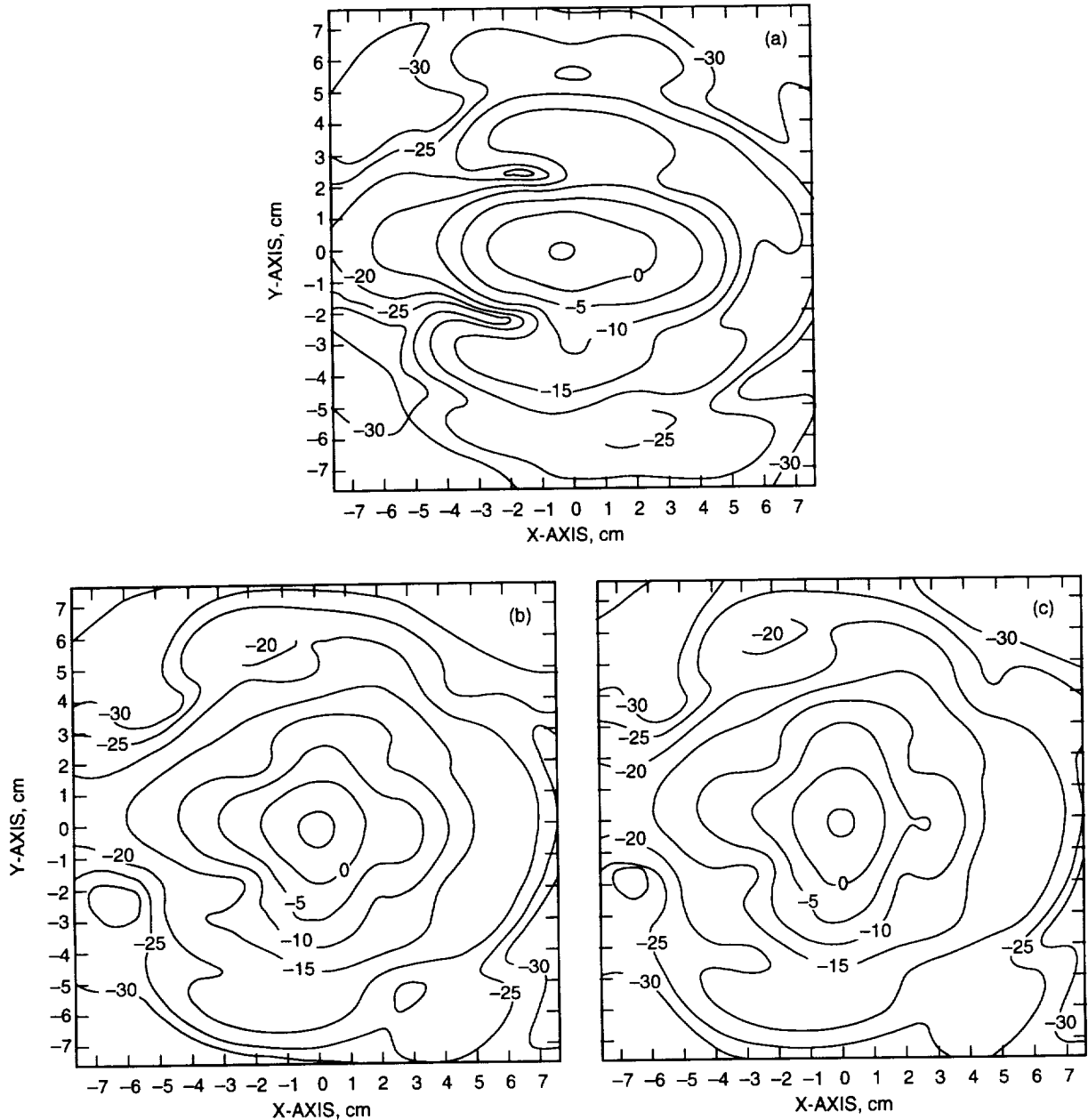
Fig. 22. The effects of axial focus changes on the focal fields at an elevation angle of 7.5 deg: (a) z = 0.0 cm, (b) z = –6.35 cm, and (c) z = –8.89 cm.

of 45 deg. For an elevation angle of 45 deg, the variation is 0.02 dB for both the center horn and the array. The performances for both the center horn and the array are the same since, at an elevation angle of 45 deg, the outer horns have very little effect. The variation in performance at an elevation angle of 7.5 deg is 0.03 dB for the center element and, for the array, 0.13 dB. To determine the best rotational alignment of the array at F3, the array was rotated about the optical axis at F3 in fractions of the angle subtended by the width of a horn aperture in the ring surrounding the center horn. A series of calculations in effect would rotate one horn into the position previously occupied by the next horn in the ring before the calculations began. For an elevation angle of 7.5 deg, the gain of the array varied by 0.16 dB. For optimal results, the array should be rotationally adjusted.
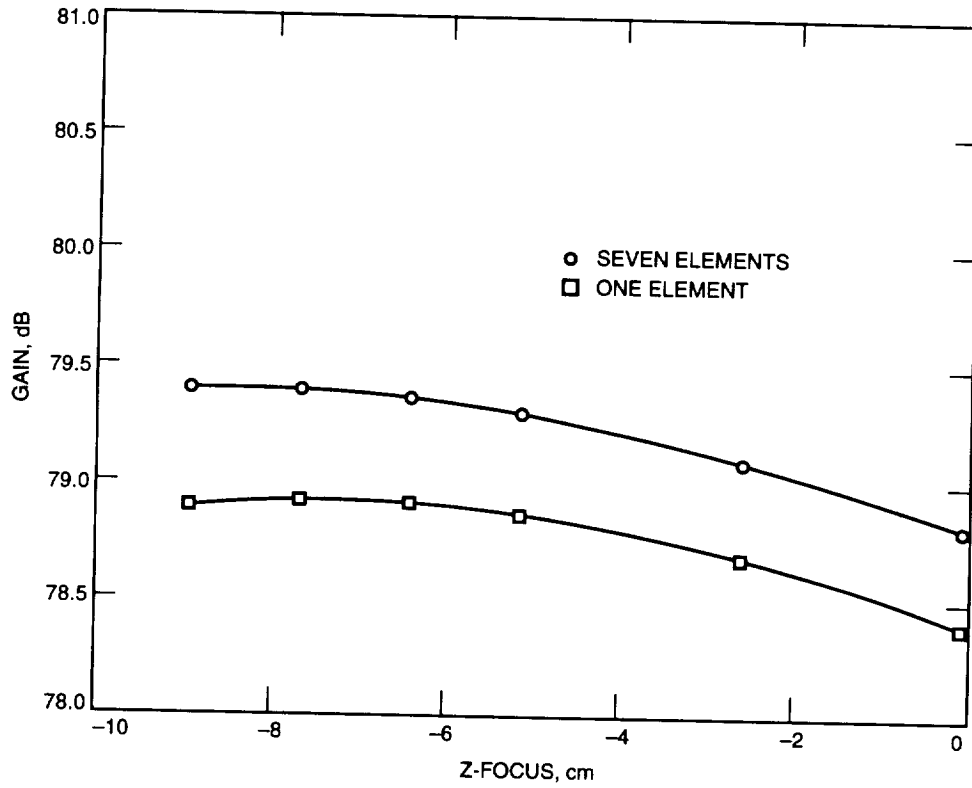
Fig. 23. DSS-13 antenna gain versus z-focus at F3, 7.5-deg elevation angle.
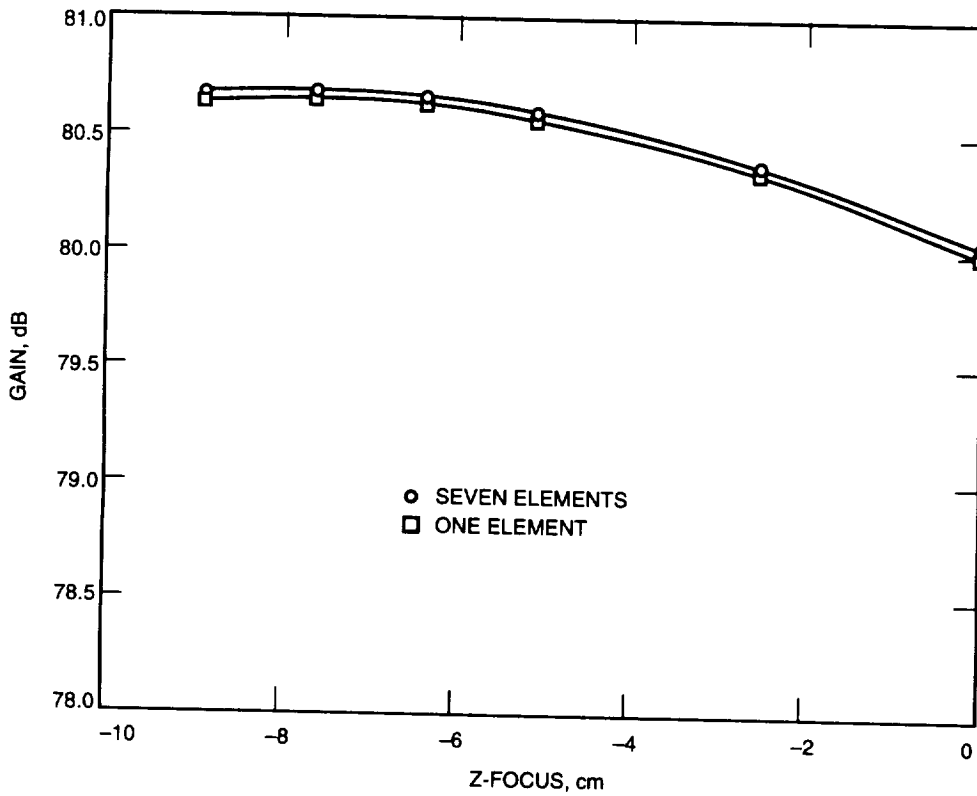
Fig. 24. DSS-13 antenna gain versus z-focus at F3, 45-deg elevation angle.
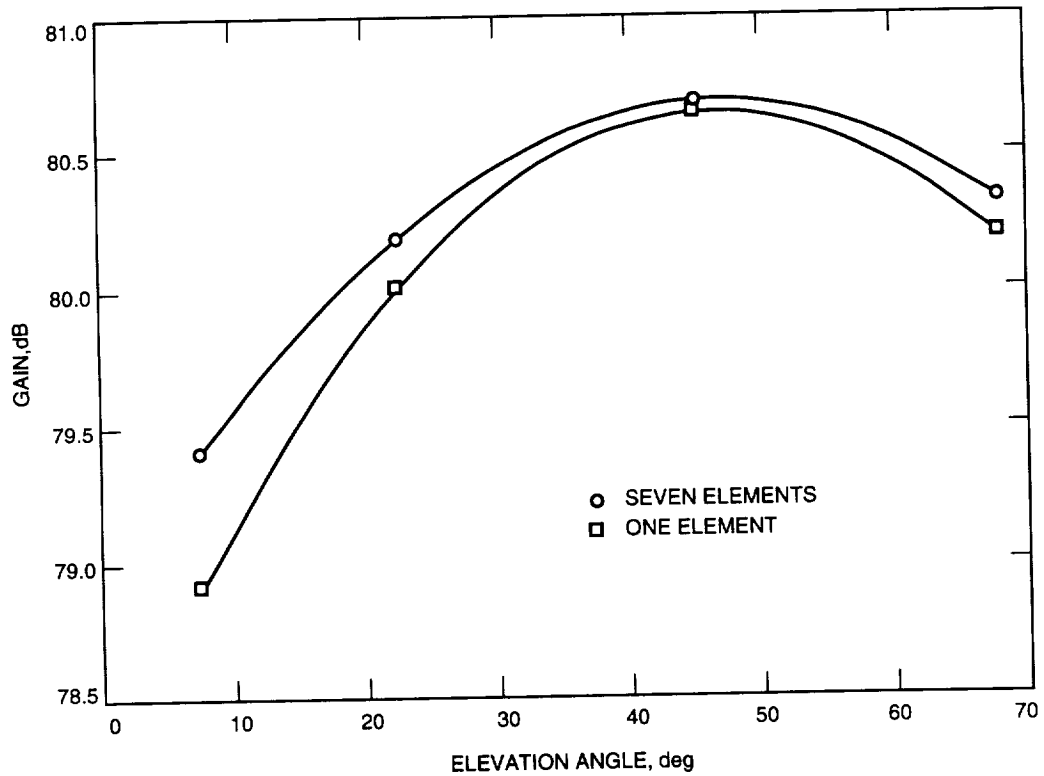
Fig. 25. DSS-13 antenna gain versus elevation angle: focus position, z = –8.890 cm.

VIII. Conclusions

The focal plane optimization technique was shown to provide a method of recovering performance losses for two antenna problems: (1) the aberration losses due to scanning the beam of an antenna and (2) the losses associated with antenna reflector distortions that result from changes in the antenna elevation position. The second case really demonstrates the power of the focal plane analysis technique. For the antenna configuration associated with the second case, it takes 5.6 h on a Cray Y-MP2 computer to perform one forward scattering calculation to determine the far-field pattern for a single-feed horn. The scattering calculation must be repeated seven times to include the effect of each array feed horn for a seven-horn array, requiring 39.2 h per antenna configuration. The time to compute the optimum gain from the far-field patterns for each feed horn is small compared to the scattering calculation time and will be neglected. If the process is repeated for 13 feed sizes, as was done in the example in Section VI.A of this article, a total time of 509.6 h is needed! The computation time required for the focal plane optimization technique can be determined as follows: Assume the time to do the reverse scattering calculation through the antenna and beam-waveguide optical system is the same as for the forward scattering case, or 5.6 h. The time required to calculate the currents in the focal plane to the required resolution is 3.3 h. This gives a one-time total time of 8.9 h, which does not have to be repeated unless the antenna geometry changes. The time required to perform the focal plane optimization that must be repeated for each feed size or array geometry ranged from 2 min for the smallest feed size to 33 min for the largest feed size and 22.5 min for the optimum feed size. The total time to perform the optimization calculation for all 13 feed element sizes studied was 2.7 h. The grand total time, including the scattering calculations, comes to 11.6 h. Reducing the computation time from 509.6 h to 11.6 h illustrates the usefulness of this technique. The objection can be raised that you do not need to consider so many element sizes to determine the optimum element size. But that is not the issue. There might also be a need to trade off the array geometry and/or the horn type, such as single mode, dual mode, hybrid mode, or any other type. This could result in the need to analyze more cases than the 13 element sizes considered in the example. The

point is that significant time savings can be obtained by doing the optimization in the focal plane for situations where the scattering calculation times are significant, such as is the case for beam-waveguide antennas where five or more scattering surfaces must be considered and where their sizes in terms of wavelengths are very large.

The focal plane approach is very accurate. Agreement between the focal plane or reverse scattering technique and the classical transmit approach was on the order of 0.02 dB.

Acknowledgment

References

[1] R. F. Harrington, *Time Harmonic Electromagnetic Fields*, New York: McGraw Hill, pp. 116–120, 1961.

[2] P. J. Wood, *Reflector Antenna Analysis and Design*, London, England: Peter Peregrinus Limited, Institution of Electrical Engineers, p. 190, 1980.

[3] Y. Rahmat-Samii, R. Mittra, and V. Galindo-Israel, "Computation of Fresnel and Fraunhofer Fields of Planar Apertures and Reflector Antennas by Jacobi–Bessel Series—A Review," *Journal of Electromagnetics*, vol. 1, pp. 155–185, April–June 1981.

[4] W. A. Imbriale and R. Hodges, "Linear Phase Approximation in the Triangular Facet Near-Field Physical Optics Computer Program," *Applied Computational Electromagnetics Society Journal*, vol. 6, no. 2, pp. 74-85, Winter 1991.

[5] P. W. Cramer, "Initial Studies of Array Feeds for the 70-Meter Antenna at 32 GHz," *The Telecommunications and Data Acquisition Progress Report 42-104, October–December 1990*, Jet Propulsion Laboratory, Pasadena, California, pp. 50–67, February 15, 1991.

On-Wafer, Cryogenic Characterization of Ultra-Low Noise HEMT Devices

J. J. Bautista
Radio Frequency and Microwave Subsystems Section

J. Laskar
University of Hawaii, Honolulu

P. Szydlik
State University of New York, Plattsburgh

Significant advances in the development of high electron-mobility field-effect transistors (HEMTs) have resulted in cryogenic, low-noise amplifiers (LNAs) whose noise temperatures are within an order of magnitude of the quantum noise limit (hf/k). Further advances in HEMT technology at cryogenic temperatures may eventually lead to the replacement of maser and superconducting–insulator– superconducting front ends in the 1- to 100-GHz frequency band. Key to identi- fication of the best HEMTs and optimization of cryogenic LNAs are accurate and repeatable device measurements at cryogenic temperatures. This article describes the design and operation of a cryogenic coplanar waveguide probe system for the characterization and modeling of advanced semiconductor transistors at cryogenic temperatures. Results on advanced HEMT devices are presented to illustrate the utility of the measurement system.

I. Introduction

The noise and gain of high electron-mobility field-effect transistor (HEMT) devices have steadily improved as the technology is being developed and commercialized worldwide for room temperature applications. Although device noise temperatures continue to drop at room temperature, there is no guarantee that the same improvements will occur at cryogenic temperatures. In order to successfully develop ultra-low noise HEMTs for cryogenic applications, one must have quick, accurate, and repeatable cryogenic data and a good device model.

The cryogenic on-wafer noise and scattering parameter measurement system under development is key to the systematic investigation of the dc and microwave properties of advanced HEMT devices. The measured parameters are required to evaluate and verify room temperature and cryogenic device models for the identification of the optimum cryogenic HEMT structure. The measured parameters along with the device models are also needed to design and optimize input, interstage, and output matching circuits for multiple-stage HEMT low-noise amplifiers (LNAs).

A cryogenic study and an empirical model for the cryogenic operation of an advanced pseudomorphic HEMT (PHEMT) device are presented. The original apparatus for making these measurements and the

new system currently under development are described. The methods for making accurate, high-frequency variable temperature scattering (45-MHz to 40-GHz) and noise parameter (2-to 18-GHz) measurements from 11 to 300 K are discussed. Details of the experimental technique, including calibration considerations, are also presented.

II. Cryo-Probe Measurement System

Over the past several years, the development of a complete on-wafer cryogenic microwave measurement system has been primarily driven by the need for (1) greater understanding of the device physics in advanced high-speed transistor technologies, (2) continued advancement of cryogenic LNAs with noise temperatures less than five times the quantum limit ($T_n < 5hf/k$) for ground and space-based applications, and (3) hybrid and monolithic microwave integrated-circuit (MMIC) semiconductor–superconductor circuits.

In 1976, Liechti and Larrick [1] designed a microwave test fixture that could be immersed in liquid nitrogen. Similar types of setups have been used [2–7] to evaluate HEMT performance from 300 to 15 K. To date, it has been difficult to make broadband scattering (S)-parameter measurements in such an environment, due to the limited accuracy of the full two-port calibrations.

The cryogenic microwave system in this work uses coplanar waveguide probes in a vacuum station coupled to a vector network analyzer for scattering parameter measurements, and a noise meter and noise test set with a noise system for microwave noise parameter measurements. The microwave measurement system currently under development, schematically shown in Fig. 1(a), incorporates measurement tools originally developed for the first system in 1989 [8,9]. The cryogenic probe measurement system, shown in Fig. 1(b), contains ports for RF cables, thermometers, vacuum pumps, dry nitrogen back-fill lines, coplanar probes with manipulators, and a closed-cycle refrigerator cold head. The probe body, shown in Fig. 1(c), rests on a copper block attached to a fiberglass post. The fiberglass reduces the thermal load, and copper braiding from the cold head thermally anchors the probe to the 12-K cold station, assuring sample temperatures of 12 to 20 K. The mechanical and thermal stability of the wafer stage is established by supporting it on fiberglass posts above the cold head and thermally anchoring it to the cold station with flexible copper braids.

The most important feature of this design is the incorporation of a closed-cycle helium refrigeration system. The first successful designs of on-wafer cryogenic systems used open-cycle cooling to reduce start-up costs and avoid mechanical vibrations. However, for long term use at the rate of one cool down per week, a closed-cycle system is significantly less expensive. In fact, after the first 6 months of operation, the savings in liquid helium is comparable to the price of a the closed-cycle refrigerator. Decoupling and damping of the vibrations from the cold head to the probe station are accomplished with a two-dimensional bellows and vibration mounts, shown in Fig. 1(b). This system allows small-signal microwave measurements from dc to 40 GHz over a physical temperature range of 16 to 300 K. Since the microwave hardware is insulated by vacuum, there are no frost buildup or large thermal gradients, resulting in a system that is accurate, reliable, and flexible (active and passive discrete devices as well as MMICs can be measured).

III. Calibration and Measurement Considerations

The key to accurate on-wafer microwave and millimeter-wave measurements is proper establishment of the electrical reference plane. The reference plane can be determined with either the line-reflect-match (LRM) or the short-open-load-thru (SOLT) calibration method using an impedance standard substrate (ISS) available from Cascade Microtech [10]. The LRM method requires fewer standards, and the reflect standards need not be well known. In addition, experience has shown that the LRM calibration is slightly better in accuracy than is the SOLT at cryogenic temperatures. In the SOLT method, the short standard

(a)

| CASCADE MILLIMETER-WAVE ROOM TEMPERATURE PROBE SYSTEM 1 TO 75 GHz | ↔ | HEWLETT PACKARD (HP)85109E75 AUTOMATIC NETWORK ANALYZER | ↔ | PC CONTROLLER DC AND RF PARAMETER EXTRACTION |

ATN ON-WAFER LOW-NOISE TESTING 2 TO 26 GHz (20 TO 300 K)

CRYOGENIC MILLIMETER-WAVE PROBE SYSTEM (20 TO 400 K) (1 TO 75 GHz)

HP 730X WORKSTATION ELECTROMAGNETIC AND CIRCUIT SIMULATION

(b)

MICROSCOPE

WAFER SAMPLE CHAMBER AT 25 K

CRYO-PROBE MANIPULATOR

CRYO-PROBE MANIPULATOR

VACUUM PUMP OUT

VIBRATION ISOLATION BELLOWS

CTI MODEL 350

(c)

RF INPUT/OUTPUT CONNECTOR

THERMALLY ISOLATED SUPPORT ARM

COPLANAR PROBE TIP

DIODE THERMOMETER

12 K THERMAL STRAP

Fig. 1. Cryo-probe (a) measurement system, (b) system, and (c) tip.

introduces uncertainty in the reference plane location because of sensitivity to probe tip placement. The LRM method obviates this problem by replacing the short with an open and by having the probe tip held approximately 10 mils above the substrate during the calibration sequence.

The measurement accuracy is also directly related to the calibration conditions. Thermal gradients across the gold-plated ceramic probe tips and coax to coplanar transitions [11] alter the electrical characteristics of the measurement lines. The process of cooling the sample in the laboratory can also produce changes in the calibration. The network analyzer typically requires a new calibration if the ambient laboratory temperature varies by greater than ± 1 deg C. The proximity of the cooled probe system to the network analyzer can change the ambient environment (both temperature and humidity). The combined results of these effects are appreciable errors in cryogenic temperature measurements. For example, room temperature calibrations have been shown to introduce as much as a 20-percent [8] error in the cryogenic measurement. In addition, measured results have been reported with room temperature calibrations with moding effects [11,12] and deviations from one-pole roll-off [4,11].

Since the microwave probe offers a significant thermal load to the device under test, it is evident that the chuck and device temperatures are different. For example, with a chuck temperature of 20 K and the probes contacting the device under test (DUT), a DUT temperature as high as 50 K has been observed. This large temperature differential affects calibration and skews the interpretation of data collected at different device temperatures.

The solution to maintaining calibration integrity and achieving low sample temperatures is to thermally anchor the probe body and perform cryogenic calibrations. By thermally anchoring the probe to the cold head at 12 K, the thermal load to the DUT is minimized. The remaining microwave hardware [connectors, cables, and input to the automatic network analyzer (ANA)] are thermally isolated via vacuum and stainless steel hardware. The thermally anchored probe can be calibrated at specific temperatures during a measurement cycle. This eliminates the problem of moding (deviation from one-pole roll-off) and allows accurate correlation of DUT temperature and measured characteristics. The S-parameter data shown in Fig. 2 are an example of data collected in this manner.

A reliable cryogenic, two-port calibration for S-parameter measurements must satisfy several criteria. The return loss of the transmission through standard should be better than −45 dB, and the insertion loss should vary within ±0.1 dB of 0 dB. Next, the calibrated open standard, as noted in the previous paragraph, should also be within ±0.1 dB of 0 dB, as shown in Fig. 3. A more extensive verification can be performed by evaluating additional representative elements not used in the calibration sequence. These measurements may include the reflection from a coplanar transmission line (open circuit stub) and a 10-dB pad. The input and output scattering parameters of the open circuit stub should be concentric spirals on the Smith Chart, with a magnitude of less than 1 and the insertion loss of the pad within ±2 percent of 10 dB.

The most accurate and repeatable method of measuring noise parameters at cryogenic temperatures is to place the impedance generator within a wavelength of the DUT input. The equivalent noise temperature of the noise source must also be comparable to the DUT noise temperature. This approach would, however, require development of a cryogenic noise generator and noise source.

For this initial investigation of on-wafer noise parameter measurements at cryogenic temperatures, only the probe tips are cooled while the impedance state generator and solid-state noise source (both commercially available) are kept at room temperature (several wavelengths away from the DUT). In this configuration, the input losses introduce noise comparable to or greater than the noise of the device under test (DUT) and reduce the range of available impedance states. For example, in the frequency range of 2 to 18 GHz for cryogenic temperatures, the worst-case noise temperature error is ±25 K, while device noise temperatures are typically under 10 K. Although this configuration does not provide accurate single-frequency noise parameter measurements, it does provide for fast and efficient broadband

$\Box = S_{11}$ $\Diamond = S_{12}$

$+ = S_{21}$ $\times = S_{22}$

$Z_0 = 50.0$

—— 300 K   •••• 45 K
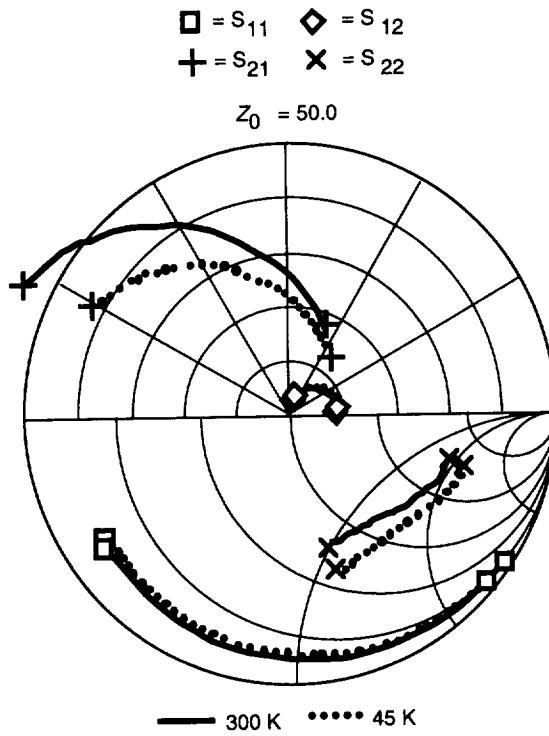
Fig. 2. Cryo-probe measured scattering parameters of an HEMT device at 300 and 45 K from 2 to 20 GHz.

FREQUENCY, GHz
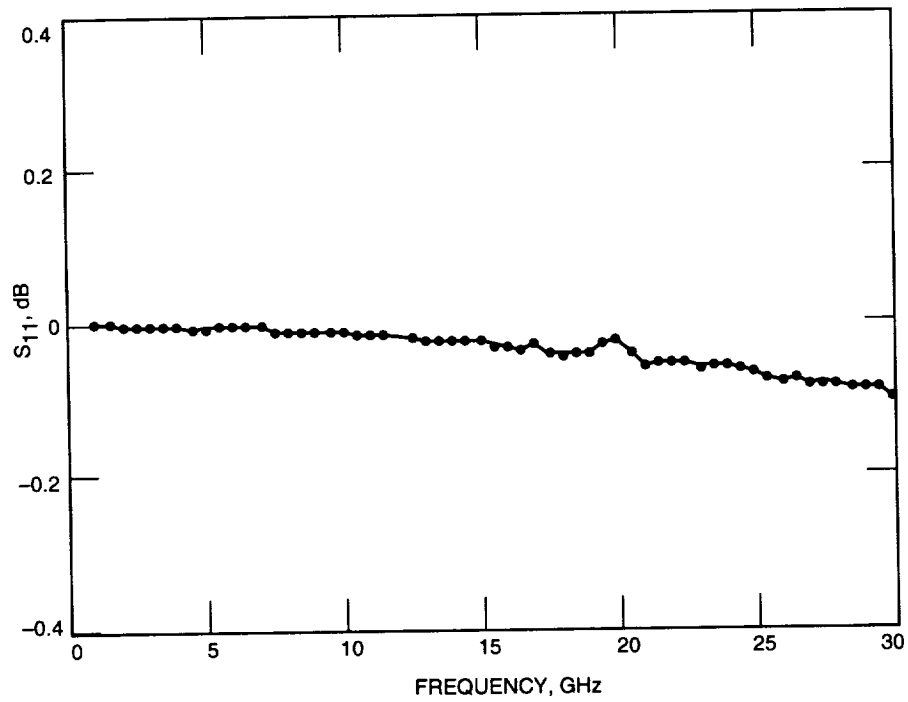
Fig. 3. Variation in open standard at a physical temperature of 20 K using LRM calibration.

108

(2- to 18-GHz) on-wafer measurements. The noise calibration must pass all the S-parameter calibration criteria and accurately measure the minimum noise temperature (T_m) and associated gain (G_A) of a 10-dB attenuator. An example of the insertion loss of a 10-dB attenuator is shown in Fig. 4. For the noise calibration, the T_m and G_A should be repeatable to within ±5 percent for the attenuator at a variety of temperatures.

IV. Small-Signal Modeling

A detailed knowledge of the HEMT small-signal equivalent circuit is necessary for designing high-speed circuits and low-noise amplifiers and for understanding the device physics. There are three main methods for small signal parameter extraction: (1) complete parameter extraction from calculations on the measured S-parameters [13], (2) parameter extraction based upon iterative computer optimization routines, and (3) a combination of (1) and (2) where as many elements as possible are quickly identified, providing constraints to the software optimization routine that serves as the validity check.

All of the above methods can be applied to the standard HEMT small-circuit model, the hybrid-π circuit topology [14]. The small-signal elements in Fig. 5 are broken down into the intrinsic and extrinsic elements. The intrinsic elements are the transconductance, g_m; output conductance, g_{ds}; gate-source capacitance, C_{gs}; gate-drain capacitance, C_{gd}; drain-source capacitance, C_{ds}; gate-source resistance, R_{gs}; and delay time, τ. These elements are bias dependent and important to the understanding of device behavior. The extrinsic elements are independent of bias and include the three terminal inductances, L_g, L_d, and L_s, the contact resistances for the three terminals, R_g, R_d, and R_s, and the parasitic pad capacitances, C_{pg} and C_{pd}.

The simplest and most straight-forward method is the complete parameter extraction method. It has been shown that, with a sequence of microwave and dc measurements, each term can be uniquely determined [13]. A so-called shell technique can be applied to remove the inductances, the pad parasitics, and the contact resistances. For this technique, the S-parameters of the device are measured for a variety of drain-to-source voltage conditions. By using the simplifying assumptions that $\omega^2 C_{gs}^2 R_{gs}^2 < 0.01$ and that $\omega\tau << 1$, one can determine the parasitic elements uniquely, leaving only the intrinsic circuit to be determined. The drawbacks to this method are that several measurements must be made under different bias conditions and simplifying assumptions must be made, increasing the uncertainty of the extracted parameters.

The second method of extraction is to simply fit the measured S-parameters to the equivalent circuit by iteratively solving for the individual elements. The disadvantage to this technique is that, with such a large parameter space, it is very difficult to uniquely identify each element. This frequently produces unrealistic values for a number of the circuit elements.

The most desirable and accurate method is to apply the techniques from the complete parameter extraction method coupled with small-signal circuit optimization routines that serve as a validity check. The important parasitics are estimated by measuring a simple test structure and by independent dc measurements. Although a test structure for the parasitic elements was not available, this was the method used for this work, and it is described in more detail in the next section.

V. Measurement Results

For this device study, a passivated, planar doped pseudomorphic 0.25×75 μm (gate length × width) HEMT manufactured by GE was selected. This structure is grown on a semi-insulating GaAs wafer. To inhibit impurity diffusion into the active InGaAs region, the first layer grown is a 1-μm thick GaAs buffer layer. A spacer layer of undoped AlGaAs 45 Å thick is grown between the doping and the active region to reduce dopant donor ion/conduction electron interactions. The silicon dopant concentration
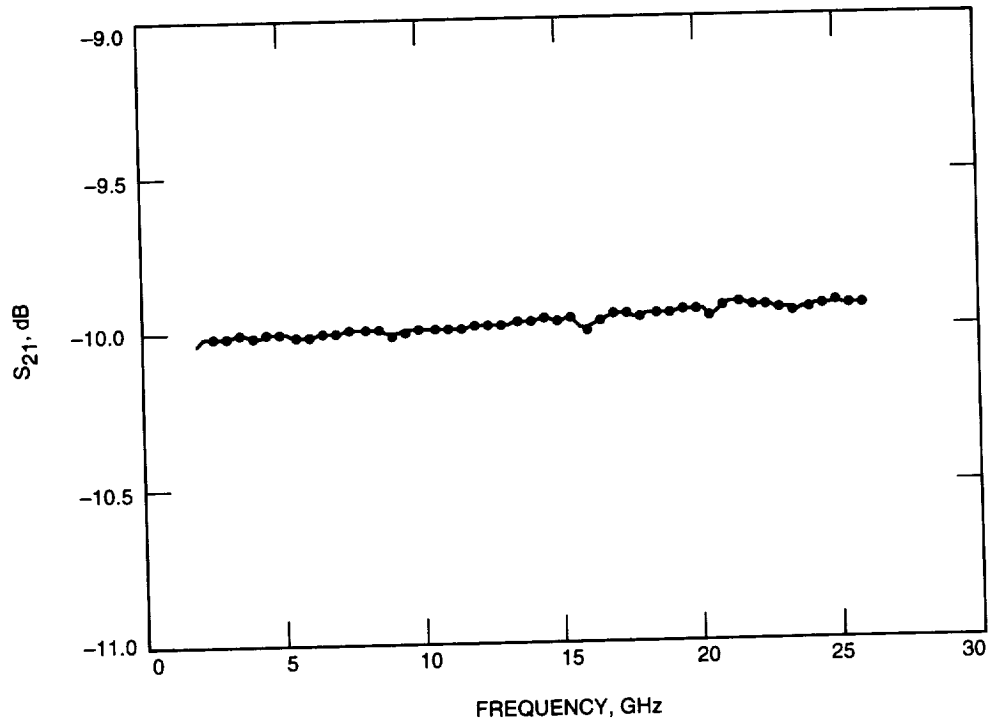
Fig. 4. Transmission through a 10-dB attenuator at a physical
temperature of 20 K using LRM calibration.
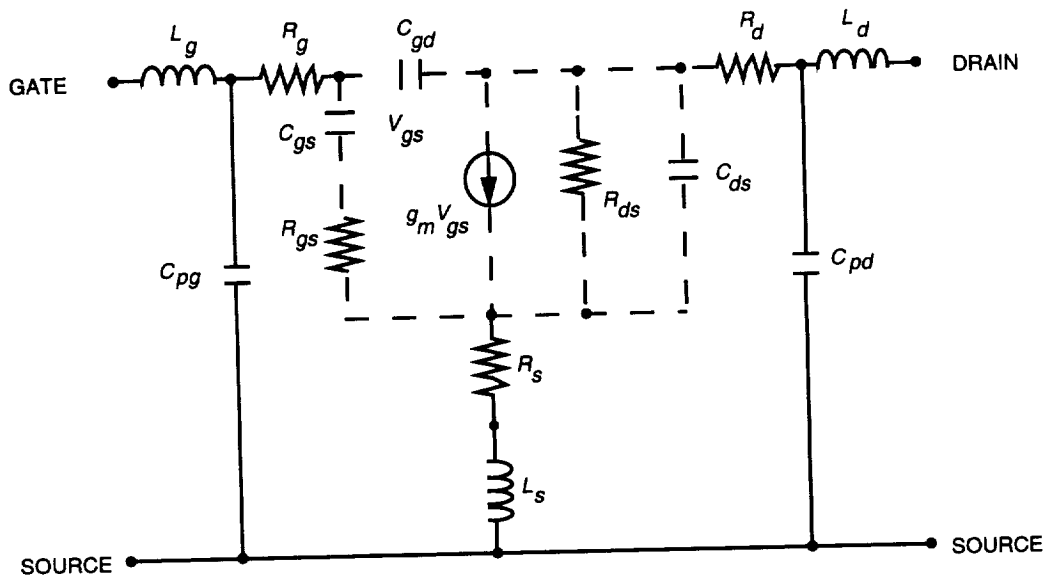
Fig. 5. Small-signal circuit diagram of PHEMT showing intrinsic and extrinsic elements.

of 3×10^{12} atoms/cc is grown in a single plane approximately 3 Å thick. Heavily doped AlGaAs and GaAs layers 400 and 350 Å thick, respectively, are grown to provide ohmic contacts. A schematic representation of this heterostructure is shown in Fig. 6. This layered structure produces a conduction band discontinuity that forms a triangular one-dimensional quantum well at the AlGaAs/InGaAs heterojunction.
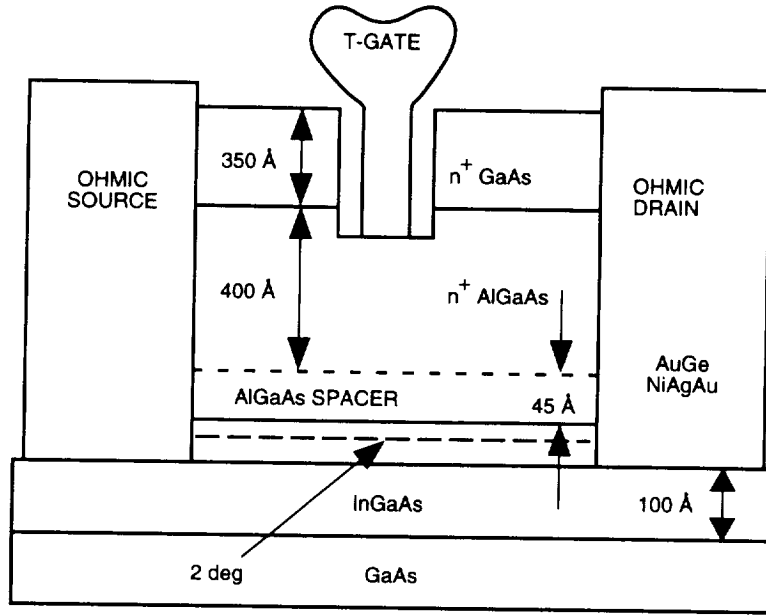
Fig. 6. Schematic representation of the PHEMT.

The noise and scattering parameters were measured for a variety of temperatures and bias conditions over a broad frequency span. Scattering parameters were measured from 1 to 25 GHz, while noise parameter measurements were attempted from 2 to 18 GHz for the same bias and temperature conditions. For all of the experimental conditions, all the S-parameters were measured with an error of less than 2 percent. A polar plot comparing S_{21} at two physical temperatures, 16 and 300 K, is shown in Fig. 7. Unfortunately, all four noise parameters could not be reliably measured for the physical temperature and frequency spans of interest. At room temperature, all four noise parameters were obtained. A plot from 2 to 18 GHz showing the scatter in the measured optimum source impedance (real part $= RE[\Gamma_{opt}]$; imaginary part $= IM[\Gamma_{opt}]$) at room temperature is displayed in Fig. 8. At cryogenic temperatures, however (as discussed in Section III), because of the lossy input and long electrical distance of the impedance generator from the device input, only the minimum noise temperature was reliably determined. In fact, at the lower frequencies (2 to 8 GHz) and physical temperatures (11 to 39 K) the percentage error in the noise parameters was too large ($\approx$ 80 percent) to be useful. For frequencies above 8 GHz, the percentage error in the minimum noise temperature was determined to be less than 25 percent. The resulting measurements were then fit to a straight line. The fitting error varied from 6 to 11 percent. Figure 9 shows a plot of the measured minimum noise temperature as a function of percentage drain to source saturation current at 18 GHz at five physical temperatures, from 16 to 300 K. Over this temperature range, the rms error in the minimum noise temperature varied from $\pm$ 12 K to $\pm$ 6 K.

For this study, the device small-signal circuit elements were determined using two sets of measured S-parameters and with the measurement probes calibrated with LRM standards at the physical temperatures of interest. The first set, or cold FET ($V_{ds} = 0$), measurements determine the bias independent extrinsic elements, while the biased device measurements are used to determine the intrinsic elements. All of the extracted elements for the different physical temperatures and bias settings are displayed in Table 1 along with $R_t(R_s + R_g + R_{gs})$, estimated T_d, and the calculated T_{min} per unit frequency.

To determine the uniqueness of the extracted intrinsic circuit elements, the extraction algorithm was run several times and the results compared. For this test, the extrinsic elements were kept constant and initial starting values for a variety of the intrinsic elements were purposely chosen to be up to a factor of two larger or smaller than the final value. For all the cases tried, the worst variation of any of the
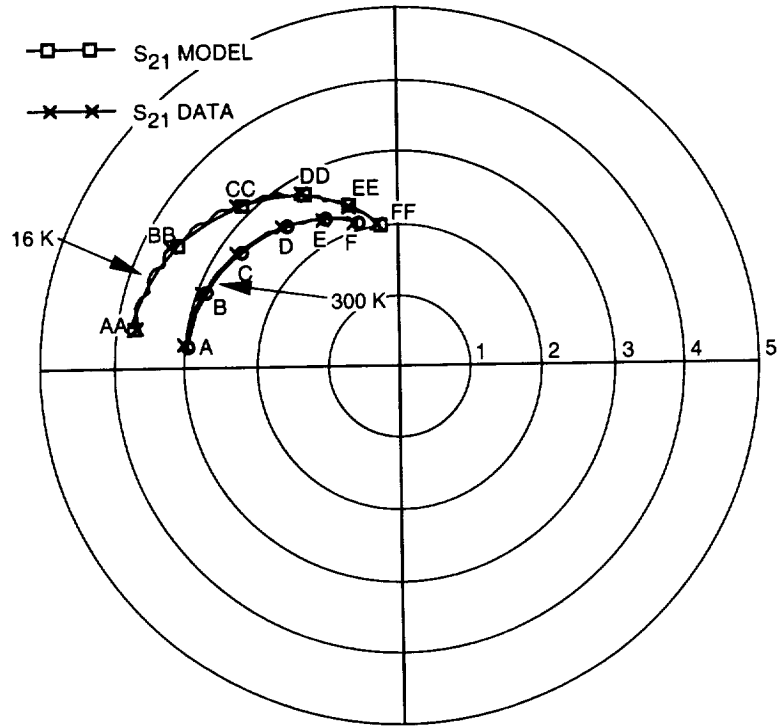
Fig. 7. A comparison of S_{21} for the PHEMT, at 16 and 300 K (frequency: 2 to 25 GHz).
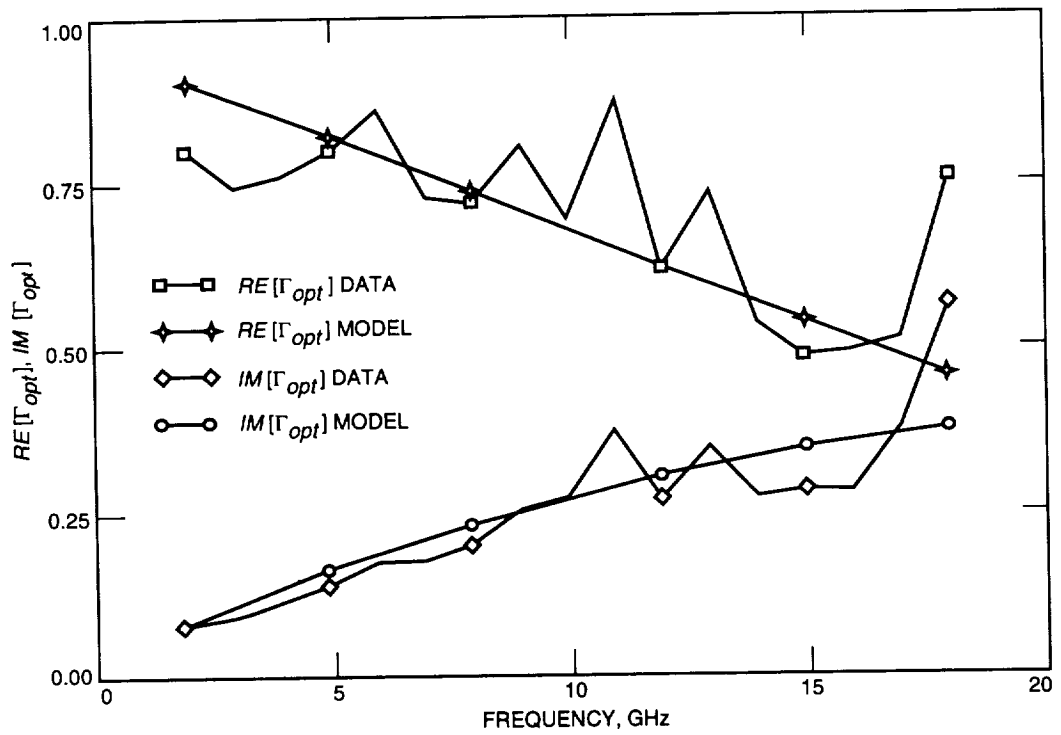
Fig. 8. Scatter in the measured optimum source impedance at room temperature (2 to 18 GHz).
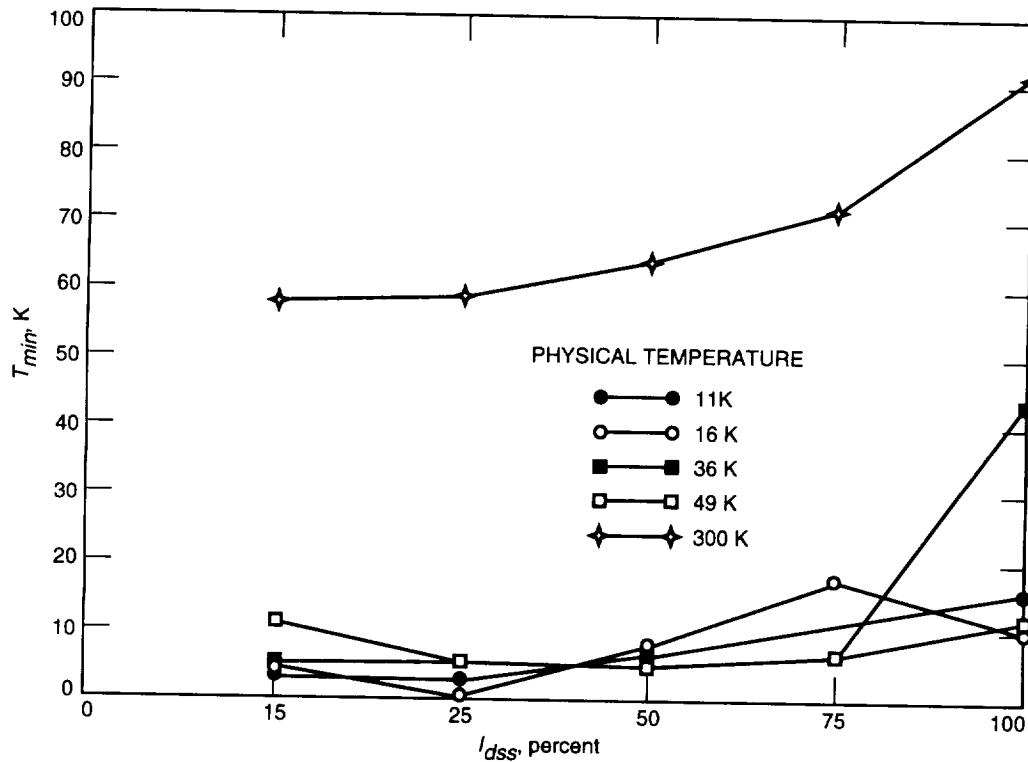
Fig. 9. Measured noise temperature at 18 GHz at several temperatures.

intrinsic elements was no more than 2 percent. Additionally, S-parameters for a biased device were used to simultaneously extract both intrinsic and extrinsic element values. In this case, for the same value of fitting error, some of the element values varied as much as 110 percent for R_{gs} or as little as 5 percent for C_{gs}.

VI. Analysis and Discussion

The pioneering work of Weinreb and Pospieszalski [15,16] has led to the development of HEMT-based LNAs that are the lowest noise transistor circuits produced to date. These impressive results have been achieved without the benefit of cryogenic, broadband noise measurements. Pospieszalski's method relies on dc cryogenic measurements (g_m and R_{ds}), manufacturers or measured room-temperature broadband S-parameter data (remaining circuit elements), and a single-frequency cryogenic noise-parameter measurement (T_d and T_g) to determine all of the circuit parameters for his empirical noise model.

For the Pospieszalski noise model [17], the measured noise parameters are required to determine T_d, the equivalent drain temperature associated with g_{ds}, and the equivalent gate temperature T_g associated with R_{gs} and as an additional check on the intrinsic element values. Pospieszalski [18] found that, for a variety of different HEMT and FET devices, T_g was equal to the ambient temperature for I_{ds} less than 20 mA. On the other hand, T_d is strongly dependent on I_{ds} and, within measurement error, a single function may describe its dependence for all devices. (At room temperature, using on-wafer noise and scattering parameters from 4 to 18 GHz, Pospieszalski used measured and modeled values for the intrinsic R_{opt} and T_{min} using a least-squares fit to arrive at values of T_d and T_g.)

Ideally, for low-noise device studies and circuit modeling, it is preferable to have both broadband measured noise and scattering parameters. Since only the measured minimum noise temperatures were obtained, only the predicted and measured noise temperatures as a function of drain currents (I_{ds}) at

Table 1. Extracted elements for the different physical temperatures and bias settings.

I_{dss}, %	I_{dss}, mA	L_d, pH	L_g, pH	L_s, pH	R_d, Ω	R_g, Ω	R_s, Ω	C_{ds}, fF	C_{gd}, fF	C_{gs}, fF	G_m, ms	R_{ds}, Ω	R_{gs}, Ω	R_t, Ω	T_d, K	T_{min}/f, K/GHz
								$T_{phys} = 11$ K								
15	2.9	4	15	4	5.0	3.8	1.00	17.20	22.90	76.50	39.70	576.70	1.00	5.80	234	0.123
25	4.7	4	15	4	4.6	3.8	1.00	17.40	22.20	84.30	50.30	450.00	1.00	5.80	373	0.153
50	9.6	4	15	4	4.7	3.5	1.00	17.30	21.60	91.40	65.00	370.00	1.00	5.50	750	0.196
75	14.9	4	15	4	6.7	3.0	1.00	18.80	21.20	92.20	72.00	344.20	0.70	4.70	1158	0.212
100	18.7	4	15	4	6.0	3.0	1.00	19.00	19.72	103.00	72.00	331.80	1.50	5.50	1451	0.292
								$T_{phys} = 16$ K								
15	2.4	4	15	4	6.0	3.0	2.00	18.80	31.10	68.60	36.25	589.00	2.00	7.00	201	0.147
25	3.9	4	15	4	6.0	3.0	1.00	17.00	31.00	71.00	45.30	480.00	2.00	6.00	316	0.157
50	8.4	4	15	4	6.0	2.0	1.00	17.90	30.40	78.70	60.90	368.00	2.00	5.00	663	0.195
75	12.7	4	15	4	6.0	3.0	1.00	15.70	30.10	80.80	68.50	344.80	2.00	6.00	994	0.247
100	16.4	4	15	4	6.0	3.0	2.30	17.60	25.50	123.60	67.00	303.00	2.00	7.30	1279	0.515
								$T_{phys} = 36$ K								
15	2.5	4	15	4	6.0	3.0	2.27	22.25	24.77	72.19	35.07	625.75	11.21	16.48	229	0.381
25	4.1	4	15	4	6.0	3.0	2.27	21.42	24.41	80.78	47.44	469.76	7.92	13.19	352	0.403
50	8.3	4	15	4	6.0	3.0	2.27	21.88	23.39	92.24	64.56	352.77	6.00	11.27	675	0.500
75	12.5	4	15	4	6.0	3.0	2.27	15.47	29.67	90.21	74.60	298.41	5.50	10.77	999	0.547
100	16.4	4	15	4	6.0	3.0	2.27	16.91	24.56	133.61	66.91	303.99	5.50	10.77	1299	1.021
								$T_{phys} = 49$ K								
15	2.2	4	15	4	6.0	3.0	2.27	21.83	24.93	72.19	35.42	526.80	10.88	16.15	218	0.464
25	3.7	4	15	4	6.0	3.0	2.27	21.51	24.39	71.92	47.40	468.31	7.20	12.47	334	0.398
50	7.5	4	15	4	6.0	3.0	2.27	21.88	23.39	92.24	64.56	352.77	6.00	11.27	627	0.562
75	11.1	4	15	4	6.0	3.0	2.27	20.65	23.06	96.51	72.77	324.14	6.00	11.27	904	0.654
100	15.8	4	15	4	6.0	3.0	2.27	21.69	17.45	137.63	66.24	315.41	6.00	11.27	1266	1.229
								$T_{phys} = 300$ K								
15	2.7	4	15	4	6.0	3.1	3.40	17.10	19.50	69.60	28.13	798.00	2.00	8.50	508	1.253
25	4.6	4	15	4	6.0	3.0	4.90	19.30	18.33	83.60	40.36	560.00	2.00	9.90	654	1.533
50	9.1	4	15	4	6.0	1.5	3.40	18.70	18.02	90.00	51.00	464.90	2.00	6.90	1001	1.480
75	13.8	4	15	4	6.0	3.0	3.50	18.40	17.41	96.60	57.90	417.70	2.00	8.50	1363	1.912
100	18.4	4	15	4	6.0	1.96	3.70	18.24	17.05	101.60	60.40	398.30	2.00	7.66	1717	2.104

18 GHz for a variety of different temperatures are compared. The predicted minimum noise temperature is calculated using Pospieszalski's expression,

$$T_{min} = \frac{2\pi f C_{gs} \sqrt{g_{ds} R_t T_g T_d}}{g_m}$$

for the minimum noise temperature. The small-signal circuit elements are those extracted from the measured S-parameters, while T_g is the device physical temperature and T_d is estimated from the results in [18].

Figure 10 shows a comparison of the room temperature results as a function of percentage of drain saturation current. The measured minimum noise temperature is more than a factor of two larger than the predicted values. This discrepancy is probably associated with an unrealistic extracted value for R_t. The extracted value for R_t at room temperature is approximately the same as the value at 11 and 16 K and 50 percent smaller than the 36- and 49-K extract value (see Table 1 and Fig. 11). The room temperature, R_t, should have been 2 to 4 times the cryogenic value. However, at cryogenic temperatures for low drain-current values, the measured and modeled results agree within the measurement uncertainties (see Fig. 12).

For single-frequency measurements at 18 GHz, the worst-case errors for the measured minimum noise temperature are ± 25 K and ± 15 K for the calculated model values. That the cryogenic results agree is possibly fortuitous. However, that there is agreement indicates that a closer examination with a more accurate and reliable method of cryogenic noise parameter measurement and small-signal element extraction technique is absolutely necessary.

Three of the four intrinsic circuit elements, g_m, g_{ds}, and C_{gs}, that determine T_{min} behaved as expected. The transconductance, g_m, and the output conductance, g_{ds}, were observed to show significant increases upon cooling and increasing drain current (see Figs. 13 and 14). The C_{gs} shown in Fig. 15 is relatively constant with temperature but increases linearly with increasing bias while, on the other hand, the gate resistance, R_{gs}, flip-flops, increasing in resistance as the temperature is lowered toward 36 K but dropping to its room temperature value at 16 K and half that value at 11 K (see Fig. 11). In addition, for high drain-current values, the resistance appears to be independent of drain current value. Clearly, more accurate noise-parameter measurements at these cryogenic temperatures will significantly increase our knowledge of the temperature behavior of the parameters that determine cryogenic noise performance of HEMTs.

VII. Conclusion

The feasibility of cryogenic, broadband on-wafer scattering parameter measurements has been demonstrated. It was also shown that a commercial noise-parameter measurement system is inadequate for cryogenic applications. Although some useful cryogenic noise temperature data were obtained, it was not of sufficient density or accuracy for a systematic device study. Systematic studies are necessary to develop device technologies for future applications and to properly select, develop, and design high-performance cryogenic LNAs.

The development of a cryogenic probe tip integrated with a cryogenic noise and impedance generator capable of performing both scattering and noise parameter measurements will circumvent the limitations posed by the current characterization techniques. This type of probe will allow nondestructive characterization of devices and circuits while still in wafer form. This measurement technique will provide significant cost savings by improving accuracy and design methodology and by reducing test verification costs. Once operational, such a system will be beneficial in studying HEMT LNAs as well as hybrid semiconductor/superconductor circuits.
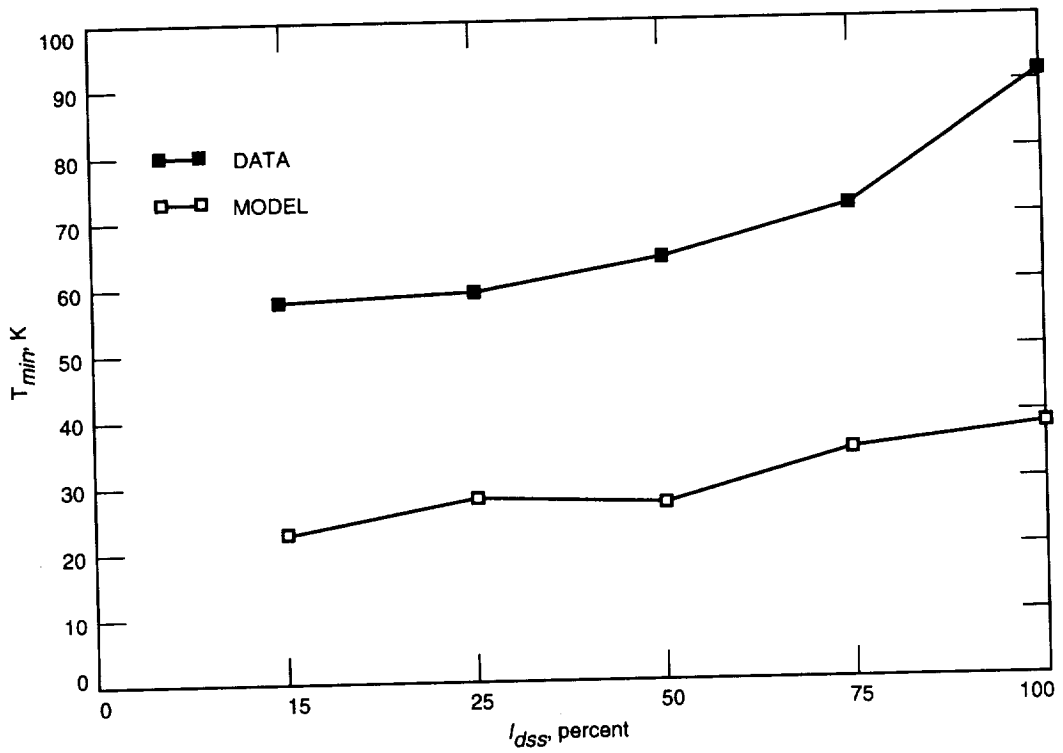
Fig. 10. Measured data versus model at a 300-K physical temperature at 18 GHz.
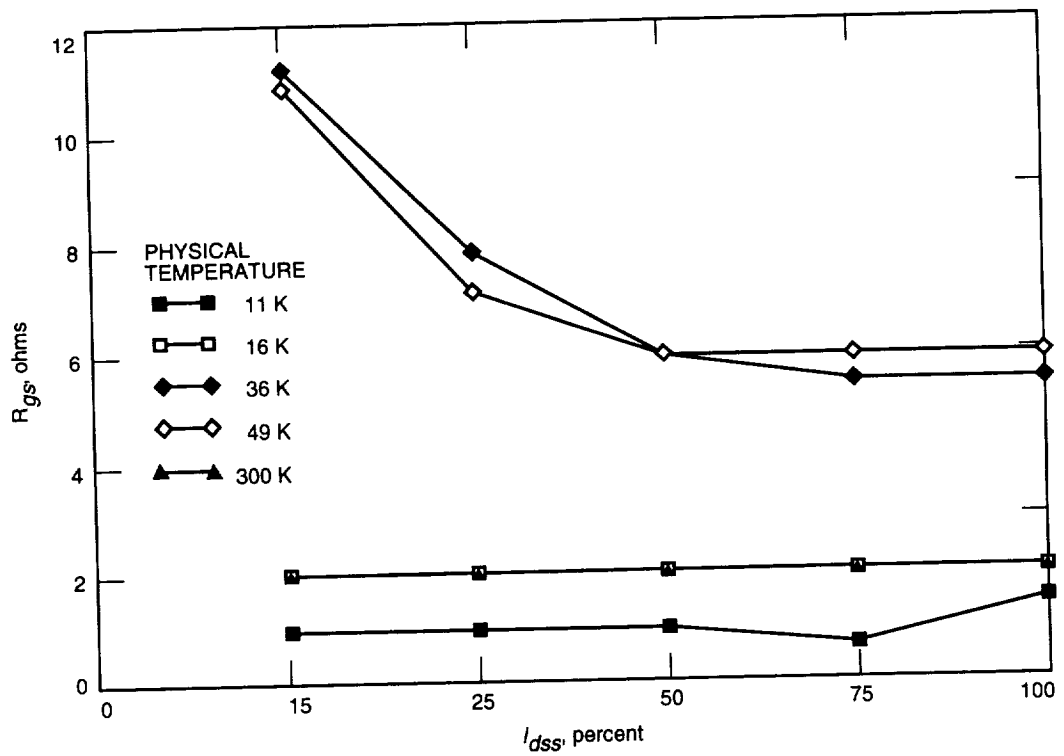
Fig. 11. R_{gs} at several temperatures.

116
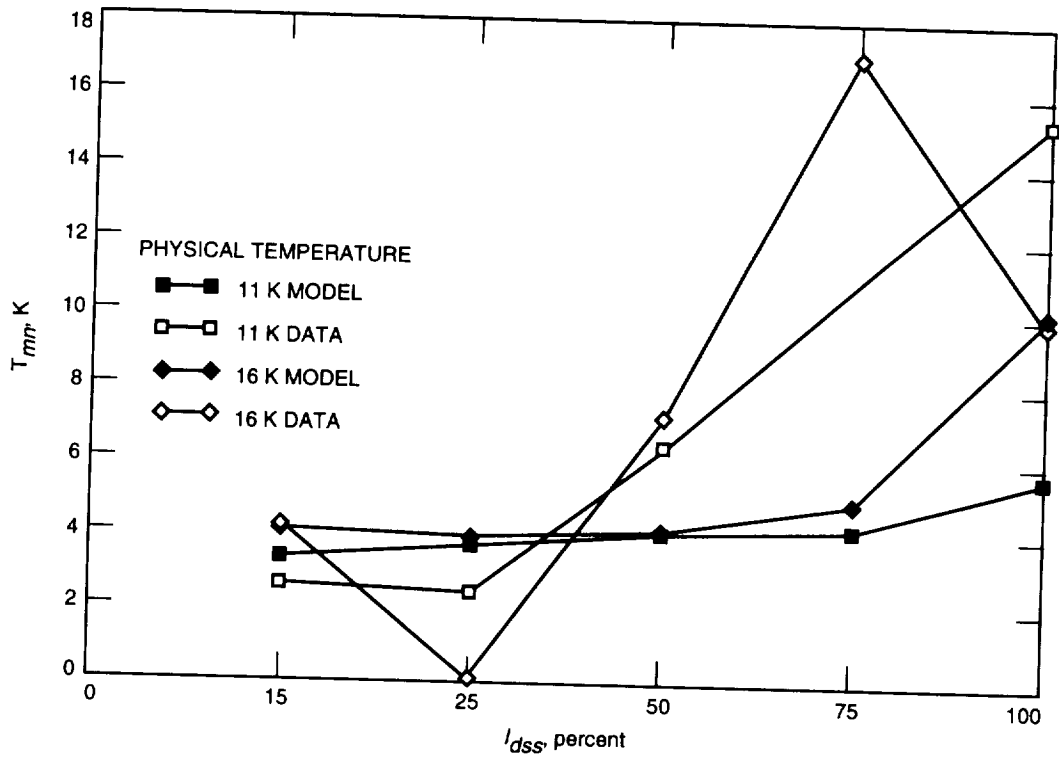
Fig. 12. Model and measured data at 18 GHz; 11 and 16 K.
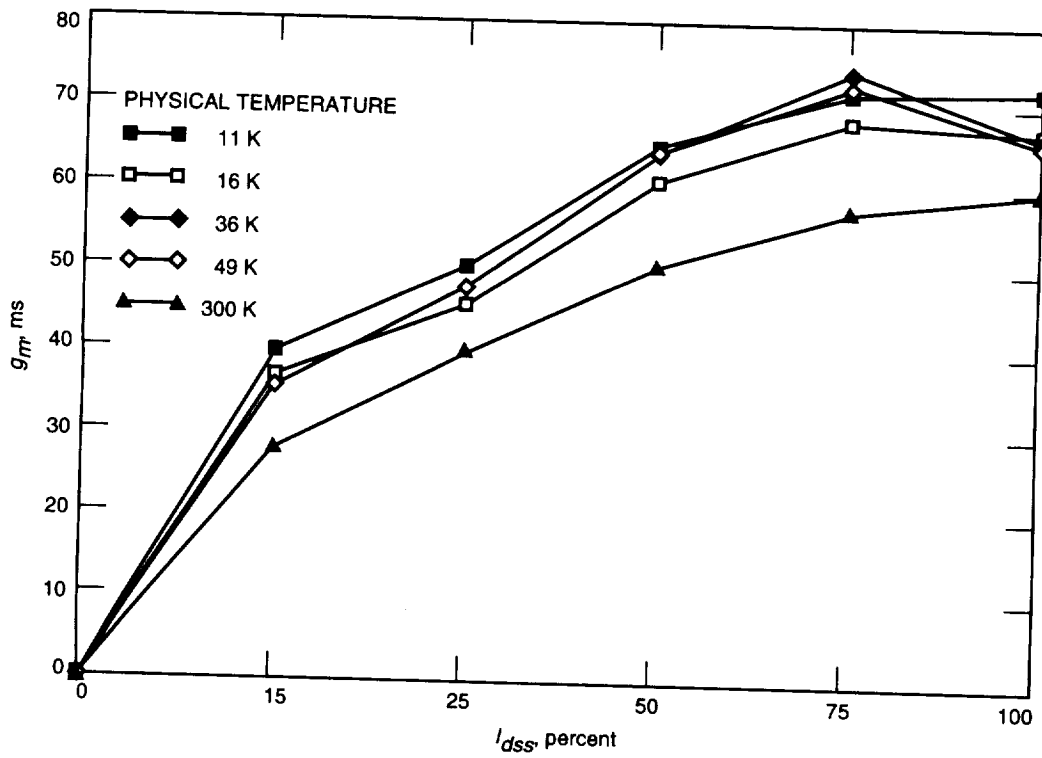
Fig. 13. G_m for several temperatures.
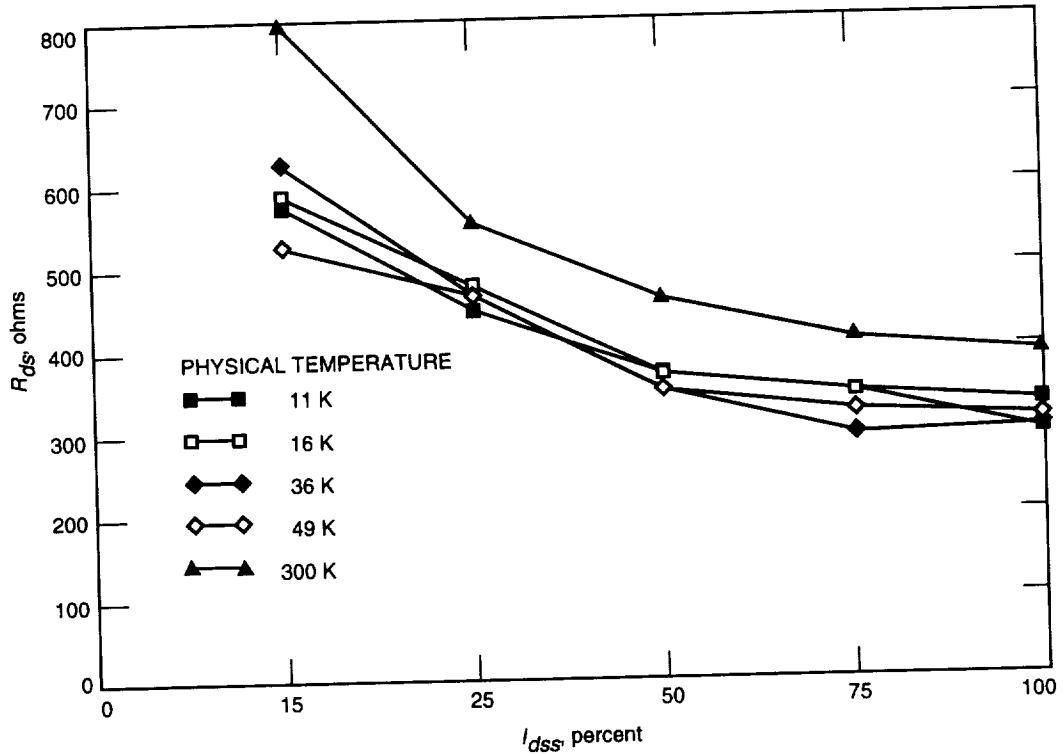
Fig. 14. R_{ds} at several temperatures.
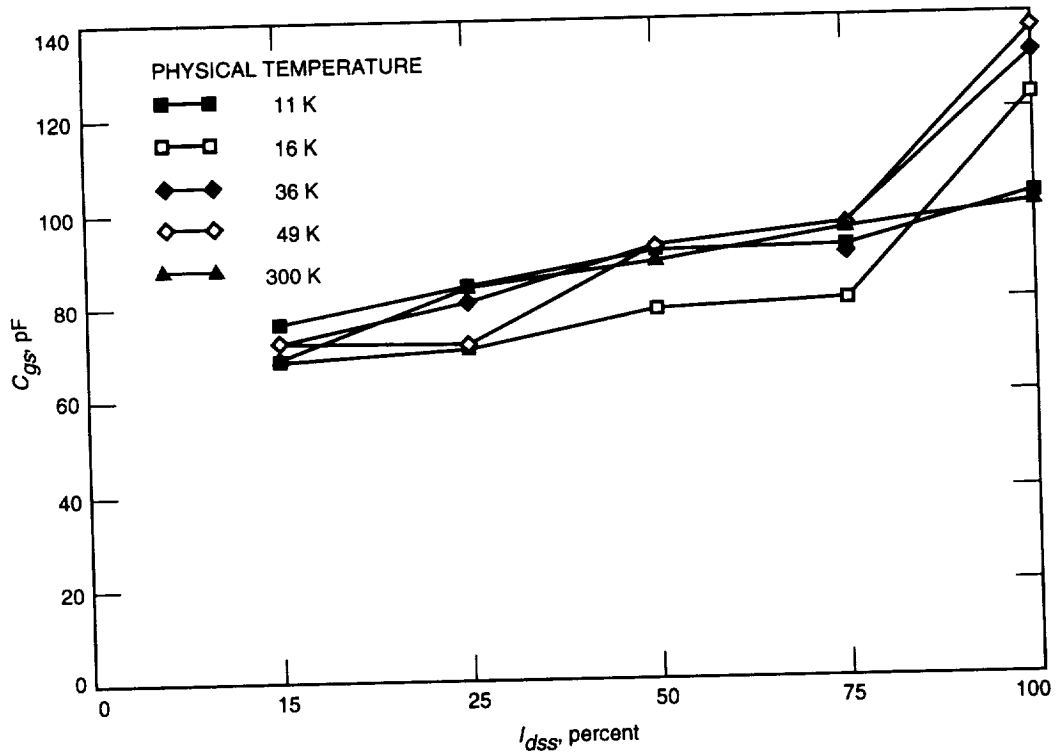
Fig. 15. C_{gs}, at several temperatures.

JPL's experience with HEMT-based LNAs is that they are easier to operate and less costly than masers. Although masers provide the lowest noise temperature, HEMTs can, in principle, perform as well as masers. The development of an integrated probe for cryogenic, broadband scattering and noise-parameter measurements will significantly bolster the existing JPL HEMT program to continue the development of HEMT devices and LNAs with maser-like noise temperatures. The advent of super-low noise HEMT devices will lead to greater frequency coverage and economical cryogenic, single- and multiple-element feed systems for routine telemetry and radio navigation.

References

[1] C. A. Liechti and R. B. Larrick, "Performance of GaAs MESFET's at Low Temperatures," *IEEE Trans. Microwave Theory Tech.*, vol. MTT-24, pp. 365–370, June 1976.

[2] W. Brockerhoff, H. Meschede, W. Prost, K. Heime, G. Weimann, and W. Schapp, "RF Measurements and Characterization of Heterostructure Field-Effect Transistors at Low Temperatures," *IEEE Trans. Microwave Theory Tech.*, vol. 37, pp. 1380–1388, September 1989.

[3] S. T. Fu, M. Das, P. C. Chao, K. Duh, P. Ho, and J. Ballingall, *Workshop on Low Temperature Semiconductor Electronics*, p. 19, 1989.

[4] J. Kolodzey, H. Laskar, S. Boor, S. Reis, A. Ketterson, I. Adesida, D. Sivco, R. Fischer, and A. Y. Cho, "Cryogenic Temperature Performance of Modulation Doped Field Effect Transistors," *Electon. Lett.*, vol. 25, pp. 777–778, 1988.

[5] R. Lai, P. K. Bhattacharya, D. Yang, T. L. Brock, A. A. Alterovitz, and A. N. Downey, *IEEE Trans. on Elec. Dev.*, vol. 39, p. 2206, 1992.

[6] J. W. Smuk, M. G. Stubbs, and J. S. Wight, "Vector Measurements of Microwave Devices at Cryogenic Temperatures," *1989 IEEE MTT-S International Microwave Symposium*, New York: The Institute of Electrical and Electronic Engineers, Inc., pp. 1195–1198, June 1989.

[7] S. Weinreb, "Low-Noise Cooled GASFET Amplifiers," *IEEE Trans. Microwave Theory Tech.*, vol. MTT-28, pp. 1041–1054, October 1980.

[8] J. Laskar and J. Kolodzey, "Vacuum Cryogenic High Frequency Probe Station," *J. Vac. Sci. Technol. B*, vol. 8, pp. 1161–1165, September–October 1990.

[9] J. Laskar and M. Feng, "An On-Wafer Cryogenic Microwave Probing System for Advanced Transistor and Superconductor Applications," *Microwave Journal*, vol. 36, pp. 104–114, February 1993.

[10] *Cascade Microtech Model 42D User's Manual*, Cascade Microtech, Beaverton, Oregon, 1987.

[11] H. Meschde, R. Reuter, J. Albers, J. Kraus, D. Peters, W. Brockerhoff, F. Tegude, M. Bode, J. Schubert, and W. Zander, "On-Wafer Microwave Measurement Setup for Investigations on HEMT's and High Tc Superconductors at Cryogenic Temperatures Down to 20 K," *IEEE Trans. Microwave Theory Tech.*, vol. 40, pp. 2325–2331, December 1992.

[12] Y. Kwark, P. Solomon, and D. Tulipe, *Proc. of IEEE/Cornell Univ. Conf. on Advanced Concepts in High Speed Semic. Dev. and Ckts.*, New York, p. 208, 1989.

[13] G. Dambrine, A. Cappy, F. Heliodor, and E. Playez, "A New Method for Determining the FET Small-Signal Equivalent Circuit," *IEEE Trans. Microwave Theory Tech.*, vol. 36, pp. 1151–1159, July 1988.

[14] C. A. Liechti, "Microwave Field-Effect Transistors—1976," *IEEE Trans. Microwave Theory Tech.*, vol. 24, pp. 279–300, June 1976.

[15] S. Weinreb, R. Harris, and M. Rothman, "Millimeter-Wave Noise Parameters of High Performance HEMT's at 300 K and 17 K," *1989 IEEE MTT-S International Microwave Symposium Digest*, New York: The Institute of Electrical and Electronic Engineers, Inc., pp. 813–816, June 1989.

[16] M. W. Pospieszalski, "Cryogenically Cooled HFET Amplifiers and Receivers: State-of-the-Art and Future Trends," *1992 IEEE MTT-S International Microwave Symposium Digest*, New York: The Institute of Electrical and Electronic Engineers, Inc., pp. 1369–1372, June 1992.

[17] M. W. Pospieszalski, "Modeling of Noise Parameters of MESFET's and MODFET's and Their Frequency and Temperature Dependence," *IEEE Trans. Microwave Theory and Tech.*, vol. MTT-37, pp. 1340–1350, September 1989.

[18] M. W. Pospieszalski and A. C. Niedwiecki, "FET Noise Model and On-Wafer Measurement of Noise Parameters," *1991 IEEE MTT-S International Microwave Symposium Digest*, New York: The Institute of Electrical and Electronic Engineers, Inc., pp. 1117–1122, June 1991.

TDA Progress Report 42-120

February 15, 1995

Radio-Science Performance Analysis Software

D. D. Morabito and S. W. Asmar
Telecommunications Systems Section

The Radio Science Systems Group (RSSG) provides various support functions for several flight project radio-science teams. Among these support functions are uplink and sequence planning, real-time operations monitoring and support, data validation, archiving and distribution functions, and data processing and analysis. This article describes the support functions that encompass radio-science data performance analysis. The primary tool used by the RSSG to fulfill this support function is the STBLTY program set. STBLTY is used to reconstruct observable frequencies and calculate model frequencies, frequency residuals, frequency stability in terms of Allan deviation, reconstructed phase, frequency and phase power spectral density, and frequency drift rates. In the case of one-way data, using an ultrastable oscillator (USO) as a frequency reference, the program set computes the spacecraft transmitted frequency and maintains a database containing the in-flight history of the USO measurements. The program set also produces graphical displays. Some examples and discussion on operating the program set on Galileo and Ulysses data will be presented.

I. Introduction

The radio science investigations of the different flight projects require a diverse set of tools for ensuring that acquired radio science data satisfy experimenter requirements. For example, the gravitational wave experiments on Galileo, Ulysses, Mars Observer, and Cassini each has specific stability requirements on the received signal frequency and amplitude. The Radio Science Systems Group (RSSG) utilizes various software tools to verify that the received data satisfy the requirements and that the required configurations are in place. STBLTY is the primary analysis tool used by the RSSG to characterize the performance of the radio science instrument. The STBLTY program set has been utilized by the RSSG to perform measurements of ultrastable oscillator (USO) frequency for the Galileo Solar Redshift Experiment [1,2], to characterize the performance of the Galileo Orbiter USO [3], to verify performance of the Mars Observer USO,[1] and to verify performance for the gravitational wave experiments on Galileo [2] and Ulysses [4]. The characterization of the Galileo USO is important for occultation radio science experiments that will be performed during the Jupiter tour [5]. This article will focus on describing the algorithms that are performed by the individual component programs of the STBLTY program set and will present examples using STBLTY on Galileo and Ulysses radio science data.

The version of STBLTY used for Voyager radio science was inherited by the Galileo and Ulysses radio science projects. This version was used primarily for one-way data occultation analysis, where

---

[1] D. D. Morabito, "Mars Observer 93-049 USO Test Processed Through STBLTY," JPL Interoffice Memorandum 3394-93-077 (internal document), Jet Propulsion Laboratory, Pasadena, California, June 17, 1993.

a baseline frequency signature was used to remove all effects other than those due to the planetary atmosphere. Hence, the inherited version did not have the stringent accuracy requirements needed for Galileo and Ulysses radio science experiments. In order to make STBLTY suitable for Galileo and Ulysses cruise data, several upgrades were made to the program set after the Voyager era (Neptune 1989). These upgrades included adding the capability of computing coherent two-way Doppler residuals, modeling the effects of a spinning spacecraft, upgrading the troposphere calibration model, introducing an ionosphere calibration algorithm using tracking system analytic calibration (TSAC) data as input, and estimating a more accurate trajectory model. The new trajectory model includes effects due to nutation, irregularities in Earth rotation (UT1-UTC), polar motion, equation of the equinoxes, zonal tides, and more comprehensive formulation of state vectors.

Figure 1 is a block diagram displaying the interconnections between the component programs of the STBLTY program set. Input radio science data consist of closed-loop data from the DSN tracking system in the form of archival tracking data files (ATDFs) or open-loop data from the radio science system in the form of original data record (ODR) tapes. The input celestial reference set (CRS) file from the Navigation Team of a supported project provides the spacecraft-state vectors necessary to model the spacecraft trajectory from the observable data.
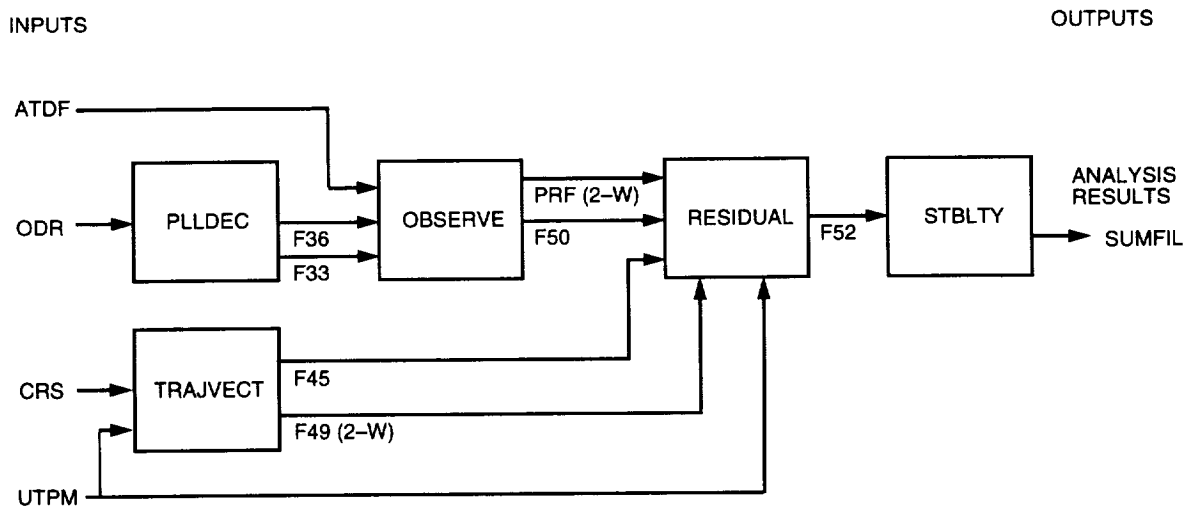
Fig. 1. The STBLTY program set block diagram displaying program names, input, output, and intermediate tape/file products.

The program TRAJVECT reads in body-centered spacecraft state vectors from the CRS file, translates the Earth-centered vectors to the location of the observing station, and performs light-time solutions. TRAJVECT produces a set of downlink state vectors at the time of signal reception (in file F45), and if data are two-way, produces a set of uplink vectors at the time of signal transmission (in file F49). These data sets are passed to the program RESIDUAL.

The closed-loop tracking system utilizes a phase-locked loop (PLL) that performs signal acquisition, lock-up, and detection in real time. The closed-loop data are conditioned by the Multi-Mission Navigation Team, which produces and delivers an ATDF to the RSSG. Among the quantities on an ATDF are Doppler counts, Doppler "pseudoresiduals" (residuals based on predicted frequencies used to tune the receivers), signal strengths (AGCs), and Doppler reference frequencies either in the form of a constant frequency or uplink ramps. OBSERVE reads the Doppler extractor cycle counts and Doppler extractor reference information from the ATDF and reconstructs these into received sky frequencies (in file F50). If data are two-way, OBSERVE writes the uplink ramps into the programmable ramp file (PRF).

The open-loop system mixes an incoming intermediate frequency (IF) signal with a signal whose frequency is a linear approximation of the predicted frequency, also known as the programmable oscillator control assembly (POCA) ramps. The baseband signal is passed through a filter whose bandpass is centered at the expected frequency and has a sufficiently wide bandwidth to allow for any unexpected signal frequency excursions. A set of analog-to-digital converters (ADCs) digitizes the received bandwidth and then writes the samples onto the ODR tapes. The program PLLDEC reads the ODR tapes and performs signal detection on the recorded samples, outputs an F36 file with the detected frequencies and signal strengths, and extracts the open-loop receiver tuning information (POCAs) from the ODR headers and writes these to an F33 file. The program OBSERVE reads the PLLDEC F36 and F33 output files and reconstructs the information into received sky frequencies and writes these in an F50 file that is passed to RESIDUAL.

The program RESIDUAL reads the observed sky frequency F50 file and, if the data are two-way, the PRF file output from OBSERVE and the spacecraft trajectory vectors from the TRAJVECT F45 (one-way or two-way) and F49 (two-way only) output files. RESIDUAL computes model frequencies from the F45 and F49 trajectory vectors and a spacecraft spin model. These model sky frequencies are subtracted from the observed sky frequencies to produce residual frequencies that are written onto the RESIDUAL output F52 file.

The F52 residual frequencies are input to the STBLTY program, which performs further corrections and produces Allan deviations, frequency and phase power spectral densities, and other quantities. In the case of one-way USO data, STBLTY computes the spacecraft transmitted frequency and writes out records for each pass onto a database summary file, SUMFIL, which is accessed by other programs for USO measurement analysis. The SUMFIL is also delivered to the radio science investigator, who performs an analysis for the purpose of measuring the solar gravitational redshift [1].

II. Program Descriptions

A more detailed description of each of the component programs of STBLTY follows.

A. PLLDEC—Open-Loop Data Signal Detection

The scheme employed for detecting signal frequency and power from the digitized samples of the open-loop system is a digital second-order phase-locked loop program called PLLDEC. The digitized samples output from the ADCs in the Deep Space Communications Complex (DSCC) spectrum processing (DSP) subsystem are written onto the ODR tapes (see Fig. 1) that are input to PLLDEC. A theoretical background that supplements the following discussion is given in [6], and a detailed description of a similar version of PLLDEC (using noncoherent AGC requiring high signal-to-noise ratio (SNR) signals) is contained in an internal memorandum.[2]

PLLDEC reads the set of digitized samples, $x(i), i = 1, \cdots, N$, from the ODR tape. An initial frequency, f_0, for the PLL is obtained from a fast Fourier transform (FFT) performed on an initial subset of samples. The output signal frequency, $y(nT)$, is expressed as a linear combination (recursive function) of the recorded samples, $x(i)$, and the previous output signal-frequency estimates, $y(iT)$.

The implemented phase-locked loop consists of a mixer (phase detector) and loop filter providing the forward gain path, $F(s) = (1 + as)/bs$; a low-pass filter, $K(s)$, for suppressing the mixer sum product (with negligible baseband response); and an integrator, $G(s) = 1/s$. The closed-loop transfer function (the transform of the PLL phase over the transform of the input phase) is given by

$$L(s) = \frac{F(s)G(s)}{1 + F(s)G(s)} = \frac{1 + as}{1 + as + bs^2}$$

The desired s-domain transfer function of the second-order PLL of the output detected frequency to the input phase is given by

$$W(s) = \frac{s(1 + as)}{1 + as + bs^2}$$

The continuous time analysis of the discrete time PLL is justified by assuming that the product of the PLL noise bandwidth and sample period is much less than unity, $(B_{PLL}T \ll 1)$. In order to realize the digital PLL implementation, the bilinear transformation from s-space to z-transform space is employed:

$$s \simeq \frac{2}{T} \frac{1 - z^{-1}}{1 + z^{-1}} \tag{1}$$

It has been shown that this transformation outperforms others for the case of low sample rates [7].

By substituting Eq. (1) for s into $G(s)$, the following z-domain expression for the integrator is obtained:

$$G(z) = \frac{T}{2} \left(\frac{1 + z^{-1}}{1 - z^{-1}} \right) \tag{2}$$

By substituting Eq. (1) for s into $F(s)$, the corresponding z-domain function for the loop filter is obtained:

$$F(z) = \frac{T + 2a}{2b} \frac{\left[1 + z^{-1}((T - 2a)/(T + 2a)) \right]}{1 - z^{-1}} \tag{3}$$

The relations for a and b are given by

$$a = \frac{R + 1}{4B_{PLL}}$$

$$b = \frac{a^2}{R}$$

where R is the loop damping parameter, which is set equal to 2, the optimum value of loop performance specified by Jaffee and Rechtin [8] when the initial phase is unknown but uniformly distributed. A typical value for the one-sided loop bandwidth used for Galileo and Ulysses radio-science data processing is $B_{PLL} = 1$ Hz.

A single-pole low-pass filter is also employed to suppress the mixer sum product and has the following s-domain representation:

$$K(s) = \frac{1}{1 + (s/a)}$$

Using the bilinear transformation, the implemented z-domain transfer function of the low-pass filter is given by

$$K(z) = \frac{aT}{2 + aT} \; \frac{1 + z^{-1}}{[1 - z^{-1}\,((2 - aT)/(2 + aT))]} \tag{4}$$

where a is set equal to 10 B_{PLL}. The bilinear form of Eqs. (2), (3), and (4) are used to determine the appropriate coefficients that multiply the previous input samples and previous output values to yield each output estimate of signal phase or frequency.

The contribution to the Allan deviation due to additive white Gaussian noise (AWGN) over the PLL bandwidth B_{PLL} can be estimated from the following equation:

$$\sigma_y(\tau) = \frac{\sqrt{3 B_{PLL} CNR^{-1}}}{2\pi f_0 \tau}$$

where B_{PLL} is the PLL bandwidth, Hz; CNR is the carrier signal-to-noise ratio of the signal; f_0 is the observing frequency, Hz; and τ is the time interval, s. By knowing the expected signal strengths and system noise temperatures, one can use this equation to estimate the B_{PLL} required to obtain an estimate of the AWGN contribution to the Allan deviation. By reducing B_{PLL} appropriately, one can reduce this contribution below other effects, thereby allowing visibility of those effects. Typical CNRs for Galileo and Ulysses result in AWGN contributions to the Allan deviations at 1000 s, which lie well below the measured values that are limited by media (for two-way Galileo and Ulysses) and USO (for Galileo one-way) when using 1 Hz for B_{PLL}.

B. TRAJVECT—Trajectory Vector Conditioning

The program TRAJVECT reads spacecraft state vectors from the CRS file, corrects Earth-center vectors to the observing-station location, and performs light-time solutions to yield a set of downlink state vectors at the time of signal reception, and (if two-way) performs a light-time solution to yield a set of uplink state vectors at the time of signal transmission. The conditioned set of state vectors is then passed to RESIDUAL. For discussions on how the NAV orbit determination solutions are performed, from which the CRS files are derived, the reader is referred to [9] for Galileo and [10] for Ulysses.

1. **Input CRS File State Vectors.** For cruise processing, where the gravitational effects of the planets are assumed negligible, it suffices that the CRS file contains EME 1950 (Earth mean equator and equinox of B1950.0) state vectors of the spacecraft relative to the Sun and the Earth, as follows:

$$\mathbf{x}^{\oplus-s/c}(t_k) = \text{Earth center-to-spacecraft position vector}$$

$$\mathbf{v}^{\oplus-s/c}(t_k) = \text{Earth center-to-spacecraft velocity vector}$$

$$\mathbf{x}^{\odot-s/c}(t_k) = \text{Sun-to-spacecraft position vector}$$

$$\mathbf{v}^{\odot-s/c}(t_k) = \text{Sun-to-spacecraft velocity vector}$$

where k is the index of the vectors which are evenly spaced in time, T s apart. The time tag, t_k, is referenced at the spacecraft in ephemeris time in seconds past 1950.0.

2. **Conversion to Sun Center.** The state vectors from the CRS file are referred to Sun center using the following translations:

$$\mathbf{x}^{\oplus - \odot}(t_k) = \mathbf{x}^{\oplus - \mathbf{s/c}}(t_k) - \mathbf{x}^{\odot - \mathbf{s/c}}(t_k) \tag{5}$$

$$\mathbf{x}^{\mathbf{s/c} - \odot}(t_k) = -\mathbf{x}^{\odot - \mathbf{s/c}}(t_k) \tag{6}$$

$$\mathbf{v}^{\oplus - \odot}(t_k) = \mathbf{v}^{\oplus - \mathbf{s/c}}(t_k) \left(\frac{+}{\mathrm{rel}}\right) - \mathbf{v}^{\odot - \mathbf{s/c}}(t_k) \tag{7}$$

$$\mathbf{v}^{\mathbf{s/c} - \odot}(t_k) = -\mathbf{v}^{\odot - \mathbf{s/c}}(t_k) \tag{8}$$

where the $(+/\mathrm{rel})$ notation means that the velocities add relativistically.

3. Calculation of Observing Station Vectors. TRAJVECT translates the Earth–Sun vectors [Eqs. (5) and (7)] to the location of the observing station. The station–Earth vectors are computed in the EME 1950 frame and are added to the Earth–Sun vectors [Eqs. (5) and (7)] to produce the required station-to-Sun state vectors. Among the corrections applied to the station vectors are precession, nutation, UT1–UTC, polar motion, equation of the equinoxes, and solid Earth tides.

A table of station locations in cylindrical coordinates (referenced to the mean pole, equator, and prime meridian of 1900.05) are read to obtain the observing station coordinates: radius off the spin axis, r_s (km); height above the equatorial plane, z (km); and longitude in degrees east of the Greenwich meridian, λ. Thus, the body-fixed station vector in rectangular coordinates is

$$\mathbf{x}^{\mathbf{dss}} = \begin{bmatrix} r_s \cos \lambda \\ r_s \sin \lambda \\ z \end{bmatrix}$$

Several notations are used to denote time: the corresponding Julian date of t_k,

$$t_k^{JD} = \frac{t_k}{86,400} + 2,433,282.5$$

the number of Julian centuries of 36,525 mean solar days that have elapsed since 1950.0, T_k,

$$T_k = \frac{t_k}{3,155,760,000}$$

and the difference of ephemeris time (ET) and universal time (UT1), Δt_k.

To translate the station vectors to the frame of the current epoch, several translations and rotations are applied. Polar motion matrix rotations are applied, and the vectors are then rotated to the correct position in the frame of the current epoch. The rotation matrices that perform these corrections use values of universal time and polar motion obtained from the monthly publications of the International Earth Rotation Service (IERS). These values are interpolated to the appropriate time tag, t_k, of the vectors, yielding the Earth orientation values of Δt_{UT1R} (UT1R–UTC) and polar motion X_p and Y_p. The Δt_{UT1R} is further corrected by adding the effects of short-period zonal tides (monthly and fortnightly), to yield Δt_{UT1}. The zonal tides are computed using the formulation of Yoder et al. [11].

The angle of the Greenwich meridian at the current epoch, corrected for variation in Earth rotation, $\alpha_G(t_k)$, is known as Greenwich mean sidereal time, or the Greenwich hour angle of the mean equinox of date, and is given by

$$\alpha_G(t_k) = \alpha_0(t_k) + \alpha_1(t_k) + \alpha_2(t_k) + \alpha_3(t_k) \tag{9}$$

where $\alpha_0(t_k) = -(1.002737909294 + T_k 0.589 \times 10^{-10})((\Delta t_k)/240) + 100.0755426042 + T_k^2 0.0003870833$ is the fraction of a turn (in degrees) of the Earth over T_k Julian centuries, $\alpha_1(t_k) = MOD[(t_k/240), 360]$ is the fraction of a turn (in degrees) due to daily rotation, $\alpha_2(t_k) = MOD[36,000T_k, 360]$ is the fraction of a turn (in degrees) due to the revolution of the Earth in its orbit, and $\alpha_3(t_k) = 0.7693120833T_k$ is the fraction of a turn (in degrees) over T_k Julian centuries, which accounts for the slowing down of the Earth due to the exertion of tidal forces.

The nutation model used by the program set is the International Astronomical Union (IAU) 1980, or Wahr nutation model, which was adopted by the IAU in 1984 and uses a series developed by Wahr based on the nutation model of P. K. Seidelmann [12]. The expected accuracy of this model (1 milliarc) [13], translates to about a 1-mHz error at 8.4 GHz, but is expected to be constant over a tracking pass. The angles of nutation estimated from this model are $\Delta\epsilon$, the nutation in obliquity; $\Delta\Psi$, the nutation in longitude; and ϵ_m, the mean obliquity of the ecliptic. The derivatives are computed from the differences of the nutation angles evaluated at two slightly different times divided by the time difference. The obliquity is added to the mean obliquity to yield the true obliquity of the ecliptic, ϵ.

The Greenwich mean sidereal time in Eq. (9), $\alpha_G(t)$, is converted to Greenwich apparent sidereal time, $\alpha_{GA}(t)$ (the Greenwich hour angle of the true equinox of date), by applying the correction of the equation of the equinoxes:

$$\alpha_{GA}(t_k) = \alpha_G(t_k) + \Delta\Psi \cos\epsilon$$

The space-fixed station vector projected in the celestial frame at t_k (the position of date) is computed from the body-fixed station vector by applying a series of rotations that corrects for polar motion ($\mathbf{R}_1$ and $\mathbf{R}_2$) and Earth rotation ($\mathbf{R}_3$). This "true of-date" space-fixed station vector is corrected for nutation ($\mathbf{N}$), which performs the rotation from the true of-date equator and equinox to the "mean of-date" equator and equinox. Finally, the station vector is rotated from the mean of-date equator to the mean equator of the reference epoch (EME 1950) using the precession rotation matrix, $\mathbf{P}$. See the Appendix for definitions of $\mathbf{P}$ and $\mathbf{N}$. The rotation matrices $\mathbf{R}_1, \mathbf{R}_2$, and $\mathbf{R}_3$ are given by

$$\mathbf{R}_3(\alpha_{GA}(t_k)) = \begin{bmatrix} \cos\alpha_{GA}(t_k) & -\sin\alpha_{GA}(t_k) & 0 \\ \sin\alpha_{GA}(t_k) & \cos\alpha_{GA}(t_k) & 0 \\ 0 & 0 & 1 \end{bmatrix}$$

$$\mathbf{R}_2(X_p) = \begin{bmatrix} \cos X_p & 0 & -\sin X_p \\ 0 & 1 & 0 \\ \sin X_p & 0 & \cos X_p \end{bmatrix}$$

$$\mathbf{R}_1(Y_p) = \begin{bmatrix} 1 & 0 & 0 \\ 0 & \cos Y_p & \sin Y_p \\ 0 & -\sin Y_p & \cos Y_p \end{bmatrix}$$

The station position vector in EME 1950 coordinates is computed as follows:

$$\mathbf{x}^{dss-\oplus}(t_k) = \mathbf{PN}[\mathbf{R}_3\mathbf{R}_2\mathbf{R}_1\mathbf{x}^{dss} + \Delta\vec{\mathbf{x}}_{tides}] \tag{10}$$

where $\mathbf{R_1}, \mathbf{R_2}$, and $\mathbf{R_3}$ are the "Earth platform" rotation matrices given above, $\mathbf{N}$ is the nutation rotation matrix, $\mathbf{P}$ is the precession rotation matrix, and $\Delta \mathbf{x}_{tides}(t_k)$ designates the perturbations due to solid Earth tides which, along with velocity perturbations, $\Delta \mathbf{v}_{tides}$, are induced by the Sun and Moon.[3]

The station velocity vector is given by[4,5,6]

$$\mathbf{v}^{dss-\oplus}(t_k) = [\dot{\mathbf{P}}\mathbf{N} + \mathbf{P}\dot{\mathbf{N}}][\mathbf{R_3}\mathbf{R_2}\mathbf{R_1}\mathbf{x}^{dss} + \Delta \mathbf{x}_{tides}(t_k)] + \mathbf{P}\mathbf{N}[\dot{\mathbf{R}}_3\mathbf{R_2}\mathbf{R_1}\mathbf{x}^{dss} + \Delta \mathbf{v}_{tides}(t_k)] \qquad (11)$$

where the $\dot{\mathbf{N}}$ and $\dot{\mathbf{P}}$ matrices (see the Appendix) denote the derivatives of the nutation and precession matrices, respectively, $\Delta \mathbf{v}_{tides}(t_k)$ is the station velocity perturbations due to tides, and $\dot{\mathbf{R}}_3$ is given by

$$\dot{\mathbf{R}}_3(\alpha_{GA}(t_k)) = \begin{bmatrix} -\sin \alpha_{GA}(t_k) & -\cos \alpha_{GA}(T_k) & 0 \\ \cos \alpha_{GA}(t_k) & -\sin \alpha_{GA}(t_k) & 0 \\ 0 & 0 & 0 \end{bmatrix}$$

4. Light-Time Solutions. The light-time solution is performed as follows. First, an initial estimate of the one-way light time is made using Eqs. (5) and (6):

$$\tau_0(t_k) = \frac{|\mathbf{x}^{\oplus-\odot}(t_k) - \mathbf{x}^{s/c-\odot}(t_k)|}{c}$$

where the "0" subscript denotes the initial estimate. The ith estimate of the time tag of downlink reception a one-way light time later is made as follows:

$$t_{k,i} = t_k + \tau_i(t_{k,i-1}) \qquad (t_{k,0} = t_k) \qquad (12)$$

The three sets of vectors with time tags, t_{l-1}, t_l, and t_{l+1}, lying closest to the estimated received time, $t_{k,i}$, are quadratically interpolated to yield estimates of the state vectors at $t_{k,i}$. The station–Earth vectors [Eqs. (10) and (11)] are evaluated at $t_{k,i}$ and added to the Earth–Sun vectors (Eqs. (5) and (7) interpolated at $t_{k,i}$) as follows:

$$\mathbf{x}^{dss-\odot}(t_{k,i}) = \mathbf{x}^{dss-\oplus}(t_{k,i}) + \mathbf{x}^{\oplus-\odot}(t_{k,i}) \qquad (13)$$

$$\mathbf{v}^{dss-\odot}(t_{k,i}) = \mathbf{v}^{dss-\oplus}(t_{k,i}) \left(\frac{+}{\text{rel}} \right) \mathbf{v}^{\oplus-\odot}(t_{k,i}) \qquad (14)$$

The correction to the light-time of the next iteration is

[3] T. D. Moyer, "Correction to Earth Fixed Station Coordinates Due to Solid Earth Tides, Ocean Loading, and Pole Tides and Calculation of Periodic Terms of UT1," JPL Engineering Memorandum 314-505 (internal document), Jet Propulsion Laboratory, Pasadena, California, July 4, 1991.

[4] N. A. Mottinger and T. D. Moyer, "A Close Encounter With a Doppler Observable," JPL Interoffice Memorandum 314.5-1025 (internal document), Jet Propulsion Laboratory, Pasadena, California, June 18, 1984.

[5] T. D. Moyer, "Proposed Changes to ODP Transformation Between Body-Fixed and Space-Fixed Coordinates for the Planets and the Sun," JPL Engineering Memorandum 314-271 (internal document), Jet Propulsion Laboratory, Pasadena, California, June 16, 1982.

[6] T. D. Moyer, "Time Derivative and Partial Derivatives of the Body-Fixed to Space-Fixed Coordinate Transformation for the Sun, Planets and Planetary Satellites," JPL Engineering Memorandum 314-379 (internal document), Jet Propulsion Laboratory, Pasadena, California, August 22, 1985.

$$\Delta\tau_{i+1}(t_{k,i}) = \frac{|\mathbf{x}^{\mathbf{dss}-\odot}(t_{k,i}) - \mathbf{x}^{\mathbf{s/c}-\odot}(t_{k,i})|}{c} - \tau_i(t_{k,i-1}) \tag{15}$$

and the new light-time is

$$\tau_{i+1}(t_{k,i}) = \tau_i(t_{k,i-1}) + \Delta\tau_{i+1}(t_{k,i})$$

The time tag for the next iteration is refined as [Eq. (12), substituting $i + 1$ for i]

$$t_{k,i+1} = t_k + \tau_{i+1}(t_{k,i})$$

The correction [Eq. (15)] is compared against a preset tolerance that should be tight enough for accurate vector determination given the stability requirements of the experiment being processed and the time spacing of the input CRS vectors. The current value used for Galileo and Ulysses cruise data is 10^{-4} s, assuming vectors separated by 30 s. Once the criterion is met, the iterative solution is completed and returns the estimated vectors at $t_{k,(i+1)}$. If the criterion is not met, then additional iterations are performed until it is satisfied. In the case of the uplink vectors, the procedure is the same except that a minus sign replaces the plus sign in the appropriate equations.

The time tag of the final iteration of the light-time solution for the downlink output vectors is redefined for notational convenience as

$$t_k^* \stackrel{\Delta}{=} t_k + \tau_{i+1}(t_{k,i}) = t_{k,i+1}$$

The M state vectors from the CRS file are processed this way such that a set of M heliocentric station and spacecraft state vectors referenced at times $t_k^*, k = 1, \cdots, M$ is produced in the EME 1950 reference frame. These vectors are passed to RESIDUAL via the downlink vector file F45 and uplink vector file F49. For downlink,

$$\mathbf{x}_{\mathbf{dn}}^{\mathbf{dss}-\odot}(t_k^*) = \text{station position}$$

$$\mathbf{v}_{\mathbf{dn}}^{\mathbf{dss}-\odot}(t_k^*) = \text{station velocity}$$

$$\mathbf{x}_{\mathbf{dn}}^{\mathbf{s/c}-\odot}(t_k^*) = \text{spacecraft position}$$

$$\mathbf{v}_{\mathbf{dn}}^{\mathbf{s/c}-\odot}(t_k^*) = \text{spacecraft velocity}$$

For uplink,

$$\mathbf{x}_{\mathbf{up}}^{\mathbf{dss}-\odot}(t_l^*) = \text{station position}$$

$$\mathbf{v}_{\mathbf{up}}^{\mathbf{dss}-\odot}(t_l^*) = \text{station velocity}$$

$$\mathbf{x}_{\mathbf{up}}^{\mathbf{s/c}-\odot}(t_l^*) = \text{spacecraft position}$$

$$\mathbf{v}_{\mathbf{up}}^{\mathbf{s/c}-\odot}(t_l^*) = \text{spacecraft velocity}$$

where the subscript k is the index of the kth vector in the F45 downlink vector file, and the subscript l is the index of the lth vector in the F49 uplink vector file.

C. OBSERVE—Sky Frequency Reconstruction

1. Closed-Loop System. The program OBSERVE reads in "Doppler" cycle counts from the closed-loop system, $\phi(t_j)$, along with information needed to compute the Doppler extractor reference frequency, $f_{ref}(t_j)$. The cycle counts consist of an integer number of counts output from the Doppler counter, plus a fractional term output from the Doppler resolver. The Doppler reference frequency may either be a constant synthesizer frequency (SIM), normally used as the reference during one-way data acquisition, or be computed from uplink ramps used as the reference during two-way data acquisition. The ramps used to tune the uplink frequency consist of a series of programmable frequencies and ramps that drive a digitally controlled oscillator (DCO), which is multiplied up and input to the exciter that drives the transmitter. The ramps are written to the PRF file, which is input to RESIDUAL, where they are used to reconstruct the uplink frequencies for two-way data.

For closed-loop data read off an ATDF for a standard Deep Space Station (DSS), OBSERVE computes the received biased Doppler frequencies from the accumulated cycle counts as follows:

$$f_{dop}(t_j) = \frac{\phi(t_{j+1}) - \phi(t_{j-1})}{t_{j+1} - t_{j-1}}$$

In the case of a modulo reset, where $\phi(t_j)$ is less than $\phi(t_{j-1})$,

$$f_{dop}(t_j) = \frac{\phi(t_{j+1}) + 2^{32} - \phi(t_{j-1})}{t_{j+1} - t_{j-1}}$$

The Doppler frequency is converted to a 2.3-GHz sky frequency by

$$f^s(t_j) = 96\frac{240}{221}f_{ref}(t_j) \quad -B\ (f_{dop}(t_j) - 10^6)$$

where 10^6 is the 1-MHz bias, B is the sign of the bias, f_{ref} is the Doppler extractor reference frequency interpolated to the time tag of the measured Doppler, and 240/221 is the spacecraft transponder ratio. For 8.4 GHz,

$$f^x(t_j) = 96\frac{880}{221}f_{ref}(t_j) \quad -B\ (f_{dop}(t_j) - 10^6)$$

In the case of the 34-m high-efficiency (HEF) station, the 8.4-GHz frequency is given by[7]

$$f_{sky}(t_j) = \frac{880}{749}[32(4.68125f_{ref}(t_j) - 81.4125\ 10^6) + 6500\ 10^6] \quad -B\ (f_{dop}(t_j) - 10^6)$$

2. Open-Loop System. For the case of open-loop data, the frequencies detected from the recorded samples by PLLDEC, f_{rec}, in the F36 file are converted to sky frequencies, f^s or f^x, using the tuning frequencies, f_{poca}, interpolated from the POCA offsets and ramps in the F33 file at the f_{rec} time tag. For the radio science IF–VF converter assembly (RIV) receivers,

---

[7] T. D. Moyer, "Change to the ODP and ODE for Processing X-Band Uplink Data," JPL Engineering Memorandum 314-430 (internal document), Jet Propulsion Laboratory, Pasadena, California, October 15, 1987.

$$f^s(t_j) = 3\left(f_{poca}(t_j) + \left(\frac{790}{11} \times 10^6\right)\right) + (1950 \times 10^6) - f_{samp} + f_{rec}(t_j)$$

$$f^x(t_j) = 11(f_{poca}(t_j) - \left(10 \times 10^6\right) + \left(8050 \times 10^6\right) - 3f_{samp} + f_{rec}(t_j)$$

where f_{samp} is the sampling frequency of the recorded samples. For the multimission receivers (MMRs),

$$f^s(t_j) = 48f_{poca}(t_j) + \left(300 \times 10^6\right) - \frac{3}{4}f_{samp} + f_{rec}(t_j)$$

$$f^x(t_j) = \frac{11}{3}\left[48f_{poca}(t_j) + \left(300 \times 10^6\right) - \frac{3}{4}f_{samp}\right] + f_{rec}(t_j)$$

The observed sky frequencies from OBSERVE are input to RESIDUAL, where model and residual frequencies are calculated.

D. RESIDUAL—Residual Frequency Calculation

The program RESIDUAL reads the sky frequencies from the OBSERVE output F50 file and the state vectors from the TRAJVECT output F45 and F49 files to compute model frequencies based on the spacecraft trajectory, and produces frequency residuals for either 2.3 GHz, 8.4 GHz, or differenced S-3/11X data. RESIDUAL applies a polarization-dependent correction for a spinning spacecraft[8] and can estimate and remove a sinusoidal signature induced by an off-axis antenna on a spinning spacecraft (e.g., low-gain antenna (LGA)-2 on Galileo).

1. Spin Correction. For the constant spin correction, specific default values are built into the code to account for different spacecraft configurations. This correction assumes the 2.3-GHz one-way default values for f_{spin} shown in Table 1 (note that Galileo has a 3-rpm spin rate and Ulysses has a 5-rpm spin rate). This correction could also be obtained from attitude-control telemetry data and the defaults therefore overridden. For Galileo passes involving LGA-2, the spin rate could also be solved for from a three-parameter sinusoid fit of the trajectory corrected residuals.

Table 1. One-way default values for f_{spin}.

Spacecraft	Antenna	Spin mode	$f_{spin}^{S,1-way}$, Hz
Galileo	LGA1, HGA	Dual	0.052
	LGA2	Dual	−0.052
	LGA1, HGA	All	0.048
	LGA2	All	−0.048
Ulysses			−0.0833
Any other			0.00

RESIDUAL applies the appropriate spin correction to the sky frequency depending upon the spacecraft spin configuration and frequency band. If the data are 2.3-GHz one-way, f_{spin} is applied as given in Table 1. For the case of two-way data with a 2.3-GHz downlink and a 2.3-GHz uplink,

---

[8] P. Priest and J. Breidenthal, "Galileo Spin Effects," JPL Interoffice Memorandum 3393-90-186 (internal document), Jet Propulsion Laboratory, Pasadena, California, November 30, 1990.

$$f_{spin}^{S/S} = \left(\frac{240}{221} + 1\right) f_{spin}^{S,1-way}$$

For the case of two-way data with an 8.4-GHz downlink and a 2.3-GHz uplink,

$$f_{spin}^{S/X} = \left[\frac{240}{221}\frac{11}{3} + 1\right] f_{spin}^{S,1-way}$$

For the case of dual-frequency S–X residuals, the spin correction applied is given by

$$f_{spin}^{S-X} = \frac{8}{11} f_{spin}^{S,1-way}$$

2. One-Way Data Processing. The state vectors from the TRAJVECT F45 file are interpolated to the time tag of the observable frequency (t_i^{dss} at the observing station and $t_i^{s/c}$ at the spacecraft) and are used to estimate the downlink Doppler correction factors:

$$d_1 = \sqrt{\frac{(c - |\mathbf{v}^{s/c-\odot}(t_i^{s/c})|)(c + |\mathbf{v}^{s/c-\odot}(t_i^{s/c})|)}{c^2}} \tag{16}$$

$$d_2 = 1 - \frac{\mathbf{v}^{dss-\odot}(t_i^{dss})}{c} \cdot \frac{\mathbf{x}^{dss-\odot}(t_i^{dss}) - \mathbf{x}^{s/c-\odot}(t_i^{s/c})}{|\mathbf{x}^{dss-\odot}(t_i^{dss}) - \mathbf{x}^{s/c-\odot}(t_i^{s/c})|} \tag{17}$$

$$d_3 = 1 - \frac{\mathbf{v}^{s/c-\odot}(t_i^{s/c})}{c} \cdot \frac{\mathbf{x}^{dss-\odot}(t_i^{dss}) - \mathbf{x}^{s/c-\odot}(t_i^{s/c})}{|\mathbf{x}^{dss-\odot}(t_i^{dss}) - \mathbf{x}^{s/c-\odot}(t_i^{s/c})|} \tag{18}$$

$$d_4 = \sqrt{\frac{[c - |\mathbf{v}^{dss-\odot}(t_i^{dss})|][c + |\mathbf{v}^{dss-\odot}(t_i^{dss})|]}{c^2}} \tag{19}$$

The gravitational redshift correction factors that account for the frequency shifts due to the masses of the Sun and the Earth, evaluated at t_i, are given by

$$d_\odot = \frac{G \, M_\odot}{c^2}\left[\frac{1}{|\mathbf{x}^{dss-\odot}|} - \frac{1}{|\mathbf{x}^{s/c-\odot}|}\right]$$

$$d_\oplus = \frac{G \, M_\oplus}{c^2}\left[\frac{1}{|\mathbf{x}^{dss-\oplus}|} - \frac{1}{|\mathbf{x}^{s/c-\oplus}|}\right]$$

The radiated 2.3-GHz frequency of the spacecraft is computed from the received frequency of the first data point as follows:

$$f_{s/c}(t_1) = \frac{f^s(t_1)}{(d_1 d_2/d_3 d_4) + d_\odot + d_\oplus} + f_{spin}$$

where the Doppler and redshift terms are evaluated at t_1. The estimated sky frequencies (evaluated at t_i) are computed from this transmitted spacecraft frequency at the first data point (evaluated at t_1) using the above correction factors (evaluated at t_i) as follows:

$$\hat{f}^s(t_i) = f_{s/c}(t_1) \left[\frac{d_1 d_2}{d_3 d_4} + d_\odot + d_\oplus \right]$$

For the one-way case, the residuals are defined such that the first data point is anchored to zero. Given the set of observable frequencies output from the OBSERVE F50 file, $f^s(t_i)$, the estimated frequency for the first data point is, by definition,

$$\hat{f}^s(t_1) = f^s(t_1)$$

The residual frequencies are computed by differencing the model from the observable as follows:

$$\Delta f^s(t_i) = f^s(t_i) - \hat{f}^s(t_i)$$

The residual frequencies and the spacecraft transmitted frequency are passed to STBLTY in the F52 file for further processing.

3. Two-Way Data Processing. This section discusses the computations of two-way Doppler frequencies and residuals. The downlink Doppler corrections [Eqs. (16)–(19)] are evaluated at the time tag of the received signal frequency, t_i^{dss}, as described in the previous section. In addition, the uplink vectors from the F49 file are interpolated to the time of uplink signal transmission, t_i^{up}, and the Doppler correction terms for the uplink signal leg are similarly computed as follows:

$$u_1(t_i) = \sqrt{\frac{(c - |\mathbf{v}^{dss-\odot}(t_i^{up})|)(c + |\mathbf{v}^{dss-\odot}(t_i^{up})|)}{c^2}} \tag{20}$$

$$u_2(t_i) = 1 - \frac{\mathbf{v}^{s/c-\odot}(t_i^{s/c})}{c} \cdot \frac{\mathbf{x}^{s/c-\odot}(t_i^{s/c}) - \mathbf{x}^{dss-\odot}(t_i^{up})}{|\mathbf{x}^{s/c-\odot}(t_i^{s/c}) - \mathbf{x}^{dss-\odot}(t_i^{up})|} \tag{21}$$

$$u_3(t_i) = 1 - \frac{\mathbf{v}^{dss-\odot}(t_i^{up})}{c} \cdot \frac{\mathbf{x}^{s/c-\odot}(t_i^{s/c}) - \mathbf{x}^{dss-\odot}(t_i^{up})}{|\mathbf{x}^{s/c-\odot}(t_i^{s/c}) - \mathbf{x}^{dss-\odot}(t_i^{up})|} \tag{22}$$

$$u_4(t_i) = \sqrt{\frac{(c - |\mathbf{v}^{s/c-\odot}(t_i^{s/c})|)(c + |\mathbf{v}^{s/c-\odot}(t_i^{s/c})|)}{c^2}} \tag{23}$$

The radiated frequency at the time of signal transmission, t_i^{up}, is obtained from the uplink ramps in the PRF file, interpolated at t_i^{up}, and then multiplied up to sky frequency, $f_u^{st}(t_i^{up})$. The estimated 2.3-GHz received frequency is computed as follows:

$$\hat{f}^s(t_i) = \left[f_u^{st}(t_i^{up}) \frac{240}{221} \frac{u_1 u_2}{u_3 u_4} - f_{spin}^{s/s} \right] \frac{d_1 d_2}{d_3 d_4}$$

The 2.3-GHz residual frequency is computed from the observed and estimated received frequencies at time t_i as follows:

$$\Delta f^s(t_i) = f^s(t_i) - \hat{f}^s(t_i)$$

Likewise, for 8.4 GHz,

$$\hat{f}^x(t_i) = \left[f_u^{st}(t_i^{up}) \frac{11}{3} \frac{240}{221} \frac{u_1 u_2}{u_3 u_4} - f_{spin}^{s/x} \right] \frac{d_1 d_2}{d_3 d_4}$$

$$\Delta f^x(t_i) = f^x(t_i) - \hat{f}^x(t_i)$$

4. Correction for Off-Axis Antenna on a Spinning Spacecraft. A sinusoidal signature due to an off-axis antenna on a spinning spacecraft can be removed by fitting a three-parameter model to the bias-corrected residuals:

$$\Delta \overline{f}^s(t_i) = C_1 \sin(C_2 t_i + C_3)$$

where t_i is the time tag of the data point. The spacecraft transmitted frequency is corrected so that it is referenced to the phase center of the spacecraft spin. This is done by removing the value at the first data point:

$$f_{s/c}(t_1) = f_{s/c}(t_1) - C_1 \sin(C_3)$$

The residuals are adjusted accordingly:

$$\Delta f_c^s(t_i) = \Delta f^s(t_i) + C_1 \sin(C_2 t_i + C_3) - C_1 \sin(C_2 t_1 + C_3)$$

The spacecraft transmitted frequency, $f_{s/c}$, is passed to the program STBLTY in the F52 file along with other header information, observed frequencies, and residuals.

E. STBLTY—Media Correction, Display Plots, and Output File

STBLTY is the final program that applies additional corrections to the data, writes out records to a database file for USO and gravitational redshift analysis, and produces plots. At this point, the residual frequencies $\Delta f^s(t_i)$ and/or $\Delta f^x(t_i)$ for L data points $i = 1, 2, \cdots, L$ are read in from the RESIDUAL F52 output file. If both bands are available, STBLTY then combines the observable frequencies to produce the differential data type:

$$\Delta f^{sx}(t_i) = f^s(t_i) - \frac{3}{11} f^x(t_i) \tag{24}$$

For one-way data, the spacecraft transmitted frequency referenced to the first data point, $f_{s/c}(t_1)$, is passed in the header.

1. Ionosphere/Charged-Particle Calibration. The charged particle effect can be "removed" from the radio science data in one of two ways: (1) When dual-frequency data are available, a differential

correction computed from the differential data type, Eq. (24), is applied to the individual frequency bands or (2) a TSAC-supplied polynomial describing the ionosphere path delay signature can be converted into frequency and removed from the frequency residuals. The TSAC correction removes ionospheric effects for either dual- or single-band downlink passes.

For the case where two simultaneous downlink frequency channels exist, the charged particle can be removed using the differential frequency type $f^s - 3f^x/11$, given in Eq. (24). Given that the frequency residuals to be corrected are $\Delta f^s(t_i)$ for 2.3 GHz and $\Delta f^x(t_i)$ for 8.4 GHz, the corrected residuals are

$$\Delta f_c^s(t_i) = \Delta f^s(t_i) - \frac{121}{112}\Delta f^{sx}(t_i)$$

for a one-way 2.3-GHz downlink;

$$\Delta f_c^x(t_i) = \Delta f^x(t_i) - \frac{33}{112}\Delta f^{sx}(t_i)$$

for a one-way 8.4-GHz downlink;

$$\Delta f_c^s(t_i) = \Delta f^s(t_i) - \left[\frac{240}{221}\frac{121}{112} + \frac{121}{112}\right]\Delta f^{sx}(t_i)$$

for a two-way 2.3-GHz uplink/2.3-GHz downlink; and

$$\Delta f_c^x(t_i) = \Delta f^x(t_i) - \left[\frac{240}{221}\frac{121}{112} + \frac{33}{112}\right]\Delta f^{sx}(t_i)$$

for a two-way 2.3-GHz uplink/8.4-GHz downlink, where the subscript c denotes the corrected value of the residual frequency.

The TSAC group produces and delivers ionosphere calibration files to the RSSG, where they are archived and sometimes delivered to the radio science experimenters. The files contain polynomial coefficients describing the mapped ionosphere path delay in meters (referenced to a 2295-MHz carrier) for each DSCC and for each time period that overlaps a tracking pass for a given spacecraft. TSAC determines these coefficients from observations of Earth-orbiting satellites at each complex and maps to the line of sight of the spacecraft.

The TSAC coefficients and time tags are converted to frequency corrections in Hz (referenced to 2.3 GHz) by STBLTY. Given the start time, (t_b), and end time, (t_f), of the interval for which the polynomial is defined, and the polynomial coefficients $(a_i, i = 0, \cdots, 5)$, the ionosphere path delays to the spacecraft at regularly spaced intervals of time t_j are computed as follows:

$$\Delta \rho_{ion}(t_j) = \sum_{i=0}^{5} a_i x_j^i$$

where

$$x_j = 2\left[\frac{t_j - t_b}{t_f - t_b}\right] - 1$$

The path delays computed at time offsets $\pm T/2$ about t_j are differenced and scaled to yield the one-way 2.3-GHz ionosphere frequency correction at t_j:

$$f_{ion}^s(t_j) = \frac{f^s\left[\Delta\rho_{ion}\left(t_j + (T/2)\right) - \Delta\rho_{ion}\left(t_j - (T/2)\right)\right]}{cT}$$

Figure 2 is an example of a typical path delay profile derived from a TSAC polynomial. Figure 3 is the corresponding ionosphere frequency profile at 2.3 GHz.

The set of time tags, t_j, and corrections, $f_{ion}(t_j)$, that overlaps the tracking pass is used to perform the calibration only if dual-frequency charged-particle calibration was not previously performed. Given the frequency residual, $\Delta f^s(t_i)$ or $\Delta f^x(t_i)$, and the above ionosphere correction interpolated to time $t_i, f_{ion}^s(t_i)$, the corrected residuals are then computed as follows: For a one-way 2.3-GHz downlink,

$$\Delta f_c^s(t_i) = \Delta f^s(t_i) - f_{ion}^s(t_i)$$

for a one-way 8.4-GHz downlink,

$$\Delta f_c^x(t_i) = \Delta f^x(t_i) - \frac{3}{11}f_{ion}^s(t_i)$$

for a two-way 2.3-GHz uplink/2.3-GHz downlink,

$$\Delta f_c^s(t_i) = \Delta f^s(t_i) - f_{ion}^s(t_i) - \frac{240}{221}f_{ion}^s(t_i - t_r)$$

and for a two-way 2.3-GHz uplink/8.4-GHz downlink,

$$\Delta f_c^x(t_i) = \Delta f^x(t_i) - \frac{3}{11}f_{ion}^s(t_i) - \frac{11}{3}\frac{240}{221}f_{ion}^s(t_i - t_r)$$

where t_r is the round-trip light time.

For the case of differential $f^s - 3f^x/11$ two-way data, the contribution of the common 2.3-GHz uplink will be zero after differencing the two downlink channels. The remaining charged-particle contribution in the Δf^{sx} data type (SX) will be due to the downlink only. Therefore, this data type is corrected as follows:

$$\Delta f_c^{sx}(t_i) = \Delta f^{sx}(t_i) - \frac{8}{11}f_{ion}^s(t_i) \tag{25}$$

2. Troposphere Calibration. The troposphere calibration is performed after the ionosphere calibration so that the remaining time-dependent signature of the residuals over elevation angle more closely follows the troposphere ray-path function. The troposphere can be removed using either a model with a specified zenith troposphere path delay (default 2.1-m) or the zenith path delay can be fit and removed from the data if there is sufficient arc over elevation angle. The ray-path mapping function used is the CfA (Center for Astrophysics) mapping function [14]:
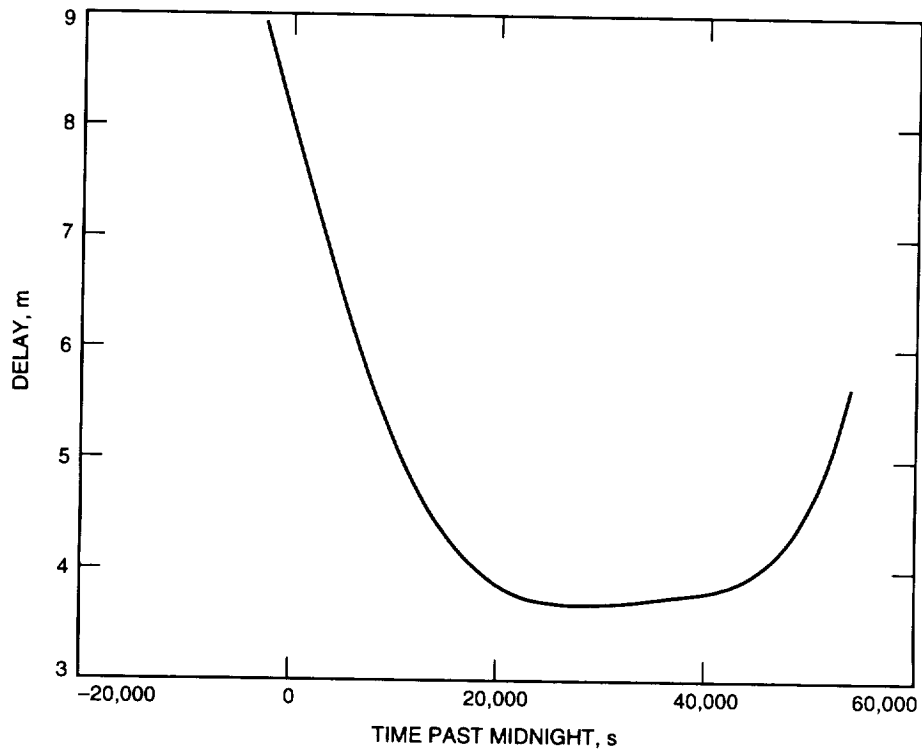
Fig. 2. An example of a typical ionosphere path delay profile derived from a TSAC polynomial.
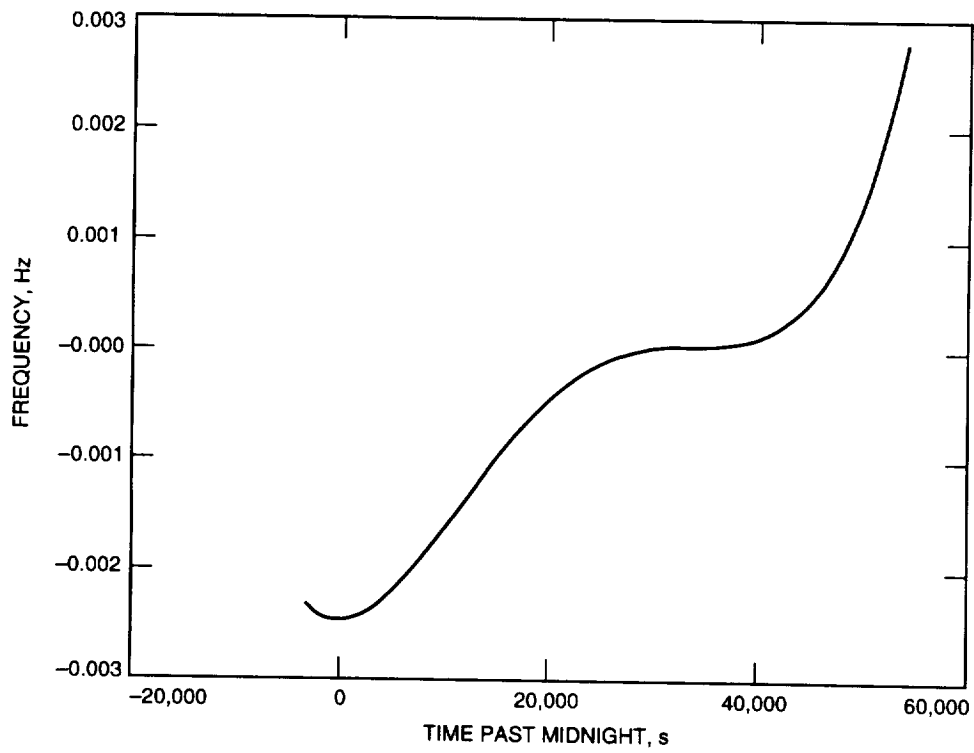
Fig. 3. An example of a typical frequency profile over a pass derived from the TSAC delay profile of Fig. 2.

$$R(t_i) = \frac{1}{\sin e(t_i) + (b_1/(\tan e(t_i) + (b_2/(\sin e(t_i) + b_3))))}$$

where $e(t_i)$ is the elevation angle and the coefficients b_k are functions of meteorological parameters, given by

$$b_1 = 0.0002723[1 + (2.642 \times 10^{-4} p_0) - (6.400 \times 10^{-4} e_0) + (1.337 \times 10^{-2} T_o) - (8.550 \times 10^{-2} \alpha) - (2.456 \times 10^{-2} h_2)]$$

$$b_2 = 0.0004703[1 + (2.832 \times 10^{-5} p_0) + (6.799 \times 10^{-4} e_0) + (7.563 \times 10^{-3} T_0) - (7.390 \times 10^{-2} \alpha) - (2.961 \times 10^{-2} h_2)]$$

$$b_3 = -0.0090$$

Reasonable values of surface pressure ($p_0 = 900$ mbar), partial water vapor pressure ($e_0 = 5$ mbar), surface temperature ($T_0 = 292$ K), tropopause altitude ($h_2 = 12.2$ km), and dry model parameter ($\alpha = 5.0$) are used in the computation of these coefficients. This model is in agreement with predictions made by Lanyi [15] to the 1-cm level down to a 5-deg elevation angle.

The one-way troposphere correction to the observed 2.3-GHz frequency residual is given by

$$f^s_{trop}(t_i) = -\frac{f^s(t_i)\Delta\rho_z}{cT}\left[R\left(t_i + \frac{T}{2}\right) - R\left(t_i - \frac{T}{2}\right)\right]$$

where $f^s(t_i)$ is the downlink sky frequency, $\Delta\rho_z$ is the zenith troposphere path delay, c is the velocity of light, and $T/2$ is a chosen time offset about t_i. For the cases of two-way 2.3-GHz uplink/2.3-GHz downlink and 2.3-GHz uplink/8.4-GHz downlink, the corrections are

$$f^s_{trop}(t_i) = \frac{-f^s(t_i)\Delta\rho_z}{cT}\left(\left[R\left(t_i + \frac{T}{2}\right) - R\left(t_i - \frac{T}{2}\right)\right] + \frac{240}{221}\left[R\left(t_i + \frac{T}{2} - t_r\right) - R\left(t_i - \frac{T}{2} - t_r\right)\right]\right)$$

$$f^x_{trop}(t_i) = \frac{-f^x(t_i)\Delta\rho_z}{cT}\left(\left[R\left(t_i + \frac{T}{2}\right) - R\left(t_i - \frac{T}{2}\right)\right] + \frac{240}{221}\left[R\left(t_i + \frac{T}{2} - t_r\right) - R\left(t_i - \frac{T}{2} - t_r\right)\right]\right)$$

where t_r is the round-trip light time. The one-way frequency residuals are adjusted accordingly:

$$\Delta f^s_c(t_i) = \Delta f^s(t_i) - f^s_{trop}(t_i) + f^s_{trop}(t_1)$$

$$\Delta f^x_c(t_i) = \Delta f^x(t_i) - f^x_{trop}(t_i) + f^x_{trop}(t_1)$$

effectively removing the signature of the troposphere relative to the first data point, because $f_{s/c}(t_1)$ was evaluated here. A bias correction evaluated from the average of the corrected residuals is applied to the transmitted spacecraft frequency to refer it to the center of mass of the residuals. The spacecraft transmitted frequency at 2.3 GHz is corrected as follows:

$$f^s_{c,s/c}(t_{mid}) = f^s_{s/c}(t_1) + f^s_{trop}(t_1) + \overline{\Delta f^s_c}$$

where the last term is the average of the corrected residuals over the data span and t_{mid} is the time tag of the midpoint of the data acquisition interval.

138

The two-way frequency residuals are corrected for troposphere as follows:

$$\Delta f_c^s(t_i) = \Delta f^s(t_i) - f_{trop}^s(t_i)$$

$$\Delta f_c^x(t_i) = \Delta f^x(t_i) - f_{trop}^x(t_i)$$

III. STBLTY Performance Analysis Results and Discussion

The following sections will discuss examples using STBLTY on Galileo and Ulysses flight data.

A. Galileo Results

Examples of running STBLTY on Galileo radio science data will be presented in the following two sections.

1. One-Way Data. The results of routine processing of Galileo USO data using STBLTY will be briefly discussed in this section. For further details on this analysis of closed-loop one-way USO data acquired during the first 2 years of cruise (1989–1991), the reader is referred to [3].

Due to the undeployed high-gain antenna (HGA), only 2.3-GHz data from the LGA antennas were available. The passes were conducted weekly on the average, were typically 2 hours in duration, and were centered about meridian crossing where the troposphere effect was minimal. For troposphere calibration, it was sufficient to remove a model (versus fit and remove) using a default zenith path delay. The error incurred by not performing an ionosphere calibration is expected to be at the mHz level or below for a 2-hour pass centered about meridian crossing at 2.3 GHz.

The Allan deviation results were consistent with the values expected at the appropriate time intervals, given the known signal levels and noise mechanisms. At the short time intervals, the noise in the signal was dominated by thermal noise due to the low signal levels that were due to transmitting through the LGA. At the long time intervals, the noise in the signal was dominated by the USO itself. The transmitted USO-referenced spacecraft frequency followed a behavior that was consistent with known aging mechanisms of the USO, having an rms scatter of 17 mHz about a fitted aging model.

2. Two-Way Data. The testing of different calibration schemes using STBLTY on Galileo two-way 2.3-GHz data will be discussed in this section. STBLTY was run on three passes: (1) a DSS-63 tracking pass on day 91-123, (2) a DSS-63 pass on day 93-081, and (3) a DSS-14 pass on day 93-082. The latter two passes are from the 1993 Gravitational Wave Experiment.

Table 2 displays the processing results for these three passes using different calibration schemes. The first column denotes the year and day number of the pass; the next column is the DSN station identification; the next column denotes the ionosphere calibration employed (see the key for an explanation of the codes); the next column denotes the troposphere calibration employed (see the key for an explanation of the codes); the next column is the zenith path delay and uncertainty in the troposphere calibration (if the code in the TRP column is "F," this value is from the least-square fit); the next column is the slope from a linear fit of the residuals after calibrations have been performed; and the last four columns are the Allan deviations of the postcalibration residuals at 1, 10, 100, and 1000 s.

Four different calibration schemes were employed for each pass. The first run (ION:T, TRP:F) involved calibrating the ionosphere utilizing TSAC polynomial coefficients and calibrating the troposphere by fitting the model over the elevation angle for a zenith path delay and bias. The second run (ION:N,

TRP:F) involved no ionosphere calibration and calibrating the troposphere as described in the first scheme. The third run (ION:T, TRP:M) involved calibrating the ionosphere using TSAC polynomial coefficients and calibrating the troposphere by removing the model using the default zenith path delay of 2.1 m (no fitting performed). The last run (ION:N, TRP:N) did not employ any media calibration.

The zenith path delay for the TSAC ionosphere/troposphere fit run (T,F) for passes 91-123 and 93-081 are in reasonable agreement with the expected 2.1-m zenith path delay. The zenith path delay fit from the data when no ionosphere is removed (N,F) is consistently lower than those of the TSAC calibrated runs (T,F) and (T,M). This suggests that the TSAC calibration does contribute to removing nontropospheric trends from the data.

The linear slope of the residuals tends to increase in magnitude as fewer calibrations are performed. The magnitude of the linear slope tends to be smaller for the runs involving both troposphere fit and TSAC ionosphere calibration (T,F) and larger for the run involving no calibrations (N,N).

The Allan deviations at the time intervals of 1, 10 and 100 s do not differ significantly between the different schemes over each given pass. The Allan deviation at 1000 s for the three runs involving a troposphere calibration (T,F), (N,F), and (T,M) are in reasonable agreement. The 1000-s Allan deviations are consistent with values predicted due to solar plasma at the known solar elongation angles using the model of Armstrong, Woo, and Estabrook [16]. However, the Allan deviations at 1000 s are significantly larger for the no-media calibration case (N,N), clearly showing that the removal of the systematic troposphere signature with elevation angle is important for obtaining meaningful results at this time interval.

For Galileo at 2.3 GHz, trajectory errors of 0.018-mm/s in velocity translate to Allan deviations at 1000 s of about 6×10^{-14}. This lies below the 10^{-13} level expected due to plasma (for two-way data) and the instability of the USO (for one-way data).

Table 2. Galileo media calibration test results.

Pass, yr-day	DSS	ION	TRP	Zenith path delay, m	Linear slope, 10^{-7} Hz/s	$\sigma_y(1)$, 10^{-14}	$\sigma_y(10)$, 10^{-14}	$\sigma_y(100)$, 10^{-14}	$\sigma_y(1000)$, 10^{-14}
91-123	63	T	F	1.96 ± 0.03	0.12 ± 0.29	—	357	27.7	24.8
91-123	63	N	F	0.98 ± 0.03	0.16 ± 0.29	—	357	27.6	27.0
91-123	63	T	M	2.1	0.84 ± 0.29	—	357	27.7	25.0
91-123	63	N	N	—	-5.01 ± 0.29	—	357	27.7	38.2
93-081	63	T	F	2.17 ± 0.03	0.77 ± 0.27	1947	206	25.4	17.9
93-081	63	N	F	1.70 ± 0.04	1.55 ± 0.27	1947	206	25.5	23.3
93-081	63	T	M	2.1	0.58 ± 0.27	1947	206	25.4	18.4
93-081	63	N	N	—	-3.55 ± 0.27	1947	206	26.1	50.5
93-082	14	T	F	1.11 ± 0.04	0.39 ± 0.32	1808	194	26.9	14.5
93-082	14	N	F	0.80 ± 0.05	0.75 ± 0.31	1808	195	26.9	17.9
93-082	14	T	M	2.1	2.73 ± 0.32	1808	195	26.9	13.4
93-082	14	N	N	—	-1.14 ± 0.32	1808	195	27.1	29.1

T = TSAC ionosphere calibration.
D = Dual-frequency $(f^s - 3f^x/11)$ charged-particle calibration.
N = No calibration performed.
F = Troposphere calibration (model removed using fit zenith path delay).
M = Troposphere calibration (model removed using default zenith path delay).

B. Ulysses Results

For Ulysses, two sets of two-way data were analyzed: (1) closed-loop data from a dual-band pass from the first opposition 91-004 (DSS 14) and (2) open-loop data from a dual-band pass from the second opposition 92-064 (DSS 14). Table 3 displays the results for these data sets and for each of the applicable data types within each pass. For the single-band data (2.3 and 8.4 GHz), the following runs were performed: (1) TSAC ionosphere and troposphere fit (T,F), (2) dual-frequency calibration of charged particles, and troposphere fit (D,F), (3) no ionosphere/charged-particle and troposphere fit (N,F), and (4) TSAC ionosphere and troposphere model removed using the default zenith path delay (T,M). The no-calibration case (N,N) is not presented in this table since the (N,N) Galileo runs (Section III.A) clearly illustrate the degradation when not applying a media correction. The description of Table 3 is the same as that of Table 2 in the proceeding section except that the data type code (S, X, or SX) follows the year-day number in the first column.

Figure 4 is a plot of the 8.4-GHz residuals for pass 91-004 for the fully calibrated (T,F) run. Figure 5 is a plot of the averaged residuals where every 60 points have been averaged to allow long period trends to be easily examined. Figure 6 is a plot of the reconstructed phase for this pass, and Fig. 7 is a plot of the corresponding Allan deviation. Figure 8 is a plot of the averaged residuals prior to the removal of the troposphere, thus illustrating the signature of an unmodeled troposphere. Figure 9 displays the elevation profile over the pass and the troposphere model that was fit from the data of Fig. 8 and then removed from the residuals, resulting in the plots displayed in Figs. 4–7. Figure 10 displays the TSAC ionosphere correction at 2.3 GHz for this pass.

Table 3. Ulysses media calibration test results.

Pass, yr-day	DSS	ION	TRP	Zenith path delay, m	Linear slope, 10^{-7} Hz/s	$\sigma_y(1)$, 10^{-14}	$\sigma_y(10)$, 10^{-14}	$\sigma_y(100)$, 10^{-14}	$\sigma_y(1000)$, 10^{-14}
91-004 S	14	T	F	1.50 ± 0.06	−0.001 ± 0.71	1080	116	15.4	4.8
91-004 S	14	D	F	1.90 ± 0.08	0.08 ± 1.71	2624	276	32.5	2.4
91-004 S	14	N	F	0.44 ± 0.06	0.09 ± 0.71	1081	116	15.4	6.2
91-004 S	14	T	M	2.1	1.35 ± 0.71	1081	116	15.4	6.7
91-004 X	14	T	F	1.69 ± 0.03	0.29 ± 1.65	621	66	9.3	1.9
91-004 X	14	D	F	1.40 ± 0.04	0.65 ± 1.83	756	80	12.8	3.7
91-004 X	14	N	F	1.05 ± 0.04	0.42 ± 1.65	621	66	9.3	2.8
91-004 X	14	T	M	2.1	3.51 ± 1.65	621	66	9.3	3.6
91-004 SX	14	T	N	—	0.66 ± 0.67	1107	116	13.3	3.3
91-004 SX	14	N	N	—	1.51 ± 0.67	1107	116	13.4	5.2
92-064 S	14	T	F	1.54 ± 0.05	0.19 ± 0.12	335	46	16.7	6.7
92-064 S	14	D	F	1.65 ± 0.04	−0.004 ± 0.12	384	45	16.4	7.4
92-064 S	14	N	F	1.17 ± 0.04	0.13 ± 0.12	335	46	16.7	5.9
92-064 S	14	T	M	2.1	1.26 ± 0.12	335	46	16.7	6.6
92-064 X	14	T	F	1.43 ± 0.03	0.12 ± 0.25	147	30	13.6	5.6
92-064 X	14	D	F	1.46 ± 0.04	0.15 ± 0.27	187	31	13.8	6.1
92-064 X	14	N	F	1.38 ± 0.04	0.23 ± 0.25	147	30	13.6	5.7
92-064 X	14	T	M	2.1	4.63 ± 0.24	147	30	13.6	6.2
92-064 SX	14	T	N	—	0.15 ± 0.09	303	32	9.4	4.1
92-064 SX	14	N	N	—	0.49 ± 0.09	303	32	9.4	4.1
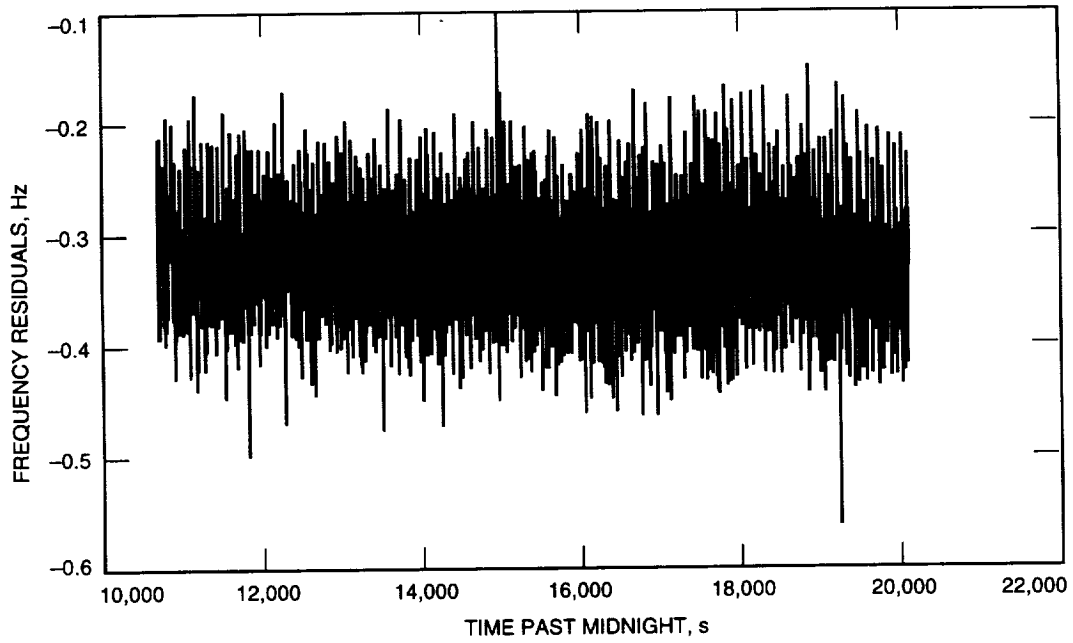
Fig. 4. An example of 8.4-GHz frequency residuals from a Ulysses pass conducted at DSS 14 on January 4, 1991.
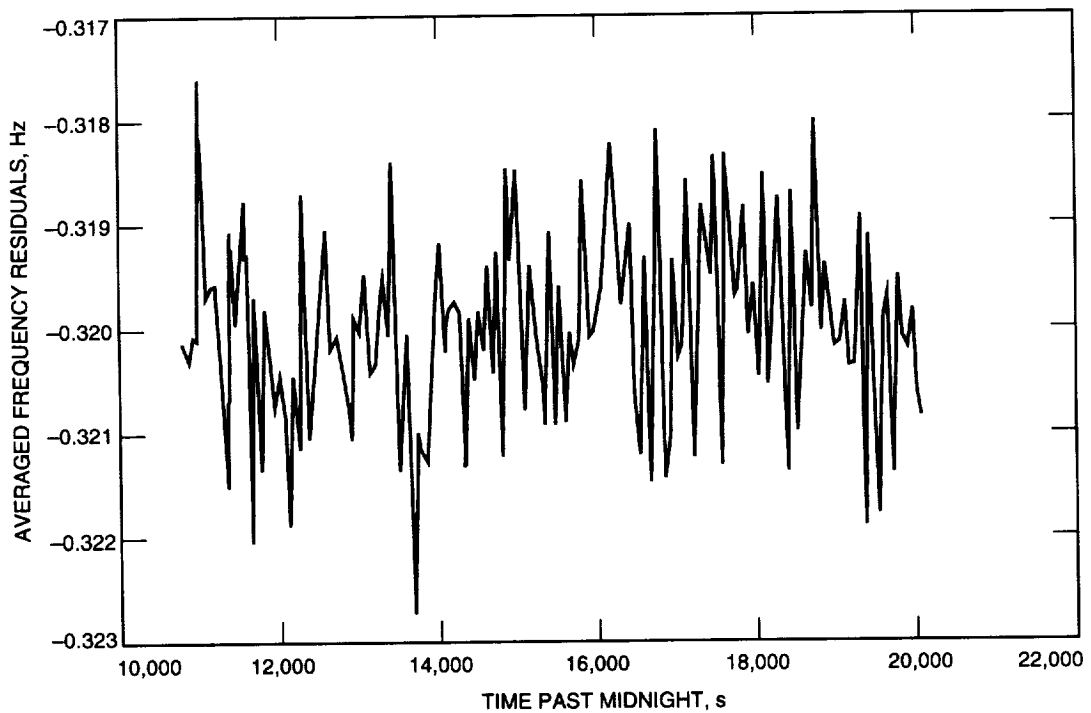
Fig. 5. An example of 8.4-GHz frequency residuals from Fig. 4 averaged every 60 s from a Ulysses pass conducted at DSS 14 on January 4, 1991.
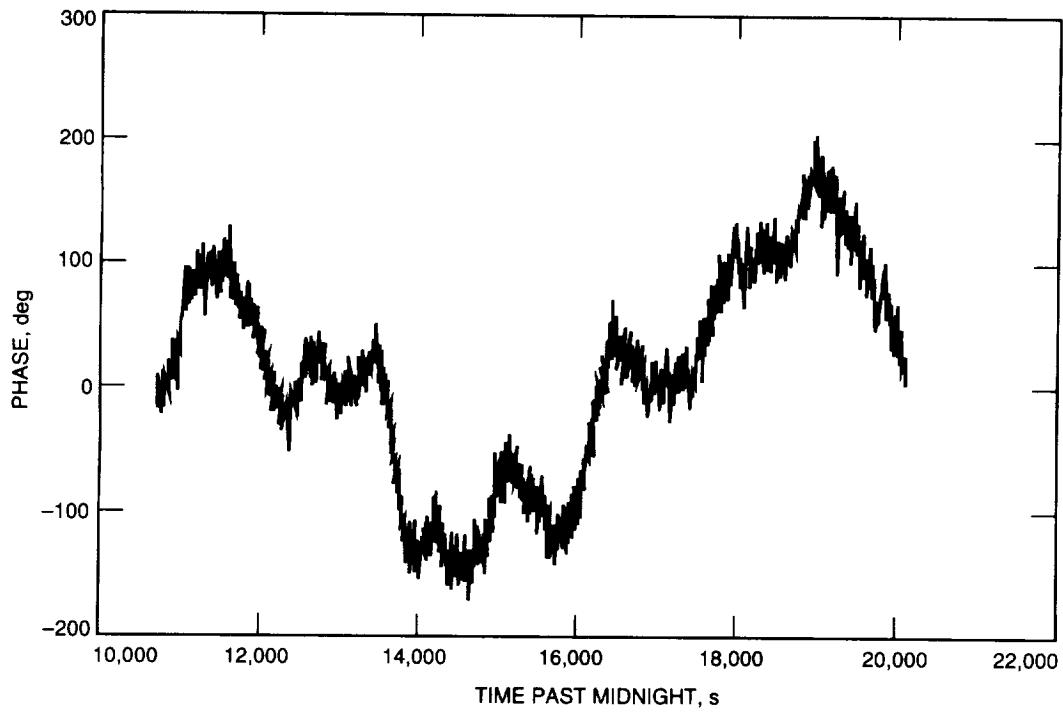
Fig. 6. An example of phase reconstructed from the frequency residuals of Fig. 4.
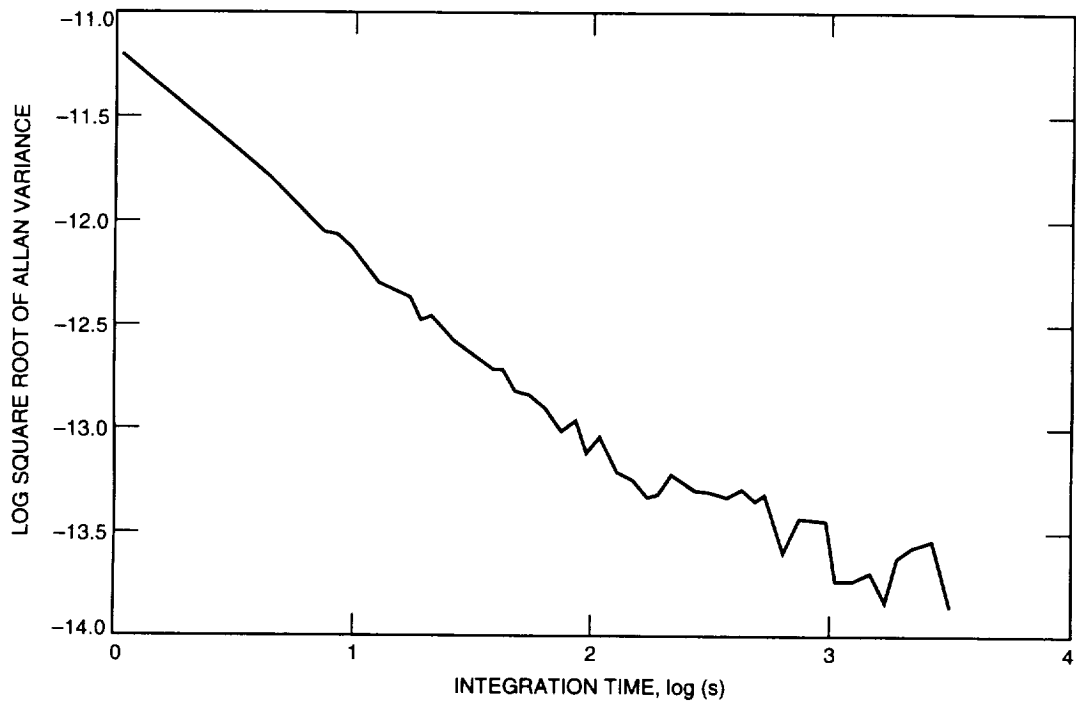
Fig. 7. An example of Allan deviations of the frequency residuals of Fig. 4.
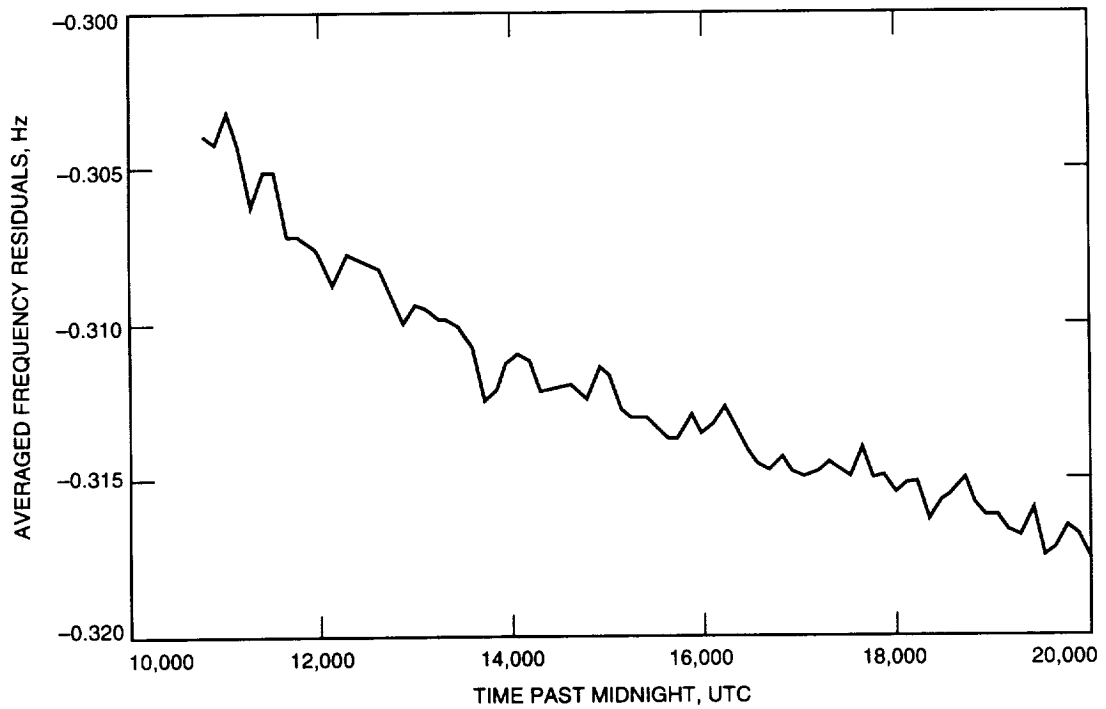
Fig. 8. An example of averaged frequency residuals from a Ulysses pass conducted at DSS 14 on January 4, 1991, without calibrating troposphere.
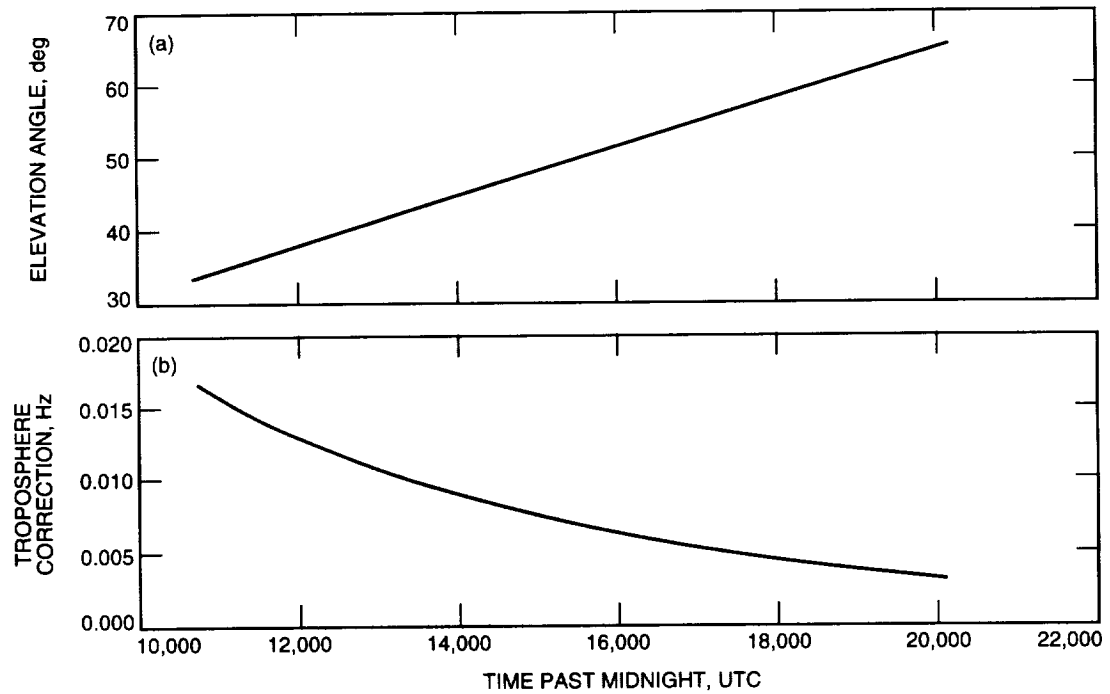
Fig. 9. The (a) elevation angle profile and (b) troposphere correction fit from the frequency residuals of Fig. 8. This signature was then removed from the data, resulting in the calibration illustrated in Figs. 4 through 7.
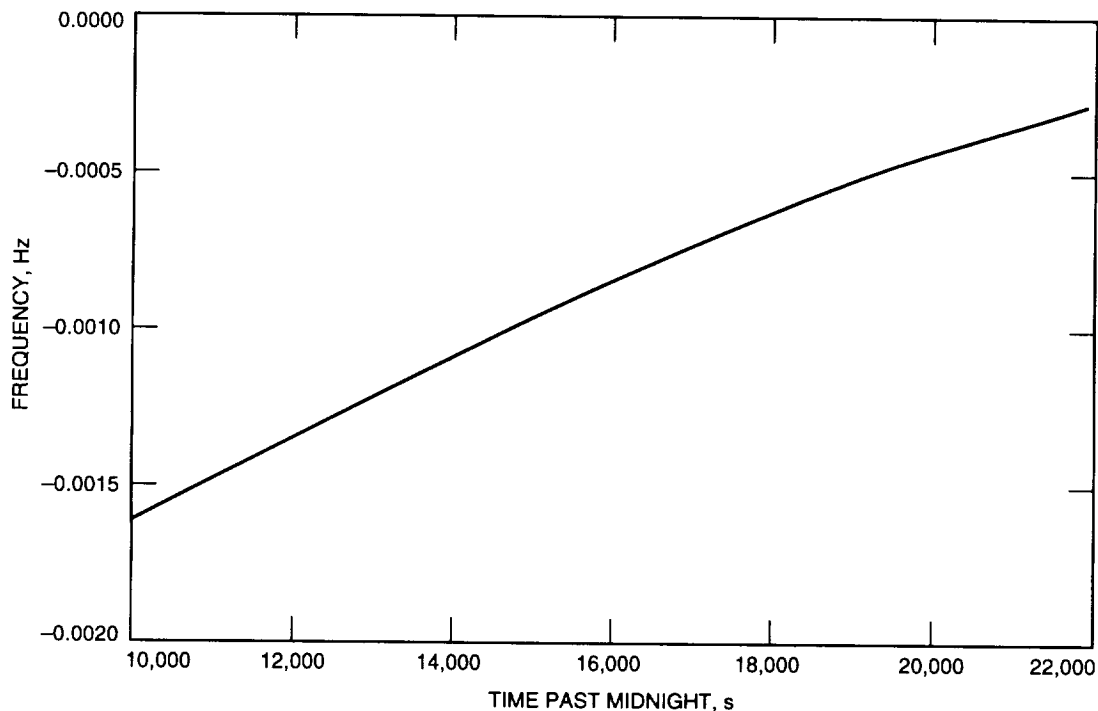
Fig. 10. Ionosphere frequency correction at 2.3 GHz, derived from a TSAC polynomial for the DSS-14 Ulysses pass of January 4, 1991.

The fitted zenith path delays for case (T,F) appear reasonable but are somewhat low compared to the expected 2.1-m values. Unmodeled trends, which blend with the signature of the troposphere, are assumed to exist in the data and thus influence the fit.

The linear slope from a straight line least-squares fit of the postcalibrated residuals tends to be of insignificant or of marginal magnitude when a troposphere fit is performed. When a model troposphere is removed, the fitted linear slopes of the residuals are significant. This suggests that significant unknown trends may be present in the data set that are absorbed by the troposphere fit or that the troposphere model using the default zenith path delay is not sufficient.

The Allan deviations at 1, 10 and 100 s do not change significantly between the different runs for a given band, except for the dual-frequency charged-particle calibrated runs (D in the ION column), where significant system noise at these time intervals is introduced into the data. At 1000 s, dual-frequency charged-particle calibration (D,F) results in the lowest Allan deviations at 2.3 GHz for the 91-004 pass and no significant changes at 2.3 GHz for pass 92-064. At 8.4 GHz, the TSAC calibrated run for pass 91-004 produced the lowest Allan deviation, 1.9×10^{-14}. For the 92-064 DSS-14 pass, no significant improvement was noted in the 8.4-GHz 1000-s Allan deviation between the different runs. The 91-004 Allan deviations agree with independently measured values [4].

For the $f^s - 3f^x/11$ data type (SX), the following runs were performed: (1) TSAC correction [Eq. (25)](T) and no troposphere (N) and (2) no ionosphere calibration (N) and no troposphere calibration (N). Since the difference frequency eliminates all nondispersive effects, troposphere calibration is not performed. For 91-004 SX and 92-064 SX, the slopes of the calibrated runs were of insignificant or marginal magnitudes, suggesting the effectiveness of using TSAC polynomials to remove long period trends from the SX data type and illustrating the dominance of the time variability of the ionosphere over that of the solar plasma during these observations near solar opposition. The Allan deviations do not change significantly between runs for the SX data type, except that the 1000-s value for pass 91-004 SX shows an improvement from 5.2×10^{-14} to 3.3×10^{-14} when applying the TSAC calibration.

Figure 11 displays the averaged residuals for this pass without applying TSAC (N,N). Here, all nondispersive effects should cancel out, and the resulting signature is presumably due to dispersive sources. The corresponding TSAC S-X frequency calibration for this pass is shown in Fig. 12. The averaged residuals after applying the TSAC calibration (T,N) are shown in Fig. 13. The resulting signature is considerably flatter than that of the non-TSAC calibration run (N,N) of Fig. 11, but a long period trend of order 0.5-mHz over this pass is apparent upon closer inspection. This is consistent with the observation of Bertotti et al. [4] that the error of the TSAC calibration is not negligible and can be as large as 0.5 mHz. The long period trends on the order of 0.5 mHz that remain in the data after applying media calibrations are consistent with known uncertainties in the calibration schemes. The zenith path delays for the TSAC ionosphere can be in error by as much as 75 cm for day passes and 15 cm for night passes. The troposphere can be in error by 5 cm.[9] An overall 15-cm zenith path delay error (for these nighttime solar opposition passes) can map into variations at the 1-mHz level over a pass, consistent with what is observed in these data.

For Ulysses at 8.4 GHz, trajectory errors of 0.012 mm/s in velocity at 1000 s translate to Allan deviations at about 4×10^{-14}, which is comparable with the observed values. These are also comparable with expected noise due to media. After removal of the ionosphere and troposphere calibration models, significant random fluctuations in the data remain. These fluctuations have different characteristics with different frequencies, solar elongations, local weather conditions, and local ionospheric variability. These are usually masked by system noise at the lower time intervals, whose magnitudes depend upon received signal levels and received noise power of a given spacecraft. Expected levels of these fluctuations at 1000 s for Ulysses at 8.4 GHz are about 3×10^{-14} for the troposphere, an upper bound of 3×10^{-14} for plasma noise, and 2.5×10^{-14} for the system noise of the closed-loop receiver [4].

Figure 14 displays the 8.4-GHz Allan deviation curves for a set of different calibration schemes for the 91-004 DSS-14 pass. For the case of two-way data over a sufficient elevation angle arc, the best estimate of system stability is obtained by applying a TSAC ionosphere correction and by fitting and removing a troposphere model.

IV. Conclusion

A description of the STBLTY program set has been presented with details on model implementation and residual analysis. Examples of the use of this program set on Galileo and Ulysses data were also presented. The frequency of a spacecraft signal received on the ground is the observable data type. All known effects are removed from this observable to produce residuals that can be inspected to evaluate performance. Among the errors in the residuals are those due to white noise, media, and trajectory. For a sufficiently high SNR, random media effects appear to be the limiting error source at the 1000-s time scale for both Galileo and Ulysses coherent data sets.

Future upgrades to STBLTY will focus on modeling the gravity fields of planets in order to remove these effects from the data during flybys or orbital operations. The first use for this capability will involve the Galileo Jupiter orbital operations when Galileo is expected to tour the Jovian system starting in late 1995. Other future upgrades include modifying the code to process 32.0-GHz downlink data such as that expected for the Cassini radio science experiments, to process coherent downlink data that involve 8.4- or 32.0-GHz (Ka-band) uplink signals, converting the code to manipulate vectors in the J2000 system, and incorporating a planetary atmospheric model for occultation data analysis. The program set was recently modified to process three-way data (implemented in a developmental version).

---

[9] T. McElrath, personal communication, Navigation Systems Section, Jet Propulsion Laboratory, Pasadena, California, 1994.
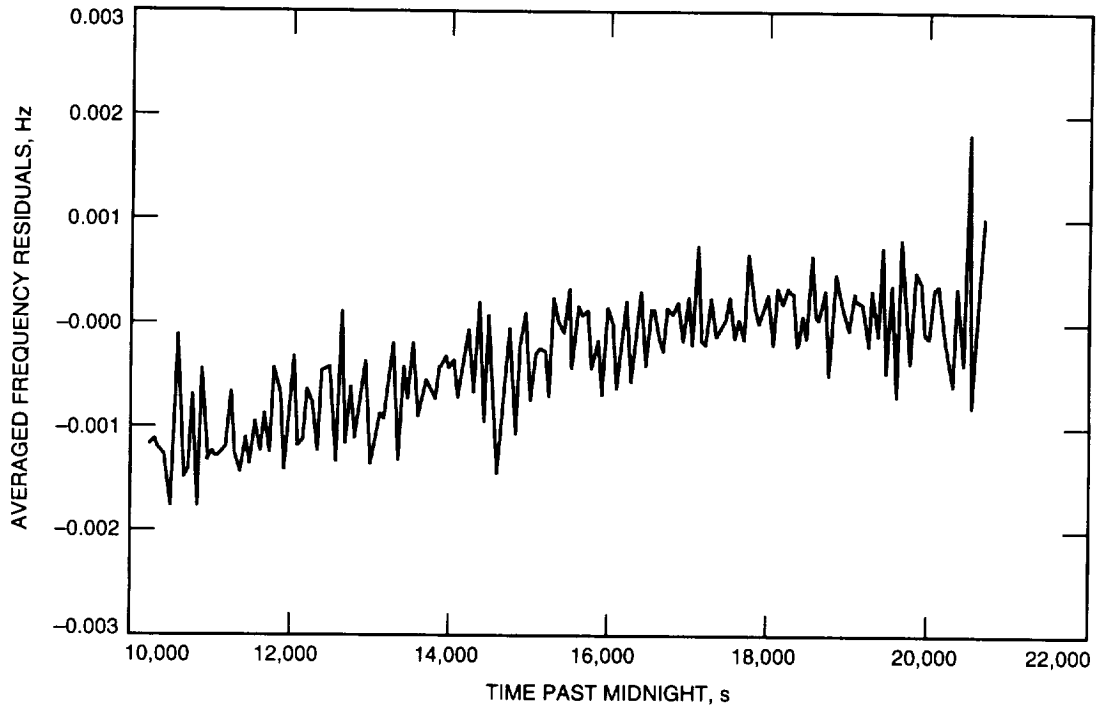
Fig. 11. Averaged differenced frequency residuals (dual-band) for the DSS-14 Ulysses pass of January 4, 1991.
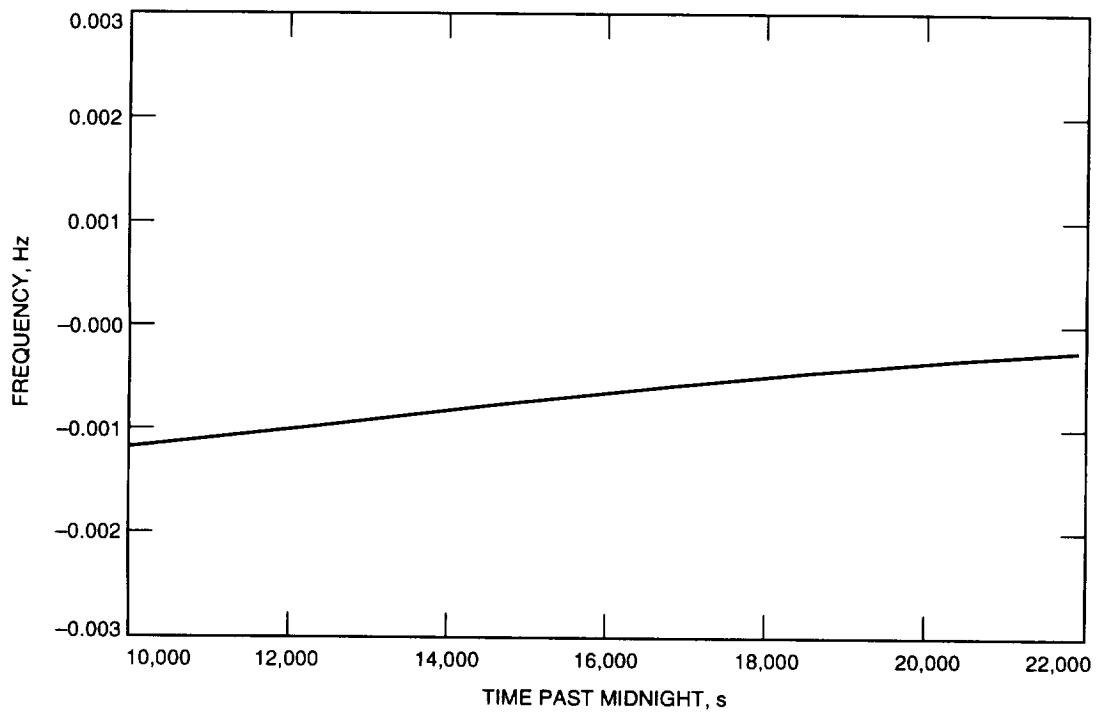
Fig. 12. Ionosphere frequency correction for dual-band derived from a TSAC polynomial for the DSS-14 Ulysses pass of January 4, 1991.
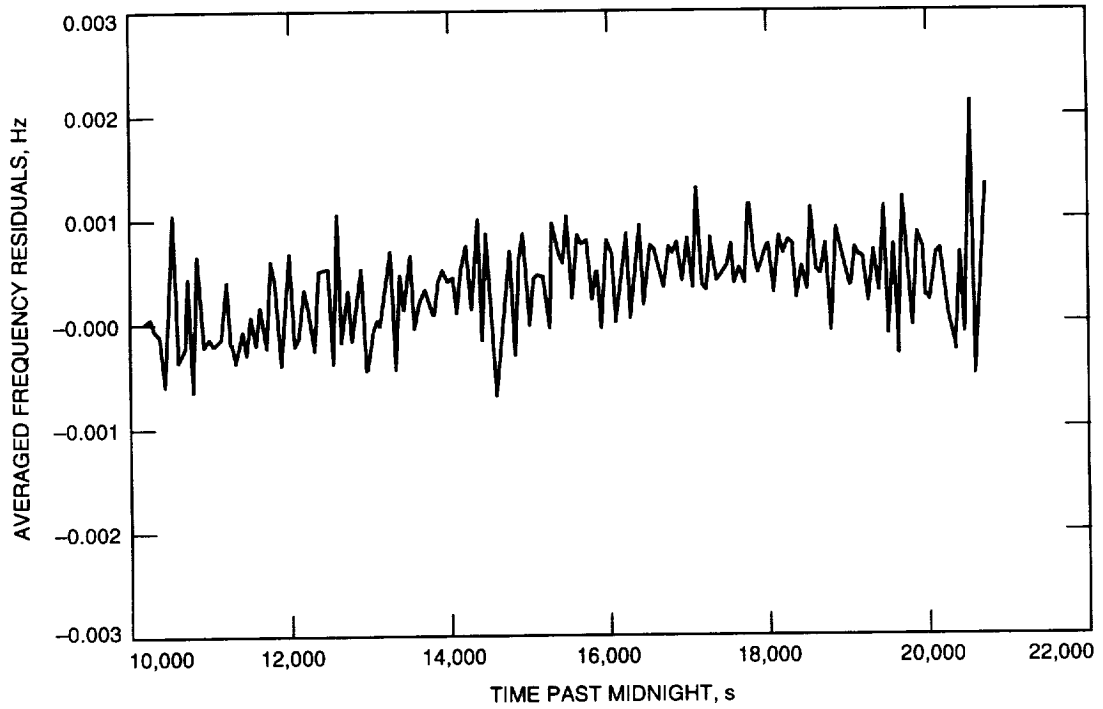
Fig. 13. Averaged differenced frequency residuals (dual-band) of Fig. 11 after removing the TSAC correction of Fig. 12.

A = NO MEDIA CALIBRATION

B = TROPOSPHERE MODEL ONLY

C = TROPOSPHERE MODEL AND IONOSPHERE MODEL

D = TROPOSPHERE FIT ONLY

E = TROPOSPHERE FIT AND IONOSPHERE MODEL
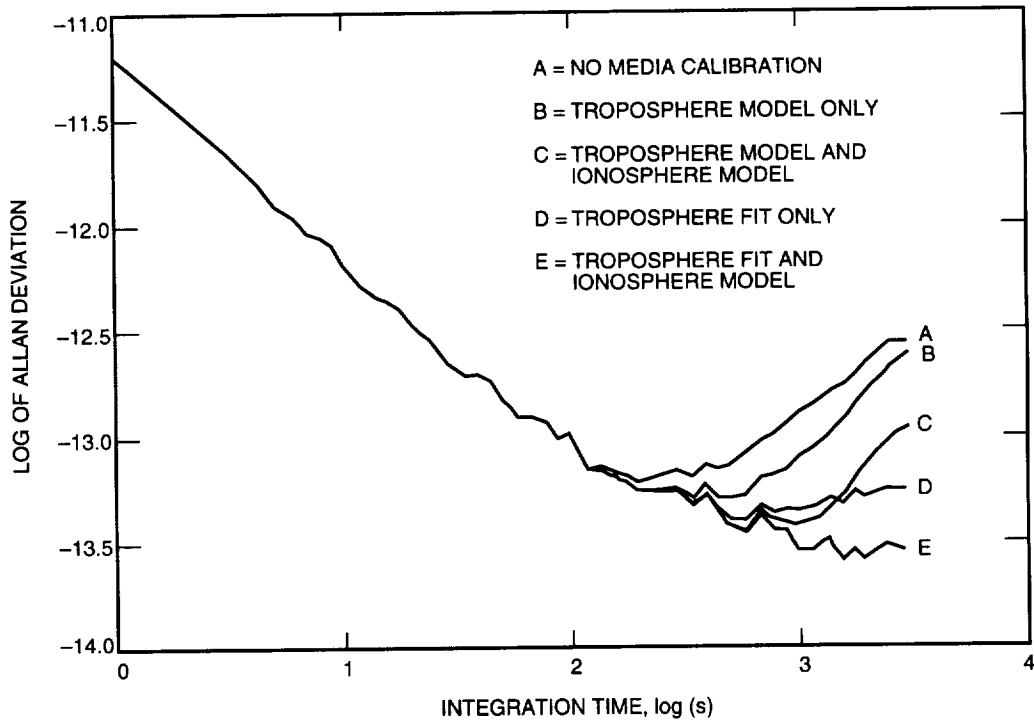
Fig. 14. Allan deviation curves for a set of different calibration schemes for the DSS-14 Ulysses pass of January 4, 1991.

Acknowledgments

References

[1] T. P. Krisher, D. D. Morabito, and J. D. Anderson, "The Galileo Solar Redshift Experiment," *Physical Review Letters*, vol. 70, pp. 2213–2216, April 12, 1993.

[2] J. D. Anderson, J. W. Armstrong, J. K. Campbell, F. B. Estabrook, T. P. Krisher, and E. L. Lau, "Gravitation and Celestial Mechanics Investigations With Galileo," *Space Science Review*, vol. 60, pp. 591–610, 1992.

[3] D. D. Morabito, T. P. Krisher, and S. W. Asmar, "The Flight Performance of the Galileo Orbiter USO," *Proceedings of the IEEE Frequency Control Symposium*, IEEE Catalog No. 93CH3244-1, Salt Lake City, Utah, pp. 788–805, June 2–4, 1993.

[4] B. Bertotti, R. Ambrosini, S. W. Asmar, J. P. Brenkle, G. Comoretto, G. Giampieri, L. Iess, A. Messeri, R. Vecchio, and H. D. Wahlquist, *Ulysses Gravitational Wave Experiment Report on the First Opposition*, IFI-91-25, Istituto di Fisica dello Spazio Interplanetario, Frascati, Italy, December 1991.

[5] H. T. Howard, V. R. Eshleman, D. P. Hinson, A. J. Kliore, G. F. Lindal, R. Woo, M. K. Bird, H. Volland, P. Edenhofer, M. Pätzold, and H. Porche, "Galileo Radio Science Investigation," *Space Science Review*, vol. 60, pp. 565–590, 1992.

[6] A. C. Densmore, "A Digitally Implemented Phase-Locked Loop Detection Scheme for Analysis of the Phase and Power Stability of a Calibration Tone," *The Telecommunications and Data Acquisition Progress Report 42-93, January–March 1988*, Jet Propulsion Laboratory, Pasadena, California, pp. 207–213, May 15, 1988.

[7] T. M. Nguyen, S. M. Hinedi, H.-G. Yeh, and C. Kyriacou, "Performance Evaluation of Digital Phase-Locked Loops for Advanced Deep Space Transponders," *The Telecommunications and Data Acquisition Progress Report 42-117, January–March 1994*, Jet Propulsion Laboratory, Pasadena, California, pp. 175–193, May 15, 1994.

[8] R. M. Jaffee, and E. Rechtin, "Design and Performance of Phase Locked Circuit Capable of Near Optimum Performance Over a Wide Range of Input Signal and Noise Levels," *IRE Transactions on Information Theory*, vol. IT-1, pp. 66–76, March 1955.

[9] V. M. Pollmeier and P. H. Kallemeyn, "Galileo Orbit Determination From Launch Through the First Earth Flyby," *Proceedings of the 47th Annual Meeting of the Institute of Navigation*, Williamsburg, Pennsylvania, pp. 9–16, June 10–12, 1991.

[10] T. McElrath, B. Tucker, P. Menon, E. Higa, and K. Criddle, "Ulysses Navigation at Jupiter Encounter," *AIAA/AAS Astrodynamics Conference Proceedings*, AIAA 92-4524, pp. 1–9, August 10–12, 1992.

[11] C. Yoder, J. G. Williams, and M. Parke, "Tidal Variations of Earth Rotation," *Journal of Geophysical Research*, vol. 86, p. 881–891, 1981.

[12] P. K. Seidelmann, "1980 IAU Theory of Nutation: The Final Report of the IAU Working Group on Nutation," *Celestial Mechanics*, vol. 27, p. 79–106, 1982.

[13] D. D. McCarthy and B. J. Luzan,"Observations of Luni-Solar and Free Core Nutation," *Astronomical Journal*, vol. 102, no. 5, pp. 1889–1895, November 1991.

[14] J. L. Davis, T. A. Herring, I. I. Shapiro, A. E. E. Rogers, and G. Elgered, "Geodesy by Radio Interferometry: Effects of Atmospheric Modeling Error on Estimated Baseline Length," *Radio Science*, vol. 20, pp. 1593–1607, 1985.

[15] G. Lanyi, "Tropospheric Delay Effect in Radio Interferometry," *The Telecommunications and Data Acquisition Progress Report 42-78, April–June 1984*, Jet Propulsion Laboratory, Pasadena, California, pp. 152–159, August 15, 1984.

[16] J. W. Armstrong, R. Woo, and F. B. Estabrook, "Interplanetary Phase Scintillation and the Search for Very Low Frequency Gravitational Radiation," *Astrophysical Journal*, vol. 230, pp. 570–574, June 1, 1979.

Appendix

Formulation of Precession and Nutation Matrices

The following definitions for system rotation matrices and their derivatives apply when defining the precession and nutation rotation matrices and their derivatives:

$$(\theta)_x = \begin{bmatrix} 1 & 0 & 0 \\ 0 & \cos\theta & \sin\theta \\ 0 & -\sin\theta & \cos\theta \end{bmatrix} \quad \frac{d}{dt}(\theta)_x = \begin{bmatrix} 0 & 0 & 0 \\ 0 & -\sin\theta & \cos\theta \\ 0 & -\cos\theta & -\sin\theta \end{bmatrix} \dot{\theta} = \left(\frac{\pi}{2} - \theta\right)_x \dot{\theta}$$

$$(\theta)_z = \begin{bmatrix} \cos\theta & \sin\theta & 0 \\ -\sin\theta & \cos\theta & 0 \\ 0 & 0 & 1 \end{bmatrix} \quad \frac{d}{dt}(\theta)_z = \begin{bmatrix} -\sin\theta & \cos\theta & 0 \\ -\cos\theta & -\sin\theta & 0 \\ 0 & 0 & 0 \end{bmatrix} \dot{\theta} = \left(\frac{\pi}{2} - \theta\right)_z \dot{\theta}$$

I. Precession Rotation Formulation

The precession matrix, $\mathbf{P}$, is the product of the following three system rotations using the definitions given above:

$$\mathbf{P} = \left(\frac{\pi}{2} - \alpha_{1950}\right)_z \left(\frac{\pi}{2} - \delta_{1950}\right)_x (-\Delta_{1950})_z$$

where the precession rotation angles in terms of Julian centuries since 1950, T, are given by

$$\Delta_{1950} = [89.9999986565 - 0.64027801T - (3.042075 \times 10^{-4})T^2 - (5.0837 \times 10^{-6})T^3]\frac{\pi}{180}$$

$$\delta_{1950} = [89.9999988317 - 0.5567500297T + (1.185607 \times 10^{-4})T^2 + (1.16119 \times 10^{-5})T^3]\frac{\pi}{180}$$

$$\alpha_{1950} = [(-1.3435 \times 10^{-6}) - 0.6402780091T - (8.39481 \times 10^{-5})T^2 - (0.50003 \times 10^{-5})T^3]\frac{\pi}{180}$$

The derivative of the precession matrix is as follows:

$$\dot{\mathbf{P}} = (\pi - \alpha_{1950})_z \left(\frac{\pi}{2} - \delta_{1950}\right)_x (-\Delta_{1950})_z \left[\frac{-d}{dt}\alpha_{1950}\right]$$

$$+ \left(\frac{\pi}{2} - \alpha_{1950}\right)_z (\pi - \delta_{1950})_x (-\Delta_{1950})_z \left[\frac{-d}{dt}\delta_{1950}\right]$$

$$+ \left(\frac{\pi}{2} - \alpha_{1950}\right)_z \left(\frac{\pi}{2} - \delta_{1950}\right)_x \left(\frac{\pi}{2} - \Delta_{1950}\right)_z \left[\frac{-d}{dt}\Delta_{1950}\right]$$

where

$$\frac{d}{dt}\Delta_{1950} = [-0.64027801 - (2 \times 3.042075) \times 10^{-4}T - (3 \times 5.0837) \times 10^{-6}T^2]\frac{\pi}{180}$$

$$\frac{d}{dt}\delta_{1950} = [-0.5567500297 + (2 \times 1.185607) \times 10^{-4}T + (3 \times 1.16119) \times 10^{-5}T^2]\frac{\pi}{180}$$

$$\frac{d}{dt}\alpha_{1950} = [-0.6402780091 - (2 \times 8.39481) \times 10^{-5}T - (3 \times 0.50003) \times 10^{-5}T^2]\frac{\pi}{180}$$

II. Nutation Rotation Formulation

The nutation rotation matrix is the product of the following three rotations using the matrix rotation definitions given above:

$$\mathbf{N} = (-\epsilon_m)_x(\Delta\Psi)_z(\epsilon_m + \Delta\epsilon)_x$$

where the nutation angles are the IAU 1980 model values defined in the text. The derivative of the nutation rotation matrix is thus given as

$$\dot{\mathbf{N}} = -\dot{\epsilon}\left(\epsilon_m + \frac{\pi}{2}\right)_x (\Delta\Psi)_z(\epsilon_m + \Delta\epsilon)_x + \Delta\dot{\Psi}(-\epsilon_m)_x\left(-\Delta\Psi + \frac{\pi}{2}\right)_z$$

$$\times (\epsilon_m + \Delta\epsilon)_x + \dot{\epsilon}(-\epsilon_m)_x(\Delta\Psi)_z\left(-\epsilon_m - \Delta\epsilon + \frac{\pi}{2}\right)_x$$

Analysis of a Microstrip Reflectarray Antenna for Microspacecraft Applications

J. Huang
Spacecraft Telecommunications Equipment Section

A microstrip reflectarray is a flat reflector antenna that can be mounted conformally onto a spacecraft's outside structure without consuming a significant amount of spacecraft volume and mass. For large apertures (2 m or larger), the antenna's reflecting surface, being flat, can be more easily and reliably deployed than a curved parabolic reflector. This article presents the study results on a microstrip reflectarray with circular polarization. Its efficiency and bandwidth characteristics are analyzed. Numerous advantages of this antenna system are discussed. Three new concepts using this microstrip reflectarray are also proposed.

I. Introduction

JPL is currently developing microspacecraft technologies for future deep space missions in order to meet NASA's goal of having small, efficient, and inexpensive spacecraft. The microspacecraft, having sizes on the order of one-half meter, will certainly require components that are small both in size and mass. High-gain antennas are one part of the telecommunications equipment that warrants attention since they generally require a significant amount of real estate and mass. The conventional high-gain antennas most often used are parabolic reflectors. Although they are efficient radiators, parabolic reflectors are generally bulky in size and large in mass, due to their curved reflecting surfaces. As a result, a flat reflector called a microstrip reflectarray [1,2] is being proposed as a future candidate high-gain antenna. It is well known that when a required antenna gain is given at a particular frequency, the antenna aperture size is more or less fixed. The only significant size reduction that may be achieved for an antenna is its profile thickness. The flat-plate microstrip reflectarray offers such an advantage of profile size reduction as compared to a conventional parabolic reflector.

The reflectarray antenna as shown in Fig. 1 represents World War II technology [3]. However, the low-profile printed reflectarray is a fairly new concept. The microstrip reflectarray, being one of the printed low-profile antenna technologies, consists of a very thin, flat reflecting surface and an illuminating feed, as shown in Fig. 2. On the reflecting surface, there are many isolated microstrip patch elements without any power division network. To each patch element is attached a short segment of phase-adjusting transmission line to compensate for the phase delay over the path from the illuminating feed. Because of the phase adjustment capability of the patch elements, the reflecting surface can be flat or conformal to its mounting structure and still maintain a constant phase aperture field. A detailed description of this antenna concept, as well as its advantages, is given in the following sections. Theoretical analysis of the antenna performance parameters, such as radiation pattern, efficiency, and bandwidth, is also presented.
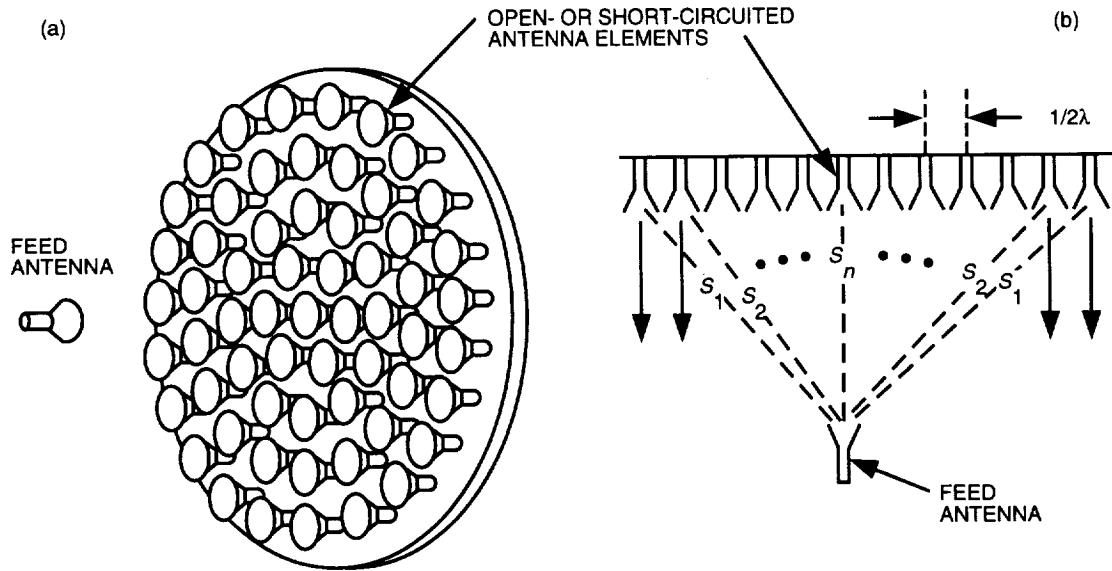
Fig. 1. Reflectarray configuration: (a) three-dimensional view and (b) two-dimensional view.
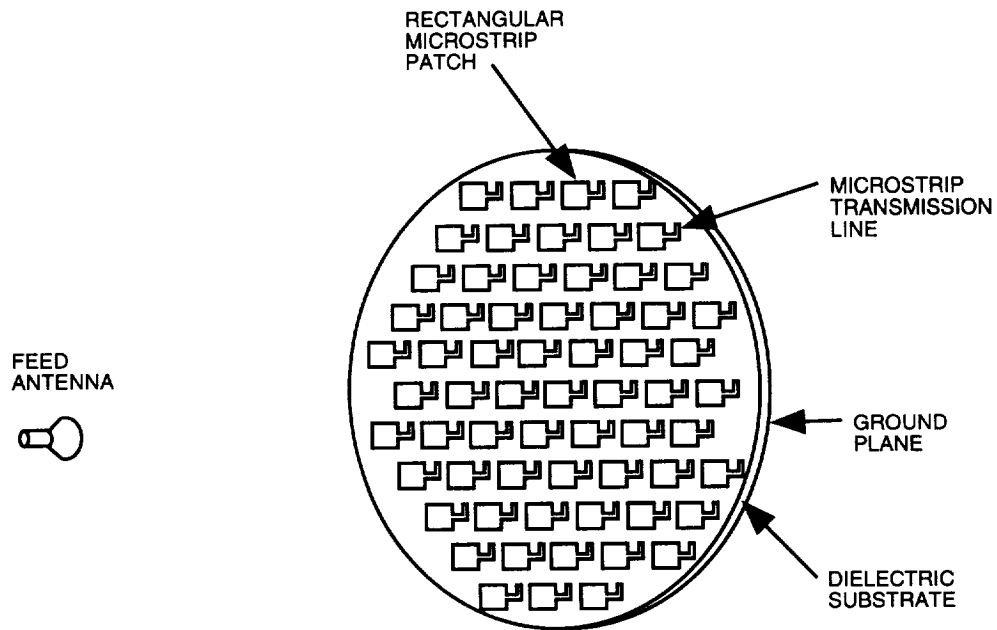
Fig 2. Flat-plate microstrip reflectarray with identical patches but different-length microstrip transmission lines.

II. Description of the Microstrip Reflectarray

When many antenna elements with open- or short-circuited terminations are arranged in a planar aperture and are illuminated by a feed antenna, as shown in Fig. 1, these elements will reradiate their illuminated energy into space. The total reradiated energy will be noncophasal if all the elements and their terminations are identical. This is because the fields that propagate to the elements from the

154

feed have different path lengths, $S_1, S_2, \cdots, S_N$, as shown in Fig. 1(b), and thus form different phases. However, if each element's phase is adjusted to compensate for these different path lengths, the total reradiated field can be made cophasal and concentrated toward a specific direction. The array antenna formed by the above concept is named the reflectarray and was introduced [3] many decades ago using a horn, dipole, open-ended waveguide, etc., for the element. Since these elements are large in size at lower microwave frequencies and many elements are needed in a reflectarray in order for it to be efficient, the earlier reflectarray antennas were bulky in size and heavy in weight. Due to the recent advancement of the lightweight and low-profile printed antennas, such as the microstrip patch, the printed reflectarray becomes physically more realizable and attractive. Several different versions of the printed reflectarray have recently been developed. One version, shown in Fig. 2, has all identical microstrip patch elements but with different-length microstrip transmission lines. This microstrip reflectarray was first patented by Munson and Haddad [4] and then openly published and analyzed by Huang [2] and Metzler [5]. Litva, Zhuang, and Wu [6], as well as Chang and Huang [7], have demonstrated the concept via hardware development. Malibu Research Center developed a different reflectarray [8] with printed dipoles having different sizes and no phase delay lines. The required path delay-compensating phases from the elements are achieved primarily via the differing lengths of the dipoles. Different lengths yield different input impedances (complex quantity) at a particular frequency, which in turn give different phases. Targonski and Pozar [9] developed a microstrip reflectarray with patches having different sizes and no delay lines. It is expected that the reflectarray with printed dipoles or patches having different sizes will not radiate as efficiently as the identical-patch reflectarray with different-length delay lines. This is because, for a particular frequency, there is only one optimal size of the resonant structure (dipole or patch) to reflect or reradiate energy; other sizes will result in lower amplitudes. This is similar to the phenomenon observed with frequency selective surfaces (FSS), where only a narrow spectrum will yield total reflection.

By reason of its expected higher efficiency, the microstrip reflectarray with patches having identical sizes and different phase-delay lines is proposed and studied here. This flat reflector antenna, as shown in Fig. 2, is composed of a thin (≤ 0.03 wavelength) slab of dielectric material having one side completely covered with a thin layer of metal (serving as a ground plane) and the other side etched with many identical metallic microstrip patches. A feed antenna, located at an optimally designed distance from the array elements, will effectively illuminate all the patches. The size of each patch, which can be rectangular, square, or circular, is designed to resonate at the frequency of the feed antenna. A short transmission line is connected to each patch at one end with the other end of the line either open or short circuited. To generate circular polarization, two equal-length transmission lines are needed to be orthogonally connected to each square or circular patch, as shown in Fig. 3. In this case, the feed has to be circularly polarized. The short transmission line connected to each patch can be either a microstrip line etched on the same side of the patch or a stripline sandwiched in an additional layered structure placed behind the patch's ground plane. The advantage of the microstrip line is ease of fabrication, while that of the stripline is minimum interference to the patch's radiation. When the radiation field of the feed antenna (in transmit mode) strikes each patch, the received resonant field of the patch will travel through its connected transmission line and be reflected by its open- or short-circuited termination and then reradiated by the patch into space. Thus, all the microstrip patches behave as reradiators, while the short transmission lines serve as phase delay lines. The lengths of these transmission lines are intentionally made different for differently located patches to compensate for the path delay differences from the feed antenna. With proper design and calibration of these line lengths, the reradiated fields from all the patches can be made cophasal in the broadside direction. Also, by redesigning the line lengths, the main beam can be directed toward other directions at large angles (up to more than 50 deg) from the broadside direction. Since the required phase changes for all the elements are between 0 and 360 deg, the maximum length needed for the transmission line is only one-half wavelength. Consequently, the insertion loss associated with these short lines will be insignificantly small. The transmission line should be impedance matched to the patch radiator, which can be done using a quarter-wave-long impedance matching section. Because this is a phase-delay approach and not a time delay, as frequency changes, a phase excursive error will occur, especially for the outer elements of the array (assuming the feed is located at the center axis of the array). In other words, the phase will accumulate more error for the

outer elements as the frequency changes, and this limits the bandwidth performance of the reflectarray. This accumulated phase error can be reduced by using longer transmission lines for the center elements (time delay approach) or by using a larger f/D ratio, where f is the distance between the feed and the array center and D is the array diameter.

Since the microstrip reflectarray does not require any power divider, its efficiency in a large array system is much higher than a conventional array having the same aperture size. One possible drawback is that, in addition to the reradiated fields from the patches, there will also be scattered field from the patches, reflected field from the ground plane (especially away from the resonant frequency of the patch), scattered field from the phase delay lines, and diffracted field from the edge of the reflectarray. These backscattered fields may increase the sidelobe level and possibly distort the main beam shape. However, because most of these scattered fields are noncophasal, and as long as the aperture directivity of the reflectarray is sufficiently higher (20 dB or more) than the feed directivity, the backscattered energy is generally small relative to the desired main beam. In other words, the microstrip reflectarray can be an efficient antenna system only if it has a large number of array elements (500 or more).

(a)   (b)
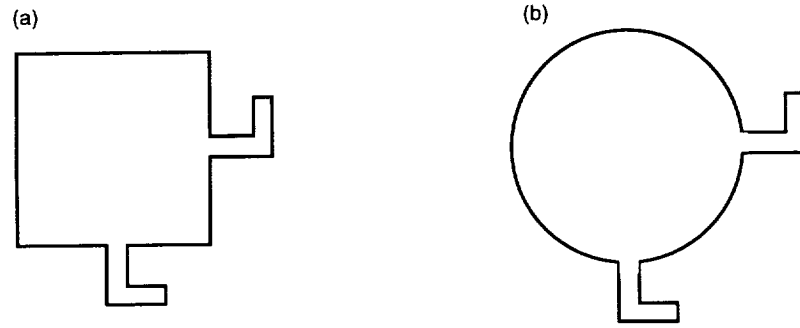
Fig. 3. Reflectarray (a) square and (b) circular microstrip elements, for
circular polarization.

III. Radiation Analysis of the Microstrip Reflectarray

When a rectangular planar array with $M \times N$ microstrip patch elements is nonuniformly illuminated by a low-gain feed at r_f, as shown in Fig. 4, the reradiated field from the patches in an arbitrary direction, $\hat{u}$, will be of the form

$$E(\hat{u}) = \sum_{m=1}^{M} \sum_{n=1}^{N} F\left(\vec{r}_{mn} \cdot \vec{r}_f\right) A\left(\vec{r}_{mn} \cdot \hat{u}_o\right) A\left(\hat{u} \cdot \hat{u}_o\right) \exp\left\{-jk_o\left[|\vec{r}_{mn} - \vec{r}_f| + \vec{r}_{mn} \cdot \hat{u}\right] + j\alpha_{mn}\right\}$$

(1)

where F is the feed pattern function, A is the pattern function of the microstrip patch, r_{mn} is the position vector of the mnth patch, $\hat{u}_o$ is the desired main-beam pointing direction, and α_{mn} is the required transmission-line phase delay of the mnth element. The condition for the aperture distribution to be cophasal in the desired direction $\hat{u}_o$ is

$$\alpha_{mn} - k_o\left[|\vec{r}_{mn} - \vec{r}_f| + \vec{r}_{mn} \cdot \hat{u}_o\right] = 2n\pi, \qquad n = 0, 1, 2, \cdots$$

(2)

For a circular aperture, which is desirable for better aperture efficiency as compared with a rectangular aperture, the summation signs in Eq. (1) can be truncated to 0 (no calculation) for patches located outside of the circular aperture.

156
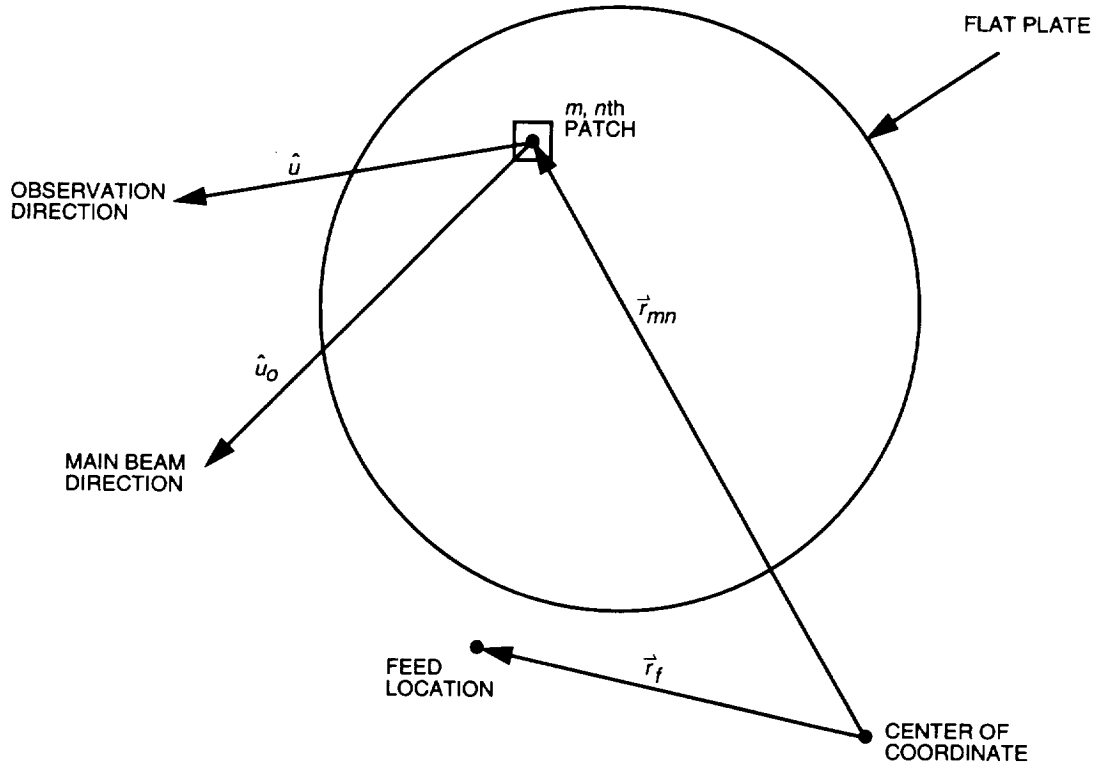
Fig. 4. Coordinate system for reflectarray pattern analysis.

Equation (1) gives a nonpolarized (scalar) field. For circularly polarized radiation, the field of Eq. (1) can be separated into θ and ϕ components:

$$E_\theta = E\left(\hat{u}\right)\left[\left(\hat{f}_1 \cdot \hat{p}_1\right)\hat{p}_1 \cdot \hat{\theta} + \left(\hat{f}_2 \cdot \hat{p}_2\right)\hat{p}_2 \cdot \hat{\theta}\right] \tag{3a}$$

$$E_\phi = E\left(\hat{u}\right)\left[\left(\hat{f}_1 \cdot \hat{p}_1\right)\hat{p}_1 \cdot \hat{\phi} + \left(\hat{f}_2 \cdot \hat{p}_2\right)\hat{p}_2 \cdot \hat{\phi}\right] \tag{3b}$$

where $\hat{f}_1$ and $\hat{f}_2$ are the two orthogonal polarization vectors of the feed horn at the patch location, $\hat{p}_1$ and $\hat{p}_2$ are the two orthogonal patch polarization vectors, and $\hat{\theta}$ and $\hat{\phi}$ are the orthogonal far-field spherical coordinate unit vectors. For a right-hand circularly polarized feed, the far-field copolarized radiation from the reflectarray is

$$E_{co-pol} = \frac{1}{\sqrt{2}}\left(E_\theta + jE_\phi\right) \tag{4a}$$

and the cross-polarized radiation is

$$E_{x-pol} = \frac{1}{\sqrt{2}}\left(E_\theta - jE_\phi\right) \tag{4b}$$

In Eq. (1), the feed pattern function F is modeled by a $\cos^q \Psi$ function. For the pattern function A of the single microstrip patch, a simple closed-form model using the dual-slot theory [1] is employed. This

simple model, which is accurate enough for large array prediction, allows the computation time of many thousands of patch elements to become more realistic as compared with other more rigorous techniques. Consequently, mutual coupling effects between patches are not included. For a substrate thickness of less than 0.03 free-space wavelength, beam scan angles of less than 45 deg, and no extremely low sidelobe requirement, the mutual coupling effects can generally be neglected for the microstrip array. Experimental reports [10] demonstrated that, due to the low-profile nature of the microstrip antenna, mutual coupling has not been found to be a serious problem in most of the array applications.

In addition to the reradiated field given in Eq. (1), there is a certain amount of backscattered field, such as the scattered field from the phase delay transmission lines, the patches, the ground plane, and the ground plane edges. However, as long as the reflectarray is designed with proper element spacing (avoiding the grating lobe condition) and the patch element is designed to resonate at the correct frequency, the backscattered fields can be minimized. Furthermore, if the directivity of the feed antenna is significantly lower (by at least 20 dB) than the directivity of the reflectarray aperture, the effect of the noncophasal backscattered field will generally be insignificant [1] when compared with the cophasal reradiated fields from the patches. To summarize, with proper design and large enough array size, Eq. (1) is an excellent approximation with which to efficiently calculate the far-field radiation pattern of the reflectarray. It should be able to predict the main beam and the first few sidelobes with good accuracy.

IV. Antenna Efficiency Analysis

The two primary factors that govern the efficiency of the microstrip reflectarray are very similar to those for the parabolic reflector. These are the aperture illumination efficiency and the feed spillover efficiency [11]. Other minor factors that contribute to the reflectarray efficiency are the patch element loss and the back scattered field loss. The aperture illumination efficiency is caused by the unequal illumination of the array aperture due to the feed's tapered pattern. A uniformly illuminated aperture is defined as having 100-percent illumination efficiency. The spillover efficiency is the ratio of the amount of feed energy that illuminates the entire array to the total amount of energy that is radiated by the feed, which includes the amount that spills outside the array aperture. It is clear that the illumination and the spillover efficiencies are complementary to each other. In other words, if one increases, the other will decrease, and vice versa.

Let us define the total aperture efficiency (η) as the product of the illumination (η_{ill}) and spillover (η_s) efficiencies:

$$\eta = \eta_{ill} \cdot \eta_s \tag{5}$$

From Silver [12] and Fig. 5,

$$\eta_{ill} = \frac{|\int_{\theta=o}^{\theta_e} \int_{\phi=o}^{2\pi} \vec{E} \cdot P\hat{x} ds|^2}{s \int_{\theta=o}^{\theta_e} \int_{\phi=o}^{2\pi} |\vec{E}|^2 ds} = \frac{|I|^2}{sII} \tag{6}$$

where $s = \pi \rho_e^2 = \pi f^2 \tan^2 \theta_e$, and

$$\eta_s = \frac{\int_{\theta=o}^{\theta_e} \int_{\phi=o}^{2\pi} |\vec{E}|^2 ds}{\int_{\theta=o}^{\pi/2} \int_{\phi=o}^{2\pi} |\vec{E}|^2 ds} = \frac{II}{III} \tag{7}$$
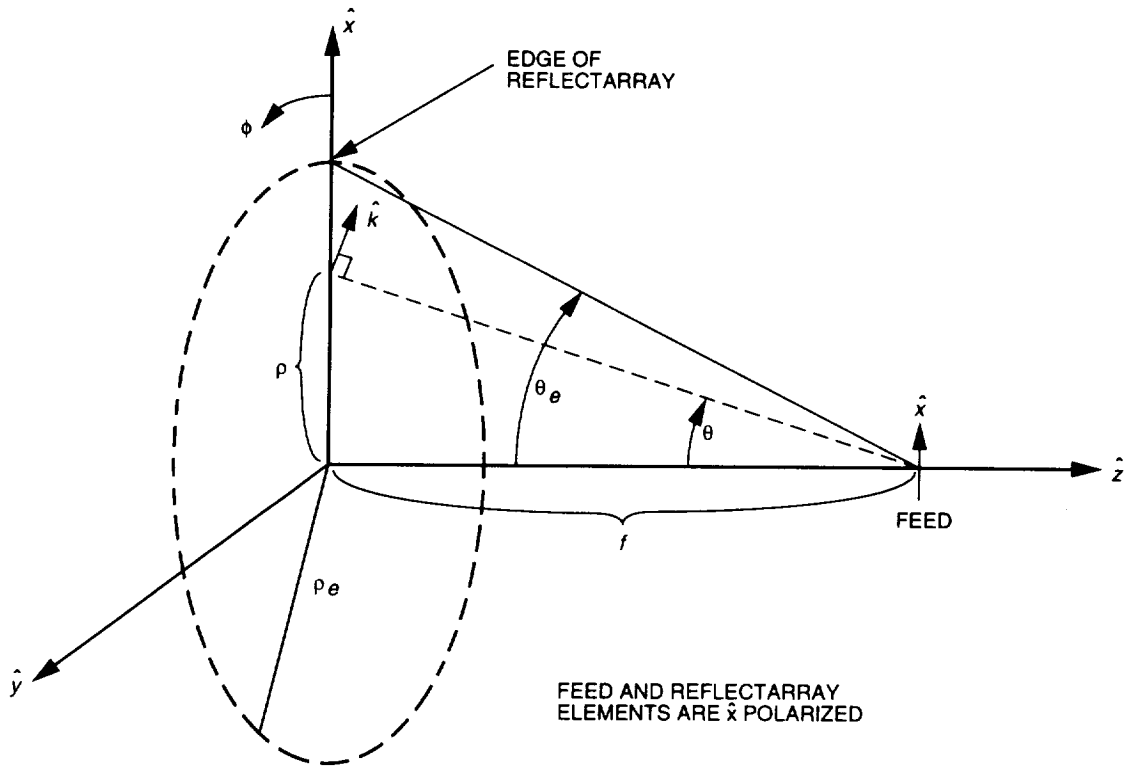
Fig. 5. Coordinate system for reflectarray efficiency analysis.

where $|I|^2$ is the power distributed across the reflectarray aperture, II is the total power radiated by the feed within the reflectarray aperture, and III is the total power radiated by the feed to its front hemisphere. The analysis here assumes the feed has a $\cos^q \theta$ pattern and is polarized in the $\hat{x}$ direction. All the patch elements are also polarized in the $\hat{x}$ direction. The $\hat{E}$ vector in both Eqs. (6) and (7) is the feed far-field function and is given by

$$\vec{E} = |E|\hat{k} = C_o \frac{\cos^q \theta}{r} \left(\cos \phi \hat{\theta} - \sin \phi \hat{\phi} \right) \tag{8a}$$

where the phase term e^{-jkr} is suppressed since phase does not play a role here for the efficiency calculation. The function P in Eq. (6) is the far-field pattern function of the patch element in the reflectarray and is assumed to be $\cos \theta$.

$$\vec{E} \cdot P\hat{x} = C_o \frac{\cos^q \theta}{r} \left(\cos \theta \cdot \cos^2 \phi + \sin^2 \phi \right) \cos \theta \tag{8b}$$

The last term, $\cos \theta$, in Eq. (8b) is the patch element pattern effect on the incoming wave from the feed.

$$I = \int_o^{\theta e} \int_o^{2\pi} \frac{C_o \left(\cos^{q+2} \theta \cos^2 \phi + \cos^{q+1} \theta \sin^2 \phi \right)}{r} ds$$

Because $ds = \rho \, d\rho \, d\phi, \rho = r \sin \theta, r = f / \cos \theta$, and $d\rho = (f / \cos^2 \theta)d\theta$,

159

$$I = \int_o^{\theta e} \int_o^{2\pi} c_o \left(\cos^{q+2} \theta \cos^2 \phi + \cos^{q+1} \theta \sin^2 \phi \right) \sin \theta \frac{f}{\cos^2 \theta} d\phi d\theta = c_o f \pi \left[\frac{1 - \cos^{q+1} \theta_e}{q+1} + \frac{1 - \cos^q \theta_e}{q} \right]$$

$$(9)$$

$$II = \int_o^{\theta \epsilon} \int_o^{2\pi} \frac{c_o^2 \cos^{2q} \theta}{r^2} r d\theta \cdot \rho d\phi$$

Because $\rho = r \sin \theta$,

$$II = 2\pi c_o^2 \frac{1 - \cos^{2q+1} \theta_e}{2q+1} \tag{10}$$

$$III = \int_o^{\pi/2} \int_o^{2\pi} \frac{c_o^2 \cos^{2q} \theta}{r^2} r d\theta \cdot \rho d\phi = 2\pi c_o^2 \frac{\left[1 - \cos^{2q+1}(\pi/2) \right]}{2q+1} = \frac{2\pi c_o^2}{2q+1} \tag{11}$$

By using Eqs. (6), (7), (9), (10), and (11),

$$\eta_{ill} = \frac{|I|^2}{sII} = \frac{\left[\left((1 - \cos^{q+1} \theta_e)/(q+1) \right) + \left((1 - \cos^q \theta_e)/q \right) \right]^2}{2 \tan^2 \theta_e \left[(1 - \cos^{2q+1} \theta_e)/(2q+1) \right]} \tag{12}$$

and

$$\eta_s = \frac{II}{III} = 1 - \cos^{2q+1} \theta_e \tag{13}$$

By using Eqs. (12) and (13), the efficiencies are plotted against the feed pattern shapes in Fig. 6 with a given reflectarray diameter of 0.5 m at 32 GHz (Ka-band) and a f/D ratio of 1.0. The element spacing is half of the free-space wavelength, and the total number of patch elements is 8,937. These curves clearly indicate that the illumination and the spillover efficiencies are complementary to each other. The optimal aperture efficiency can be designed with a feed q factor equal to 10.3. Another curve (Fig. 7) gives the optimum f/D ratio when an arbitrarily selected feed pattern is given ($q = 8$). Equations (12) and (13) are very important tools that aid in the design of an optimal reflectarray configuration.

As mentioned previously, there are other efficiency factors, in addition to aperture efficiency, in the complete characterization of the reflectarray antenna system. The various contributors to the overall efficiency factor are estimated and listed in Table 1 for a Ka-band 0.5-m reflectarray with $f/D = 1.0$ and feed q factor $= 10.3$.

It should be noted that the above feed loss does not include loss in the transmission line between the feed and the transceiver.

V. Bandwidth Study

Bandwidth is often an important quantity for satellite communication, especially with the increasing demand for higher data rates. At 32 GHz, 1 GHz of bandwidth (3 percent) is anticipated. In addition, it is expected that, for Ka-band deep space satellite communication, 32 GHz will be used for downlink
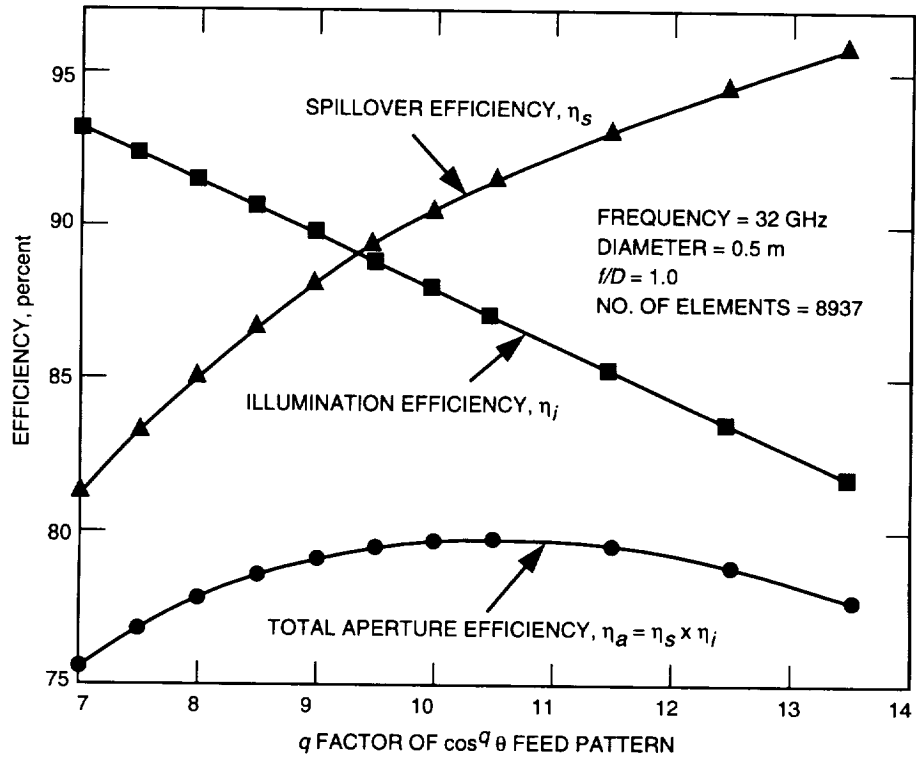
Fig. 6. Microstrip reflectarray spillover and illumination efficiencies versus feed pattern shape.
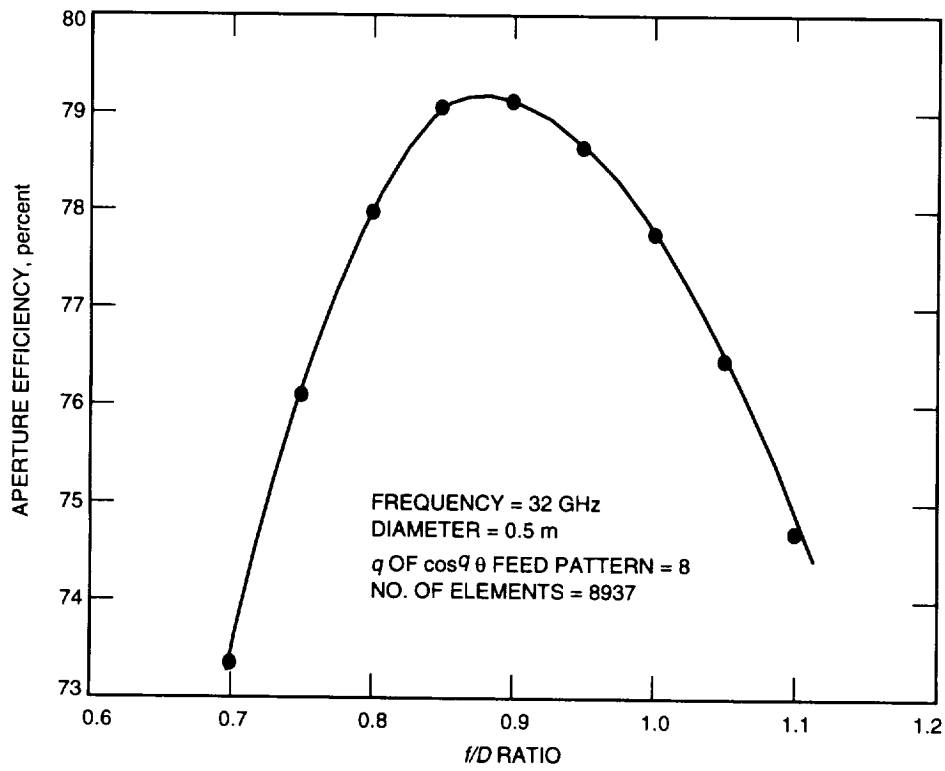
Fig. 7. Microstrip reflectarray aperture efficiency versus f/D ratio.

Table 1. Estimated efficiency of the microstrip reflectarray.

Type of efficiency	Efficiency, percent	Loss, dB
Illumination	87	0.60
Spillover	91	0.41
Patch loss	97	0.13
Delay line loss	95	0.22
Feed loss	95	0.22
Cross-pol loss	95	0.22
Total	66	1.80

and 34 GHz for uplink. If a reflectarray antenna needs to cover both uplink and downlink frequencies, a bandwidth of more than 6 percent is required. Certainly, the bandwidth performance of the reflectarray is no match to the parabolic reflector, which has, theoretically, an infinite bandwidth. It is the intention of this section to study the bandwidth characteristics of the microstrip reflectarray and to optimize it for a given application.

The bandwidth performance of a microstrip reflectarray can be limited by four factors: (1) the microstrip patch element, (2) the array element spacing, (3) the feed antenna bandwidth, and (4) the differential spatial phase delay. Due to its thin cavity, the microstrip patch element can generally achieve a bandwidth of only 3 percent. To achieve a bandwidth larger than 3 percent, techniques such as the stacked dual patch or the patch with a thicker substrate can be employed. Ten- to fifteen-percent bandwidths for microstrip antennas have been reported. The array element spacing limits the reflectarray performance such that, as frequency is decreased, the electrical element spacing becomes small, and excessive mutual coupling effects start to degrade the array performance. As the frequency is increased, the electrical element spacing becomes large, and undesirable grating lobes begin to appear. Fortunately, previous calculations and experiences have shown that the element spacing effect will not be detrimental until the frequency variation is more than 30 percent ($\pm$15 percent around center frequency). The third bandwidth limiting factor is the feed antenna, which can be designed to operate over a bandwidth of at least 10 percent while maintaining a relatively constant beam shape and input impedance. Waveguide horns and cavity-backed dipoles are good candidates. If desired, an Archimedean spiral can be used to achieve more than 100 percent of bandwidth. The fourth limiting factor, differential spatial phase delay, has not been well understood and is separately detailed in the following paragraph.

The differential spatial phase delay can best be explained by referring to Fig. 8, where the differential spatial phase delay, Δs, is the difference between the electrical paths S_1 and S_2. This Δs can be many multiples of the wavelength at the center operating frequency, such as $\Delta s = N.d\lambda_o$, where N is an integer and $.d$ represents the fractional number of a free-space wavelength λ_o. At each patch location on the reflectarray, $N.d$ could be different numbers. In order to achieve constant aperture phase for the reradiated waves, the $.d$ at each patch location is compensated for by the appropriate length of the phase delay line attached to the patch. However, as frequency changes, the $N.d$ will change accordingly. Since the phase delay lines are fixed, a frequency excursion error will occur in the reradiated phase front. The old $N.d\lambda_o$ now becomes $N.d(\lambda_o + \Delta\lambda_o)$, where $\Delta\lambda_o$ is directly proportional to the frequency change. The amount of phase change is, therefore, $N.d\Delta\lambda_o$, which can be a significant portion of a wavelength (360 deg). To reduce the amount of frequency excursion error, the integer number N must be reduced. There are two ways to reduce N. One is to design the reflectarray with a larger f/D ratio, and the other is simply to use a reflectarray with a small electrical diameter. With a fixed f/D ratio, the larger the electrical diameter, the larger the N will be. The effects of the f/D ratio and the diameter on bandwidth performance are calculated by using Eq. (1) and are plotted in Figs. 9 and 10, where beam directivity versus frequency change is shown. The bandwidth effects of the patch element and the feed
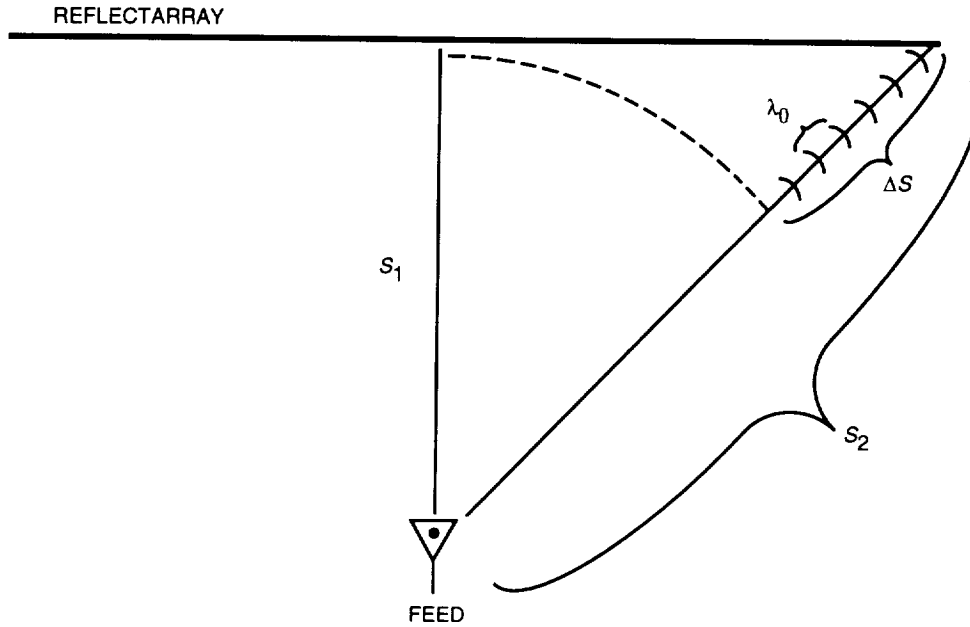
REFLECTARRAY

Fig. 8. Spatial phase delay of the reflectarray.
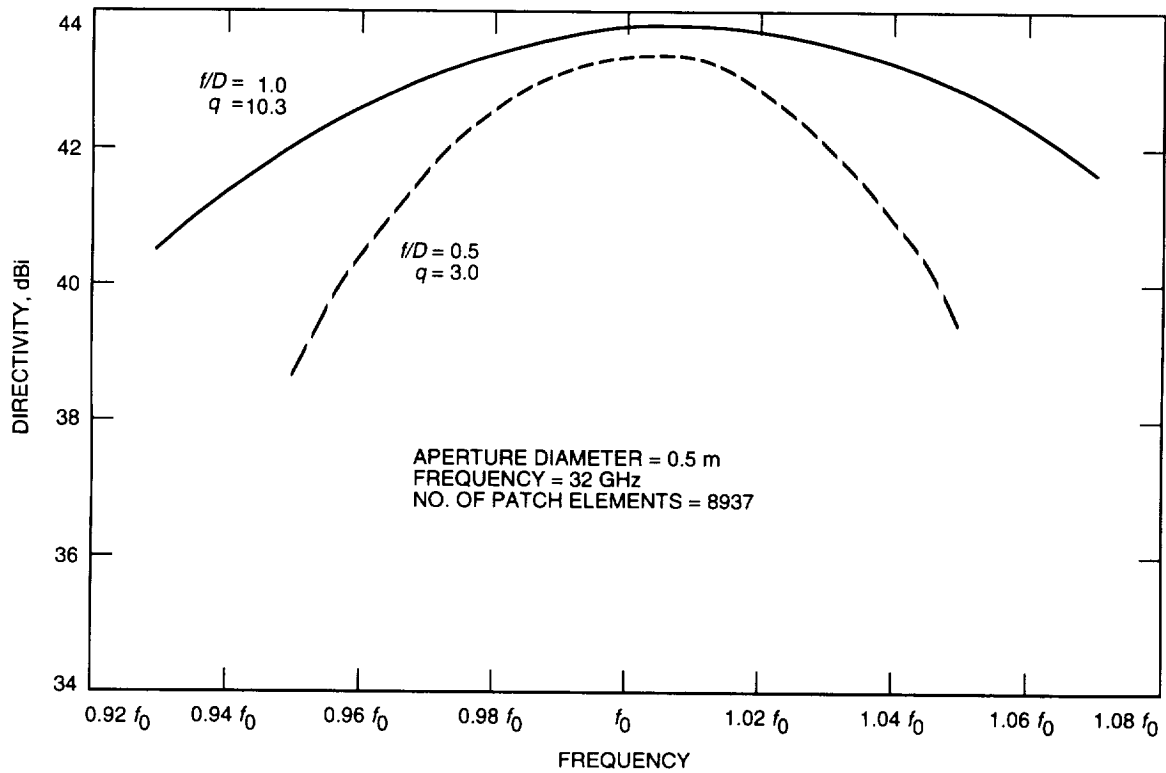
Fig. 9. Antenna directivity versus frequency for a 0.5-m Ka-band microstrip reflectarray.
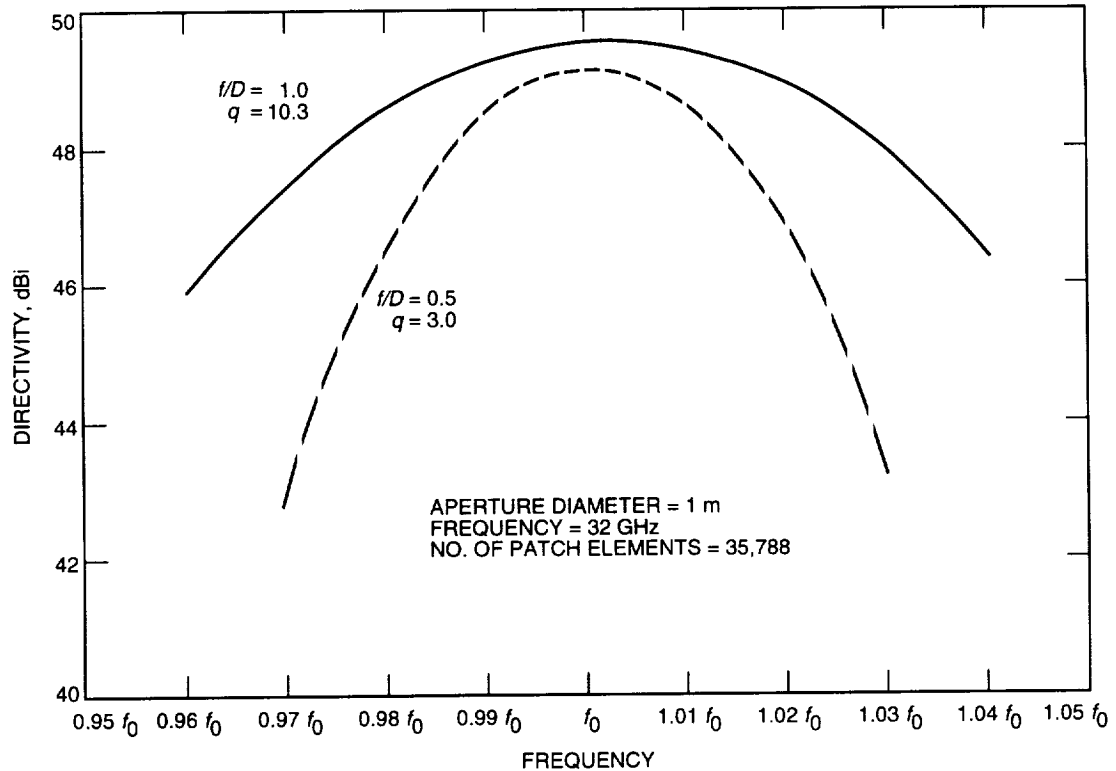
Fig. 10. Antenna directivity versus frequency for a 1.0-m Ka-band microstrip reflectarray.

antenna are not included in these figures. Figure 9 is plotted for a 32-GHz reflectarray having a diameter of 0.5 m and a total of 8,937 patch elements. Two f/D ratios of 0.5 and 1.0 are plotted in this figure. It is obvious that an f/D of 1.0 gives better bandwidth performance. Similar curves are plotted in Fig. 10 for a 1-m-diameter reflectarray at 32 GHz. The number of patch elements in this case is 35,788. By comparing Figs. 9 and 10, the 1-m reflectarray with the same f/D gives less bandwidth than the 0.5-m one. This implies that, with the same f/D ratio, the larger the reflectarray, the smaller the bandwidth it will provide. The bandwidth performances of Figs. 9 and 10 are summarized in Table 2.

Table 2. Bandwidth performance of the 32-GHz reflectarray.

f/D	0.5-m diameter, percent	1.0-m diameter, percent
\-1-dB gain-drop bandwidth		
0.5	4.8	2.6
1.0	8.5	4.5
\-3-dB gain-drop bandwidth		
0.5	8.4	4.3
1.0	14.0	7.5

The radiation patterns of the reflectarray will change as frequency changes. These differences are illustrated in Figs. 11 and 12 for two different f/D ratios. The pattern defocusing effect as frequency deviates from the center (design) frequency is clearly demonstrated in these figures.

From the above results, it can be concluded that, among the four bandwidth limiting factors, the element spacing and the feed antenna are not serious concerns in designing the reflectarray if the bandwidth requirement is 15 percent or less. It also can be concluded that a 3-percent bandwidth (1-GHz bandwidth at 32 GHz) for the reflectarray is fairly easy to achieve. An 8-percent bandwidth to cover both the uplink frequency (34 GHz) and the downlink frequency (32 GHz) may require an f/D ratio close to 1.0 and a specially designed patch element.

VI. Advantages of the Microstrip Reflectarray

The microstrip reflectarray antenna takes the best characteristics and eliminates the poor features of the parabolic reflector, the array, and the microstrip patch. This contributes to the microstrip reflectarray's six significant advantages, which are separately discussed below.

A. Surface Mountable With Lower Mass and Volume

Since the antenna's reflecting surface is a thin, flat structure, it can be flush mounted onto the surface of a structure, such as a spacecraft's main body or a building, with less supporting structure mass and volume as compared with the curved parabolic reflector. One possible application is shown in Fig. 13, where the reflectarray is surface mounted onto one side panel of a pentagonally shaped microspacecraft. Another application is given in Fig. 14, where the reflectarray is surface mounted onto a house wall for direct broadcast satellite (DBS) television service. In addition to the capability of surface mounting onto a flat structure, the reflectarray can also be mounted conformally onto a slightly curved structure (either concave or convex). The phase deviation of the curved structure can be compensated for in the design of the set of phase delay lines.

B. Easily Deployable

When a deployment mechanism is needed for a large aperture antenna, the flat structure of the reflectarray can be folded or unfolded by a simple hinge type of mechanism. A single or a double folding mechanism for a flat structure is significantly simpler (approximately an order of magnitude simpler) than that for a curved parabolic structure and is also more reliable.[1] The flat panel folding technique has been commonly used in the deployment of solar panels and has shown excellent reliability.

C. Lower Manufacturing Cost

The reflectarray, being in the form of a printed microstrip antenna, can be fabricated with a simple and low-cost etching process, especially when it is produced in large quantities. The antenna also can be cost effective just because of its flat structure. For example, the special molding process that is generally required for fabricating a curved paraboloid is not needed for a flat structure.

D. Scannable Beam

The main beam of the microstrip reflectarray can be designed to point at a large fixed angle (up to 60 deg) from the broadside direction, while a parabolic reflector can only have a very limited beam tilt (several beamwidths). If cost permits, phase shifters can be placed in the phase delay transmission lines for electronic beam scanning.

---

[1] Personal communication with R. Freeland, Mechanical Engineer, Applied Mechanics Technologies Section, Jet Propulsion Laboratory, Pasadena, California, 1994.
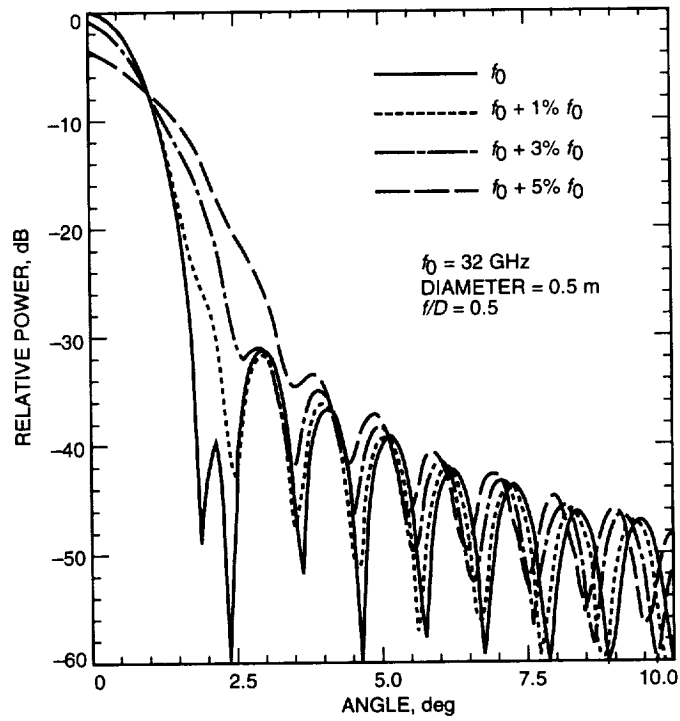
Fig. 11. Change of radiation patterns as frequency deviates from its center frequency for a reflectarray with an *f/D* ratio of 0.5.
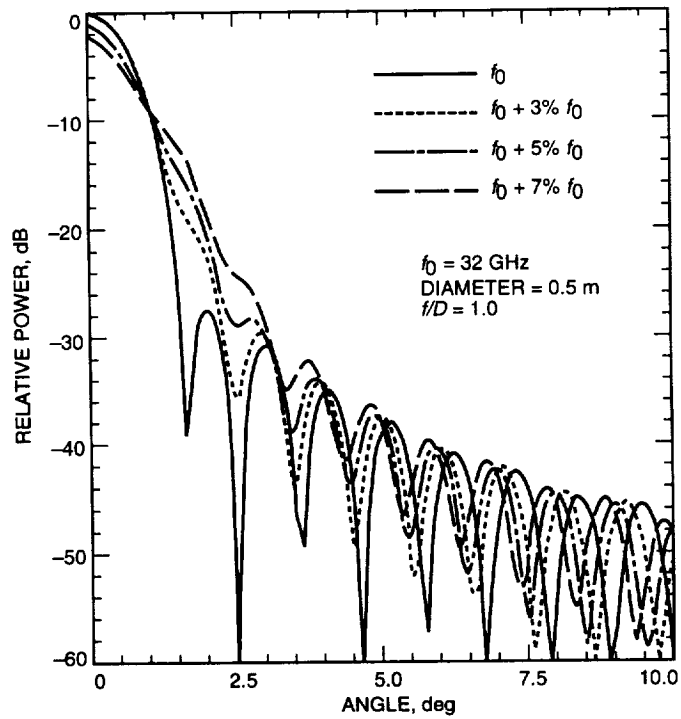
Fig. 12. Change of radiation patterns as frequency deviates from its center frequency for a reflectarray with an *f/D* ratio of 1.0.
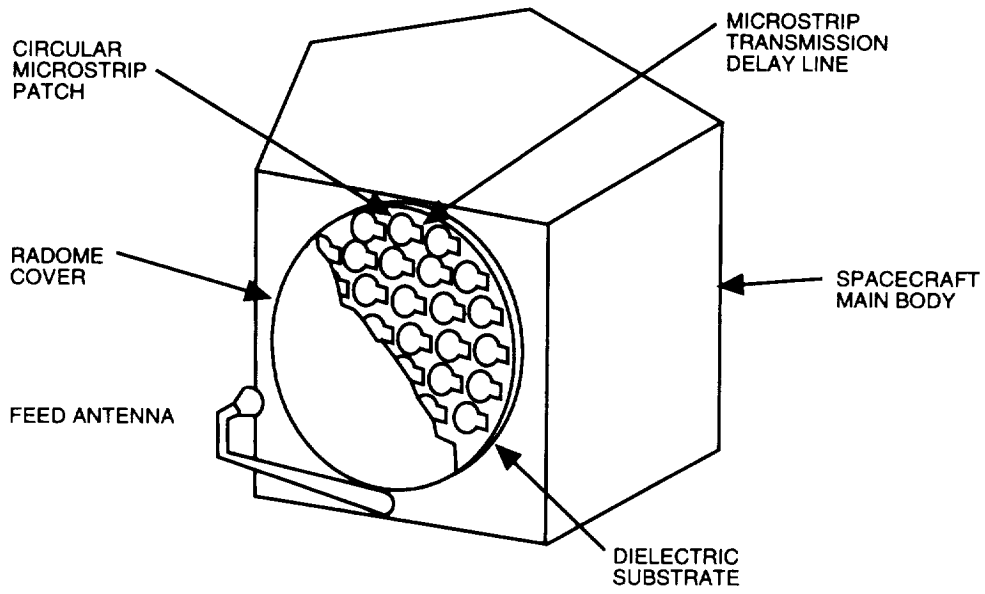
Fig. 13. Surface mounting of a microstrip reflectarray onto the side panel of a microspacecraft.
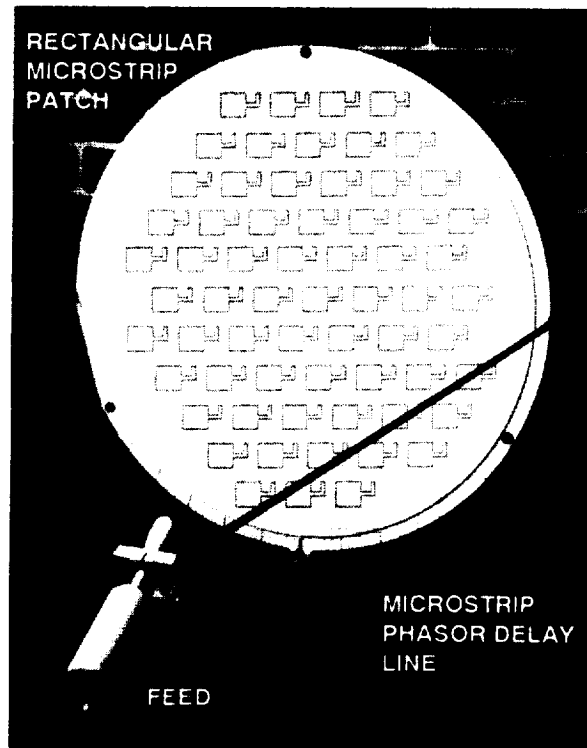
Fig. 14. Surface mounting of a microstrip reflectarray onto a house wall for a DBS application.

E. Integratable With a Solar Array

Since both the solar array and the reflectarray antenna are in the form of large, flat panels, they have the possibility of being integrated together to save space and mass. There are two possible configurations for the integration. One is for a lower-frequency application (below 5 GHz) where the patch radiator is large enough to place solar cells on top of it. This is shown in Fig. 15, where the RF energy radiates from the perimeter of the patch and is not affected by the solar cells. The other configuration, proposed by Malibu Research [8], is to use thin wire dipoles as reflectarray radiators. This is illustrated in Fig. 16, where the thin dipoles are suspended on thin wires and placed in front of the solar panel. A metallic wire-mesh ground plane is placed between the dipoles and the solar cells. This ground plane is needed for the dipoles to reradiate effectively. This concept should be feasible for frequencies below 15 GHz. For frequencies higher than 15 GHz, the dipoles and the mesh ground plane may become too dense for significant amounts of sunlight to penetrate, and the mechanical support structure for the dipoles (with mesh ground plane) may be difficult to implement. Even for frequencies lower than 15 GHz, because the dipoles are placed in front of a wire mesh and not a continuous perfect ground plane, the RF efficiency will be impaired. In addition, because the dipoles and the wire mesh ground plane will partially block the sunlight, the solar cell efficiency will also be reduced. The degrees of impairment of RF and solar cell efficiencies remain to be studied.

F. Very Large Aperture Array

Due to the fact that no power divider is needed, the insertion loss of thousands of microstrip patches in the reflectarray is the same as that of a few patch elements. Thus, the reflectarray can achieve as good an efficiency as a large array antenna system. As a possible application, a very large, flat reflectarray can be constructed on flat land (array aperture parallel to the land) with its feed mounted on top of a high tower. The size of the antenna is only limited by the tower height. A feed height of 300 m with an f/D ratio of 0.5 will result in an array with a diameter of 600 m. At 10 GHz, this antenna size can produce a pencil beam 0.0035 deg in beamwidth and 95 dBi of directivity. Such an antenna can be used in astrophysics applications.

VII. Proposed New Configurations of the Microstrip Reflectarray

To improve the performance of the microstrip reflectarray, three novel concepts are introduced here. They are separately presented below.

A. The Cassegrain Feed Reflectarray

As mentioned previously, in order to achieve a wider bandwidth, a large f/D ratio is generally needed for the reflectarray. A large f/D implies that the focal feed has to protrude far from the array aperture, which will result in larger volume and larger mass. The proposed Cassegrain configuration, shown in Fig. 17, will reduce the feed height while maintaining the same or a higher effective f/D ratio. In addition, the transmission line loss between the feed and the transceiver is significantly reduced, which is especially important at higher frequencies, such as Ka-band.

B. Bandwidth Enhancement by Subarray Arrangement Techniques

The second concept uses specially arranged subarrays in the entire array aperture to improve the bandwidth performance. Figure 18 shows that, for linear polarization, each two-patch subarray uses the antiphase method [13] and, for circular polarization, each four-patch subarray uses the sequential rotation method [14] to improve the bandwidth. For conventional microstrip arrays, these subarraying techniques have been successfully demonstrated to increase bandwidth from 3 percent to more than 8 percent. For a single patch, as frequency changes away from its resonant frequency, higher order modes start to form in the patch's cavity, and these will impair the input impedance match and polarization quality. By using the antiphase and sequential rotation methods, these high-order modes can be canceled, causing the desired fundamental mode to continue to dominate as the frequency changes.

SOLAR CELL

MICROSTRIP PATCH
RADIATOR
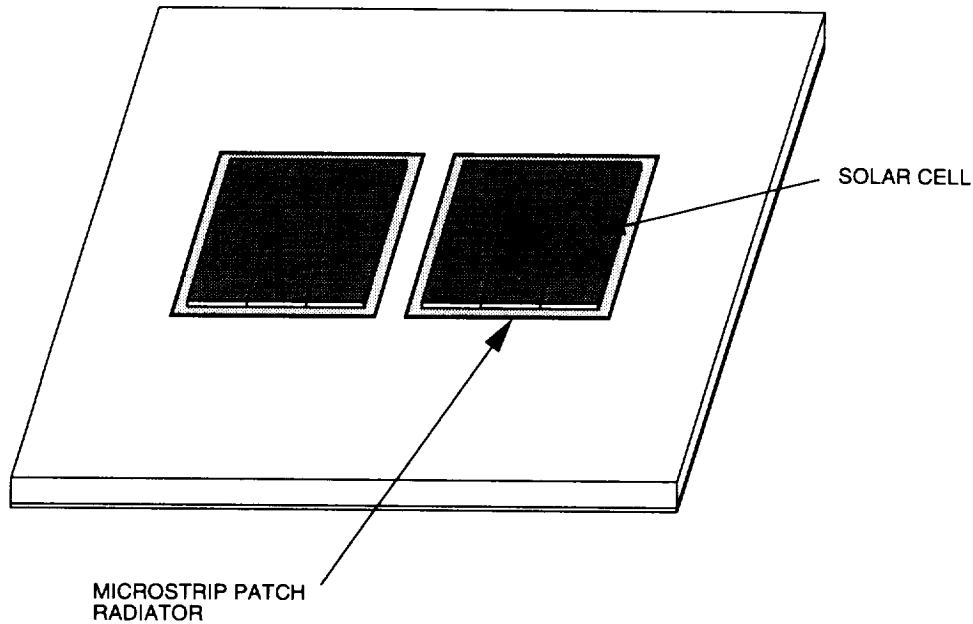
Fig. 15. Integration of solar cells and microstrip radiators for low-frequency
reflectarray applications.

MESH GROUND PLANE

SUSPENDED
CROSSED DIPOLE
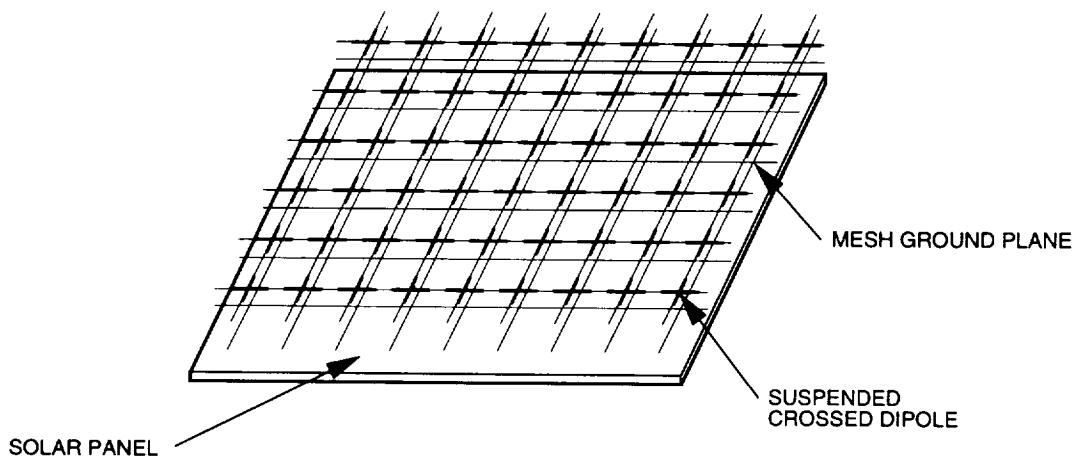
SOLAR PANEL

Fig. 16. Integration of a solar panel with a thin-wire reflectarray antenna.

C. Phase-Delay Compensation by Rotation of Identical Elements

In a circularly polarized microstrip reflectarray, the circular polarization can be achieved by having two equal-length delay lines orthogonally attached to each patch (see Fig. 3). The length of these delay lines varies from element to element to compensate for the different spatial phase delays of the feed antenna. In this newly proposed technique, the required different phase-delay compensations for each of the elements are achieved by different angular rotations of the elements, as shown in Fig. 19. All elements, except for rotations, are identical with identical delay lines. The delay lines, in this case, only serve as the angular references for rotations and not for phase-delay compensations. Especially for a circular patch, without some kind of angular reference, the rotations between different patches cannot be differentiated. The required amount of rotation in degrees is half of that required for the phase delay in degrees. This technique of rotating the circularly polarized element to achieve the required phase has been demonstrated [15] previously in a conventional array.

169
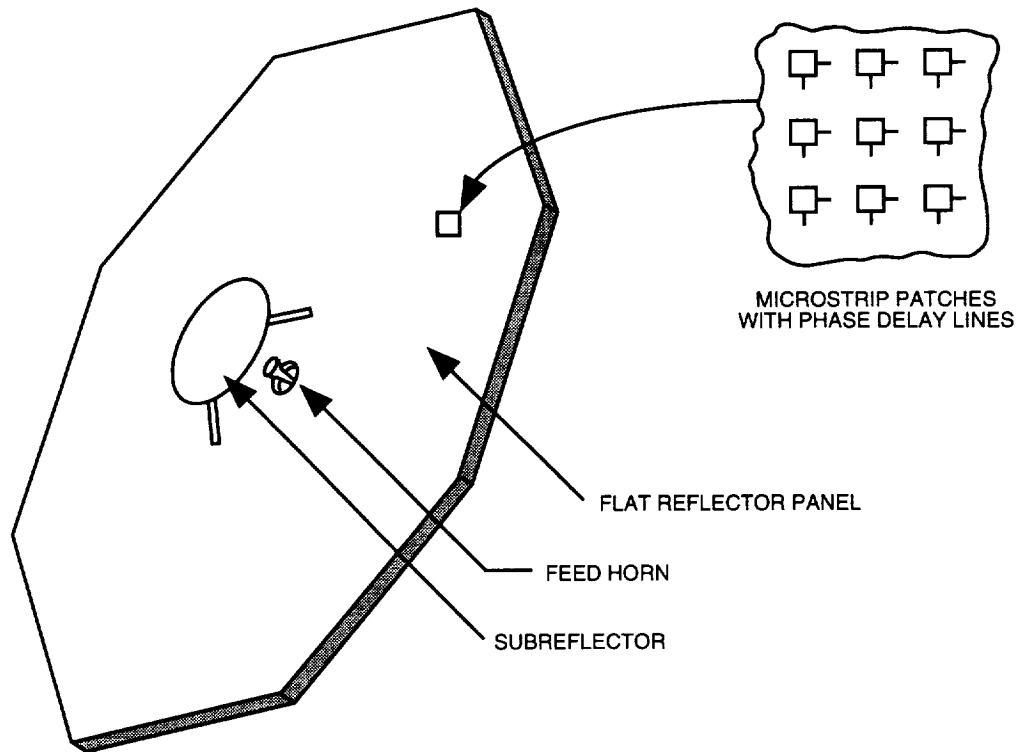
Fig. 17. Cassegrain reflectarray configuration.
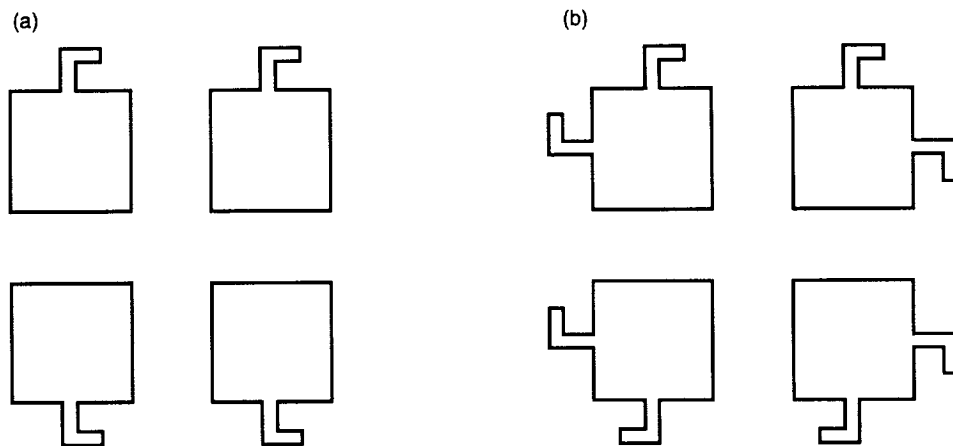
Fig. 18. Reflectarray bandwidth enhancement by subarray arrangement techniques: (a) linear polarization and (b) circular polarization.

By combining the "rotation" technique with miniature motors, the main beam of the microstrip reflectarray can be made to scan. In other words, as shown in Fig. 20, a miniature motor can be placed under each patch element to mechanically rotate the patch to achieve the required phase for beam scanning. Since all the elements in a reflectarray are isolated from each other with no need for a power divider, no rotary joint is required, which will reduce cost and enhance reliability. By using the miniature motors, high-cost phase shifters are not needed for beam scanning. Consequently, a very large, phased array antenna system with relatively low cost may be realizable.
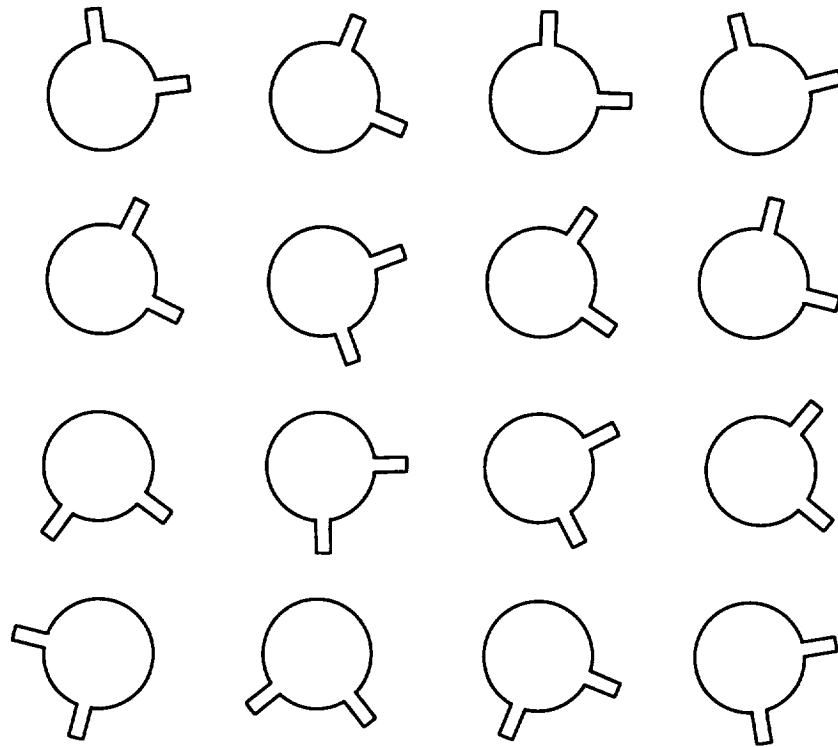
Fig. 19. Reflectarray phase-delay compensation by rotation of identical elements.
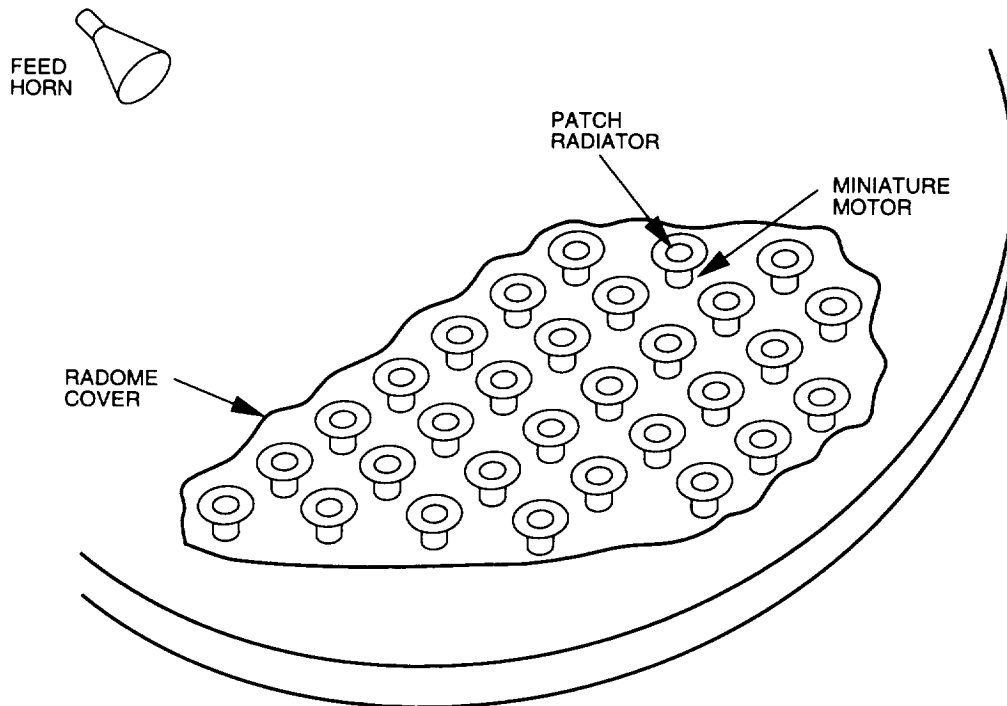
Fig. 20. Mechanically phased reflectarray—beam scan by mechanical rotation of elements.

VIII. Conclusion

The circularly polarized microstrip reflectarray has been analyzed using conventional array theory. Antenna performance parameters, such as radiation pattern quality, directivity, efficiency, bandwidth, etc., are calculated for a 0.5-m Ka-band reflectarray with 8,937 patch elements. It is found that an 8-percent bandwidth is achievable for this antenna and that bandwidth performance improves for a larger f/D ratio. An f/D ratio close to 1.0 is recommended for the 0.5-m Ka-band antenna. Overall antenna efficiency in the range of 50 to 70 percent is possible. Numerous advantages of this flat-plate reflector antenna have been discussed. Three novel configurations of the microstrip reflectarray are proposed for future studies.

References

[1] J. Huang, *Microstrip Reflectarray Antenna for the SCANSCAT Radar Application*, JPL Publication 90-45, Jet Propulsion Laboratory, Pasadena, California, November 15, 1990.

[2] J. Huang, "Microstrip Reflectarray," *IEEE AP-S/URSI Symposium*, London, Ontario, Canada, pp. 612–615, June 1991.

[3] R. C. Hansen, *Microwave Scanning Antennas*, vol. 1, New York: Academic Press, pp. 251–252, 1964.

[4] R. E. Munson and H. Haddad, *Microstrip Reflectarray for Satellite Communication and RCS Enhancement or Reduction*, U.S. Patent 4,684,952, Washington, D.C., August 1987.

[5] T. A. Metzler, *Design and Analysis of a Microstrip Reflectarray*, Ph.D. Dissertation, University of Massachusetts, Amherst, February 1993.

[6] Y. Zhuang, K. L. Wu, C. Wu, and J. Litva, "Microstrip Reflectarrays: Full-Wave Analysis and Design Scheme," *IEEE AP-S/URSI Symposium*, Ann Arbor, Michigan, pp. 1386–1389, June 1993.

[7] D. C. Chang and M. C. Huang, "Microstrip Reflectarray Antenna With Offset Feed," *Electronics Letters*, pp. 1489–1491, July 1992.

[8] A. Kelkar, "FLAPS: Conformal Phased Reflecting Surfaces," *Proceedings of the IEEE National Radar Conference*, pp. 58–62, March 12–13, 1991.

[9] S. D. Targonski and D. M. Pozar, "Analysis and Design of a Microstrip Reflectarray Using Patches of Variable Size," *IEEE AP-S/URSI Symposium*, Seattle, Washington, pp. 1820–1823, June 1994.

[10] R. J. Mailloux, J. F. McIlvenna, and N. P. Kernweis, "Microstrip Array Technology," *IEEE Transactions on Antennas and Propagation*, pp. 25–37, January 1981.

[11] A. W. Rudge, K. Milne, A. D. Olver, and P. Knight, *The Handbook of Antenna Design*, vol. 1, London, England: Peter Peregrinus Ltd., pp. 169–172, 1982.

[12] S. Silver, *Microwave Antenna Theory and Design*, New York: McGraw-Hill, Inc., pp. 177–179, 1949.

[13] J. Huang, "Dual-Polarized Microstrip Array With High Isolation and Low Cross-Polarization," *Microwave Optics Technology Letters*, pp. 99–103, February 1991.

[14] T. Teshirogi, M. Tanaka, and W. Chujo, "Wideband Circularly Polarized Array Antenna With Sequential Rotations and Phase Shift of Elements," *Proceedings of ISAP*, Japan, pp. 117–120, 1985.

[15] M. L. Oberhart and Y. T. Lo, "Simple Method of Experimentally Investigating Scanning Microstrip Antenna Arrays Without Phase-Shifting Devices," *Electronics Letters*, vol. 25, no. 16, pp. 1042–1043, August 1989.

1995115125

N95- 21542

February 15, 1995

The Efficiency Calibration of the DSS-24 34-Meter Diameter Beam-Waveguide Antenna

L. S. Alvarez, M. J. Britcliffe, M. M. Franco, S. R Stewart, and H. J. Jackson

Ground Antennas and Facilities Engineering Section

Microwave performance testing of the new Deep Space Station (DSS)-24 34-m-diameter antenna was carried out during the summer of 1994. Efficiency measurements were made at the 8.45-GHz (X-band) and 32-GHz (Ka-band) frequencies both at the antenna Cassegrain (f1) and beam-waveguide (f3) focal points. In addition, the antenna f3 efficiencies were measured on the DSS-24 operational 2.295-GHz (S-band) and 8.45-GHz feeds. This article presents the efficiency determinations as a function of elevation angle along with a corresponding error analysis of the measurements. Peak measured gains and efficiencies are tabulated for all frequencies.

I. Introduction

During an 8-week period in the summer of 1994, extensive microwave performance measurements were carried out on the new Deep Space Station (DSS)-24 34-m beam-waveguide (BWG) antenna at Goldstone, California. The testing period consisted of antenna efficiency and pointing calibration and system noise temperature measurements at the frequencies of 2.295 GHz (S-band), 8.45 GHz (X-band), and 32 GHz (Ka-band).[1] In addition, microwave holography and subsequent main antenna reflector-panel adjustments were carried out at the Cassegrain (f1) focus before the start of the efficiency calibration period. The X- and Ka-band efficiency measurements involved the use of portable microwave test packages installed at the f1 focal point and the subterranean f3 beam-waveguide focal point. The test packages were previously developed for testing of the DSS-13 research and development (R&D) antenna.[2] In addition to the measurements on the R&D feeds, the performances of the DSS-24 operational S- and X-band feeds were also characterized at the f3 focal point.

This article presents the efficiency calibration and analysis portion of the microwave DSS-24 testing. The methodology used to determine the antenna aperture efficiency from noise temperature measurements on radio source calibrators is reviewed and error analysis equations are presented. The following sections then present the results of the efficiency determination at the f1 and f3 focal points, with discussion of

[1] The testing period is described in detail in *DSS-24 Microwave Performance Characterization*, Document 829-6 (internal document), Jet Propulsion Laboratory, Pasadena, California, May 15, 1994.

[2] M. J. Britcliffe, L. S. Alvarez, D. A. Bathker, P. W. Cramer, T. Y. Otoshi, D. J. Rochblatt, B. L. Seidel, S. D. Slobin, S. R. Stewart, W. Veruttipong, and G. E. Wood, *DSS 13 Beam-Waveguide Antenna Project: Phase 1 Final Report*, JPL D-8451 (internal document), Jet Propulsion Laboratory, Pasadena, California, May 15, 1991.

N95- 21543

1995115126

15 P

Analysis of a Disk-on-Rod Surface Wave Element Inside a Corrugated Horn Using the Mode-Matching Technique

J. C. Chen
Ground Antennas and Facilities Engineering Section

A disk-on-rod inside a corrugated horn is one of the horn configurations for dual-frequency or wide-band operation. A mode-matching analysis method is described. A disk-on-rod inside a corrugated horn is represented as a series of coaxial waveguide sections and circular waveguide sections connected to each other. Three kinds of junctions need to be considered: coaxial-to-coaxial, coaxial-to-circular, and circular-to-circular. A computer program was developed to calculate the scattering matrix and the radiation pattern of a disk-on-rod inside a corrugated horn. The software was verified by experiment, and good agreement between calculation and measurement was obtained. The disk-on-rod inside a corrugated horn design gives an option to the Deep Space Network dual-frequency operation system, which currently is a two-horn/one-dichroic plate system.

I. Introduction

To design a dual-frequency horn for the DSS-13 beam waveguide antenna, an analysis tool needs to be developed. A side-view model of a circularly symmetric disk-on-rod inside a corrugated horn is shown in Fig. 1. The horn is subdivided to several sections that are either coaxial or circular waveguide sections. The junctions between these sections are either coaxial-to-coaxial, coaxial-to-circular, or circular-to-circular waveguide junctions. In order to analyze the performance of a disk-on-rod inside a corrugated horn, a computer program based on the mode-matching method was developed [1,2]. The circular waveguide program and coaxial waveguide program that calculate the scattering matrix of the circular waveguide and coaxial waveguide of different sizes, respectively, are already available [3]. In order to simulate the disk-on-rod inside a corrugated horn, it was necessary to integrate the existing circular waveguide program and coaxial program with a new third program that handles the junction between circular and coaxial waveguides.

II. Theory

The analysis of the waveguide junctions is based on the mode-matching method. The following theory is used to calculate the scattering matrix of coaxial-to-circular waveguide junctions (Fig. 2). The electromagnetic field is represented by coaxial waveguide modes in the coaxial waveguide region and circular waveguide modes in the circular waveguide region. Only waveguide modes of order 1 are considered in

Acknowledgments

References

[1] S. D. Slobin, T. Y. Otoshi, M. J. Britcliffe, L. S. Alvarez, S. R. Stewart, and M. M. Franco, "Efficiency Calibration of the DSS 13 34-Meter Beam-Waveguide Antenna at 8.45 and 32 GHz," *The Telecommunications and Data Acquisition Progress Report 42-106, April–June 1991*, Jet Propulsion Laboratory, Pasadena, California, pp. 283–297, August 15, 1991.

[2] L. S. Alvarez, "Analysis and Applications of a General Boresight Algorithm for the DSS-13 Beam-Waveguide Antenna," *The Telecommunications and Data Acquisition Progress Report 42-111, July–September 1992*, Jet Propulsion Laboratory, Pasadena, California, pp. 48–61, November 15, 1992.

[3] S. R. Stewart, "DSS-13 Beam-Waveguide Antenna Performance in the Bypass Mode," *The Telecommunications and Data Acquisition Progress Report 42-108, October–December 1991*, Jet Propulsion Laboratory, Pasadena, California, pp. 135–153, February 15, 1992.

[4] P. H. Richter and S. D. Slobin, "DSN 70-Meter Antenna X- and S-Band Calibration, Part I: Gain Measurements," *The Telecommunications and Data Acquisition Progress Report 42-97, January–March 1989*, Jet Propulsion Laboratory, Pasadena, California, pp. 314–351, May 15, 1989.

pedestal room position.[9] The predicted antenna efficiency variation between the azimuth range of 60 to 295 deg, computed for a perfectly aligned beam-waveguide mirror system, was 2 percent. As measured at DSS 24 and shown in Fig. 11, the variation is 4 percent over the same angle range.

X. Summary of Results

The aperture efficiency of the DSS-24 34-m beam-waveguide antenna has been calibrated at the S- (2.295-GHz), X- (8.45-GHz) and Ka-band (32-GHz) frequency bands. Table 2 presents a summary of the peak gains and efficiencies measured during the rf performance evaluation period. The uncertainties on the peak values are also given and are based on a propagation of measurement errors and radio-source flux and size correction errors. Table 3 gives the best-fit second-order polynomial coefficients for the X- and Ka-band efficiencies measured on the R&D feed packages. The first four peak gain and efficiency estimates in Table 2 were computed from these coefficients. The S- and X-band peak values measured on the operational feeds were derived by averaging the measurements in a small angular range about the observed peak efficiency angles. The Ka-band gravity loss as a function of elevation angle was computed from the best-fit DSS-24 f3 efficiency curve and is shown in Fig. 9. The final y- and z-axis subreflector (total) offset curves experimentally determined at the f3 focus are presented in Fig. 2 and have been left in the DSS-24 antenna-pointing controller for future tracking operations.

Table 2. Summary of DSS-24 antenna peak gains and efficiencies at the S-, X-, and Ka-band frequencies.

Frequency, GHz, and focal point	Gain, dBi	1-sigma gain error, dB	Efficiency, percent	1-sigma efficiency error, percent
8.45 at f1	68.33	0.12	75.25	2.04
8.45 at f3	68.19	0.11	72.67	1.81
32 at f1	78.97	0.16	60.60	2.18
32 at f3	78.70	0.20	57.02	2.51
8.45 operational feed at f3	68.09	0.14	71.10	2.30
2.295 operational feed at f3[a]	56.79	0.11	71.50	1.82

[a] Measured at azimuth angle = 180 deg.

Table 3. Best-fit second-order polynomial coefficients for S- and Ka-band efficiencies, without atmosphere, measured on the R&D feed packages.

Efficiency	Efficiency model $= c_0 + c_1 el + c_2 el^2$ where el = elevation angle, deg		
	c_o	c_1	c_2
X-band at f1	0.748067	0.000211491	-0.00000250421
X-band at f3	0.714972	0.000457441	-0.00000444267
Ka-band at f1	0.442223	0.00737073	-0.0000827938
Ka-band at f3	0.466983	0.00504885	-0.0000618488

[9] W. Veruttipong, "S-Band Efficiency and G/T Performance Performance for Various Azimuth Positions," JPL Interoffice Memorandum 3327-94-113 (internal document), Jet Propulsion Laboratory, Pasadena, California, June 9, 1994.
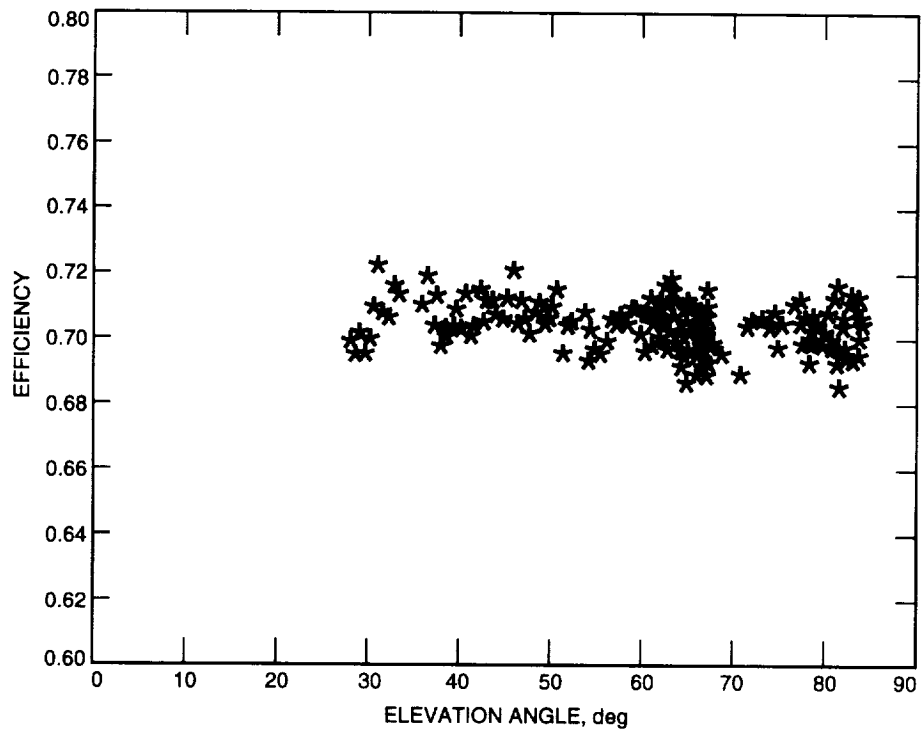
Fig. 10. DSS-24 8.45-GHz efficiency measurements on the operation feed at
the f3 focal point, without atmosphere.
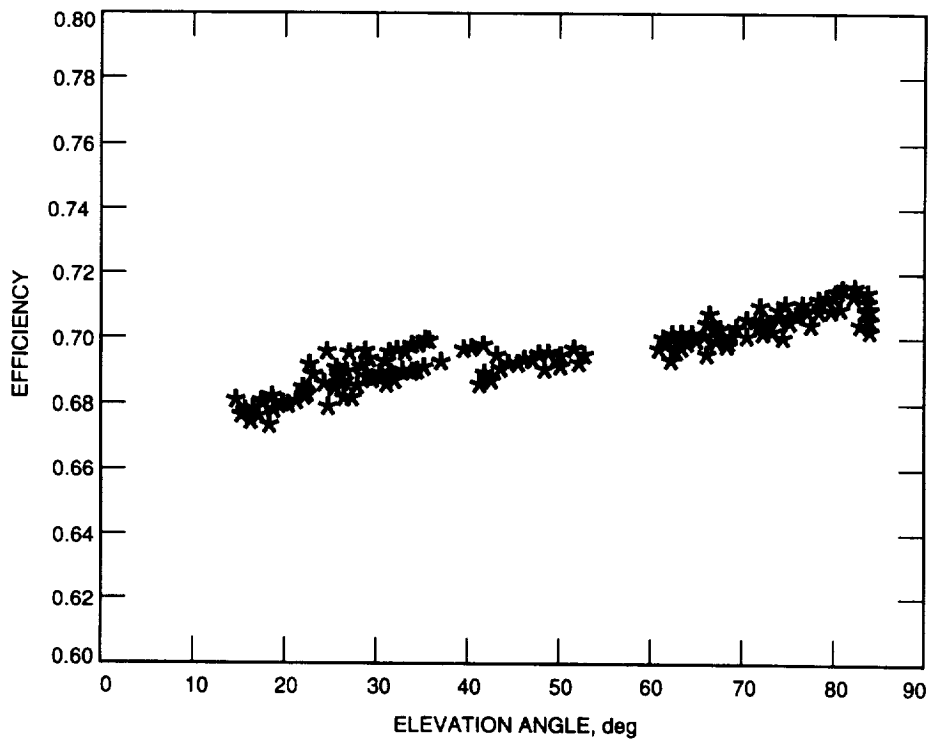
Fig. 11. DSS-24 2.295-GHz efficiency measurements on the operational feed at
the f3 focal point, without atmosphere.
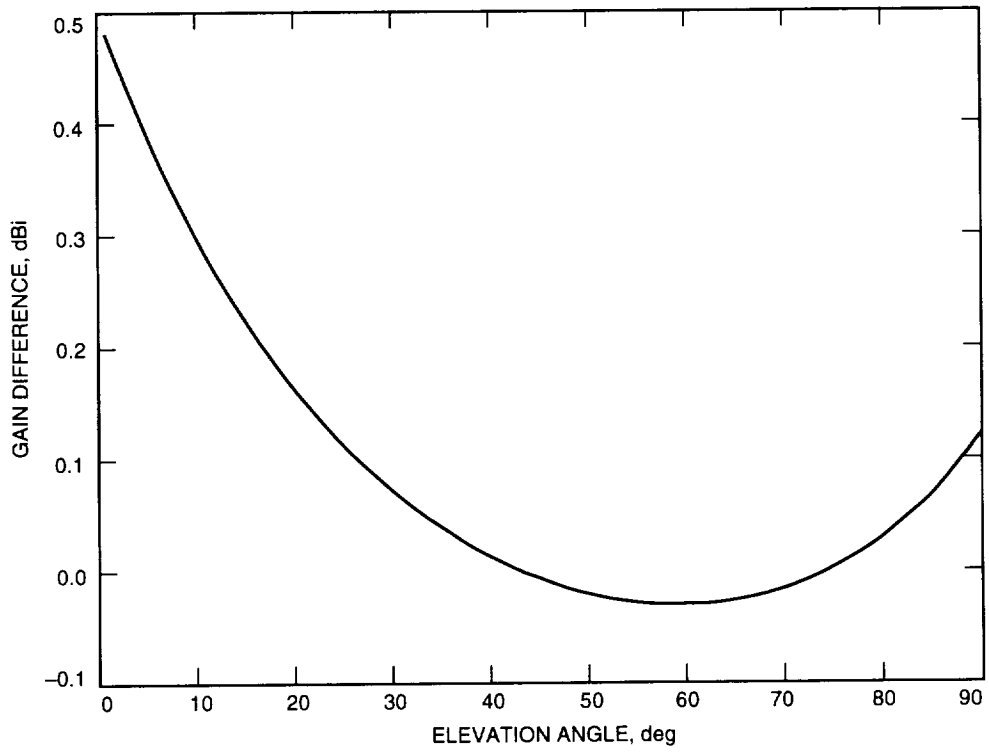
Fig. 8. The difference of normalized f3 and f1 gain curves.
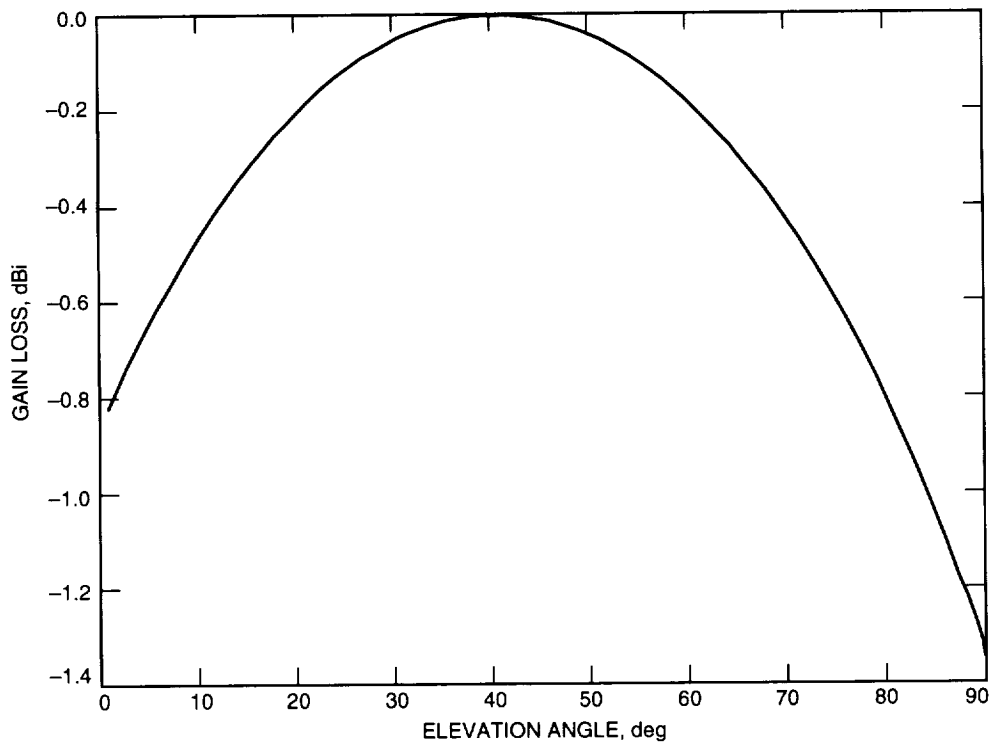
Fig. 9. DSS-24 32-GHz gravity loss for the f3 focal point.

The measurement errors, in general, are larger at f3 due to the decreased antenna gain and the apparent increase in the radio-source temperature measurement noise. The increased spread in the data in Figs. 6 and 7 is due to an azimuth dependence of the efficiency caused by a small beam-waveguide mirror misalignment. For the R&D feed location in the DSS-24 pedestal room (azimuth position = 180 deg), the efficiency is slightly higher for sources with declinations greater than 35 deg rising and setting in the north. The curve fit in Fig. 6 is computed from the combined data sets of 3C274 and 3C84. The efficiency measurements on the northern-passing 3C84 (with peak elevation of 79 deg) almost all lie above the best-fit curve, while those of the southern-passing 3C274 (with peak elevation of 67 deg) are equal to or lie below it.

A. Ka-Band Gravity Loss Analysis

The gravity-induced roll-off of the f3 efficiency curve shown in Fig. 6 is flatter than that measured at f1 (shown in Fig. 4). This is expected since the final subreflector offset curves determined at f3 with the automated subreflector optimization scheme provided better focusing than those used at f1. To quantify the performance increase, Fig. 8 presents the difference of the computed f3 and f1 Ka-band gain curves after the f3 curve has been raised by 0.27 dBi to account for the difference in the measured peak gains. As seen, the low-elevation antenna gravity performance at f3 is superior to that at f1 (e.g., 0.3 dBi greater at a 10-deg elevation). Thus, only the f3 efficiency curve should be used to predict the efficiency degradation as a function of elevation angle. The f3 gravity loss profile, computed from the best-fit efficiency curve, is shown in Fig. 9. It is assumed that there is zero loss at the peak gain elevation angle of 42 deg. Note that the asymmetry of the gravity loss curve is more probably due to an artifact of the differing profiles of the individual radio-source efficiency measurements, as discussed above, than to errors in the experimentally determined high-elevation angle subreflector focusing curves.

VIII. Efficiency Measurements: X-Band Operational Feed

Efficiency measurements at f3 were made on the X-band operational feed with the S-/X-band dichroic plate installed for the 3 days of 207–209. During this period, the computed zenith attenuation varied from 0.034 to 0.038 dB. The adjusted efficiency data points are shown in Fig. 10.

On the X-band operational feed, the noise temperature measurements were taken at the input of the downconverter. However, as seen in Fig. 10, gain instability was a problem during the measurements. It was determined that the X-band maser was stable to ± 0.1 dB, corresponding to a 0.2-K noise temperature measurement stability on the principal calibrator, 3C274. Thus, at any elevation angle, the measurement noise on the efficiency measurements was 1.5 to 2 percent alone, rendering a quadratic curve fit impractical. The peak efficiency was estimated by averaging the data points between 42 and 48 deg. The peak efficiency on the X-band operational feed was computed to be 71.10 percent with an estimated uncertainty of 2.30 percent. This corresponds to a peak X-band gain for the operational feed of 68.09 dBi ± 0.14 dBi.

IX. Efficiency Measurements: S-Band Operational Feed

S-band efficiency measurements were made on the operational feed on DOY 186–188. The radio sources tracked were 3C274 and 3C123, both southern-passing targets. Figure 11 shows the measurements, corrected for atmospheric absorption with an average zenith attenuation value of 0.03 dB, as a function of elevation angle. The azimuth angles for the data points range from 60 to 295 deg, with southern (180-deg azimuth) transit elevation angles of 67.5 deg for 3C274 and 83 deg for 3C123. The peak S-band efficiency was computed to be 71.50 percent, measured for both sources at the 180-deg azimuth angle. The uncertainty on the peak value is 1.82 percent, which corresponds to a peak S-band gain of 56.79 dBi ± 0.11 dB.

The variation of antenna efficiency as a function of azimuth angle shown in Fig. 11, with the peak operational gain at the 180-deg azimuth, was predicted by rf analysis for the S-band feed in the 270-deg
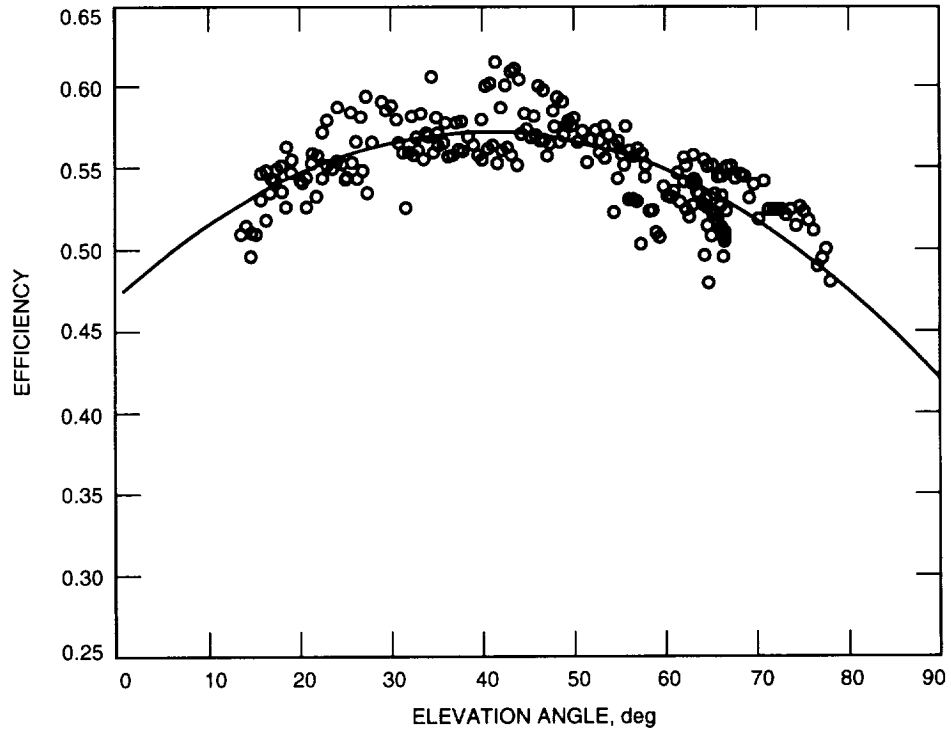
Fig. 6. DSS-24 32-GHz efficiency at the f3 focal point, without atmosphere.
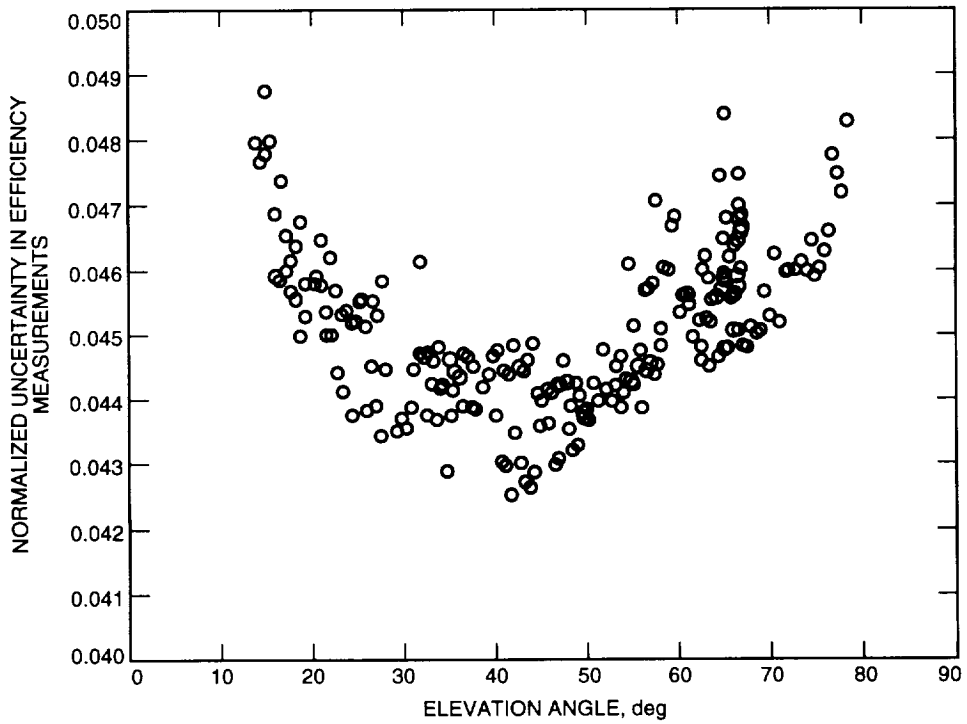
Fig. 7. DSS-24 32-GHz normalized efficiency uncertainty ($\sigma_\eta(el)/\eta(el)$) at the f3 focal point, without atmosphere.
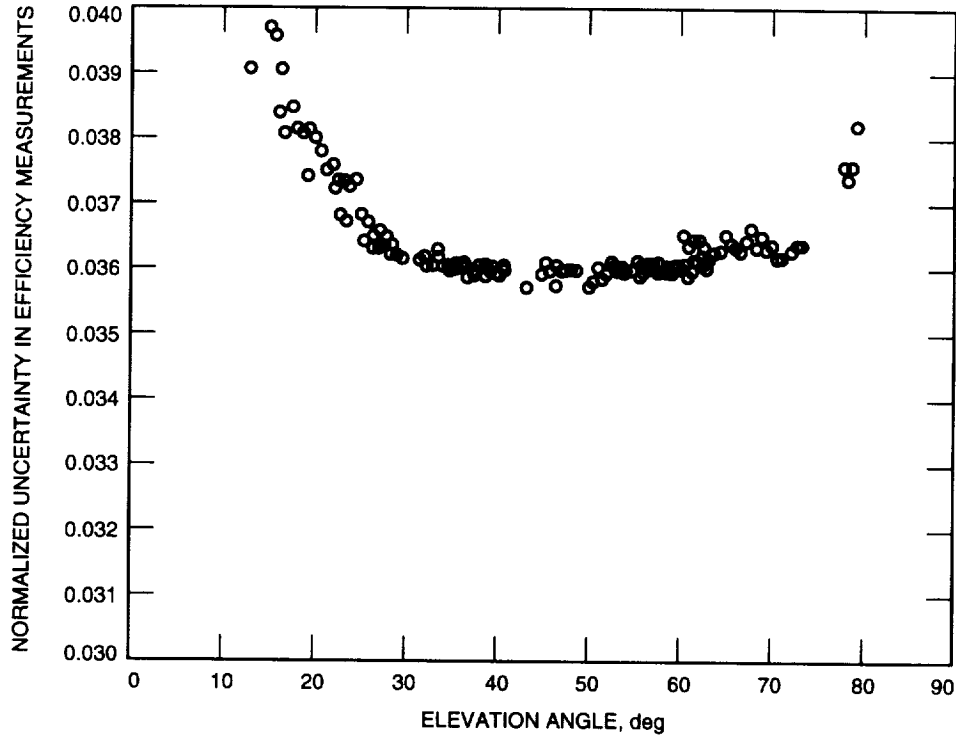
Fig. 5. DSS-24 32-GHz normalized efficiency uncertainty ($\sigma_\eta(el)/\eta(el)$) at the f1 focal point, without atmosphere.

temperature is maximum (i.e., the largest signal-to-noise ratio condition). The uncertainty ratio increases when the elevation angle deviates from the rigging angle since the efficiency decreases due to gravity, and the largest magnitude is at the lower elevations due to the increased atmospheric attenuation variance $\sigma_{L(el)}^2$. The one–standard deviation uncertainty σ_η on the peak efficiency of 60.60 percent at 44.5 deg is 2.18 percent (i.e., 60.6 × 0.036). The peak Ka-band efficiency and uncertainty at f1 correspond to a peak gain of 78.97 dBi ± 0.16 dB.

VII. Efficiency Measurements: Ka-Band at f3

The Ka-band R&D microwave test package was moved to the f3 focal point after the X-band f3 calibrations. The initial tracks focused on refining the subreflector offset curve determined at f1. The optimization procedure used at f1 was automated in the automatic boresighting computer. Two days of star tracking yielded the final total subreflector-commanded position curves (labeled f3) shown in Fig. 2. The best-fit coefficients to the offset curves were input to an APC model file so that the offsets could be automatically applied during tracking operations. This is analogous to the pointing calibration and model determination. The final 2 days of tracking (DOY 174–175) provided the most stable and repeatable measurements for calibration. The zenith attenuation values for these 2 days, computed from SPC-10 weather recordings, varied from 0.10 to 0.12 dB, indicating a drier period than during the Ka-band measurements at f1. The best-fit efficiency curve and the adjusted data points for Ka-band at f3 are shown in Fig. 6.

The Ka-band peak efficiency at f3 was calculated to be 57.02 percent at an elevation angle of 42.0 deg. This is a decrease of 3.6 percent from the peak Ka-band f1 efficiency. The uncertainty ratio, $\sigma_{\eta(el)}/\eta(el)$, for the efficiency measurements is shown in Fig. 7. The uncertainty, σ_η, on the peak efficiency of 57.02 percent at 42.0 deg is 2.51 percent. This corresponds to a peak gain of 78.70 dBi ± 0.20 dB.
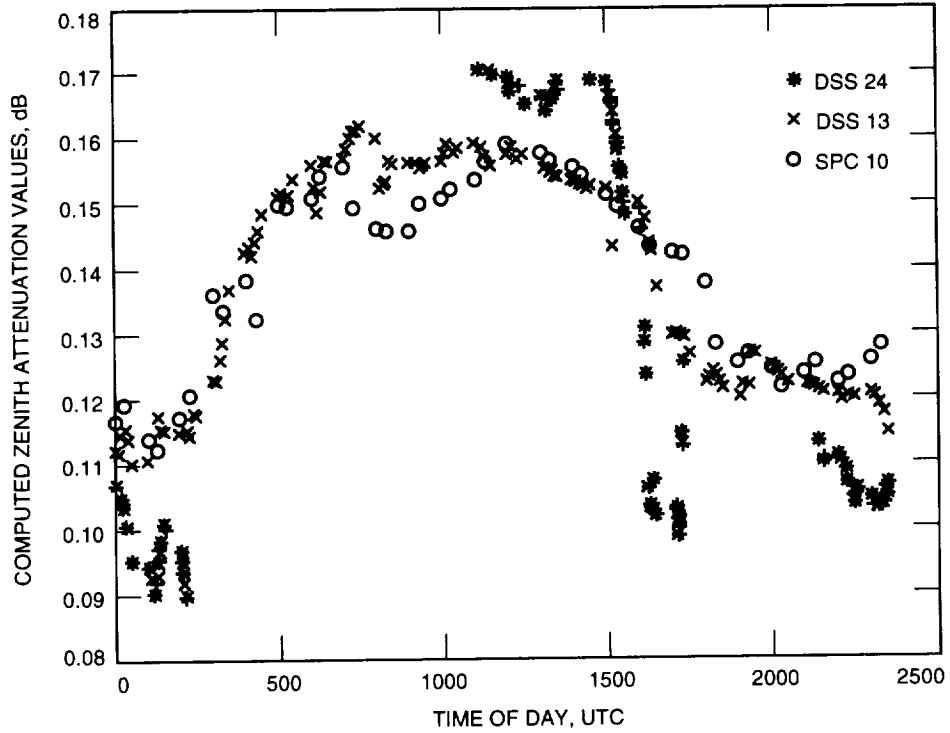
Fig. 3. Computed 32-GHz zenith attenuation values for DOY 158.
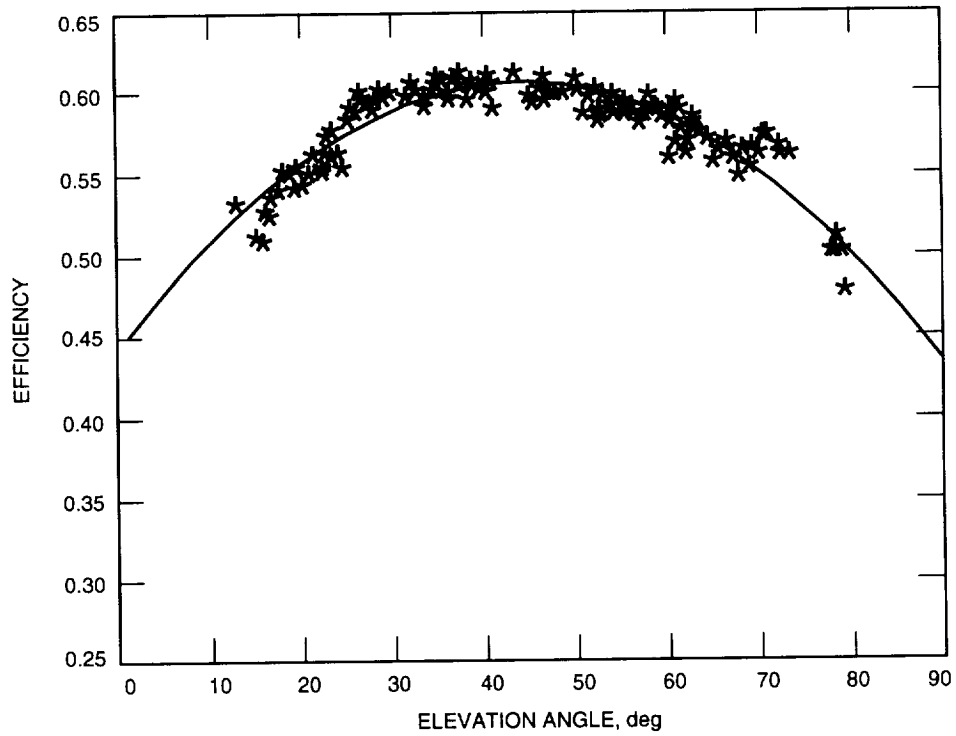
Fig. 4. DSS-24 32-GHz efficiency at the f1 focal point, without atmosphere.

at most in an $\approx$ 0.08-dB pointing loss for a 0.017-deg Ka-band full-width half-power beamwidth). A 0.001-deg upper bound on the tracking error in each axis was a practical calibration goal given that the pointing-error measurement accuracy was not expected to be much better than 0.001 deg due to the low signal-to-noise operating conditions during radio source tracking. In addition to beam-pointing calibration, approximately 3 days were also devoted to obtaining the best subreflector offset positioning during the efficiency measurements. The optimization procedure, based on manually entering subreflector offsets into the APC in between boresights and postprocessing the output data together with the structural predict models, yielded the total f1 offset curves shown in Fig. 2. These new focusing curves were then used for the remainder of the f1 testing. The final 2 days of tracking (DOY 158 and 159) resulted in sufficient data points on 3C274 and 3C84 for the efficiency calibration curve.
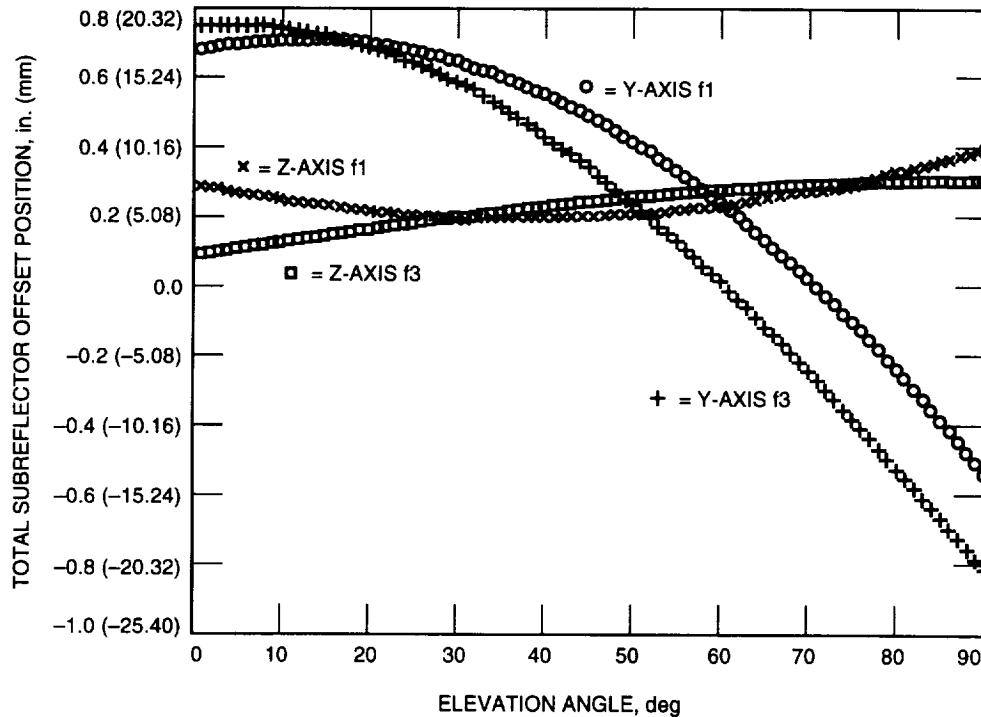
Fig. 2. Subreflector position offset curves used during Ka-band measurements at f1 and f3.

The effects of the atmospheric attenuation become more significant with increasing frequency band. For this reason, the logged weather readings were closely reviewed. Figure 3 shows the computed 32-GHz zenith attenuation values for DOY 158, based on weather data logged at DSS 24 (sensors mounted on the X-band test package on the ground), and from readings logged daily at DSS 13 and SPC 10. In Fig. 3, the SPC-10 and DSS-13 values for A_{zen} show good agreement, but the data points for DSS 24 appear inconsistent, indicating a problem with the local sensors. Note that the readings at DSS 24 were logged only during the tracking periods. Since DSS 24 is closer in location to SPC 10 than to DSS 13, the SPC-10 weather data were used to remove the effects from the efficiency measurements. As seen in Fig. 3, the values for A_{zen} varied from 0.11 to 0.16 dB during the course of the star tracks. The best-fit efficiency curve and the adjusted data points for Ka-band at f1 are shown in Fig. 4.

The Ka-band peak efficiency at f1 was calculated to be 60.60 percent at an elevation angle of 44.5 deg. From Eq. (8), the uncertainty estimate for the efficiency measurements was computed for all elevation angles. A plot of the uncertainty ratio $\sigma_{\eta(el)}/\eta(el)$ on the efficiency data is shown in Fig. 5. As expected, the error in measuring the efficiency is minimum at 45-deg elevation, where the measured source noise
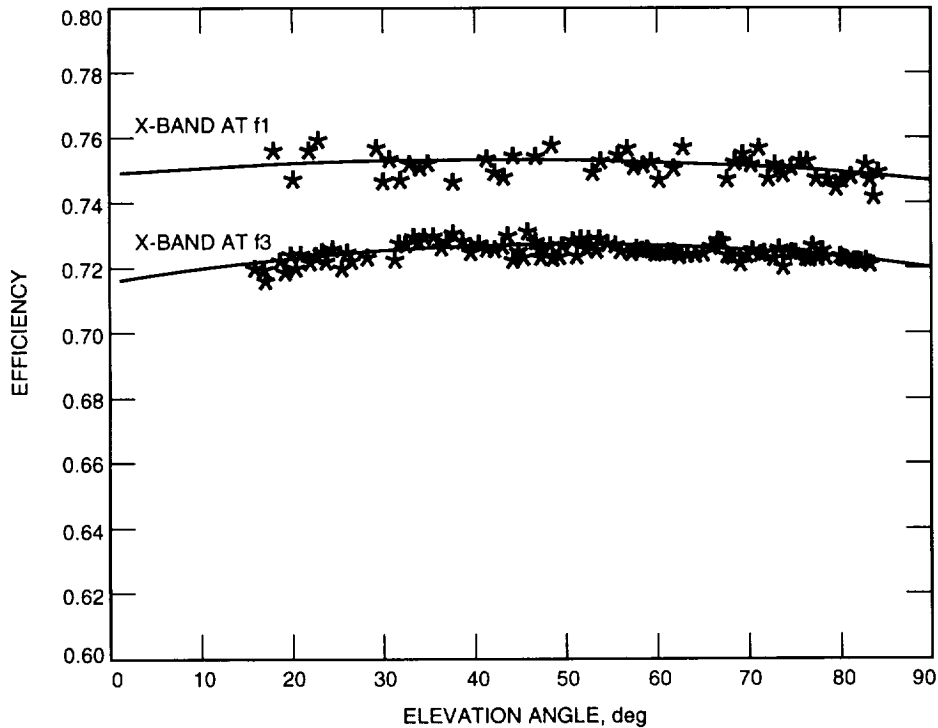
Fig. 1. DSS-24 8.45-GHz efficiency at the f1 and f3 focal points, without atmosphere.

V. Efficiency Measurements: X-Band at f3

X-band efficiency measurements at the f3 focal point were taken over 5 days (DOY 174–178) using the R&D microwave test package. Following the general data-taking strategy, the sources 3C274 and 3C84 were tracked until efficiency curves could be computed on each source. The peak efficiency on the variable source 3C84 was then normalized to the peak 3C274 value. All of the measurements were compensated for atmospheric absorption on a point-by-point basis. For the final 2 days of tracking, the computed zenith attenuation values ranged only from 0.0334 to 0.035 dB. The best-fit efficiency curve based on these final days and the adjusted measurements is shown in Fig. 1.

The peak X-band efficiency at f3 was calculated to be 72.67 percent at an elevation angle of 49 deg. From Eq. (8), the computed uncertainty on the peak efficiency is 1.81 percent. The peak X-band efficiency and uncertainty at f3 correspond to a peak gain of 68.19 dBi ± 0.11 dB. As seen in Fig. 1, the efficiency data points taken on the two radio sources are numerous and repeatable over the elevation range. The uncertainty estimate of 1.81 percent is assumed constant with elevation angle since the last two error contributors (measurement noise and attenuation errors) in Eq. (8) contribute less than 10 percent to the total. As will be discussed below, radiometry techniques were applied to derive a total subreflector offset curve for use at Ka-band at f3 that differed from that used during the above X-band tracks and the Ka-band f1 tracks. However, the effects on the presented X-band efficiency results are negligible.

VI. Efficiency Measurements: Ka-Band at f1

The Ka-band R&D microwave test package was used for efficiency calibration at both the DSS-24 f1 and f3 focal points. At f1, just over a week was devoted to star tracks at Ka-band. The tracks from the first days, combined with the previous X-band boresight data, yielded the first pointing model for the antenna. This was requisite in order to keep the scan-to-scan error in each axis under 0.001 deg (resulting

178

C1-3

III. Radio Source Calibration Values

At all of the frequency bands, S-, X- and Ka-bands, the radio source 3C274 (Virgo A) is used as the principal calibrator. Due to a constrained time schedule during the radio frequency (rf) performance evaluation period, the main measurement strategy consisted of first obtaining a full track of 3C274 (rise to set) to establish the peak efficiency near the rigging angle (40–50 deg). Since 3C274 is only near a 12-deg declination, higher declination sources (3C84 and 3C123) are then tracked to establish the upper efficiency curve. For the X- and Ka-bands, the efficiency curves generated for these latter sources are normalized to the measured 3C274 peak value.

Table 1 summarizes the flux, source size correction values, calibration temperatures $T_a = T_{100}/C_r$, and the estimated uncertainties for the radio sources 3C274 and 3C123 (the latter is used for calibration at S-band only). These values are taken directly from Richter[8] and are calculated for a DSN 34-m antenna with half-power beamwidths of 0.240 deg for S-band, 0.063 deg for X-band, and 0.017 deg for Ka-band. The uncertainties are used in the error analysis of the efficiency calculations.

Table 1. Radio sources used for DSS-24 efficiency calibration.

Source and frequency, GHz	Flux density, Janskys	C_r	T_a, K	T_a 1-sigma, K
3C274 at 8.42	44.69	1.087	13.518	0.324
3C274 at 32	16.22	1.270	4.200	0.130
3C274 at 2.295	137.24	1.060	42.570	1.022
3C123 at 2.295	31.00	1.000	10.190	0.245

IV. Efficiency Measurements: X-Band at f1

The X-band efficiency measurements were made at the f1 focal point with the R&D feed package. As these were the first measurements made after holography, all of the star tracks applied the holography-determined best 45-deg subreflector offsets (in the y- and z-axis). These offsets are superimposed onto the structural (elevation-dependent) predict curves resident in the antenna-pointing controller (APC). No pointing model was used during the f1 X-band tracks. However, subsequent analysis of the pointing errors (relative to the last boresight) indicated that no more than 0.002 deg of total pointing error was built up between the peak noise temperature estimates. This resulted in only a very small gain loss ($\approx$ 0.01 dB for a 0.063-deg X-band full-width half-power beamwidth) and, hence, measurements from the first two star tracks on 3C274 and 3C84 were used for efficiency calculation.

The zenith attenuation values for the 2-day tracking period (DOY 144–145) varied from 0.036 to 0.042 dB. The best-fit efficiency curve and the adjusted data points are shown in Fig. 1. The peak X-band efficiency at f1 was determined to be 75.25 percent at an elevation angle of 42.5 deg. Using Eq. (8), the one–standard deviation uncertainty on the best-fit peak efficiency is computed to be 2.04 percent. The peak X-band efficiency and uncertainty correspond to a peak gain of 68.33 dBi $\pm$ 0.12 dB. The uncertainty on the efficiency below 30-deg elevation is greater due to insufficient (and nonrepeatable) measurement points available for the curve fit. At 20 deg, the one–standard deviation error is estimated to be 3 percent.

---

[8] P. Richter, op. cit.

$$T_{p,v}(el) = L(el)T_p(el) \tag{4}$$

where $T_p(el)$ is the actual peak source temperature output from the boresight measurement, and the loss factor, $L(el)$, is given by

$$L(el) = 10^{(A(el)/10)} \tag{5}$$

C. Error Analysis

From Eq. (2), the variance of the efficiency, σ_η^2, may be expressed as

$$\left(\frac{\sigma_{\eta(el)}}{\eta(el)}\right)^2 = \left(\frac{\sigma_{T_a}}{T_a}\right)^2 + \left(\frac{\sigma_{T_p}}{T_p(el)}\right)^2 + \left(\frac{\sigma_{L(el)}}{L(el)}\right)^2 \tag{6}$$

where σ_{T_a}, σ_{T_p}, and σ_L are, respectively, the uncertainties of the absolute calibration source temperature, the measured source temperature, and the atmospheric attenuation loss factor. It can be shown that propagation of the loss factor, $L(el)$, with respect to the zenith attenuation value, A_{zen}, from Eq. (5) results in

$$\left(\frac{\sigma_{L(el)}}{L(el)}\right)^2 = (\ln(10)\log(L(el)))^2 \left(\frac{\sigma_{A_{zen}}}{A_{zen}}\right)^2 \tag{7}$$

which, inserted into Eq. (6), yields the efficiency variance function as

$$\left(\frac{\sigma_{\eta(el)}}{\eta(el)}\right)^2 = \left(\frac{\sigma_{T_a}}{T_a}\right)^2 + \left(\frac{\sigma_{T_p}}{T_p(el)}\right)^2 + (\ln(10)\log(L(el)))^2 \left(\frac{\sigma_{A_{zen}}}{A_{zen}}\right)^2 \tag{8}$$

A term-by-term computation of the error variance follows. The values of the pair (T_a, σ_{T_a}) for various radio source calibrators are taken from Richter[6] for a 34-m antenna at each of the S-, X-, and Ka-frequency bands. The magnitude of the efficiency calibration is directly dependent on the value of T_a and its accuracy. The uncertainty, σ_{T_p}, is obtained from the residual sum of squares of the best-fit quadratic curve to the peak noise temperature samples, $T_p(el)$, versus elevation angle. It is an estimate of the on-source radiometer measurement noise and is assumed to be constant with respect to time and elevation angle. The loss factor uncertainty, $\sigma_L(el)$, is computed from a probable error of 10 percent on the zenith attenuation value,[7] i.e., $\sigma_{Azen} = 0.1A_{zen}$. Note that since A_{zen} is calculated from surface weather measurements, it is a time-varying quantity. However, the error statistic $\sigma_{A_{zen}}$ is modeled as stationary. For the DSS-24 calibration period, values for A_{zen} are computed and analyzed using weather instrumentation recordings from DSS 24 (mounted on the microwave front-end test package itself), DSS 13, and Signal Processing Center (SPC) 10.

Lastly, it is assumed that there is no systematic efficiency loss due to beam-pointing errors during the boresight measurements since the algorithm is continually updating antenna-pointing corrections. Also, systematic efficiency losses due to errors in subreflector focusing and beam-waveguide mirror misalignments are, when applicable, added to the computed value of σ_η.

---

[6] P. Richter, op. cit.

[7] Personal communication with S. Slobin, op. cit., August 1994.

the particular circumstances of each measurement set and the data analysis. The final section presents a summary of the peak gains and efficiencies measured during the testing period.

II. Efficiency Calibration Methodology

A. Efficiency Determination

Determination of the DSS-24 aperture efficiency follows a previously developed methodology [1].[3] Peak radio-source noise temperatures are measured at different antenna orientations via a boresight (actually a step-scan) algorithm [2] resident in a PC-based radiometer system. This automated boresighting program, know as AUTOBORE, was previously developed for performance testing of DSS 13 [3].

To yield an estimate of antenna efficiency, these measured quantities are then normalized by the absolute source calibration temperature, $T_a = T_{100}/C_r$, where T_{100} is the 100-percent antenna efficiency temperature computed from the best-known radio source flux density and C_r is the source size correction factor (see [1] and [4] for more details).[4]

For this article, the aperture efficiency measured at DSS 24 is referenced to the input of the low-noise amplifier and, thus, includes the losses of the feed system. In equation form, the efficiency, $\eta(el)$, for a given elevation angle, el, as measured on site is

$$\eta(el) = \frac{T_p(el)}{T_a} \tag{1}$$

where T_p is the peak on-source temperature. The effects of atmospheric attenuation must be considered; then the Eq. (1) becomes

$$\eta(el) = \frac{L(el)T_p(el)}{T_a} \tag{2}$$

where $L(el)$ is the atmospheric attenuation loss factor, which is described below.

B. Correction for Atmospheric Attenuation

In order to report the DSS-24 efficiency without the effects of atmospheric absorption, the estimated source peak temperatures from the antenna boresight measurements must be scaled up by a computed loss factor. A computer program, SDSATM4S.BAS,[5] is used to estimate total zenith attenuation values, A_{zen}, from surface measurements of temperature, pressure, and relative humidity. From A_{zen}, the attenuation loss factor for the logged boresight elevation angles can then be calculated. For clarity, the equations for the computation given in [1] are repeated here. The attenuation at elevation angle el is computed from

$$A(el) = \frac{A_{zen}}{\sin(el)} \tag{3}$$

where A_{zen} is in units of decibels. The radio source peak temperature, in a vacuum condition, is defined by

---

[3] Ibid.

[4] Values of the temperature $T_a = T_{100}/C_r$ for radio sources used to calibrate DSN antennas are given in P. Richter, *DSN Radio Source List for Antenna Calibration*, JPL D-3801, Rev. C (internal document), Jet Propulsion Laboratory, Pasadena, California, August 19, 1993.

[5] Courtesy of S. Slobin, Telecommunications Systems Section, Jet Propulsion Laboratory, Pasadena, California.
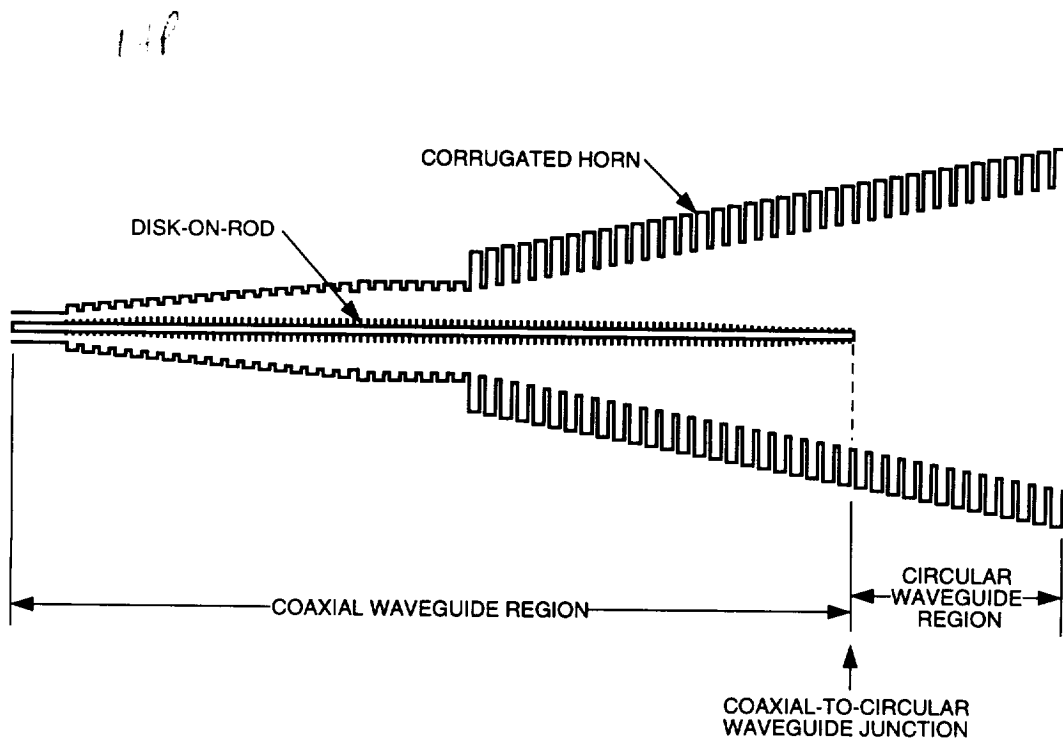
Fig. 1. A model of a disk-on-rod inside a corrugated horn.
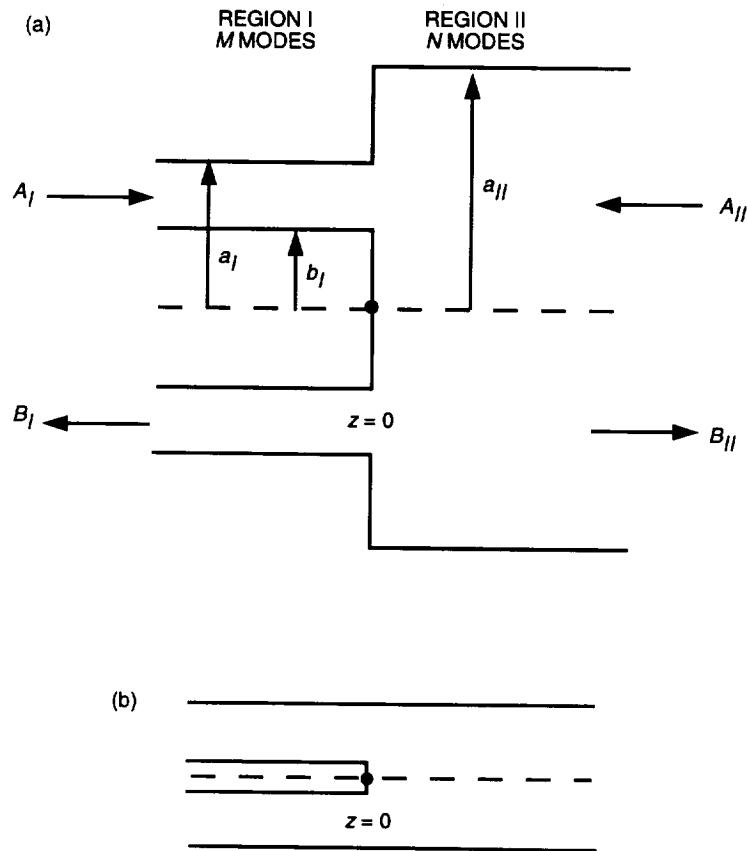
Fig. 2. Coaxial-to-circular waveguide junctions with (a) a different outer radius and (b) the same outer radius.

the analysis, and the waveguide is assumed to be nondissipative. In region I (the coaxial waveguide region), let the transverse field $\overline{E}_I, \overline{H}_I$ at $z = 0$ be represented by the modal expansion

$$\overline{E}_I = \sum_{m=1}^{M} (A_{mI} + B_{mI}) \overline{e}_{mI} \tag{1}$$

$$\overline{H}_I = \sum_{m=1}^{M} (A_{mI} - B_{mI}) \overline{h}_{mI} \tag{2}$$

where $\overline{e}_{mI}$ and $\overline{h}_{mI}$ are transverse modal field vectors and A_{mI}, B_{mI} are the forward and reflected modal coefficients in the region I to be determined. The electromagnetic fields for the TE ($e_z = 0$) and TM ($h_z = 0$) coaxial modes are as follows [4].

For the TE coaxial waveguide modes, the transverse $\overline{e}$ and $\overline{h}$ fields are

$$\overline{e} = e_r \hat{r} + e_\phi \hat{\phi} \tag{3}$$

$$\overline{h} = h_r \hat{r} + h_\phi \hat{\phi} \tag{4}$$

$$e_r = C_m \frac{F_1\left((\chi'_m r)/b_I\right)}{(\chi'_m r)/b_I} \sin \phi$$

$$e_\phi = C_m F_1'\left(\frac{\chi'_m r}{b_I}\right) \cos \phi \tag{5}$$

$$h_r = -\frac{e_\phi}{\eta_m^{TE}}$$

$$h_\phi = \frac{e_r}{\eta_m^{TE}} \tag{6}$$

where F_1 is a combination of Bessel functions of the first kind, $J_\nu(z)$, and Bessel functions of the second kind, $Y_\nu(z)$, of integral order $\nu = 1$, and is given by

$$F_1\left(\frac{\chi'_m r}{b_I}\right) = J_1\left(\frac{\chi'_m r}{b_I}\right) Y_1'(\chi'_m) - Y_1\left(\frac{\chi'_m r}{b_I}\right) J_1'(\chi'_m) \tag{7}$$

where χ'_m is the mth root of the derivative of F_1 when $r = a_I$ and C_m is a normalization constant. The impedance of the TE waveguide mode, η^{TE}, is given by

$$\eta^{TE} = \begin{cases} \dfrac{\sqrt{\mu/\varepsilon}}{\sqrt{1-(\lambda/\lambda_c)^2}} & \text{for } \lambda < \lambda_c \\[3mm] \dfrac{j\sqrt{\mu/\varepsilon}}{\sqrt{(\lambda/\lambda_c)^2-1}} & \text{for } \lambda > \lambda_c \end{cases} \tag{8}$$

190

where μ and ε are the absolute magnetic permeability and absolute dielectric constant of the medium, respectively. The free space wavelength is λ, and λ_c is the cutoff wavelength ($\lambda_c = \lambda'_{cm}$) of the TE coaxial waveguide mode, which can be expressed as

$$\lambda'_{cm} = \frac{2\pi}{((a_I/b_I) + 1)\chi'_m}(a_I + b_I) \qquad m = 1$$

$$\lambda'_{cm} = \frac{2\pi}{((a_I/b_I) - 1)\chi'_m}(a_I - b_I) \qquad m = 2, 3, 4, \cdots$$

(9)

For the TM coaxial waveguide modes, the transverse $\overline{e}$ and $\overline{h}$ fields can be expressed as

$$e_r = -C_m G'_1\left(\frac{\chi_m r}{b_I}\right)\cos\phi$$

$$e_\phi = C_m \frac{G_1(\chi_m r/b_I)}{\chi_m r/b_I}\sin\phi$$

(10)

$$h_r = -\frac{e_\phi}{\eta_m^{TM}}$$

$$h_\phi = \frac{e_r}{\eta_m^{TM}}$$

(11)

where G_1 is a combination of Bessel functions of the first kind, $J_\nu(x)$, and Bessel functions of the second kind, $Y_\nu(x)$, of integral order $\nu = 1$, and is given by

$$G_1\left(\frac{\chi_m r}{b_I}\right) = J_1\left(\frac{\chi_m r}{b_I}\right)Y_1(\chi_m) - Y_1\left(\frac{\chi_m r}{b_I}\right)J_1(\chi_m)$$

(12)

where χ_m is the mth root of G_1 when $r = a_I$. The impedance of the TM waveguide mode, η^{TM}, is

$$\eta^{TM} = \begin{cases} \sqrt{\frac{\mu}{\varepsilon}}\sqrt{1 - \left(\frac{\lambda}{\lambda_c}\right)^2} & \text{for } \lambda < \lambda_c \\ -j\sqrt{\frac{\mu}{\varepsilon}}\sqrt{\left(\frac{\lambda}{\lambda_c}\right)^2 - 1} & \text{for } \lambda > \lambda_c \end{cases}$$

(13)

The cutoff wavelength of the TM coaxial waveguide mode, $\lambda_c = \lambda_{cm}$, can be expressed as

$$\lambda_{cm} = \frac{2\pi}{((a_I/b_I) - 1)\chi_m}(a_I - b_I)$$

(14)

In region II, the transverse fields $\overline{E}_{II}, \overline{H}_{II}$ at $z = 0$ can be represented by the modal solution in region II (the circular waveguide region) as follows:

$$\overline{E}_{II} = \sum_{n=1}^{N}(A_{nII} + B_{nII})\overline{e}_{nII} \tag{15}$$

$$\overline{H}_{II} = \sum_{n=1}^{N}(A_{nII} - B_{nII})\overline{h}_{nII} \tag{16}$$

where $\overline{e}_{nII}$ and $\overline{h}_{nII}$ are transverse modal fields and A_{nII}, B_{nII} are the forward and reflected modal coefficients in region II to be determined.

The transverse $\overline{e}$ and $\overline{h}$ fields of the TE circular waveguide modes are

$$e_r = C_n \frac{J_1\left((\chi_n' r)/a_{II}\right)}{(\chi_n' r)/a_{II}} \sin\phi$$

$$\tag{17}$$

$$e_\phi = C_n J_1'\left(\frac{\chi_n' r}{a_{II}}\right)\cos\phi$$

$$h_r = -\frac{e_\phi}{\eta_n^{TE}}$$

$$\tag{18}$$

$$h_\phi = \frac{e_r}{\eta_n^{TE}}$$

where χ_n' is the nth nonvanishing root of the derivative of the Bessel function $J_1'(\chi_n') = 0$. The C_n is a normalization constant. The impedance of the TE waveguide mode, η^{TE}, is defined in Eq. (6), and the cutoff wavelength of the TE circular waveguide mode, $\lambda_c = \lambda_{cn}'$, can be expressed as

$$\lambda_{cn}' = \frac{2\pi}{\chi_n'}a_{II} \tag{19}$$

For TM circular waveguide modes, the transverse $\overline{e}$ and $\overline{h}$ fields are

$$e_r = -C_n J_1'\left(\frac{\chi_n r}{a_{II}}\right)\cos\phi$$

$$\tag{20}$$

$$e_\phi = C_n \frac{J_1((\chi_n r)/a_{II})}{(\chi_n r)/a_{II}} \sin\phi$$

$$h_r = -\frac{e_\phi}{\eta_n^{TM}}$$

$$\tag{21}$$

$$h_\phi = \frac{e_r}{\eta_n^{TM}}$$

192

and χ_n is the nth nonvanishing root of $J_1(\chi_n) = 0$. The impedance of the TM waveguide mode, η^{TM}, is defined in Eq. (11), and the cutoff wavelength, $\lambda_c = \lambda_{cn}$, of the TM circular waveguide mode can be expressed as

$$\lambda_{cn} = \frac{2\pi}{\chi_n} a_{II} \tag{22}$$

By applying the boundary conditions that are discussed in detail in [1], the following pair of simultaneous matrix equations is obtained:

$$[P]\{[A_I] + [B_I]\} = [Q]\{[A_{II}] + [B_{II}]\} \tag{23}$$

$$[P]^T\{[B_{II}] - [A_{II}]\} = [R]\{[A_I] - [B_I]\} \tag{24}$$

where $[A_I]$ and $[B_I]$ are column matrices of M elements containing the unknown modal coefficients in region I; $[A_{II}]$ and $[B_{II}]$ are column matrices of N elements containing the unknown modal coefficients in region II; $[P]^T$ is a transpose matrix of $[P]$; $[P]$ is an M-by-N matrix; $[Q]$ is an N-by-N diagonal matrix; and $[R]$ is an M-by-M diagonal matrix. The elements of these three matrices, $[P], [Q]$, and $[R]$, are defined as follows:

$$P_{mn} = \int\limits_{S_I} \underline{e}_{mI} \times \underline{h}_{nII} \cdot ds \tag{25}$$

$$Q_{nn} = \int\limits_{S_{II}} \underline{e}_{nII} \times \underline{h}_{nII} \cdot ds \tag{26}$$

$$R_{mm} = \int\limits_{S_I} \underline{e}_{mI} \times \underline{h}_{mI} \cdot ds \tag{27}$$

In all cases, these integrals can be obtained in closed form. The R_{mm} is the integration between two circular waveguide modes and Q_{nn} is the integration between two coaxial waveguide modes in region I and region II, respectively; P_{mn} is the integration between circular and coaxial waveguide modes and can be expressed as

$$P_{mn} = \begin{cases} \left(\frac{\pi}{\eta_n^{TE}}C_nC_m\right)\frac{1}{(\chi_n'/a_{II})^2-(\chi_m'/b_I)^2}\left[\frac{2}{\pi}J_1'\left(\frac{\chi_n'b_I}{a_{II}}\right)-\frac{\chi_m'a_I}{b_I}J_1'\left(\frac{\chi_n'a_I}{a_{II}}\right)F_1\left(\frac{\chi_m'a_I}{b_I}\right)\right] \\ \qquad \text{(TE coaxial waveguide mode and TE circular waveguide mode)} \\[2ex] \left(\frac{\pi}{\eta_n^{TM}}C_nC_m\right)\frac{1}{(\chi_n/a_{II})^2-(\chi_m/b_I)^2}\left[\frac{2}{\pi}\frac{\chi_nb_I}{\chi_ma_{II}}J_1\left(\frac{\chi_nb_I}{a_{II}}\right)+\frac{\chi_na_I}{a_{II}}J_1\left(\frac{\chi_na_I}{a_{II}}\right)G_1'\left(\frac{\chi_ma_I}{b_I}\right)\right] \\ \qquad \text{(TM coaxial waveguide mode and TM waveguide circular mode)} \\[2ex] \left(\frac{\pi}{\eta_n^{TM}}C_nC_m\right)\frac{a_{II}b_I}{\chi_n\chi_m'}\left[-\frac{2}{\pi}\frac{1}{\chi_m'}J_1\left(\frac{\chi_nb_I}{a_{II}}\right)+J_1\left(\frac{\chi_na_I}{a_{II}}\right)F_1\left(\frac{\chi_m'a_I}{b_I}\right)\right] \\ \qquad \text{(TE coaxial waveguide mode and TM circular waveguide mode)} \\[2ex] 0 \\ \qquad \text{(TM coaxial waveguide mode and TE circular waveguide mode)} \end{cases} \qquad (28)$$

The submatrices $[S_{11}]$, $[S_{12}]$, $[S_{21}]$, and $[S_{22}]$ are derived from $[P]$, $[Q]$, and $[R]$ by Eqs. (21) and (22):

$$[S_{11}] = \left[\sqrt{R}\right]\left([R]+[P]^T[P]\right)^{-1}\left([R]-[P]^T[P]\right)\left[\sqrt{R}\right]^{-1} \qquad (29)$$

$$[S_{12}] = 2\left[\sqrt{R}\right]\left([R]+[P]^T[P]\right)[P]^T\left[\sqrt{Q}\right]^{-1} \qquad (30)$$

$$[S_{21}] = 2\left[\sqrt{Q}\right]\left(\sqrt{Q}+[P][P]^T\right)[P]^T\left[\sqrt{R}\right]^{-1} \qquad (31)$$

$$[S_{22}] = \left[\sqrt{Q}\right]\left([Q]+[P][P]^T\right)^{-1}\left([Q]-[P][P]^T\right)\left[\sqrt{Q}\right]^{-1} \qquad (32)$$

When there are no dimension changes in the waveguide, which is then equivalent to a transmission line, the scattering matrix depends on the propagation constants of the waveguide modes in that straight section. To obtain the overall scattering matrix, the scattering matrices need to be cascaded. The procedure is described in detail in [1].

The above theory described the waveguide mode-matching method for coaxial-to-circular waveguide junctions. The same method was applied to circular-to-circular and coaxial-to-coaxial waveguide junctions (Figs. 3 and 4).

III. Computer Program Development

The geometrical configuration of the horn (flare angle, groove depth and width, and aperture size) is represented by a series of circular waveguides of different radii and lengths while the configuration of the disk-on-rod (diameter of the rod, diameter and thickness of the disk, disk spacing) is represented by a series of disks of various radii and lengths. These two data files are then combined and regenerated as a new data file containing the geometry of the disk-on-rod inside a horn. The new input data file includes the outer radius (horn), inner radius (disk-on-rod), and the length of the (either coaxial or circular) waveguide section. The inner radius is zero for circular waveguide sections. All the sections are circularly symmetric with respect to the center axis of the feedhorn. The number of modes in each section is chosen according to the ratio $M/N = (a_I - b_I)/(a_{II} - b_{II})$ in order to converge to the correct values.
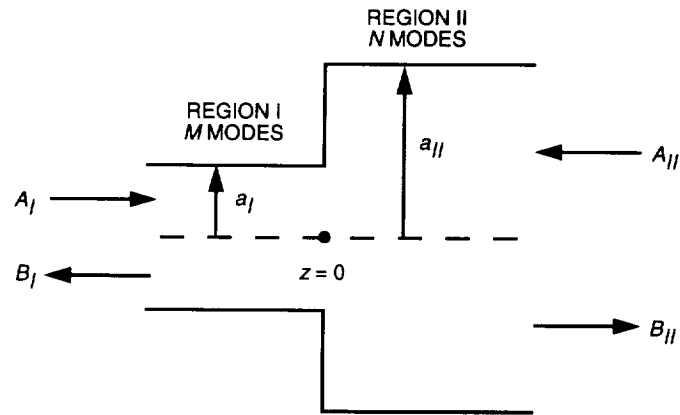
Fig. 3. Circular waveguide junctions.
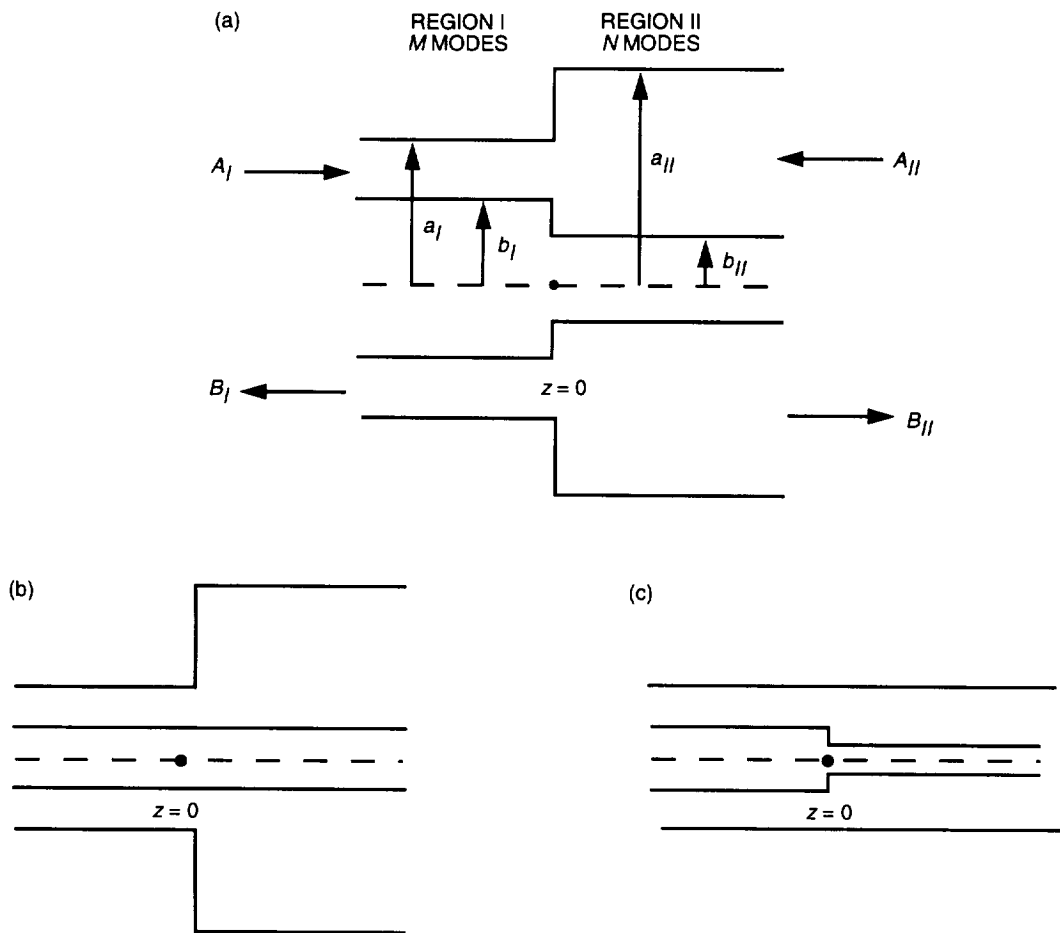
Fig. 4. Coaxial waveguide junctions with a different (a) inner and outer radius, (b) outer radius, and (c) inner radius.

The P, Q, and R are calculated [Eqs. (25)–(27)] according to the type and size of the waveguide junctions. The scattering matrix of each section is calculated and cascaded with the scattering matrix of previous sections until the scattering matrix of the whole horn is obtained.

The reflection matrix $[S_{11}]$ indicates the return loss of the horn. The radiation pattern can be computed by using the amplitude and phase of the transmitted circular waveguide modes ($[S_{12}]$) at the horn aperture [5]. Therefore, if the geometry of a feedhorn is available, both characteristics (radiation pattern and return loss) of the feedhorn are computed simply by inputting the geometrical dimensions to the computer program.

IV. Verification of the Computer Program

The program was first verified by comparing results with the existing circular waveguide program and coaxial waveguide program for appropriate junctions. Consistent results were achieved. Then an experiment was designed and performed in order to verify the scattering matrix of a circular-to-coaxial waveguide junction. The test piece is a WC137 circular waveguide with a circular aluminum rod suspended by two pieces of 0.0254 mm–thick kapton (Fig. 5). This structure includes a circular-to-coaxial and a coaxial-to-circular junction. The experiment was performed with rods of radii 7.62 and 10.16 mm and lengths of 63.5 and 76.2 mm. The amplitude and phase of the reflection (S_{11}) and transmission (S_{21}) coefficients were measured using a Hewlett Packard 8510C network analyzer. Good agreement between calculations and measurements was found in all the test cases. A test case of a rod of radius 7.62 mm and length 63.5 mm inside a WC137 circular waveguide of length 203.32 mm is shown in Figs. 6–9. The kapton in the waveguide was very thin in respect to the wavelength, so that it could be neglected in the computer modeling.

The L-/C-band dual-frequency horn, which includes a C-band disk-on-rod inside a C-band launcher and an L-band horn, was also used to check the computer codes (Fig. 10) [6]. By inputting the L-/C-band horn model in the program, the C-band and L-band radiation patterns were computed. Good agreement was shown between calculation and measurement at 5.01 GHz (C-band) and 1.668 GHz (L-band), respectively (Figs. 11–14) [7]. The slight asymmetry between the measured C-band E- and H-plane patterns was due to the C-band disk-on-rod becoming slightly off-centered during the trip to Goldstone, where the measurement was taken. All the results indicate that the software is reliable.
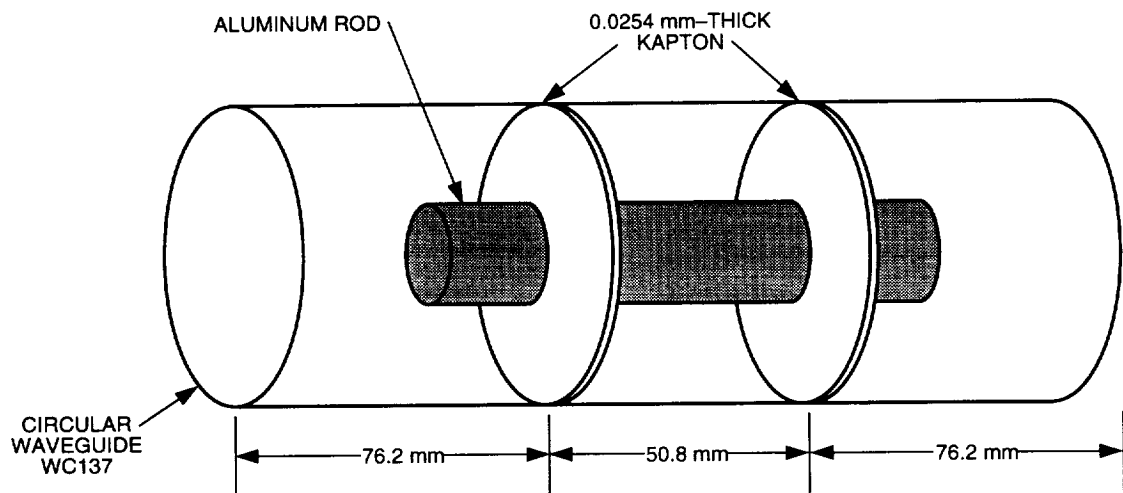
Fig. 5. The test piece for the circular-to-coaxial and coaxial-to-circular junction experiment.
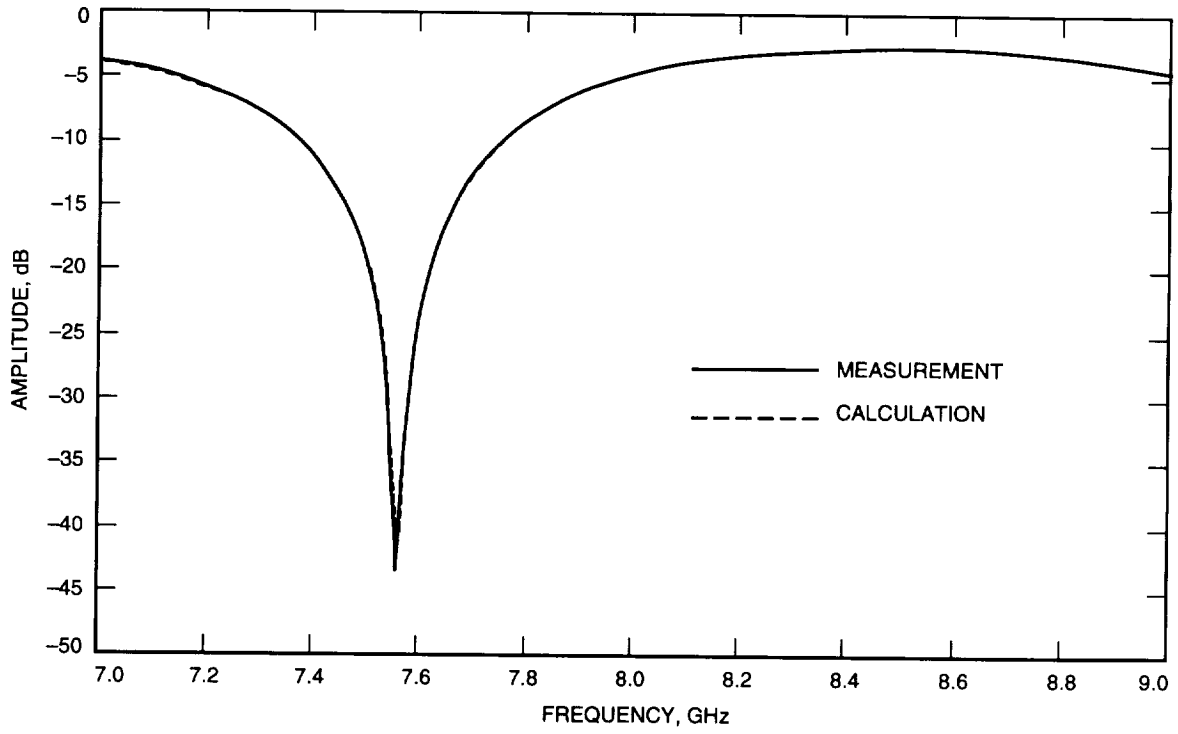
Fig. 6. Calculated and measured amplitude of S_{11} for a rod of radius 7.62 mm and length 63.5 mm inside a WC137 circular waveguide.
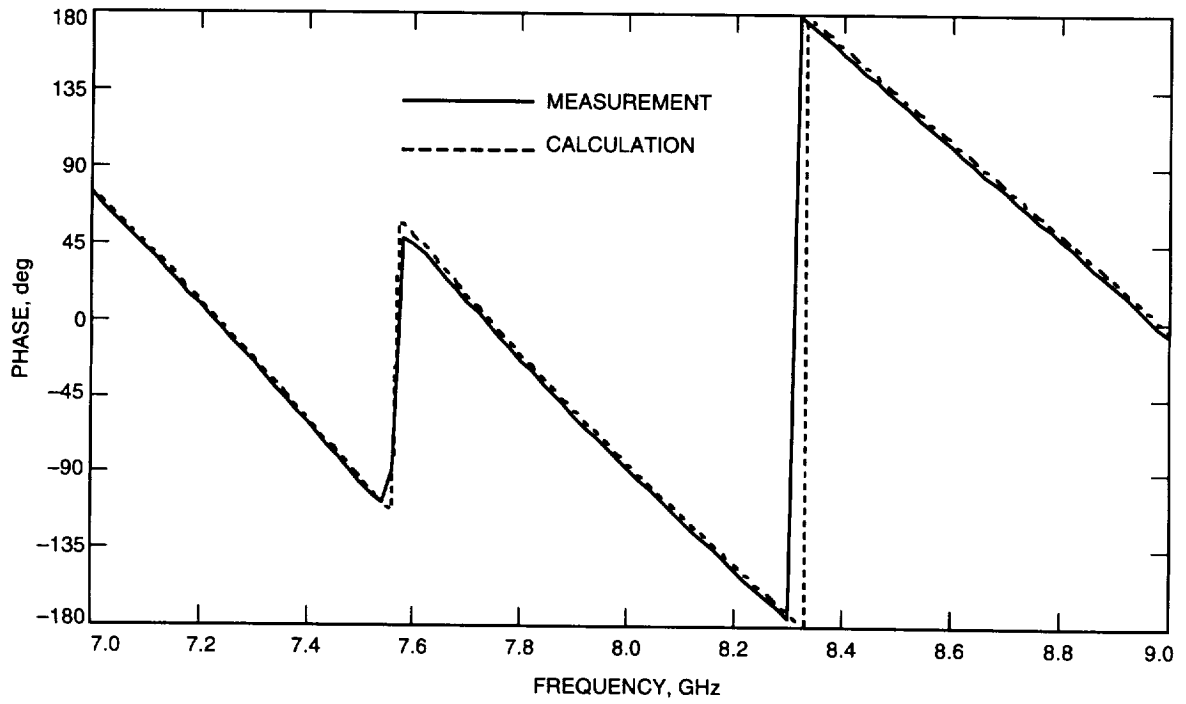
Fig. 7. Calculated and measured phase of S_{11} for a rod of radius 7.62 mm and length 63.5 mm inside a WC137 circular waveguide.
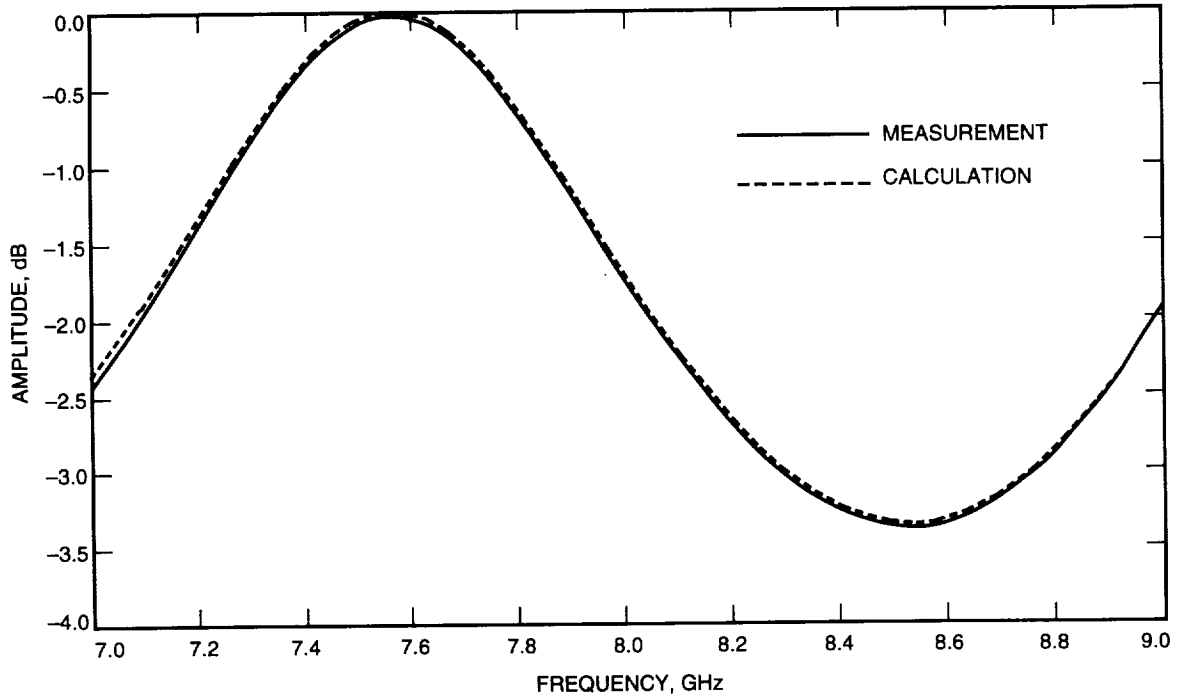
Fig. 8. Calculated and measured amplitude of S_{21} for a rod of radius 7.62 mm and length 63.5 mm inside a WC137 circular waveguide.
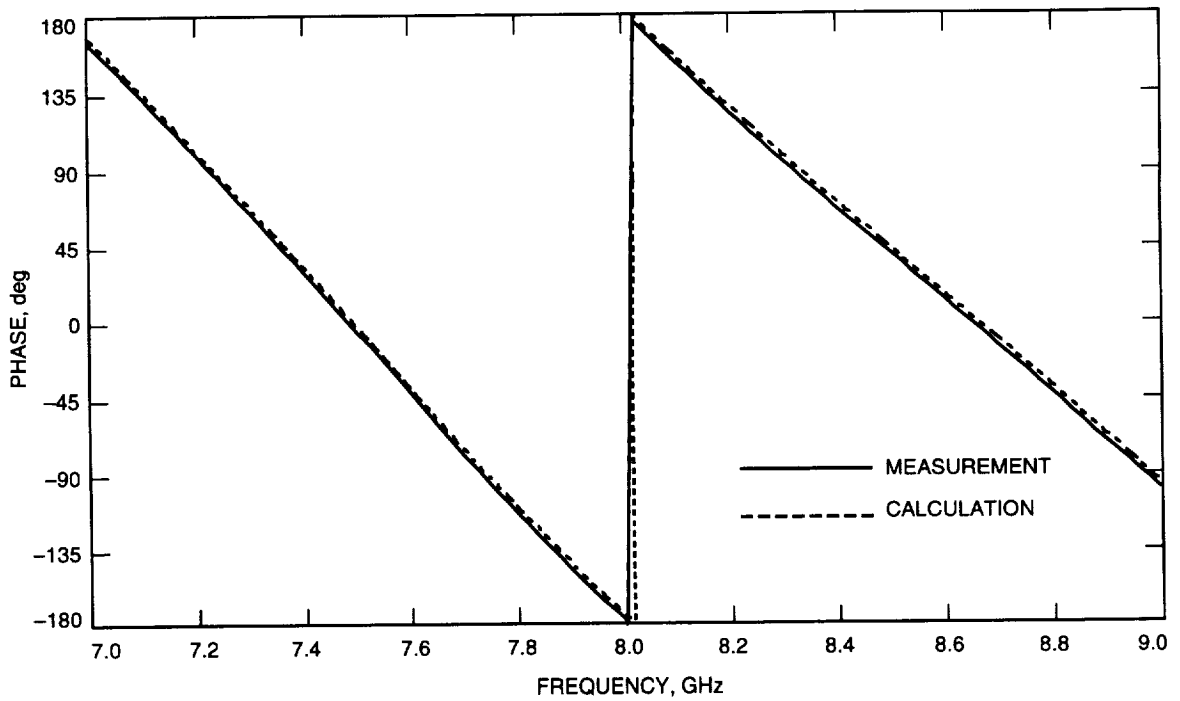
Fig. 9. Calculated and measured phase of S_{21} for a rod of radius 7.62 mm and length 63.5 mm inside a WC137 circular waveguide.

C-BAND DISK-ON-ROD

L-BAND FEEDHORN

C-BAND LAUNCHER
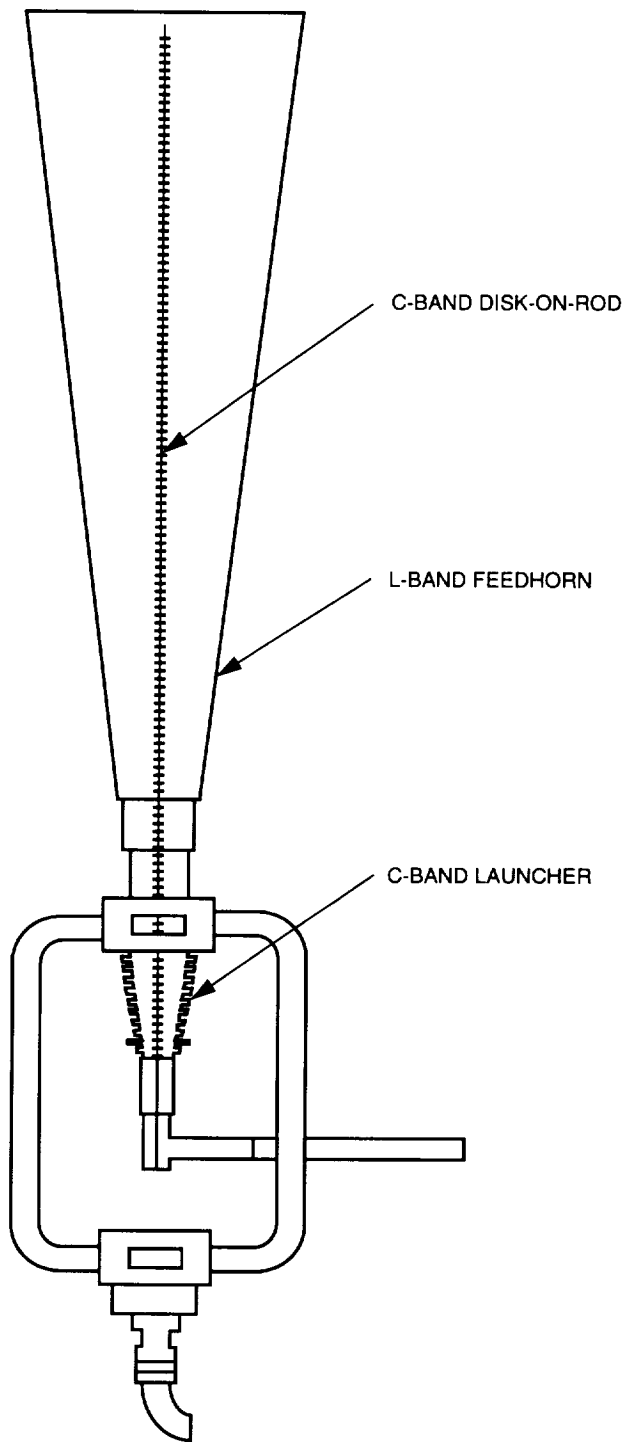
Fig. 10. The L-/C-band dual-frequency feed system.
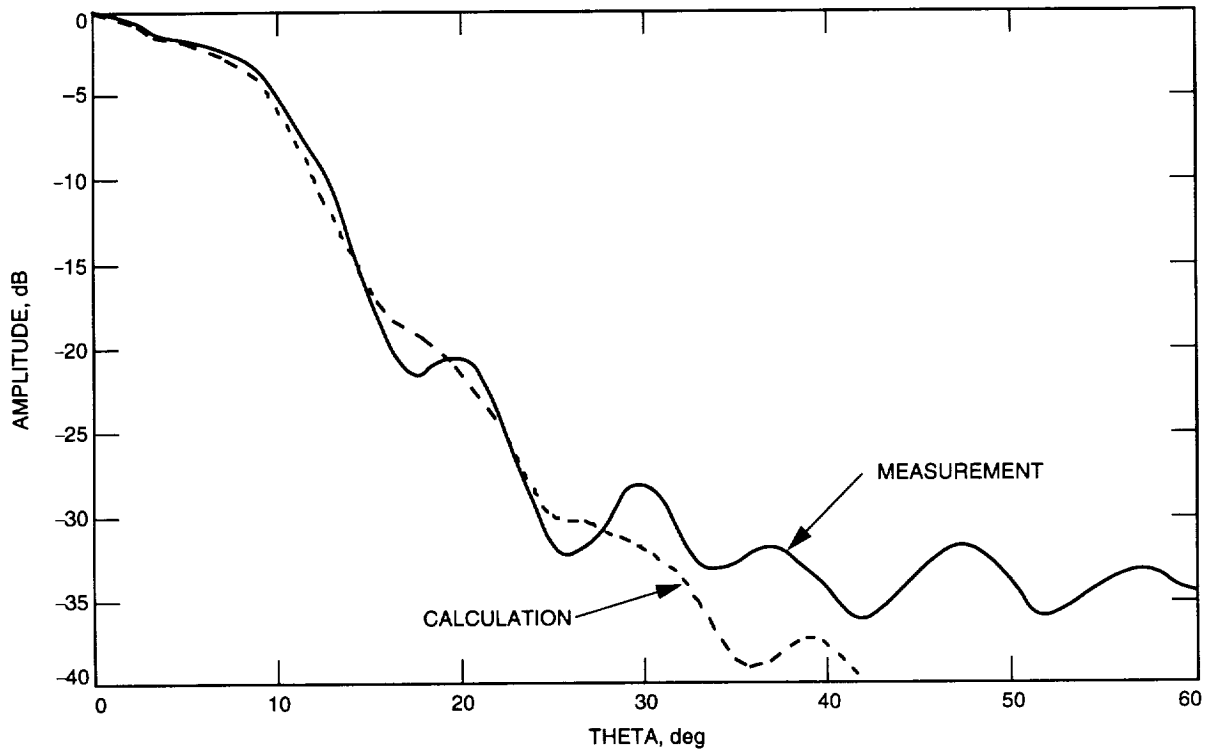
Fig. 11. Measured and calculated H-plane pattern for the L-/C-band dual-frequency horn at 5.01 GHz.
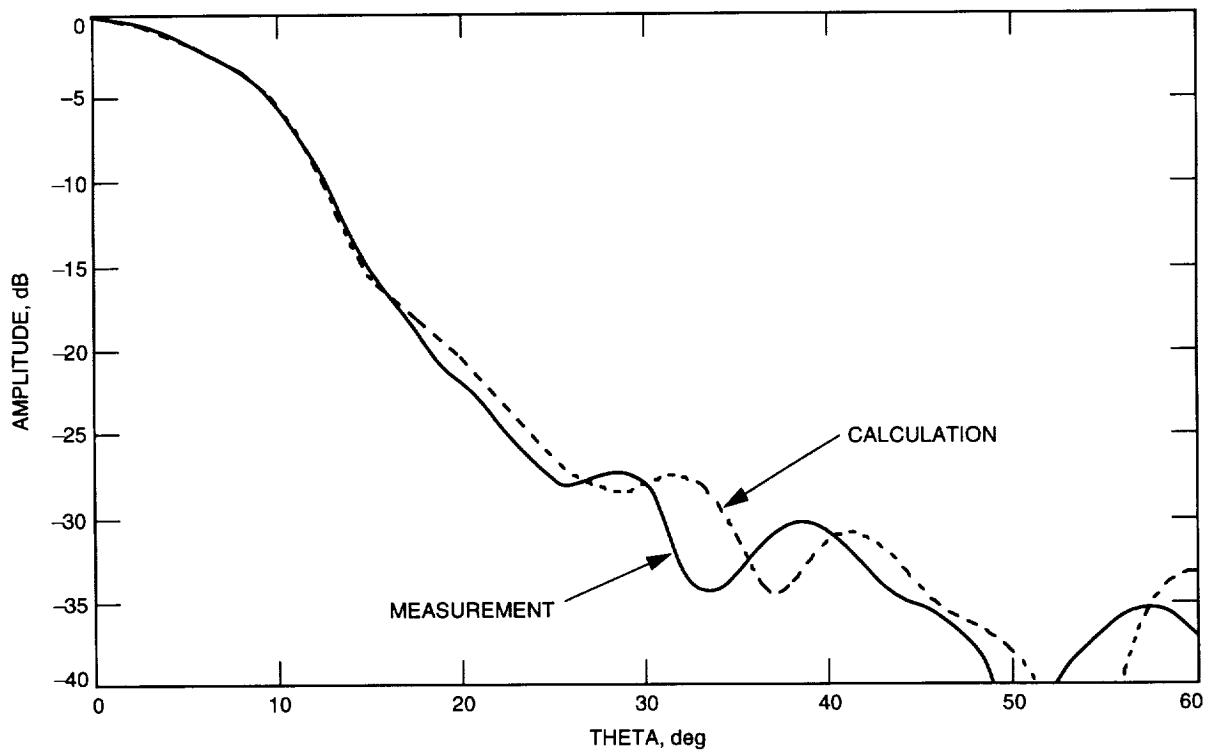
Fig. 12. Measured and calculated E-plane pattern for the L-/C-band dual-frequency horn at 5.01 GHz.

200
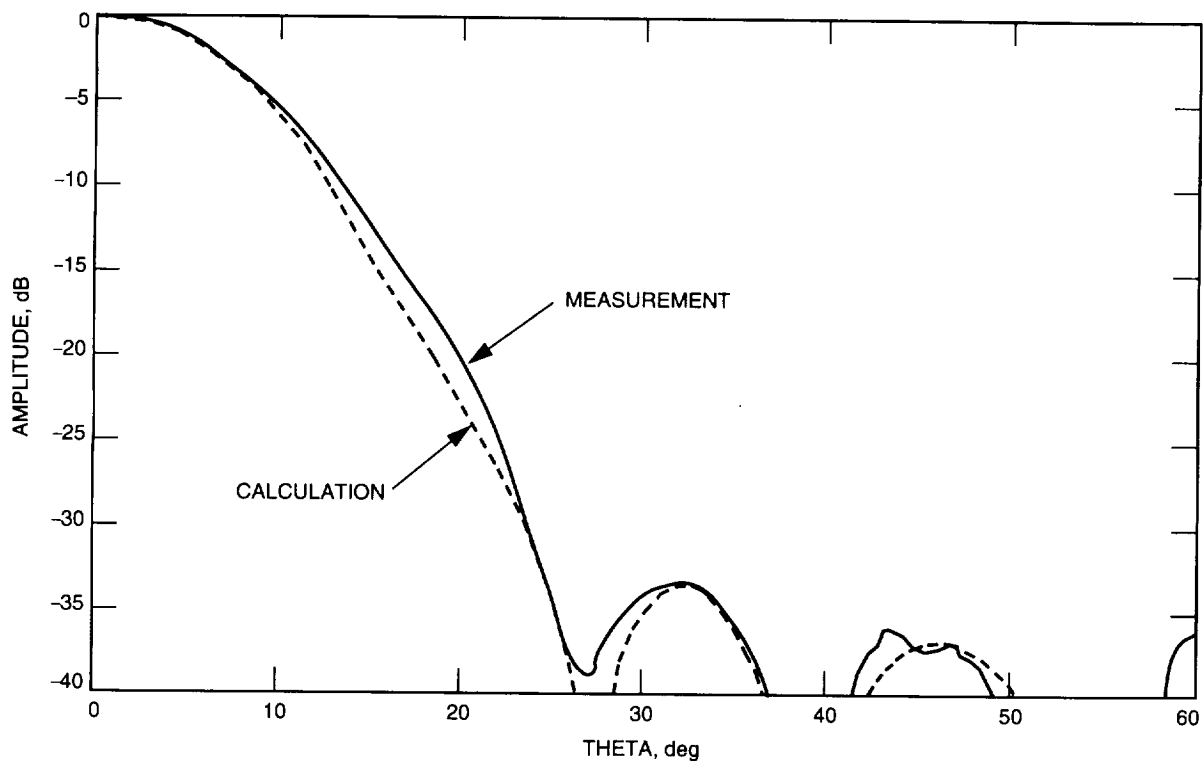
Fig. 13. Measured and calculated H-plane pattern for the L-/C-band dual-frequency horn at 1.7 GHz.
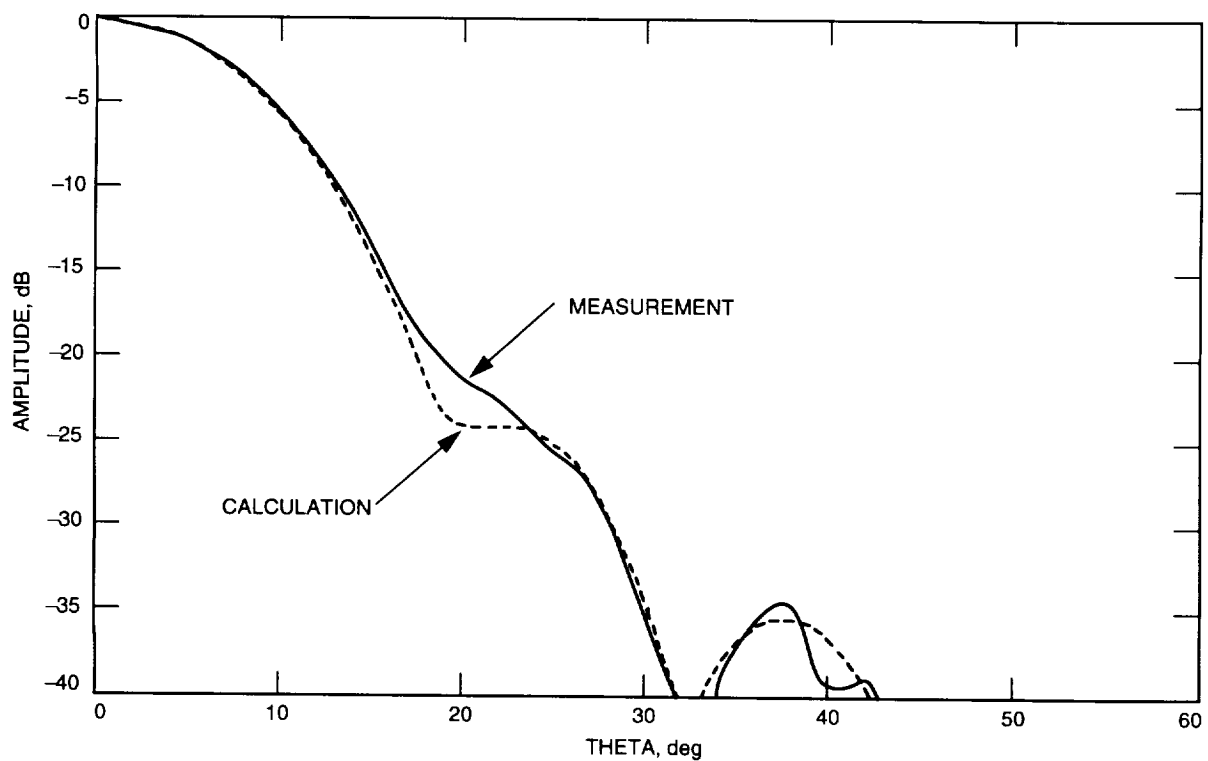
Fig. 14. Measured and calculated E-plane pattern for the L-/C-band dual-frequency horn at 1.7 GHz.

V. Conclusion

A disk-on-rod inside a horn was analyzed based on the mode-matching method. A computer program was developed to calculate the radiation pattern and the return loss of a horn by inputting the dimensions of the horn and the disk-on-rod. The computer program was verified by measurements and checked against other calculations. This software will be used to design an X-/Ka-band (8.45-GHz/33.7-GHz) dual-frequency horn for DSS 13.

Acknowledgment

References

[1] G. L. James, "Analysis and Design of TE_{11}-to-HE_{11} Corrugated Cylindrical Waveguide Mode Converters," *IEEE Transactions in Microwave Theory and Techniques*, vol. MTT-29, no. 10, pp. 1059–1066, October 1981.

[2] G. L. James and B. M. Thomas, "TE_{11}-to-HE_{11} Cylindrical Waveguide Mode Converters Using Ring-Loaded Slots," *IEEE Transactions in Microwave Theory and Techniques*, vol. MTT-30, no. 3, pp. 278–285, March 1982.

[3] D. J. Hoppe, "Modal Analysis Applied to Circular, Rectangular, and Coaxial Waveguides," *The Telecommunications and Data Acquisition Progress Report 42-95, July–September 1988*, Jet Propulsion Laboratory, Pasadena, California, pp. 89–96, November 15, 1988.

[4] N. Marcuvitz, *Waveguide Handbook*, United Kingdom: Peter Peregrinus Ltd., pp. 66–80, 1988.

[5] S. Silver, *Microwave Antenna Theory and Design*, New York: McGraw-Hill, pp. 336–337, 1949.

[6] P. H. Stanton and H. F. Reilly, Jr., "The L-/C-Band Feed Design for the DSS-14 70-Meter Antenna (Phobos Mission)," *The Telecommunications and Data Acquisition Progress Report 42-107, July–September 1991*, Jet Propulsion Laboratory, Pasadena, California, pp. 88–95, November 15,1991.

[7] M. S. Gatti, A. J. Freiley, and D. Girdner, "RF Performance Measurement of the DSS-14 70-Meter Antenna at C-Band/L-Band," *The Telecommunications and Data Acquisition Progress Report 42-96, October–December 1988*, Jet Propulsion Laboratory, Pasadena, California, pp. 117–125, February 15, 1989.

Errata

In "The Network Operations Control Center Upgrade Task: Lessons Learned," which appeared in *The Telecommunications and Data Acquisition Progress Report 42-118, April–June 1994*, August 15, 1994, the authors were listed in incorrect order. The attributions should have appeared as follows:

The Network Operations Control Center Upgrade Task: Lessons Learned

T.-L. Tran and S. Lee
Software Product Assurance Section

J. S. Sherif
Software Product Assurance Section
and
California State University, Fullerton

Author Index,[1] 1994

The Telecommunications and Data Acquisition Progress Report

42-117, January–March, May 15, 1994
42-118, April–June, August 15, 1994
42-119, July–September, November 15, 1994
42-120, October–December, February 15, 1995

Albus, J.

42-118   Pilot Retrofit Test of Refrigerant R-134a for GDSCC, pp. 125–138.

B. Brown, M. Dungao, and G. Spencer

Alvarez, L. S.

42-117   Design and Implementation of a Beam-Waveguide Mirror Control System for Vernier Pointing of the DSS-13 Antenna, pp. 49–61.

M. Moore, W. Veruttipong, and E. Andres

42-120   The Efficiency Calibration of the DSS-24 34-Meter Diameter Beam-Waveguide Antenna, pp. 174–187.

M. J. Britcliffe, M. M. Franco, S. R. Stewart, and H. J. Jackson

Andres, E.

42-117   Design and Implementation of a Beam-Waveguide Mirror Control System for Vernier Pointing of the DSS-13 Antenna, pp. 49–61.

See Alvarez, L. S.

Asmar, S. W.

42-120   Radio-Science Performance Analysis Software, pp. 121–152.

See Morabito, D. D.

Aung, M.

42-118   The Block V Receiver Fast Acquisition Algorithm for the Galileo S-Band Mission, pp. 83–114.

W. J. Hurd, C. M. Buu, J. B. Berner, S. A. Stephens, and J. M. Gevargiz

---

[1] In the case of joint authorship, the reader is referred to the citation under the first author, where all the authors of the article are listed.

205

Jin, Y.

42-118   Convolutional Encoding of Self-Dual Block Codes (II), pp. 22–25.

         See Solomon, G.

Kahn, R. D.

42-117   Spacecraft–Spacecraft Radio-Metric Tracking: Signal Acquisition Requirements and Application to Mars Approach Navigation, pp. 161–174.

         S. Thurman and C. D. Edwards

Kiely, A. B.

42-117   Bit-Wise Arithmetic Coding for Data Compression, pp 145–160

Kroger, P. M.

42-117   The Mars Observer Differential One-Way Range Demonstration, pp. 1–15.

         J. S. Border and S. Nandi

42-119   Radio–Planetary Frame Tie From Phobos-2 VLBI Data, pp. 46–82.

         See Hildebrand, C. E.

Kwok, A.

42-117   The Mars Observer Ka-Band Link Experiment, pp. 250–282.

         See Rebold, T. A.

Kyriacou, C.

42-117   Performance Evaluation of Digital Phase-Locked Loops for Advanced Deep Space Transponders, pp. 175–193.

         See Nguyen, T. M.

Lansing, F. S.

42-117   A 32-GHz Solid-State Power Amplifier for Deep Space Communications, pp. 236–249.

         See Wamhof, P. D.

Lanyi, G. E.

42-119   Evaluation of Current Tropospheric Mapping Functions by Deep Space Network Very Long Baseline Interferometry, pp. 1–11.

         See Sovers, O. J.

Laskar, J.

42-120   On-Wafer, Cryogenic Characterization of Ultra-Low Noise HEMT Devices, pp. 104–120.

         See Bautista, J. J.

Lee, K. A.

42-117   A 32-GHz Solid-State Power Amplifier for Deep Space Communications, pp. 236–249.

         See Wamhof, P. D.

Maleki, L.

42-117   Field Demonstration of X-Band Photonic Antenna Remoting in the Deep Space Network, pp. 29–34.

          See Yao, X. S.

42-117   Influence of an Externally Modulated Photonic Link on a Microwave Communications System, pp. 16–28.

          See Yao, X. S.

Manshadi, F.

42-117   DSS-13 S-/X-Band Microwave Feed System, pp. 75–80.

McEliece, R. J.

42-117   Trace-Shortened Reed–Solomon Codes, pp. 119–128.
          G. Solomon

McWatters, D.

42-117   A 1- to 10-GHz Downconverter for High-Resolution Microwave Survey, pp. 81–91.

Mellstrom, J. A.

42-118   Linear Quadratic Gaussian and Feedforward Controllers for the DSS-13 Antenna, pp. 37–55.
          See Gawronski, W. K.

42-119   Field Verification of the Wind Tunnel Coefficients, pp. 210–220.
          See Gawronski, W. K.

Moore, M.

42-117   Design and Implementation of a Beam-Waveguide Mirror Control System for Vernier Pointing of the DSS-13 Antenna, pp. 49–61.
          See Alvarez, L. S.

Morabito, D. D.

42-120   Radio-Science Performance Analysis Software, pp. 121–152.
          S. W. Asmar

Nandi, S.

42-117   The Mars Observer Differential One-Way Range Demonstration, pp. 1–15.
          See Kroger, P. M.

Nguyen, T. M.

42-117   Performance Evaluation of Digital Phase-Locked Loops for Advanced Deep Space Transponders, pp. 175–193.
          S. M. Hinedi, H.-G. Yeh, and C. Kyriacou

42-119   Adaptive Line Enhancers for Fast Acquisition, pp. 140–159.
          See Yeh, H.-G.

Yeh, H.-G.

42-117 Performance Evaluation of Digital Phase-Locked Loops for Advanced Deep Space Transponders, pp. 175–193.

See Nguyen, T. M.

42-119 Adaptive Line Enhancers for Fast Acquisition, pp. 140–159.

T. M. Nguyen

Yin, B.

42-118 The Stark Anomalous Dispersion Optical Filter: The Theory, pp. 14–21.

T. M. Shay